Università degli Studi di Cagliari

PHD DEGREE
Physics
Cycle XXXII

Radiation hardness of the upgraded LHCb muon detector electronics and prospects for a full angular analysis in multi-body rare charm decays

Scientific Disciplinary Sectors
FIS/01 FIS/04

PhD Student:	DAVIDE BRUNDU
Coordinator of the PhD Programme	Prof. PAOLO RUGGERONE
Supervisor	Dott. ALESSANDRO CARDINI

Final exam. Academic Year 2018 – 2019
Thesis defence: February 2020 Session

Davide Brundu gratefully acknowledges Università di Cagliari and the Istituto Nazionale di Fisica Nucleare (INFN) of Cagliari for the financial support of his PhD scholarship and for their very important logistical and scientific support during the entire PhD.

Radiation hardness of the upgraded LHCb muon detector electronics and prospects for a full angular analysis in multi-body rare charm decays

by

Davide Brundu

Department of Physics
Universita' degli Studi di Cagliari
Dottorato di Ricerca in Fisica - Ciclo XXXII

A dissertation submitted to the University of Cagliari in
accordance with the requirements of the degree of
Doctor of Philosophy.

Supervisor:
Dr. A. Cardini

Coordinator:
Prof. P. Ruggerone

16th January 2020

ABSTRACT

In this dissertation the results of the studies on the new readout electronics for the muon system of the LHCb experiment, and the perspectives for carrying out a full angular analysis in the rare decays $D^0 \to \pi^+\pi^-\mu^+\mu^-$ and $D^0 \to K^+K^-\mu^+\mu^-$ will be described.

The LHCb experiment studies the heavy hadron physics, containing charm or bottom quarks, in particular searching for new Charge-Parity (*CP*) symmetry violation sources, searching for rare decays and studying their properties. LHCb produced leading results in these fields so far. In order to obtain more precise measurements or be able to study new observables, many analyses need a considerable increase in statistics, thus the experiment is now being upgraded to run with an higher instantaneous luminosity of proton-proton collisions. For this reason the readout electronics has been completely replaced by a new optimised version. Several tests have been performed on the new readout electronics that will be here discussed, and that have allowed a comprehensive radiation hardness characterization of the UMC 130 nm technology, used to develop the main electronics device of the muon system readout electronics, the nSYNC chip.

On the other hand, in the last two years of data taking, 2017 and 2018, an excellent performance of the LHCb experiment has been obtained and the significant increase in statistics allowed access to new observables, especially in the field of rare decays. In particular, it has been possible to increase the statistics of rare four-body charm decays, like $D^0 \to \pi^+\pi^-\mu^+\mu^-$ and $D^0 \to K^+K^-\mu^+\mu^-$, of which LHCb already carried out the branching fractions measurement, as well as of angular and *CP* asymmetries. Since interesting results and flavour anomalies have already been obtained from angular analyses of rare B decays, it is important to study the possibility of these analyses in the complementary sector of rare charm decays. In this work the perspectives for performing a full angular analysis with $D^0 \to \pi^+\pi^-\mu^+\mu^-$ and $D^0 \to K^+K^-\mu^+\mu^-$ decays will be discussed. An angular analysis will allow to carry out several Standard Model tests in the field of rare D decays, allowing also to measure theoretically clean observables for probing effects of physics beyond Standard Model, that can occur at high energy scale.

INTRODUCTION

The Standard Model (SM) of particle physics is the quantum field theory that currently describes in the most complete way the elementary constituents of matter and their mutual interactions. It has been tested for many years and in 2012 it received one of the most awaited confirmations, i.e. the observation of the Higgs boson, responsible for the spontaneous electroweak symmetry breaking through which the SM particles acquire mass.

However, there are several open problems that cannot be explained within the model. From cosmological observations it has been shown that only 4% of the energy density present in the universe can be described by the SM; being the remaining percentage composed of dark matter and dark energy. The cosmological observations also show a too large asymmetry between matter and antimatter to be explained by the violation of the *CP* symmetry predicted by the SM. Moreover, the experimental evidence of neutrino masses is not consistent with the minimal formulation of SM, in which neutrinos are described as massless. From the theoretical point of view the most important open problems are the non-inclusion of the gravitational interaction, the presence of several free parameters and the hierarchy problem. Most of the open questions are related to the so-called flavour physics, i.e. the sector of the SM describing the different particle flavours and the mixing between them. Nevertheless, within its scope of validity, the SM remains in excellent agreement with the experimental results.

Four main experiments are currently exploiting the Large Hadron Collider (LHC), at the European Organization for Nuclear Research (CERN), in Geneva, in order to answer to these open questions in particle physics. Among them the LHCb experiment studies with high precision the *CP* violation and rare decays of hadrons containing b quark, with the aim of investigating the matter-antimatter asymmetry problem and searching for physics beyond the SM. The LHCb experiment proved to be an excellent environment also for the study of *charm* physics and rare decays of D mesons. LHCb performs the so-called *indirect* search of new physics, with high precision measurements of observables in quantum suppressed processes, in which yet undiscovered high mass particles can contribute as virtual particles. In this context a very promising research field is the study of flavour changing neutral current (FCNC) processes. They are highly suppressed in the SM since they can only occur as high order transitions, so they are potentially sensitive to new physics contributions induced by unknown particles or interactions. These hypothetically effects can enhance branching fractions of rare decays or significantly modify their angular distributions in case of multi-body decays.

The flavour anomalies already observed in angular analyses of FCNC rare B decays, like the tension in the angular parameter called P_5' in $B^0 \to K^{*0}\mu^+\mu^-$ decay, observed by LHCb [1], Belle [2] and ATLAS [3] experiments, reinforce the interest in extending these studies to the complementary field of rare D decays. From this perspective, one of the interesting decay recently studied by LHCb is the $D^0 \to h^+h^-\mu^+\mu^-$ decay, with $h = K, \pi$, that has been recently observed for the first time and its CP and angular asymmetries have been measured. At high energy scale (i.e. short-distance) the decay proceeds via a FCNC process, $c \to u\mu\mu$, while at lower energy scale (i.e. long-distance) the decay is dominated by intermediate vector resonances that enhance the branching fraction from $\mathscr{O}(10^{-9})$ to $\mathscr{O}(10^{-6})$. Even though the rich resonance structure can hide the short distance process and possibly new physics effects, especially when searching for branching fraction enhancements only, the interference between the short- and long-distance contributions in regions of phase space near resonances may significantly enhance new physics effects. Thus, using the full Run II sample (2015-2018) of LHCb data and being able to double the statistics previously used to analyse these decays, it has become interesting to study the feasibility of a complete angular analysis, exploiting the rich set of angular observables and the correlations between the final state particles of the four body decay. From an experimental point of view the presence of muons in the final state allows high trigger and selection efficiencies and an optimal particle identification, which is essential to obtain a sufficiently pure sample, not polluted by fully hadronic decays where two hadrons are misidentified as muons.

In order to further exploit the wide flavour physics program and perform higher precision measurements, LHCb is undergoing a complete detector and readout upgrade to start, from 2021, a data taking period at an increased luminosity. A significant role in this context has been played for the upgrade of LHCb muon detector, whose most important upgrade concerns the change and compliance of the readout electronics to be able to acquire data at 40 MHz. Several tests on the new electronics have been carried out, in particular concerning the radiation hardness, to assure the proper functionalities during the upgrade operation. The test allowed also to perform one of the first radiation hardness test in literature of the UMC 130 nm technology, used to develop the fundamental device of the muon readout electronics, the nSYNC chip.

The structure of the thesis is the following: in the first chapter the theoretical background of rare charm decays is discussed, focusing on the most used SM theoretical framework and new physics model predictions for the $D^0 \to h^+h^-\mu^+\mu^-$ decays. The LHCb experiment and its upgrade are described in details in the second chapter, focusing in particular on the muon detector electronics upgrade. The third chapter is dedicated to the muon readout electronics test and radiation hardness assurance. The study of the $D^0 \to h^+h^-\mu^+\mu^-$ decays using the Run II sample with an optimised selection is described in the fourth chapter; where the signal and background yields and the expected asymmetries are obtained. The development and validation of the angular fit for the $D^0 \to h^+h^-\mu^+\mu^-$ decays are discussed in the fifth chapter; where the development of a basic amplitude model and its usage is described. The model is used to perform simulated pseudo-experiments to study the feasibility and reliability of the angular analysis. The concluding remarks are given in the end.

TABLE OF CONTENTS

Introduction **iii**

Table of Contents **vii**

1 Theory of rare charm decays in the Standard Model and beyond **1**
- 1.1 The Standard Model 1
- 1.2 Weak currents and the CKM matrix 5
- 1.3 FCNC and GIM mechanism 7
- 1.4 Open problems in the Standard Model 8
- 1.5 Phenomenology of Mixing and *CP* violation 11
- 1.6 Rare Charm Decays 17
  - 1.6.1 Effective Field Theory 18
  - 1.6.2 Effective Hamiltonian for $\Delta C = 1$ 21
  - 1.6.3 New Physics models 24
- 1.7 The $D^0 \to h^+h^-\mu^+\mu^-$ decays 27
  - 1.7.1 Angular distribution 29
  - 1.7.2 Angular asymmetries 32
  - 1.7.3 *CP* asymmetry and the role of resonances 33

2 The LHCb experiment and its upgrade **35**
- 2.1 The Large Hadron Collider 35
- 2.2 The LHCb detector 37
  - 2.2.1 Dipole Magnet 38
  - 2.2.2 Tracking system 39
  - 2.2.3 Particle Identification system 42
  - 2.2.4 Trigger and data processing algorithms 51
- 2.3 LHCb upgrade 61
  - 2.3.1 Physics motivation 61
  - 2.3.2 Upgrade of LHCb readout system 62
  - 2.3.3 Upgrade of Muon system and its readout electronics 66

3 Functional and irradiation tests of upgraded muon readout electronics 75
3.1 Pre-production functionality tests 75
3.1.1 Preliminary chain test with nSYNC and MiniDAQ 80
3.1.2 Chain test with nODE and MiniDAQ 82
3.2 Introduction to radiation damage of electronics 85
3.2.1 Units and radiation environment 85
3.2.2 Radiation effects on silicon devices 87
3.2.3 Single Event Effects 90
3.3 Expected radiation levels for LHCb upgrade 92
3.4 nSYNC radiation hardness 95
3.5 Irradiation with proton beam 96
3.5.1 The proton facility 96
3.5.2 Experimental setup and test plan 97
3.5.3 Results 103
3.6 Irradiation with X-Ray 109
3.6.1 Experimental setup and X-Ray tube calibration 109
3.6.2 Results 116
3.7 Summary 118

4 Study of $D^0 \to h^+h^-\mu^+\mu^-$: selection and yields determination 121
4.1 Analysis strategy 121
4.1.1 Tagged analysis 122
4.2 Expected backgrounds 123
4.3 Data and simulated samples 124
4.4 Variables used in the selection 125
4.5 Selection 127
4.5.1 Trigger requirements 127
4.5.2 Stripping selection 129
4.5.3 Offline Preselection 131
4.5.4 Soft pion acceptance asymmetry 134
4.5.5 Multivariate offline selection 136
4.5.6 Final selection optimisation 139
4.6 Correction for phase space dependent efficiency 140
4.7 Extraction of signal and background yields 145
4.7.1 PDF determination 146
4.7.2 Expected asymmetries 149
4.8 Summary and future prospects 152

5 Development and validation of the angular fit for $D^0 \to h^+h^-\mu^+\mu^-$ 155
5.1 Development of a basic amplitude model 155
5.1.1 Resonant contributions 157
5.1.2 Helicity formalism 158
5.1.3 Helicity couplings and lineshape factor 160
5.2 Background subtracted $m(hh)$ and $m(\mu\mu)$ distributions 162
5.3 Development of the angular fit 165
5.4 Validation of the fit with pseudoexperiments 166
5.5 Summary and future prospects 171

Concluding remarks 173

Appendices

A Angular conventions and coefficients I_i 175

B Trigger Configurations for Run II 179

C Maximum Likelihood methods 181

D Development of the amplitude model 185

List of Tables 195

List of Figures 197

Acronyms 206

References 209

Acknowledgements 225

Chapter 1

Theory of rare charm decays in the Standard Model and beyond

Rare decays of mesons containing heavy quarks have branching fractions of the order of $\sim 10^{-5}$ or less, due to suppressed processes in the Standard Model (SM), and are possible only at higher perturbative orders. These decays are of considerable interest since possible New Physics (NP) contributions could be of the same order of magnitude of SM ones, introducing anomalies with respect to SM predictions and thus providing indirect hints of NP. Rare decays of mesons containing charm are dominated by non-perturbative amplitudes and possible enhancements of branching fractions due to NP can be hidden. Nevertheless, the rich dynamics of multi-body rare charm decays offer a unique opportunity to search for angular asymmetries and deviations from SM predictions by exploiting other cleaner observables. After a brief introduction on the SM, its open problems and limitations, the physics of *CP* violation, rare charm decays and the search for NP effects will be described. The phenomenology of the four-body decays $D^0 \to h^+h^-\mu^+\mu^-$ will then be discussed in detail, focusing on physical quantities describing their dynamics.

1.1 The Standard Model

The SM of particle physics is, at the moment, the most complete description of elementary particles and their interactions, strong and electroweak, with the exception of gravity. It was developed over ten years as a renormalisable Yang-Mills non-abelian quantum field theory in which the strong and electroweak interactions are determined by a local invariance principle (gauge theory) with respect to the unbroken gauge symmetry group $SU(3)_c \times SU(2)_L \times U(1)_Y$, where the subscript L indicates the fact that the group $SU(2)_L$ acts only on doublets of left-handed fields, the subscript Y stands for the weak hyper-charge and the subscript c the color charge [4–8]. The electroweak interaction, the unification of electromagnetic and weak forces, is described by the theory based on the $SU(2)_L \times U(1)_Y$ group, while strong interaction is described by quantum chromodynamics (QCD) of the $SU(3)_c$ group. The elementary particles described by the SM have experimentally no internal structure and can be completely characterized by their masses, charges, spin and the corresponding statistics, through the spin-statistics theorem. Mass and spin establish the transformation properties of particles with respect to the Poincaré group, of which they are an irreducible representation, while the charges define the possible interactions between them [9]. The strong and electroweak interactions are mediated by massless bosons, called gauge bosons, in particular W^i_μ $(i = 1, 2, 3)$ from the $SU(2)_L$ group and the B_μ boson from the $U(1)_Y$ group, as a natural consequence of the gauge invariance.

The Brout-Englert-Higgs mechanism [10–12] allows the spontaneous symmetry breaking of the $SU(2)_L \times U(1)_Y$ group and, as a consequence, the mixing of the gauge bosons into the three massive bosons, responsible of the weak interaction (W^+, W^- with mass $80.4\,\mathrm{GeV}/c^2$ and Z^0 with mass $91.2\,\mathrm{GeV}/c^2$), and the massless photon (γ).

The elementary particles composing the physical matter are 12 fermions with half-integer spin (and their respective anti-particles with all charges inverted), divided in two main classes: quarks and leptons. The latter have no color charge and do not participate in strong interaction. Both quarks and leptons are further ordered in generations: each particle of higher generation has a greater mass with respect to the corresponding particle of a previous generation, with the except of neutrinos, for which masses determination is still an open research field in particle physics. In this context particles of different generations are said to have different flavours, with an associated flavour quantum number. The three generations of quarks are grouped as (u, d), (c, s), (t, b) where the first quark (u, c, t) in each generation are up-type quark, with charge $+2/3$, while the second quarks in each generation (d, s, b) are down-type quarks, with charge $-1/3$.

All the elementary particles of the SM [13] are reported in Tab. 1.1, with the corresponding mass, spin, interactions and year of the first direct observation. The Lagrangian density of the SM contains all the information to describe the dynamics of the fields, treated as fundamental objects, and their harmonic excitations, the elementary particles. The Lagrangian density can be written as a sum of four terms:

$$\mathcal{L}_{SM} = \mathcal{L}_{gauge} + \mathcal{L}_{kin} + \mathcal{L}_{Yukawa} + \mathcal{L}_{Higgs}. \tag{1.1}$$

The $\mathcal{L}_{gauge}$ is the kinetic term of gauge bosons, containing the free field, and the interaction and auto-interaction terms through the definition of the field stress tensors. The $\mathcal{L}_{kin}$ is the kinetic term of Dirac fermions, and contains also the interaction terms with the gauge bosons, through the covariant derivatives $\not{D}$:

$$\mathcal{L}_{kin} = \bar{Q}^j\, i\not{D}_{q,L} Q^j + \overline{u}^j_R\, i\not{D}_{q,R} u^j_R + \overline{d}^j_R\, i\not{D}_{q,R} d^j_R + \overline{L}^j\, i\not{D}_L L^j + \overline{l}^j_R\, i\not{D}_R l^j_R, \tag{1.2}$$

Name	Symbol	Mass	Spin	Interactions	Discovery
Higgs					
Higgs boson	h	126 GeV	0	W	2012, CERN [14]
Gauge bosons					
photon	γ	0	1		1923, St.Louis [15]
W bosons	$W^{\pm}$	80.4 GeV	1	EM+W	1983, CERN [16, 17]
Z boson	Z	91.2 GeV	1	W	1983, CERN [16, 17]
gluons	g	0	1	S	1978, DESY [18]
Leptons					
electron	e	0.5 MeV	1/2	EM+W	1897, Cavendish [19]
muon	μ	106 MeV	1/2	EM+W	1936, Caltech [20]
tau	τ	1.78 GeV	1/2	EM+W	1975, SLAC-LBL [21]
electronic neutrino	ν_e	< 0.1 eV	1/2	W	1956, S. River Plant [22]
muonic neutrino	ν_μ	< 0.1 eV	1/2	W	1962, Brookhaven [23]
tauonic neutrino	ν_τ	< 0.1 eV	1/2	W	2000, Fermilab [24]
Quarks					
up	u	2.3 MeV	1/2	EM+W+S	1968, SLAC [25, 26]
down	d	4.8 MeV	1/2	EM+W+S	1968, SLAC [25, 26]
strange	s	95 MeV	1/2	EM+W+S	1968, SLAC [25, 26]
charm	c	1.3 GeV	1/2	EM+W+S	1974, SLAC-BNL [27, 28]
bottom	b	4.5 GeV	1/2	EM+W+S	1977, Fermilab [29]
top	t	173 GeV	1/2	EM+W+S	1995, Fermilab [30, 31]

TABLE 1.1. List of SM elementary particles with their mass, spin, interactions (W stands for weak, S for strong and EM for electromagnetic), year and place of first direct observation.

where the subscript q, L and R of the covariant derivatives indicate respectively the operation on quark fields, on left-handed and right-handed fermions. The Dirac fields appear in the kinetic term in five representations: Q^j and L^j are, respectively, the quark and lepton left-handed fields, doublets of $SU(2)$, with weak-isospin $T = 1/2$ and third component of weak-isospin $T_3 = \pm 1/2$; while u^j_R, d^j_R and l^j_R are, respectively, the up-type, down-type and lepton right-handed fields, singlets of $SU(2)_L$, thus with $T = 0$. In each term, j represents the flavour, or generation, index. It is important to note that there is no down-type right-handed lepton representation, which corresponds to neutrinos with right-handed chirality, since neutrinos are considered massless in the SM. The covariant derivatives $\not{D}$ contains different interaction terms depending on which field it operates to, the most general form is the following

$$D_\mu = \partial_\mu + ig_s G^a_\mu \frac{\lambda^a}{2} + igW^a_\mu \frac{\sigma^a}{2} + ig' B_\mu, \tag{1.3}$$

where g and g' are respectively the coupling constants to the W_μ and B_μ fields, λ^a $(a = 1, ..., 8)$ are the 3×3 Gell-Mann matrices, related to the $SU(3)_c$ generators, the σ^a $(a = 1, 2, 3)$ are the Pauli matrices, related to the $SU(2)_L$ generators. If applied to leptons, being singlets of $SU(3)_c$, the strong interaction term depending on λ^a will vanish, while if applied to right-handed fields, being singlets of $SU(2)_L$, only one of the electroweak interaction terms, containing σ^a, will vanish.

The $\mathcal{L}_{Higgs}$ describes the Higgs field, in particular it contains the kinetic and the interaction terms with gauge bosons, and the potential which Higgs field is subject to,

$$\mathcal{L}_{Higgs} = D^\mu \phi^\dagger D_\mu \phi - V(\phi^\dagger \phi), \tag{1.4}$$

where ϕ is a $SU(2)$ doublet, composed of two complex scalar fields, ϕ^+ and ϕ^0. The Brout-Englert-Higgs mechanism mentioned before [10–12] consists in defining a potential $V(\phi^\dagger\phi)$ whose minimum value corresponds to a non-vanishing vacuum expectation value (VEV) of ϕ, in particular when $\phi^\dagger\phi = v^2/2$, with $v \sim 246\,\text{GeV}$ and $\langle\phi\rangle = v/\sqrt{2}$. The number of degrees of freedom of ϕ can be reduced to 1, through the gauge invariance, and the ϕ field can be expanded around the potential minimum

$$\phi = \begin{pmatrix} \phi^+ \\ \phi^0 \end{pmatrix} \rightarrow \frac{1}{\sqrt{2}} \begin{pmatrix} 0 \\ v + H \end{pmatrix}, \tag{1.5}$$

where H is the scalar and real Higgs field.

This leads spontaneously to the $SU(2)_L \times U(1)_Y$ symmetry breaking, down to the $U(1)$ gauge group of the electrodynamics, and as a consequence it leads to the mix of electroweak gauge bosons into the observed physical ones, $W^\pm_\mu$, Z_μ, A_μ, with the emergence of physical boson mass terms in the lagrangian density,

$$W^\pm_\mu = \frac{1}{\sqrt{2}}(W^1_\mu \mp i\,W^2_\mu), \tag{1.6a}$$

$$Z_\mu = W^3_\mu \cos\theta_W - B_\mu \sin\theta_W, \tag{1.6b}$$

$$A_\mu = W^3_\mu \sin\theta_W + B_\mu \cos\theta_W, \tag{1.6c}$$

where θ_W is the Weinberg angle, with $\sin^2(\theta_W) \sim 0.23$, which is related to the electroweak couplings, g and g', by

$$\cos\theta_W = \frac{g}{\sqrt{g^2 + g'^2}} \ , \ \sin\theta_W = \frac{g'}{\sqrt{g^2 + g'^2}}. \tag{1.7}$$

The $\mathcal{L}_{Yukawa}$ describes the couplings between the Dirac fermions and the Higgs field ϕ. Before the symmetry breaking there are no explicit fermion mass terms and the Yukawa sector has the following form

$$-\mathcal{L}_{Yukawa} = Y^{ij}_d \overline{Q}^i\, \phi\, d^j_R + Y^{ij}_u \overline{Q}^i\, \widetilde{\phi}\, u^j_R + Y^{ij}_l \overline{L}^i\, \phi\, l^j_R + \text{h.c.}, \tag{1.8}$$

where Y^{ij} are complex-value matrices, $\widetilde{\phi} = i\sigma^2\phi^\dagger$ and $h.c.$ stands for hermitian conjugate. After the spontaneous symmetry breaking, substituting Eq. (1.5) in Eq. (1.8), one obtains the mass terms

$$-\mathcal{L}_{mass} = M^{ij}_d \overline{d}^i_L\, d^j_R + M^{ij}_u \overline{u}^i_L\, u^j_R + M^{ij}_l \overline{l}^i_L\, l^j_R + \text{h.c.}. \tag{1.9}$$

The quark fields, u^i and d^i, described in the previous relations are eigenstates of the weak interaction and not necessarily coincide with mass eigenstates, which can be obtained by diagonalising the mass matrices, M^{ij}, of Eq. (1.9). It is possible to find four unitary matrices, $V^{ij}_{u,L}$, $V^{ij}_{u,R}$, $V^{ij}_{d,L}$, $V^{ij}_{d,R}$, such that $\widetilde{M}^{ij}$ is diagonal:

$$\widetilde{M}^{ij}_u = V^{ik}_{u,L}\, M^{kl}_u\, V^{lj}_{u,R}, \tag{1.10a}$$

$$\widetilde{M}^{ij}_d = V^{ik}_{d,L}\, M^{kl}_d\, V^{lj}_{d,R}. \tag{1.10b}$$

The quark mass eigenstates $u^{(m)}$, $d^{(m)}$ can be then derived as follows

$$u^{i,(m)}_L = V^{ij\,\dagger}_{u,L}\, u^j_L \quad , \quad u^{i,(m)}_R = V^{ij\,\dagger}_{u,R}\, u^j_R\,, \tag{1.11a}$$

$$d^{i,(m)}_L = V^{ij\,\dagger}_{d,L}\, d^j_L \quad , \quad d^{i,(m)}_R = V^{ij\,\dagger}_{d,R}\, d^j_R\,. \tag{1.11b}$$

1.2 Weak currents and the CKM matrix

The electroweak interaction of quarks, before the symmetry breaking and the diagonalisation of the mass matrices, is contained in the $\mathcal{L}_{kin}$, in Eq. (1.2), in terms of couplings to W_μ and B_μ. After these operations, we can identify the weak charge and neutral current terms

$$\mathcal{L}_{CC} = -\frac{g}{\sqrt{2}}\Big(W^+_\mu J^\mu_{CC} + W^-_\mu J^{\mu\dagger}_{CC}\Big), \tag{1.12a}$$

$$\mathcal{L}_{NC} = -\frac{g}{\sqrt{2}\cos(\theta_W)}\Big(Z_\mu J^\mu_{NC}\Big), \tag{1.12b}$$

where J^μ_{CC} and J^μ_{NC} are the charged and neutral weak currents respectively. Focusing on quark fields only, they can be expressed in term of mass eigenstates

$$J^\mu_{CC} = \sum_i \overline{u}^i_L \gamma^\mu d^i_L = \sum_{i,j} \overline{u}^{i,(m)}_L \gamma^\mu (V^\dagger_{u,L} V_{d,L})^{ij} d^{j,(m)}_L, \tag{1.13a}$$

$$J^\mu_{NC} = \sum_q \overline{q}^i \gamma^\mu \frac{g_V - g_A \gamma^5}{2} q^i, \tag{1.13b}$$

where q indicates a generic quark, i and j are the generation index, g_V and g_A are the vector and axial weak coupling constants, that depend on the charge of the quark, its weak isospin T^3 and $\sin^2\theta_W$. Hence the coupling of the weak charge current with the $W^\pm$ bosons is possible only within generations of weak interaction eigenstates, but due to the non-coincidence of mass and weak interaction eigenstates a mixing between the generation is possible, leading to a quark flavour change in weak interaction. This can happens through the $V_{CKM} = (V^\dagger_{u,L} V_{d,L})^{ij}$ matrix, called the Cabibbo-Kobayashi-Maskawa (CKM) matrix [32, 33], that can be written as

$$V_{CKM} = \begin{pmatrix} V_{ud} & V_{us} & V_{ub} \\ V_{cd} & V_{cs} & V_{cb} \\ V_{td} & V_{ts} & V_{tb} \end{pmatrix}. \tag{1.14}$$

Before the complete theorisation of the SM and the discovery of quark charm, only three quarks were known, u, d and s, ordered according to the $SU(2) \times U(1)$ flavour symmetry in a doublet (u and d) and a singlet (s) [34, 35]. This allowed interactions between u and d, but excluded interactions of such quarks with the quark s. However, the observation of processes with violation of strangeness quantum number, as $K^+ \to \mu^+\nu_\mu$ [36, 37], and the different values for couplings in transitions $u - d$ and $u - s$ (as $h^- \to \mu^-\overline{\nu}_\mu$ with $h = K, \pi$) leads to the idea, in 1963 by N. Cabibbo [38], that in weak interactions the current with the u quark involves not only the d quark but both d and s, in a linear combinations through a mixing angle. The Cabibbo matrix was then introduced to rotate the states

$$\begin{pmatrix} d \\ s \end{pmatrix} = \begin{pmatrix} \cos\theta_c & \sin\theta_c \\ -\sin\theta_c & \cos\theta_c \end{pmatrix} \begin{pmatrix} d^{(m)} \\ s^{(m)} \end{pmatrix}, \tag{1.15}$$

where $\theta_c \simeq 13°$ is the Cabibbo angle, the unique real parameter to parametrise the matrix. Processes whose amplitude is proportional to the coupling constant $\cos\theta_c$ are called Cabibbo-Favoured (CF) processes, while those proportional to $\sin\theta_c$ are called Single Cabibbo-Suppressed processes (SCS).

The CKM matrix is the generalisation of the Cabibbo matrix to three generations of quarks, introduced by Kobayashi and Maskawa in 1973 [39] to take into account a proposed third generation and explain the observation of *CP* violation [40]. It can be parametrised by 3 angles and one complex phase. Indeed, a complex $n \times n$ matrix containing n^2 complex entries and $2n^2$ real degrees of freedom can be parametrised with a reduced number of parameters, being subject to various constraints:

- the unitarity condition, deriving from the mass matrices diagonalisation, reduces the number of degrees of freedom to n^2, through n^2 constraints,
- in the particular case of a $n \times n$ mixing matrix of quarks, the redefinition of the phases of each quark field (see Eq. (1.13)), $2n - 1$ phase differences can be removed without affecting the lagrangian density.

Hence, the number of degrees of freedom is $(n-1)^2$, consisting of $n(n-1)/2$ real parameters, called mixing angles, and $(n-1)(n-2)/2$ complex phases. For $n = 2$ generations there is only one real parameter corresponding to the Cabibbo angle and no complex phases, while for $n = 3$ there are three rotation angles and one complex phase, δ_{CKM}, that is responsible for the possibility of *CP* violation in weak interaction, i. e. the violation of the combined conservation laws of the charge conjugation (C) and parity (P). In terms of these quantities the matrix can be written as

$$V_{CKM} = \begin{pmatrix} c_{12}c_{13} & s_{12}c_{13} & s_{13}\,e^{i\delta} \\ -s_{12}c_{23} - c_{12}s_{23}s_{13}e^{i\delta} & -c_{12}c_{23} - s_{12}s_{23}s_{13}e^{i\delta} & s_{23}c_{13} \\ s_{12}s_{23} - c_{12}c_{23}s_{13}e^{i\delta} & -c_{12}s_{23} - s_{12}c_{23}s_{13}e^{i\delta} & c_{23}c_{13} \end{pmatrix}, \tag{1.16}$$

where the compact notation $s_{ij} = \sin\theta_{ij}$, $c_{ij} = \cos\theta_{ij}$ and $\delta = \delta_{CKM}$ has been used. A useful parametrisation of the CKM matrix is the Wolfenstein parametrisation [41], in which the hierarchy of the couplings, found experimentally, is more evident: the four parameters are λ, A, ρ and η, where $\lambda = |V_{us}| = \cos\theta_c \simeq 0.22$ and the parameter η represents the CP violating phase. Expanding the V_{CKM} up to $\mathscr{O}(\lambda^3)$ the following form can be obtained

$$V_{CKM} = \begin{pmatrix} 1-\lambda^2/2 & \lambda & A\lambda^3(\rho - i\eta) \\ -\lambda & 1-\lambda/2 & A\lambda^2 \\ A\lambda^3(1-\rho-i\eta) & -A\lambda^2 & 1 \end{pmatrix} + \mathscr{O}(\lambda^4), \tag{1.17}$$

where it is manifest that the CKM matrix is almost diagonal with small off-diagonal terms. The transitions within a generation are preferred (Cabibbo-favoured), with couplings of $\mathscr{O}(1)$, while transitions between other generations are suppressed by power of λ, with a hierarchy that can be easily read from this parametrisation. Most of CKM matrix elements can be studied experimentally[13, 42–46] from tree-level processes, except V_{td} and V_{ts} that are extracted from $B^0 - \overline{B}^0$ and $B^0_s - \overline{B}^0_s$ oscillations, dominated by box diagrams. The current knowledge of the CKM matrix elements [13] is reported in the following

$$|V_{CKM}| = \begin{pmatrix} 0.97446 \pm 0.00010 & 0.22452 \pm 0.00044 & 0.00365 \pm 0.00012 \\ 0.22438 \pm 0.00044 & 0.97359^{+0.00010}_{-0.00011} & 0.04214 \pm 0.00076 \\ 0.00896^{+0.00024}_{-0.00023} & 0.04133 \pm 0.00074 & 0.999105 \pm 0.000032 \end{pmatrix}. \tag{1.18}$$

1.3 FCNC and GIM mechanism

The mixing matrix introduced by Cabibbo, although it explained the decays with strangeness violation, implied the presence of processes of flavour changing neutral current (FCNC), excluded by the experiments. The most famous example is the branching fraction of the $K^0_L \to \mu^+\mu^-$ decay, which is much smaller than the charged $K^+ \to \mu^+\nu_\mu$ decay. In the case of u, d, s theory, the possibility of FCNC at tree-level processes disappears if one assumes, as proposed by Glashow, Iliopoulos and Maiani in 1970 [47], the existence of a fourth quark, the charm quark, which forms a second generation doublet with the quark s. The predicted charm quark was indeed discovered in 1974 [27, 28], confirming how indirect searches in flavour physics, based on precision tests of processes at loop level, could be highly predictive.

In that context, the structure of the neutral current becomes similar to that already written in the case of three generations, in Eq. (1.13), in which the couplings are purely diagonal, i. e. there are no transitions between quarks of different flavours induced by neutral currents, involving the exchange of the neutral Z boson. The FCNC processes, although not present at tree level, are possible at higher perturbation orders, in box or penguin diagrams, as they can occur through the exchange of multiple $W^{\pm}$ bosons. Examples of such transitions are $b \to s\ell^+\ell^-$, $b \to d\ell^+\ell^-$, and $c \to u\ell^+\ell^-$, in B and D decays respectively, where $\ell^+\ell^-$ is a pair of leptons with opposite charges. However also in these cases there is a second effect, called Glashow,

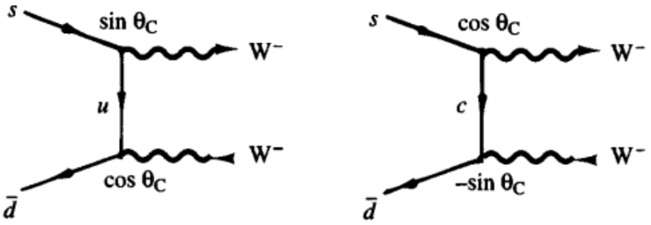

FIGURE 1.1. Feynman diagrams of $K^0 \to W^+W^-$ contributing to the $K^0 \to \mu^+\mu^-$ decay, from [49].

Iliopoulos, Maiani (GIM) suppression [48]: in the specific case of two generations there are two box diagrams that can contribute to the process with an opposite sign (in which the u quark or the c quark circulates inside the loop).

Let us consider as example the $K^0 \to \mu^+\mu^-$ decay, which proceeds via the chain $K^0 \to W^+W^- \to \mu^+\mu^-$. There are two main diagrams contributing to the decay, reported in Fig. 1.1. In the condition $m_u = m_c$ the propagators in the figure would be the same and the overall amplitude will be proportional to

$$\sin\theta_c \cos\theta_c - \cos\theta_c \sin\theta_c,$$

with a perfect cancellation. It can be demonstrated indeed that the amplitude is proportional to the difference of the masses squared of the quarks involved in the loop and can be written as [49]

$$\mathcal{A} \propto [G_F\, \sin\theta_c \cos\theta_c\, (m_u - m_c)]^2. \tag{1.19}$$

This suppression is particularly important and more effective in D mesons decays, unlike B mesons, since in the latter case the presence of the top quark in the loop reduces the suppression effect.

We can define two types of FCNC processes, depending on the changing of the flavour quantum number of one or two units, and indicated respectively as $\Delta F = 1$ or $\Delta F = 2$ transitions, being F a generic flavour quantum number:

- $\Delta F = 1$ FCNC: they describe rare decays, as $D^0 \to \ell^+\ell^-$, $D^0 \to X\ell^+\ell^-$ or $B_s^0 \to \ell^+\ell^-$, and are discussed in details in Sect. 1.6 in the specific context of charm physics.
- $\Delta F = 2$ FCNC: they describe meson-antimeson transitions, as $D^0 - \overline{D}^0$, $B^0 - \overline{B}^0$ or $B_s^0 - \overline{B}_s^0$ mixing and are discussed in Sect. 1.5.

1.4 Open problems in the Standard Model

Even though the SM is the most complete theory of elementary particles and is largely confirmed by experimental evidences with great precision, there are still several open questions that require an extension of the theory, besides the most obvious problem about the non-inclusion of the gravitational interaction.

There are two different approaches to search for physics beyond Standard Model (BSM). In *direct* searches, the production of a new heavy particle not predicted by the SM, or the interaction of it with ordinary SM particles, is searched for. Examples of experiments that perform mainly direct searches are XENON1T [50, 51] or DarkSide [52, 53], that try to detect scattering of dark matter candidates with the nuclei of the target material, or ATLAS [54] and CMS [55] at the Large Hadron Collider (LHC) [56], which search for the production of heavy BSM particles, like SUSY candidates, in high energy proton-proton collisions. This approach has the advantage that the production signature can be theoretically clean and unambiguous, but has the drawback to be limited by the total amount of energy available in the collision. In *indirect* searches, anomalies and deviations between experimental data and theoretical predictions are searched for in specific processes. In the case of dark matter, anomalies in the cosmic-rays and γ-rays flux from the galactic center can be due to dark matter self-annihilation, and can indicate an indirect sign of dark matter [57, 58]. In the case of particle physics, processes with forbidden or suppressed amplitudes, as the ones involving quantum loops, are more sensitive to BSM amplitudes [59, 60]. Thus, deviations of values for some SM observables can be measured. In indirect searches the advantage is that possible higher energy scale can be probed, even if such energy is not available in the center of mass to produce new particles directly. The inconveniences are related to the theoretical uncertainties: small deviations, potentially observed experimentally, can be due to the non-perturbative dynamics of the SM, which is studied with approximation methods and is affected by theoretical uncertainties, especially at energy scales comparable to $\Lambda_{QCD} \sim 200\,\mathrm{MeV}$.

In the following we report briefly some of the open problems in the SM. From cosmological and astronomical observations like galactic rotation curves [61, 62] and weak gravitational lensing [63] it is evident that only 4% of the mass-energy density in the universe can be taken into account by the SM. The remaining percentage of 68% and 27% is composed respectively of dark energy and dark matter. This form of mass-energy has been called *dark* since it is supposed not to interact electromagnetically: the only indirect experimental evidence is through gravitational interactions. Since dark matter cannot be explained by the SM, and since the interactions with known SM particles are very weak, the scientists have proposed several candidates as possible constituents of dark matter, covering a wide mass range and cross sections [64–68]: Weakly Interacting Massive Particles (WIMPs), like Neutralino, extra Higgs, etc.; Axions; Massive Astrophysical Compact Halo Objects (MACHOs); light or sterile neutrinos etc. Other models foresee modification of the Einstein General Relativity (GR), hence without the introduction of extra particles [69–71]. Nowadays there are no experimental confirmation of one of these models among the others.

Another important problem in the SM is the *hierarchy problem* in the Higgs sector. In general a hierarchy problem arises when the coupling constants or masses in a theory can be largely different with respect to their corresponding observed values. This problem is closely related to naturalness and fine-tuning in particle physics [72]. In the SM this happens for the Higgs mass: the radiative corrections can lead in principle to a very large Higgs mass, of the order of the 10^{16} GeV, but the small experimental observed mass of Higgs boson (125 GeV/c^2) [13] can be explained with a precise fine tuning of the SM parameters, in order to cancel out the radiative corrections [73–77]. There are different theoretical models to solve this problem. A general and common approach is to extend some of the SM symmetries, in order to get new set of particles, new bosons from spontaneous symmetries breaking or new possible interactions between existing particles. Supersymmetry (SUSY) [78, 79], little Higgs [80] and Randall-Sundrum models [81, 82], different theoretical approaches that try to solve the hierarchy problem with will be discussed in the next sections in the specific context of flavour physics and rare charm decays. Another promising model, born to extend the SM into a Grand Unification Theory (GUT), is based on a new particle species called leptoquarks [83, 84], which carry both lepton and baryon numbers, allowing transitions from quarks to leptons and vice versa. This model has recently generated interest since it can explain some observed anomalies in flavour physics [85].

The SM has a high number of unknown free parameters (19 without taking into account those introduced for neutrino masses and mixing) to be fixed by experimental inputs, 13 of which related to the flavour sector. Their nature is an open question related to the mass hierarchy of fermions along the generations [86, 87] and the nature of neutrino masses (become evident from the observation of neutrino oscillations [88, 89]), for which we have still no explanation. Minimal extensions of the SM foresee a right-handed neutrino, that does not participate to any SM interaction (hence called *sterile*) [90] and postulated to be a possible dark matter candidate. However, since it is accepted by the community that the dark matter must be of a *cold* type, the possibility of an hot dark matter of massive neutrino is highly constrained, leading to upper bounds on neutrino masses of the order of $\mathcal{O}(1\text{ eV})$, also confirmed by independent experimental constraints [91]. The origin of the such small neutrinos masses remains unexplained. Various theoretical models BSM describe the neutrino masses as a low energy manifestation of a dynamics generated at higher energy scales, implementing the so-called *see-saw mechanism* [92, 93].

Finally, another open question in cosmology and flavour physics is the experimental observation of a very small density of antimatter in the universe, compared to that of matter [94, 95]. As pointed out by Sakharov [96], a baryogenesis model that pretends to explain the cosmological matter-antimatter asymmetry needs three requirements to be satisfied: an interaction that violates CP, an interaction that violates the baryon number conservation, and the departure from thermal equilibrium. The Lorentz-invariance of the SM prevents a radical matter-antimatter difference concerning their physical properties, but within SM the three Sakharov requirements can be fulfilled (*electroweak baryogenesis*) through the CP violation in weak decays, the baryon number violation as a non-perturbative effect at high temperature through the Sphaleron solution [95] and the departure from thermal equilibrium during the electroweak phase transition. Nevertheless these effects are not sufficient to explain the observed asymmetry by 8 orders of magnitude [97–99], due to the small *CP* violation and the not enough strong departure from thermal equilibrium. Starting from the '90s many models on baryogenesis and leptogenesis were studied to explain such asymmetry, for example generating it in the lepton sector and let the Sphaleron solution to propagate it on the baryon sector [100–102]. Alternative approaches foresee the appearance of the asymmetry in quantum dynamics of primordial black holes [103–105], but these models suffer of the fact that they cannot explain simultaneously and consistently the problem of dark matter. Unfortunately all these models postulate effects at energies that are impossible to be probed directly experimentally. Indirect evidence in cosmological observables or in cosmological stochastic background of gravitational waves [106] can give additional information on the baryogenesis era. From the point of view of particle physics, models BSM promising for the matter-antimatter asymmetry and that imply new sources of *CP* violation (like SUSY) can be currently searched for or constrained indirectly.

1.5 Phenomenology of Mixing and *CP* violation

The neutral meson mixing is a FCNC process in which a neutral meson, P^0, during its time evolution, transforms in its antiparticle $\overline{P}^0$ and vice versa with repeated oscillations, through loop-level processes. The reason lies in the fact that the eigenstates of the free Hamiltonian, which governs the time evolution and that coincide with the mass eigenstates, do not coincide with the weak interaction eigenstates. The phenomenology of the process can be described by some parameters that will now be introduced, and that allow to highlight the difference between the physics of the B, D and K mesons.

Supposing to prepare an initial state that is a pure linear combination of P^0 and $\overline{P}^0$,

$$|\psi(0)\rangle = a(0)|P^0\rangle + b(0)|\overline{P}^0\rangle. \tag{1.20}$$

At time $t > 0$ the state can be expressed as

$$|\psi(t)\rangle = a(t)|P^0\rangle + b(t)|\overline{P}^0\rangle + \sum_i c_i(t)|\phi_i\rangle, \tag{1.21}$$

where the last term is a combination of states in which the mesons can decay. The theoretical approach to find out $a(t)$ and $b(t)$ is to assume an exponential time dependence, in order to describe the probability flow towards the final states $\sum_i c_i|\phi_i\rangle$, and to neglect effects at time scale much smaller than those typical of weak interaction. This is the Weisskopf-Wigner approximation (WWA) [107, 108], for which the effective Schrödinger equation can be written as [109]

$$i\frac{\partial}{\partial t}\begin{pmatrix} a(t) \\ b(t) \end{pmatrix} = \begin{pmatrix} \mathcal{H}_{aa} & \mathcal{H}_{ab} \\ \mathcal{H}_{ba} & \mathcal{H}_{bb} \end{pmatrix} \begin{pmatrix} a(t) \\ b(t) \end{pmatrix}, \tag{1.22}$$

where the 2×2 Hamiltonian matrix, $\mathcal{H}$, can be decomposed in the mass and decay matrices, $\mathcal{H} = \mathbf{M} - \frac{i}{2}\mathbf{\Gamma}$. The Hamiltonian is in this case non-Hermitian, since probability cannot be conserved in the 2×2 space spanned by P^0 and $\overline{P}^0$. The physical eigenstates of $\mathcal{H}$ are $|P_{1,2}\rangle = p|P^0\rangle + q|\overline{P}^0\rangle$, normalised by imposing $|q|^2 + |p|^2 = 1$. The time evolution of a state created at $t = 0$ in its flavour eigenstate is:

$$|\psi_{P^0}(t)\rangle = g_+(t)\,|P^0\rangle + \frac{q}{p}\,g_-(t)\,|\overline{P}^0\rangle, \tag{1.23a}$$

$$|\psi_{\overline{P}^0}(t)\rangle = g_-(t)\,|\overline{P}^0\rangle + \frac{p}{q}\,g_+(t)\,|P^0\rangle, \tag{1.23b}$$

where $|\psi_{P^0}(t)\rangle$ and $|\psi_{\overline{P}^0}(t)\rangle$ are the states at time t that were produced at time $t = 0$ in $|P^0\rangle$ or $|\overline{P}^0\rangle$ respectively. The probability to measure the same flavour at a time $t > 0$ is equal to $|g_+(t)|^2$, while the probabilities to measure a different flavour are in general different if $|q/p| \neq 1$ and are

$$|\langle\psi_{P^0}(t)|\overline{P}^0\rangle|^2 = \left|\frac{q}{p}\right|^2 |g_-(t)|^2, \tag{1.24a}$$

$$|\langle\psi_{\overline{P}^0}(t)|P^0\rangle|^2 = \left|\frac{p}{q}\right|^2 |g_-(t)|^2. \tag{1.24b}$$

If we define two convenient dimensionless parameters, called mixing parameters,

$$x = \frac{M_1 - M_2}{\Gamma}, \tag{1.25a}$$

$$y = \frac{\Gamma_1 - \Gamma_2}{\Gamma}, \tag{1.25b}$$

where Γ is the average between Γ_1 and Γ_2, the evolution coefficients can be written in a concise way as

$$|g_\pm(t)|^2 = \frac{1}{2}\,e^{-\Gamma\,t}\left(\cosh(y\Gamma t) \pm \cos(x\Gamma t)\right). \tag{1.26}$$

The mixing can occur if x or y are non-zero. The x parameter governs the periodic oscillation between flavour eigenstates, while y parameter is involved in the hyperbolic cosine term which modifies the exponential decay. The formalism described here is general and can be applied to the different flavours of neutral mesons. However the differences in the Hamiltonian elements causes a great difference in the phenomenology of mixing, according to the flavour considered. Examining for example the x mixing parameter: if $x \ll 1$ the oscillations are slow with respect to the time scale of the decay and the flavour is conserved with good approximation, this is the case of $D^0 - \overline{D}^0$ mixing, with $x = 0.003$; if $x \gg 1$ the oscillation are fast and the mesons have time to oscillate many times in a lifetime, consequently the term $\cos(x\Gamma t)$ is practically averaged to zero with time, this is the case of $B_s^0 - \overline{B}_s^0$ mixing, with $x = 26.7$; if $x \sim 1$ the time scale of the decay and the oscillation are approximately the same and the term $\cos(x\Gamma t)$ is not averaged to zero, this is the case of K^0 and B^0 mesons. Similar considerations can be done for the y parameter.

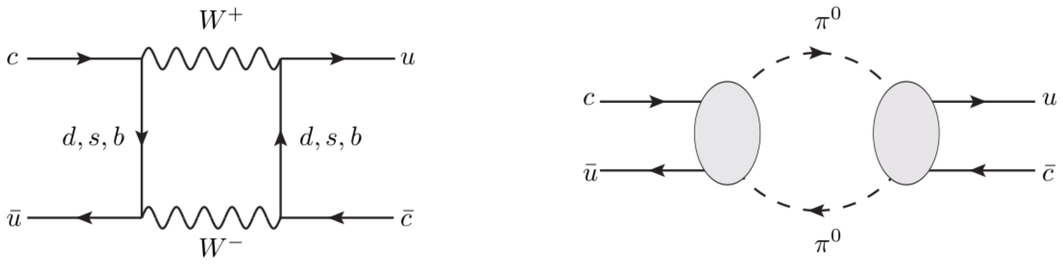

FIGURE 1.2. Examples of Feynman diagrams describing a SD contribution (left) and a LD contribution (right), mediated by two π^0 mesons, to the $D^0-\overline{D}^0$ mixing. Diagrams taken from [114].

Another important difference between D and B system is that the mixing amplitude for the former is dominated by long distance (LD) physics (a terminology explained in more detail in Sect. 1.6.1), i. e. the final state is reached through resonances and intermediate states appearing due to non perturbative effects of strong interaction, leading to a challenging theoretical estimate of the mixing parameters [110–113]. An example of two processes, one of short distance (SD) and one of LD, are shown in Fig. 1.2.

CP violation

In a general quantum field theory with a Lagrangian density $\mathcal{L}$, conservation of *CP* symmetry, i.e. the combined application of C and P, requires [115]

$$(CP)\,\mathcal{L}(t,\vec{r})\,(CP)^\dagger = \mathcal{L}(t,-\vec{r}). \tag{1.27}$$

Since this operation will cause a complex conjugation of coupling constants, *CP* conservation can happen if in the Lagrangian the coupling constants are relatively real. The freedom to perform a rephasing of the fields (or a unitary mix of fields with same quantum numbers) can be used to remove from the theory all the unphysical phases and to check if there are physical unavoidable complex phases that will cause *CP* violation. As we have seen, this is the case of the SM, where a physical complex phase arises in the CKM matrix as a result of the simultaneous presence of charged weak interaction and the complex Yukawa coupling constants. It should be stressed that the complex Yukawa couplings alone do not automatically signal *CP* violation, but it's the simultaneous presence of those couplings and the charged weak interaction to prevent the removing of the complex phase [116]. This aspect is strictly related to the quark masses: even with three generations (a necessary condition for *CP* violation), if two quarks were mass-degenerate in the same charge sector, a mix of the degenerate mass eigenstates could be possible with the opportunity to get an additional degree of freedom to remove the complex phase in V_{CKM}, as can be seen in Eq. (1.29). Thus, generalising these statements, *CP* violation arises if a part of the Lagrangian implies *CP* transformation laws that cannot be simultaneously satisfied by another part of the Lagrangian.

As already seen in the case of the Wolfenstein parametrisation, the complex phase appears in specific terms in the CKM matrix, but that position is not physically significant, since changing the parametrisation can shift the complex phase to different elements. A parametrisation independent *CP* violating quantity however can be defined, called Jarlskog invariant, J_{CP}, defined from the relation

$$\Im[V_{ij}V_{kl}V^*_{il}V^*_{kj}] = J_{CP}\sum_{m,n\in d,s,b}\varepsilon_{ikm}\varepsilon_{jln} \qquad (i,j,k,l\in d,s,b). \tag{1.28}$$

CP violation can occur in SM if $J_{CP} \neq 0$, which is then a necessary (but still not sufficient) condition. The current measurement of the Jarlskog invariant is $J_{CP} = (3.18 \pm 0.15)\cdot 10^{-5}$. A necessary and sufficient condition for *CP* violation in the SM can be written in terms of J_{CP} as

$$J_{CP}\,(m_t^2-m_c^2)(m_t^2-m_u^2)(m_c^2-m_u^2)(m_b^2-m_s^2)(m_b^2-m_d^2)(m_s^2-m_d^2)\neq 0, \tag{1.29}$$

which implies also the mass degeneration considerations discussed above. Hence the origin of *CP* violation is strictly connected with puzzle of the hierarchy of quark masses in particle physics, for which by now we have no a deeper explanation.

It is important to underline that the possibility to violate *CP* in a Lagrangian, from coupling constants considerations only, does not imply automatically the possibility to observe it experimentally. Indeed to observe *CP* violation one would need some process for which

$$\Gamma(i\to f)\neq\Gamma(\bar{i}\to\overline{f}), \tag{1.30}$$

where $\Gamma(...)$ is the decay rate of a process; i, f are generic initial and final states and $\bar{i}$, $\overline{f}$ their *CP* conjugated. Usually the deviations indicated in Eq. (1.30) are small and the experimental observations are not easy. Phenomenologically there are two main categories in which the *CP* violation condition Eq. (1.30) can be studied: through direct decays and through neutral meson mixing.

CP violation in meson decays

To study the experimental implications of *CP* violation in D meson decays, although the formalism can be applied to the others meson systems, we define the following amplitudes, which describe the transitions of a D meson, or the *CP* conjugated $\overline{D}$ meson, towards a generic final state f, or the *CP* conjugated $\overline{f}$.

$$\mathcal{A}_{D\to f} = \langle f|\mathcal{H}|D\rangle, \quad \mathcal{A}_{\overline{D}\to f} = \langle f|\mathcal{H}|\overline{D}\rangle, \tag{1.31}$$

$$\mathcal{A}_{D\to\overline{f}} = \langle \overline{f}|\mathcal{H}|D\rangle, \quad \mathcal{A}_{\overline{D}\to\overline{f}} = \langle \overline{f}|\mathcal{H}|\overline{D}\rangle, \tag{1.32}$$

where $\mathcal{H}$ is the Hamiltonian responsible for the transition. These generic decay amplitudes, $\mathcal{A}$, can be a sum of partial amplitudes with relative physical phases, which can have important observable consequences. In particular there are three types of phases [116]:

- CP-odd phases, called weak phases: they come from any complex couplings in a Lagrangian, thus they change sign in amplitudes for a process and its *CP* conjugated. Since in the SM they arise from the elements of the CKM matrix, they are referred to be "*weak*".
- CP-even phases, called strong phases: they do not change sign under a *CP* transformation. These types of phases can have different sources. They may arise from traces of an even number of Dirac matrices, which are linked, through antisymmetric tensor $\varepsilon_{\mu\nu\chi\xi}$, to triple cross product of vectors $\vec{p}_a \cdot (\vec{p}_b \times \vec{p}_c)$, that is odd under a T transformation. Another important source of CP-even phases is the final state interaction (FSI): in a decay process $i \to f$ with on-shell intermediate states such that $i \to f' \to f$, the rescattering $f' \to f$ is driven by strong or electromagnetic interaction and leads to an absorptive part in the amplitude, with the appearance of a physical CP-even phase. Since the dominant contribution of the rescattering is due to strong interaction, the phases are referred to be "*strong*".
- Spurious phases: they are global and pure conventional phases, that arise from the assumed *CP* transformation of fields, hence not originating from any dynamics. They can be set to zero with an appropriate rephasing.

If the amplitudes in Eq. (1.32) are just single amplitudes we can write

$$\mathcal{A}_{D\to f} = A\, e^{i(\delta+\phi)}, \tag{1.33}$$

$$\mathcal{A}_{\overline{D}\to\overline{f}} = A\, e^{i(\delta-\phi+\theta)}, \tag{1.34}$$

where δ, ϕ and θ are respectively a strong, weak and a spurious phase. The difference of the decay rates of these processes can be made equal to zero, since in this case the phases are global and only the moduli matter,

$$|\mathcal{A}_{D\to f}|^2 - |\mathcal{A}_{\overline{D}\to\overline{f}}|^2 = 0. \tag{1.35}$$

If we consider instead the amplitudes in Eq. (1.32) as a sum of many partial amplitudes we can write

$$\mathcal{A}_{D\to f} = \sum_k |A_k|\, e^{i(\delta_k+\phi_k)} \tag{1.36}$$

$$\mathcal{A}_{\overline{D}\to\overline{f}} = \sum_k |A_k|\, e^{i(\delta_k-\phi_k+\theta)}, \tag{1.37}$$

and from the moduli difference we can see that *CP* violation is now possible, thanks to the interference terms of the partial amplitudes,

$$|\mathcal{A}_{D\to f}|^2 - |\mathcal{A}_{\overline{D}\to\overline{f}}|^2 = -2\sum_{k,l}|A_k||A_l|\sin(\delta_k-\delta_l)\sin(\phi_k-\phi_l). \tag{1.38}$$

Thus to have *CP* violation directly in the decay process one needs at least two decay amplitudes with different weak and strong phases. In case of charged mesons this is the only type of *CP* violation possible.

To quantify the *CP* violation the direct *CP* asymmetry can be defined as

$$A_{CP}^{\mathrm{dir}} = \frac{|\mathcal{A}_{D\to f}|^2 - |\mathcal{A}_{\overline{D}\to\overline{f}}|^2}{|\mathcal{A}_{D\to f}|^2 + |\mathcal{A}_{\overline{D}\to\overline{f}}|^2}. \tag{1.39}$$

CP violation in presence of mixing

In case of neutral meson system, the *CP* violation phenomenology is enriched by the dynamics of the flavour mixing, described in the previous Sect. 1.5 for a generic neutral meson system $P^0 - \overline{P}^0$. There are in particular two types of phenomena:

- *CP* violation can occur if the probability of the transition $P^0 \to \overline{P}^0$ at time t is different from the *CP* conjugated process $\overline{P}^0 \to P^0$. Considering Eq. (1.23a), this can occur if

  $$\left|\frac{q}{p}\right| \neq 1. \tag{1.40}$$

- If a final state f (*CP* eigenstate for simplicity) is accessible from both P^0 and $\overline{P}^0$, *CP* violation can occur in the interference between the two amplitudes $\mathcal{A}(P^0 \to f)$ and $\mathcal{A}(P^0 \to \overline{P}^0 \to f)$. In order to quantify this type of *CP* violation, we can use the same notation of Eq. (1.32) and define

  $$\lambda_f \equiv \frac{q}{p}\frac{\mathcal{A}_{\bar{D}\to f}}{\mathcal{A}_{D\to f}}, \tag{1.41}$$

  then the presence of *CP* violation implies

  $$\Im(\lambda_f) \neq 0, \tag{1.42}$$

  or alternatively, $\phi_f = \arg(\lambda_f) \neq \{0,\pi\}$.

Experimentally, the first observation of *CP* violation was done at Brookhaven Laboratory in 1964, concerning the neutral kaon decays into two pions [40], paving the way of the modern theorisation of *CP* violation within the SM. In 2001 indirect observations of *CP* violation in neutral B systems were reported by BaBar and Belle collaboration [117, 118], with a subsequent series of important results of direct *CP* violation in B^0, B^+ and B_s^0 mesons [119–124], done also by LHCb collaboration. More recently the first observation of *CP* violation in charm has been done by LHCb collaboration in $D^0 \to K^+K^-$ and $D^0 \to \pi^+\pi^-$ with an integrated luminosity of 6 fb^{-1} [125]. In particular LHCb found

$$\Delta A_{CP} = A_{CP}(KK) - A_{CP}(\pi\pi) = (15.4 \pm 2.9) \cdot 10^{-4}.$$

The result is consistent with SM order of magnitude, $\mathscr{O}(10^{-4} - 10^{-3})$ [126, 127], but further future measurements and possible theoretical predictions improvements are necessary to clarify whether the result requires the presence of BSM effects.

1.6 Rare Charm Decays

The charm physics has unique characteristics and the study of its processes has historically been very important for the development of the SM, and continues to be significant for the indirect research of NP [109]. Historically, with the discovery of charmonium [27, 28] and the almost contemporary observations of Bjorken scaling [128], it was understood that quarks really act as dynamic degrees of freedom within hadrons. Moreover, research in charm physics led to the development of increasingly precise vertex detectors, which paved the way for B and top physics [129, 130]. Another remarkable aspect, linked to the fact that charm physics is quantitatively challenging, was the possibility of testing and refining theoretical models and developing new approaches to study non-perturbative and heavy flavours QCD [131–142] (for a complete discussion see [109]).

For what concern physics BSM, possibly NP effects involved in FCNC in up-type quarks could be in principle different from those involved in down-type quarks processes. In this scenario, the role of charm is unique, since among the up-type quarks it is the only one whose FCNC processes can be studied: the top quark decays before forming hadrons, not allowing NP search in transitions $\Delta T = 2$ and limiting the CP violation studies in this system; on the other hand mesons formed by u and $\overline{u}$ are their own antiparticles and there is no mixing by definition, moreover they have a limited phase space, which reduces the possibilities of CP violation [143].

One can give a simple estimate of the total amplitude for FCNC $c \to u$ processes, which involves a coherent sum of all the possible contribution in which down-type quarks circulate in the loop [144],

$$\mathcal{A}(c \to u) = V_{cs}^* V_{us}\left[f\left(\frac{m_s^2}{m_W^2}\right) - f\left(\frac{m_d^2}{m_W^2}\right)\right] + V_{cb}^* V_{ub}\left[f\left(\frac{m_b^2}{m_W^2}\right) - f\left(\frac{m_d^2}{m_W^2}\right)\right], \tag{1.43}$$

where the the terms $f(m_q^2/m_W^2)$ describe the loop content and depends on the $W^\pm$ boson and the quark mass involved. As already mentioned, charm FCNC processes $c \to u$ are very rare: the first term is small due to the similar masses of d and s quarks, which is indeed the GIM suppression already described in the case of $K^0 \to \mu^+\mu^-$ in Sect. 1.3; the second term is suppressed by the CKM factors, in particular $V_{cb}^* V_{ub} \sim \lambda^5$. For example the inclusive decay $D^0 \to X_u \ell^+\ell^-$ has branching fraction of $\mathscr{O}(10^{-9})$ or less [145].

1.6.1 Effective Field Theory

Although weak decays of mesons can be studied in a simple way from the point of view of the weak interaction only, they are complicated by the non-perturbative dynamics of the strong interaction, characterised by the energy scale $\Lambda_{QCD} \sim 200\,\text{MeV}$, the characteristic scale of confinement.

In view of the fact that to describe a physical phenomenon one would like to focus on the energy and distance scales at which it occurs, in the case of heavy meson decays it is appropriate to develop and use an *effective* field theory, where the heavy degrees of freedom do not explicitly appear in the theory, since they become relevant only at higher energy scales [146, 147]. This is possible thanks to two fundamental key concepts: the Wilson renormalisation group theory [148, 149] and the decoupling theorem by Applequist and Carazzone [150], which show that heavy degrees of freedom decouple at energy scales much lower than their mass, meaning that a suppression of such contributions occurs in the theory by inverse powers of the heavy scale, up to logarithmic contributions.

For charm decays, three energy scales are involved with the hierarchy $M_W \gg m_c > \Lambda_{QCD}$. In order to explain in more details these concepts, let's consider a field theory in which we want to compute the transition amplitude for the generic process $i \to f$, where i and f are quantum states whose energies are lower than the heavy scale M_W. An effective Hamiltonian $\mathcal{H}_{eff}$ can be written, since all the effects at scale above M_W can be considered local interactions without explicit propagators. A general approach to write the effective Hamiltonian is using the Operator Product Expansion (OPE) [146, 151, 152]

$$\langle f|\mathcal{H}_{eff}|i\rangle = \sum_k C_k(M_W)\,\langle f|\mathcal{O}_k|i\rangle\big|_{M_W}. \tag{1.44}$$

The SD physics, i.e. all the contributions at energies above the scale M_W, is absorbed and described by the complex Wilson coefficients $C_k(M_W)$, while the LD physics is described by the matrix elements of local operators $\langle f|\mathcal{O}_k|i\rangle\big|_{M_W}$. The W boson does no longer appear as a dynamical degree of freedom, and is said to be *integrated out*. Its effect is absorbed in the Wilson coefficients.

The underlying non-trivial assumption, called *factorisation* in the context of hard processes in QCD, is the possibility of such a separation of SD and LD effects [153]. From that perspective this type of factorisation has two advantages: once it is adopted (assumption that in any case has to be proven), the SD part cannot be any more dependent on the LD scale by definition, hence the mass dimension of the coefficients $C_k(M_W)$ needs to come from powers of heavy scale M_W only; on the other hand, the LD contributions can be computed with non-perturbative methods in a simpler way with respect to the original ones, since they might have a simpler structure (for example being dependent on parton distributions only) or be process independent. The main drawback however is that, in the specific context of heavy mesons decays, factorisation assumption holds in the limit $m_q \gg \Lambda_{QCD}$: power corrections to the amplitudes are suppressed by Λ_{QCD}/m_q, which can be of order 10% for B decays but potentially could be much larger for D decays. Furthermore, the closeness of m_c and Λ_{QCD} introduce additional difficulties, since the naive power counting starts to fail at m_c scale [153], and the convergence of QCD factorisation predictions are quite poor [154]. For this reason, predictions based on factorisation and effective theory in charm physics are affected by large theoretical uncertainties.

Expanding and factoring out the powers of $1/M_W$ in Eq. (1.44) the amplitude can be written as

$$\langle f|\mathcal{H}_{eff}|i\rangle = \sum_k \frac{1}{(M_W)^k} \sum_{k,j} c_j \,\langle f|\mathcal{O}_{k,j}|i\rangle\big|_{M_W}, \tag{1.45}$$

where c_j are now dimensionless Wilson coefficients. With the exception of factorisation, no other approximation has been done so far, and the sum can in principle represents an exact solution with an infinite number of contributions. However in case of weak decays of a quark with mass m_q, an analogous series in powers of m_q/M_W can be constructed and the sum can be truncated rapidly, with a small set of operators, that indeed will be discussed in Sect. 1.6.2.

An important feature of this methodology is that it is not strictly necessary to use specifically the heavy scale M_W to separate SD and LD physics: one can define another arbitrary large scale μ with a mass dimension to define such separation, with the requirement not to violate the factorisation assumption, $\Lambda_{QCD} \ll \mu$. In this way the dimensionless coefficients will depend on the ratio of the two scales, $c_j(M_W/\mu)$. Being μ an arbitrary parameter that can be shifted, the functional dependence coming from the Wilson coefficients and from the matrix elements has to cancel out:

$$\langle f|\mathcal{H}_{eff}|i\rangle = \sum_k \frac{1}{(M_W)^k} \sum_{k,j} c_j(M_W/\mu) \,\langle f|\mathcal{O}_{k,j}|i\rangle\big|_{\mu}. \tag{1.46}$$

This procedure has two important properties [155]: since the strong coupling constant α_s of QCD depends on the running energy scale μ, from the point of view of the effective field theory the parameter μ can be interpreted as a renormalisation scale, to treat SD QCD corrections due to the exchange of hard gluons at energies above μ; from the point of view of the full theory μ is just a scale to provide the factorisation within the OPE formalism, as already pointed out. Indeed, the requirement of the functional cancellation of μ between the SD and LD terms leads to the same evolution equations developed in the context of renormalisation group. This allows to calculate the Wilson coefficient in a systematic way: the initial conditions of the coefficients can be first determined by matching both the full theory and the effective one at the electroweak scale M_W, thus obtaining $c_i(M_W)$. Then, using perturbation theory, c_i can be written in powers of α_s and evolved down to the scale $\mu \sim 1\,\text{GeV}$, solving the renormalisation group equation. In this procedure, one faces with three main technical difficulties [116]:

- presence of large logarithms, dependent on the scale μ,
- mixing of the local operators,

- b quark threshold along the μ scaling.

which are briefly described in the following. Writing down the coefficients in the perturbative series we get [146]

(1.47)
$$c_i(M_W/\mu,\alpha_s) = \underbrace{\left[b_i^{(00)}\right]}_{\mathcal{O}(1)} + \underbrace{\left[b_i^{(11)}\alpha\ln\frac{M_W}{\mu} + b_i^{(10)}\alpha\right]}_{\mathcal{O}(\alpha_s)} + \underbrace{\left[b_i^{(22)}\alpha^2\ln^2\frac{M_W}{\mu} + b_i^{(21)}\alpha^2\ln\frac{M_W}{\mu} + b_i^{(20)}\alpha^2\right]}_{\mathcal{O}(\alpha_s^2)} + \ldots,$$

where we defined $\alpha = \alpha_s/4\pi$. The appearance of possible large logarithms is common in quantum field theories which involve very different scales, and an ordinary perturbation expansion in α_s can be invalidated if $\ln(M_W/\mu)$ becomes too large [156]. The renormalisation group equation allows to resum consistently all the leading logarithms appearing at all orders, of the form

$$b_i^{(nn)}\,\alpha^n\ln^n\frac{M_W}{\mu}.$$

This procedure is called leading-logarithms approximation (LLA). In case of charm decays this is absolutely necessary, because at scale $\mu\sim m_c$ logarithms are $\ln(M_W/m_c)\sim 4$, thus even the leading term containing $b_i^{22}\alpha^2$ is much larger than the one with $b_i^{10}\alpha$, despite being at an higher order. The expansion must then be reorganised in terms of power combinations of α_s and logarithms. For example, resumming contributions of the form $\alpha^n\ln^{(n-1)}$ provides the next-to-leading-logarithms (NLL) orders and so on. The second important consequence mentioned above, typical of the renormalisation group flow, is the operators mixing under the shifting of the scale μ, i.e. a contribution of the matrix element with $\mathcal{O}_{k,i}$ at μ will be absorbed in a linear combination of matrix elements of the operators at another scale,

$$\mu\frac{d}{d\mu}\langle f|\mathcal{O}_i|i\rangle = \sum_j\gamma_{ij}(\mu)\langle f|\mathcal{O}_j|i\rangle, \tag{1.48}$$

where the mixing matrix γ_{ij} is called anomalous dimension, and mixes all operators with same mass dimension and quantum numbers. The anomalous dimension depends itself on the scale μ and enters directly in the renormalisation group equation. The operator mixing has important consequences for rare charm decays, described in Sect. 1.6.2.1. The third consequence of the renormalisation procedure involves the crossing of quarks thresholds when scaling down from M_W to m_c. At the scale $\mu\sim m_b$ the b quark has to be integrated out and this can be taken into account by matching the effective theory above and below the threshold, removing the b quark from the theory. Generally the matching should be done at an higher order than NLL, therefore these procedures are affected by theoretical approximations or involve missing contributions, albeit suppressed [144].

FIGURE 1.3. Example of Feynman diagrams for current-current operators, in particular $\mathcal{O}_1$ (left) and one possible diagram with QCD correction $\mathcal{O}_2$ (right).

1.6.2 Effective Hamiltonian for $\Delta C = 1$

The effective Hamiltonian for processes with $\Delta C = 1$ and $\Delta S = 0$, like $D^0 \to \pi^+\pi^-\mu^+\mu^-$ and $D^0 \to K^+K^-\mu^+\mu^-$, can be written at the scale $\mu \sim m_c$ integrating out the b quark and the weak bosons as [157]

$$\mathcal{H}_{\text{eff}} = -\frac{G_F}{\sqrt{2}} \sum_{q\in d,s} V_{cq}^* V_{uq} \left[C_1(m_c)\mathcal{O}_1^{(q)} + C_2(m_c)\mathcal{O}_2^{(q)} + \sum_{i=3}^{10} C_i(m_c)\mathcal{O}_i \right], \tag{1.49}$$

where the operators $\mathcal{O}_{1,\ldots,10}$ are a basis of main local operators described in the following [157–162].

- Current-Current operators $\mathcal{O}_1$ and $\mathcal{O}_2$:

  $$\mathcal{O}_1^{(q)} = (\overline{u}_L^\alpha \gamma_\mu q_L^\alpha)(\overline{q}_L^\beta \gamma^\mu c_L^\beta), \qquad \mathcal{O}_2^{(q)} = (\overline{u}_L^\alpha \gamma_\mu q_L^\beta)(\overline{q}_L^\beta \gamma^\mu c_L^\alpha), \tag{1.50}$$

  where q can be a d or s quark and the indexes α and β represent the color quantum numbers. These operators describe local current-current interactions between quarks and the $\mathcal{O}_2$ operator in particular contains a color exchange between the currents, so it is not present at the leading order in QCD but appears only as QCD corrections. Examples of diagrams for such operators can be found in Fig. 1.3.

- QCD penguin operators $\mathcal{O}_3$-$\mathcal{O}_6$:

  $$\mathcal{O}_3 = (\overline{u}_L^\alpha \gamma_\mu c_L^\alpha) \sum_q (\overline{q}_L^\beta \gamma^\mu q_L^\beta), \qquad \mathcal{O}_4 = (\overline{u}_L^\alpha \gamma_\mu c_L^\beta) \sum_q (\overline{q}_L^\beta \gamma^\mu q_L^\alpha), \tag{1.51}$$

  $$\mathcal{O}_5 = (\overline{u}_L^\alpha \gamma_\mu c_L^\alpha) \sum_q (\overline{q}_R^\beta \gamma^\mu q_R^\beta), \qquad \mathcal{O}_6 = (\overline{u}_L^\alpha \gamma_\mu c_L^\beta) \sum_q (\overline{q}_R^\beta \gamma^\mu q_R^\alpha). \tag{1.52}$$

  These operators correspond to loop diagrams in which the quarks of the initial current, after changing flavour through a W boson, annihilate in a gluon that will create the final $q\overline{q}$ pair. For this reason the final pair also sees the participation of the right-handed components $\mathcal{O}_{5,6}$. The operators for QCD corrections take into account the exchange of the color charge ($\mathcal{O}_{4,6}$). Similar operators for QED, $\mathcal{O}_{3,\ldots,6}^{QED}$, can be written and play an important role in the mixing with the SD operators. It is important to note that also

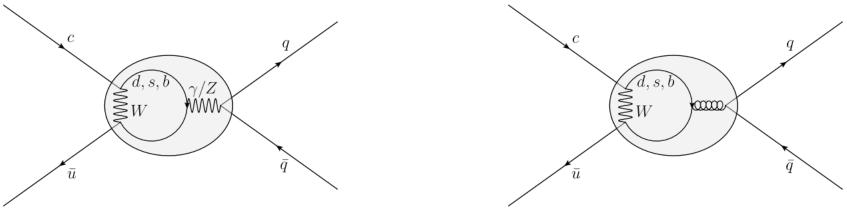

FIGURE 1.4. Example of Feynman diagrams for QCD penguin operators (right) and electroweak penguin operators (left), for which $\mathcal{O}^{QED}_{3,\ldots,6}$ are a particular case.

these operators are of the form of *current-current* local interactions: the presence and the structure of the loops can be inferred from the flavour combinations of the currents, which are different with respect to the $\mathcal{O}_{1,2}$. Examples of diagrams for such operators can be found in Fig. 1.4.

- Magnetic and chromomagnetic penguin operators $\mathcal{O}_7$-$\mathcal{O}_8$ (radiative FCNC processes):

$$\mathcal{O}_7 = \frac{em_c}{16\pi^2}(\overline{u}_L\sigma_{\mu\nu}c_R)F^{\mu\nu}, \qquad \mathcal{O}_8 = \frac{g_sm_c}{16\pi^2}(\overline{u}_L\sigma_{\mu\nu}T^ac_R)G^{\mu\nu}_a. \tag{1.53}$$

  These operators are responsible for radiative FCNC processes. The diagram structures are penguins in which the photons and gluons produced by the quarks annihilation couple with the spin components of the fermionic current. This coupling is made explicit by Gordon's decomposition of the Dirac current [163]: $\overline{\psi}_a\gamma^\mu\psi_b \propto \overline{\psi}_a[(p_a+p_b)^\mu + i\sigma^{\mu\nu}(p_a-p_b)_\nu]\psi_b$, where p are the four-vectors of the ψ_a and ψ_b spinors and $\sigma^{\mu\nu}$ is the usual antisymmetric tensor $\sigma^{\mu\nu} = i/2\,(\gamma^\mu\gamma^\nu - \gamma^\nu\gamma^\mu)$. The operator basis can include also chirality-flipped operators $\mathcal{O}'_{7,8} \propto \overline{u}_R\sigma_{\mu\nu}c_L$, whose Wilson coefficients are suppressed by a factor m_u/m_c and are usually neglected.

- Semileptonic penguin and box operators $\mathcal{O}_9$-$\mathcal{O}_{10}$ (semileptonic FCNC processes):

$$\mathcal{O}_9 = \frac{e^2}{16\pi^2}(\overline{u}_L\gamma_\mu c_L)(\bar{\ell}\gamma^\mu\ell), \qquad \mathcal{O}_{10} = \frac{e^2}{16\pi^2}(\overline{u}_L\gamma_\mu c_L)(\bar{\ell}\gamma^\mu\gamma^5\ell). \tag{1.54}$$

  These operators describe non-resonant FCNC processes involving leptons. The quark pair $\overline{u}c$, after changing flavour through a W boson, annihilates in a neutral boson, γ or Z, which decays in $\ell^+\ell^-$. In the case of the box process, the two quarks exchange a down-type virtual quark emitting two W bosons of opposite sign, which will form the final lepton pair by exchanging a virtual neutrino. Examples of diagrams for such operators can be found in Fig. 1.5.

1.6.2.1 Discussion on main local operators and C_i^{eff}

The main local operators that govern the decay amplitudes of rare charm decays, like $D^0 \to h^+h^-\mu^+\mu^-$, are the current-current operators $\mathcal{O}^{(q)}_{1,2}$, responsible for the LD contribution with

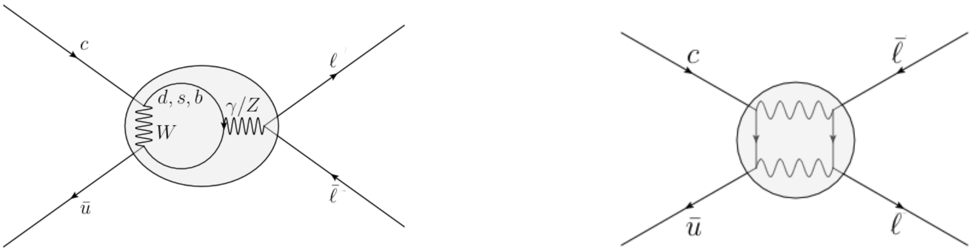

FIGURE 1.5. Example of Feynman diagrams for the semileptonic penguin (left) and box (right) operators.

intermediate resonances. In fact these operators are involved mainly in hadronic decays, since the initial quark current turns into a new quark current already at tree level. Involving highly non perturbative QCD effects, theoretical predictions are particularly difficult to obtain, but pre-QCD models such as Vector Meson Dominance (VDM) [164] continue to play an important role in calculating strongly interacting processes at long and medium distance. In VDM the D^0 decay proceeds mainly through resonances, V/V', that have the same quantum numbers of the photon, so that they can couple to a virtual photon $V \to \gamma^* \to \ell^+\ell^-$. Generally in this scenario there can be three dynamically LD contributions [165]: resonance or near-resonance exchange, the internal Bremsstrahlung and the charge radius contribution. The former has the potential to be the main contribution in $D^0 \to h^+h^-\mu^+\mu^-$ and and will be discussed in next sections, mentioning the main resonant states; the Bremsstrahlung contribution corresponds instead to radiation of a photon from a pure weak vertex $D^0 \to h_1^+h_2^-$ and foresees significant contributions only in the low dilepton mass, further strengthened in the case of $D^0 \to h^+h^-e^+e^-$ that has a lower dilepton threshold. This contribution is found to be two orders of magnitude smaller than the resonant one [165]. The charge radius contribution, subject to larger theoretical uncertainties, corresponds to radiation of a photon as a result of $D^0 - \overline{D}^0$ mixing and provide significant effect only on the decay width.

The QCD penguin operators $\mathcal{O}_{3,\dots,6}$ can contribute but are highly suppressed, while the corresponding QED operators can have important consequence along the operator mixing, as explained in the following. The most sensitive processes to NP effects are governed by magnetic and semileptonic operators, $\mathcal{O}_7$, $\mathcal{O}_9$ and $\mathcal{O}_{10}$, which describe the FCNC SD transitions, radiative in case of $\mathcal{O}_7$ or directly into a lepton current in case of $\mathcal{O}_{9,10}$. Along the energy scaling, operator mixing of these operators leads to important enhancements of effective Wilson coefficients (discussed in [145, 157, 166, 167]):

- The C_9 coefficient receives enhancements through the mixing with $\mathcal{O}_{1,2}$, and from QED penguins $\mathcal{O}_{3,\dots,6}^{QED}$. The mixing can be seen, diagrammatically, if one contracts the light quarks in a loop that can radiate a virtual photon, which can eventually couple to a dilepton pair. C_9 remains the dominant contribution, one of order of magnitude larger than the subdominant ones, like C_7.

- The C_7 coefficient receives enhancements from the two loop QCD radiative corrections in the mixing with $\mathcal{O}_2$. Nevertheless the contribution remains subdominant.

- On the contrary, the C_{10} coefficient does not receive any QCD correction enhancement due to the chiral structure of $\mathcal{O}_{10}$ and remains highly suppressed at all orders, hence $C_{10}(m_c) = C_{10}(M_W)$. Possible NP models that include processes with the same chiral structure of $\mathcal{O}_{10}$ can increase its effect, constituting a clean probe for SD transitions.

At next-to-next-to-leading-order (NNLO) the main Wilson coefficient at $\mu \sim m_c$ are [168, 169]:

$$C_{1,2} \sim \mathscr{O}(1), \quad C_7 \sim \mathscr{O}(0.001), \quad C_9 \sim \mathscr{O}(0.01), \quad C_{10} \sim 0.$$

From a theoretical point of view usually some operator matrix elements can be calculated in perturbation theory, and the perturbative coefficients of tree level matrix elements can be reabsorbed into new Wilson coefficients, called effective Wilson coefficients, C^{eff}, which now are describing also some of LD contributions, calculable perturbatively [144]. In the case of operators mentioned above, we obtain $C^{\text{eff}}_{7,9,10}$, which are equal to $C_{7,9,10}$ up to matrix elements of four-quarks operators, hence taking into account the LD effects of $\mathcal{O}_{1,2}$. This procedure induces a q^2 dependence in $C^{\text{eff}}_{7,9,10}$ and the acquisition of CP violating phases, that will be important phenomenologically to search for NP effects.

1.6.3 New Physics models

As previously discussed, FCNC contributions driven by $\mathcal{O}_{7,9,10}$ are highly suppressed in the SM and the decay rate of processes like $D^0 \to h^+h^-\mu^+\mu^-$ is dominated by resonant contributions. NP models providing tree-level FCNC processes can increase the effects of the operators mentioned above, or others NP scenarios with new couplings can enlarge the operator basis. One of the common choice to consider BSM effects in semileptonic decays is to add the following operators [168]:

$$\mathcal{O}'_9 = (\overline{u}\gamma_\mu c_R)(\overline{\ell}\gamma^\mu \ell), \quad \mathcal{O}'_{10} = (\overline{u}\gamma_\mu c_R)(\overline{\ell}\gamma^\mu\gamma^5 \ell), \tag{1.55}$$

$$\mathcal{O}_S = (\overline{u}\, c_R)(\overline{\ell}\ell), \quad \mathcal{O}'_S = (\overline{u}\, c_L)(\overline{\ell}\ell), \tag{1.56}$$

$$\mathcal{O}_P = (\overline{u}\, c_R)(\overline{\ell}\gamma^5\ell), \quad \mathcal{O}'_P = (\overline{u}\, c_L)(\overline{\ell}\gamma^5\ell), \tag{1.57}$$

$$\mathcal{O}_T = (\overline{u}\sigma^{\mu\nu} c)(\overline{\ell}\sigma^{\mu\nu}\ell), \quad \mathcal{O}_{T5} = (\overline{u}\sigma^{\mu\nu} c)(\overline{\ell}\sigma^{\mu\nu}\gamma^5\ell), \tag{1.58}$$

where $\mathcal{O}'_{9,10}$ are the chirality-flipped version of the usual $\mathcal{O}_{9,10}$ FCNC operators, while $\mathcal{O}_{S,P,T,T5}$ operators describes scalar, pseudoscalar and tensorial couplings, which do not exist or are highly suppressed in the SM. Their primed versions describe similar couplings but with a different quark chiral structure.

To study possibly NP effects there are two major categories of observables that we describe below:

- Branching fraction: deviations from SM branching fractions due to NP effects can be searched for in regions of $m\ell^+\ell^-$ far from resonant contributions. Branching fractions can be enhanced by order of magnitudes in some NP models, but the large width of resonances in the $\ell^+\ell^-$ spectrum can hide such effects. The cleanest rare charm decay for branching fraction studies is the $D^0 \to \mu^+\mu^-$ decay, which is not affected by so large uncertainties like hadronic decays. The further helicity suppression leads to a SD branching fraction of $\mathscr{O}(10^{-18})$, while LD contribution is estimated to be $\mathscr{O}(10^{-13} - 10^{-11})$ [157, 169–173]. An interesting alternative, not helicity suppressed, is the decay $D^*(2007)^0 \to \ell^+\ell^-$, which is sensitive to other operators contributions with respect to $D^0 \to \mu^+\mu^-$ [174]. Since $D^*(2007)^0$ decays strongly or electromagnetically, a way to study this channel is through $e^+e^- \to D^*$. Analysis of this type is currently being done by CMD-3 and SND at VEPP2000 [175, 176].

- Angular and *CP* asymmetries: thanks to the interference between the SD and LD amplitudes, it is possible to probe NP effects, which can occur in the appearance of asymmetries not foreseen by the SM, or in the enhancement of asymmetries already predicted. The *CP* asymmetry can manifest itself through large weak phases acquired by the coefficients $C_{7,9,10}$ in some NP models. The angular asymmetries in multi-body decays, like $D^+ \to h^+\mu^+\mu^-$ and $D^0 \to h^+h^{'-}\mu^+\mu^-$, are instead a rich source of observables: the angular distributions generated in weak and strong interactions are known, and possible new operators with a different chiral structure not foreseen by the SM, like the ones mentioned above, could leave traces in angular distributions and generate asymmetries. One important observable is the forward-backward asymmetry, A_{FB}, which is described in details in Sect. 1.7.2.

The most important NP models for rare charm decays are briefly mentioned in the following. A recent and exhaustive list of main NP models and their predictions for multi-body rare charm decays can be found in [177].

1.6.3.1 Supersymmetric models

Even though the LHC physics has already reduced the parameter spaces of these theories, supersymmetric models continue to be of theoretical interest since they can explain in a single framework most of the SM problems, the matter-antimatter asymmetry and provide dark matter candidates [78, 79]. In the Minimal Supersymmetric Standard Model (MSSM) all the fermions and bosons are organised in supermultiplets, thus each particle has a corresponding supersymmetrical partner. An important concept in this theory is the R-parity conservation, a $\mathbb{Z}_2$ symmetry that ensures conservation of baryon and lepton number

$$R_p = (-1)^{3B+L+2s},$$

where s is the spin, B the baryon number and L the lepton number. In the case of R_p conservation, loop amplitudes which contain flavour changing couplings are possible, with enhancements of

C_7, C_8 and C_9. In case of R_p violation, the process $c \to u\ell\ell$ is possible already at tree level, with large enhancements on C_9 and C_{10}. As a consequence the A_{CP} and A_{FB} can be enhanced respectively at order $\mathscr{O}(0.1\%)$ and $\mathscr{O}(10\%)$ [157, 165, 166, 172, 178].

1.6.3.2 Modified Higgs sector

Modification of the Higgs sector concerns the Little Higgs model (LH) and Little Higgs with additional T-parity (LTH) [80]. In these models the Higgs boson is a pseudo-Nambu-Goldstone boson coming from a global symmetry breaking at a TeV scale. A massive gauge boson and an up-type quark appear in the theory, with a modified weak currents. In both cases of LH and LHT models C_{10} receives large enhancements, being comparable to C_9. In case of LH, both A_{CP} and A_{FB} are enhanced up to $\mathscr{O}(0.1\%)$, while in LHT model A_{CP} can be up to $\mathscr{O}(10\%)$ [145, 179–181].

1.6.3.3 Leptoquarks

Leptoquarks (LQ) models [83, 84] foresee hypothetical particles, both with lepton and baryon numbers, so that quark and leptons are two different states of the same particle. Hence quarks can be coupled into leptons and vice versa. The existence of a new boson that couples quarks and leptons is assumed, providing a way to have an effective $c \to u\ell'\ell$ vertex. These models are of recent interest, since they can explain various SM anomalies or take into account neutrino masses and mixing. The most important key observables are SD branching fractions, enhanced by several order of magnitudes, and A_{FB} which can be largely strengthened up to $\mathscr{O}(8 \cdot 10^{-1})$ [169, 173, 182, 183].

1.6.3.4 Generic models with extra gauge bosons and fermions

In addition to LQ, there are SM extensions in which there is a new up-type quark [178, 180], a generic Z' boson [165, 183, 184] which can contribute in many rare decays of D mesons, mitigating the GIM mechanism or allowing FCNC processes at tree level, through a $c \to uZ$ vertex. In this case also there are predicted large enhancements for the C_9 and C_{10} coefficients and impact on A_{FB} which raises up to few percent.

1.6.3.5 Randall-Sundrum models

The Randall–Sundrum models [81, 82] are BSM scenarios in which a warped extra dimension is present, in particular the spacetime geometry is extended to a 5-dimensional anti-de Sitter spacetime where elementary particles are localised in a 4-dimensional slice. In these models new gauge bosons appear, that can mediate flavour violation. The most important contributions are given to C_{10}, enhanced by several order of magnitudes. Consequently, A_{CP} raises to the percent level, while A_{FB} can be enhanced up to $\mathscr{O}(5\%)$ [185, 186].

1.7 The $D^0 \to h^+h^-\mu^+\mu^-$ decays

The $D^0 \to h^+h^-\mu^+\mu^-$ $(h = K, \pi)$ are Cabibbo suppressed decays that offer a wide number of observables, being a four-body decay. The two muons, as the two hadrons, may arise from intermediate resonances that lead to a rich, non-trivial distributions over the phase-space. Since they are further suppressed with respect to the three-body case, $D^+_{(s)} \to \pi^+\mu^+\mu^-$, these decays have recently become of experimental and theoretical interest. The E791 collaboration set upper limits of the order of $\mathscr{O}(10^{-5})$ on the branching fractions of $D^0 \to h^+h^{(\prime)-}\mu^+\mu^-$ [187], while the LHCb collaboration sets an upper limit on the branching fraction of the pionic mode in the non-resonant di-muon region, of $5.5 \cdot 10^{-8}$ at 90% C.L. [188].

More recently, thanks to the first observation of the Cabibbo-favoured mode $D^0 \to K^-\pi^+[\mu^+\mu^-]_{\rho^0/\omega}$ by the LHCb collaboration [189], where the two muons are selected in $m^2(\mu\mu)$ range consistent of the ρ^0/ω mass, the first observations of $D^0 \to h^+h^-\mu^+\mu^-$ decays have been done by LHCb with a sample of proton-proton collision at center-of-mass energy of 8 TeV and an integrated luminosity of $2\,\text{fb}^{-1}$ [190]. The corresponding total and partial branching fraction in bins of $m^2(\mu\mu)$ has been also measured using $D^0 \to K^-\pi^+[\mu^+\mu^-]_{\rho^0/\omega}$ as normalisation channel. The integrated branching fractions are

$$\begin{aligned}\mathcal{B}(D^0 \to \pi^+\pi^-\mu^+\mu^-) &= (9.64 \pm 0.48 \pm 0.51 \pm 0.97) \times 10^{-7},\\ \mathcal{B}(D^0 \to K^+K^-\mu^+\mu^-) &= (1.54 \pm 0.27 \pm 0.09 \pm 0.16) \times 10^{-7},\end{aligned}$$

where the uncertainties are statistical, systematic, and due to the limited knowledge of the normalization branching fraction. The measurements are consistent with the theoretical SM prediction [165],

$$\begin{aligned}\mathcal{B}(D^0 \to \pi^+\pi^-\mu^+\mu^-)^{\text{th}} &\simeq 1.3 \cdot 10^{-6},\\ \mathcal{B}(D^0 \to K^+K^-\mu^+\mu^-)^{\text{th}} &\simeq 1.1 \cdot 10^{-7}.\end{aligned}$$

As already pointed out, these decays are dominated by LD contributions due to vector intermediate resonances in the di-muon and di-hadron spectrum. In particular, the two pions are expected to come mainly from ρ^0 meson, with a small contribution of ω meson through the $\rho - \omega$ mixing. In the di-muon spectrum, the main resonant contributions are the mesons of ρ^0, ω and ϕ. The η meson can contribute but the relative branching fraction is low ($\mathscr{O}(10^{-8})$). The non-resonant SD contribution is estimated to be of order $\mathscr{O}(10^{-10} - 10^{-11})$ and it is difficult to isolate simply binning in $m(\mu\mu)$, since the long tail of the resonances distributions, in particular of the ρ meson, cover a wide range in the phase space. Indeed at high di-muon mass, above the region of the ϕ, the influence of resonant contributions is minimal but it is sufficient to hide the non-resonant one [165, 168].

The $D^0 \to K^+K^-\mu^+\mu^-$ decay presents a significant smaller phase space: in the di-muon spectrum the main contributions are the ρ^0 and ω only, being the ϕ or other high mass resonances

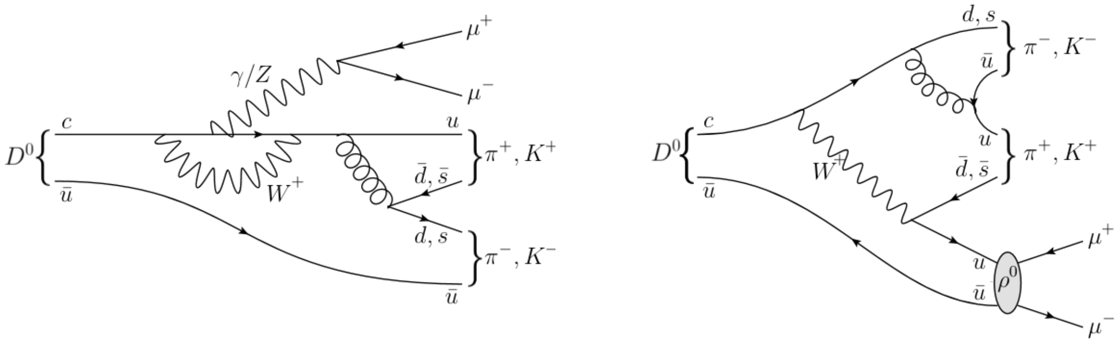

FIGURE 1.6. Example of two Feynman diagrams showing a SD penguin contribution to the $D^0 \to \pi^+\pi^-\mu^+\mu^-$ decay (left), and a diagram representing a LD contribution via the ρ^0 meson decaying in two muons (right).

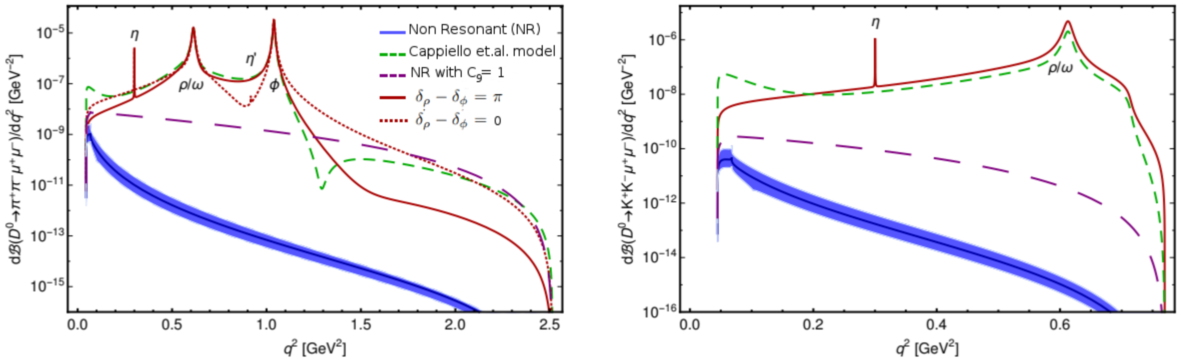

FIGURE 1.7. Differential branching fraction (modified from [168]) of $D^0 \to \pi^+\pi^-\mu^+\mu^-$ (left) and $D^0 \to K^+K^-\mu^+\mu^-$ (right) as a function of q^2, considering different models to highlight the theoretical uncertainties on the strong phases. The Cappiello et al. model refers to the theoretical model used in [165].

not kinematically allowed, while in the di-hadron spectrum the main contribution is due to the ϕ decaying in K^+K^-. The non-resonant contribution is estimated to be of order $\mathcal{O}(10^{-10})$ [165, 168] also in this case. In Fig. 1.6 two Feynman diagrams for the decay $D^0 \to \pi^+\pi^-\mu^+\mu^-$ are shown, one representing a SD penguin diagram, and another one representing a LD via the ρ^0 meson decaying in two muons. The relative branching fractions as a function of the $m(\mu\mu)$ region is shown in Fig. 1.7, while the observed branching fractions by the LHCb experiment are reported in Tab. 1.2.

$D^0 \to \pi^+\pi^-\mu^+\mu^-$		
$m(\mu^+\mu^-)$ region	[MeV/c^2]	$\mathcal{B}$ [10^{-8}]
Low mass	< 525	$7.8 \pm 1.9 \pm 0.5 \pm 0.8$
η	525–565	$< 2.4\,(2.8)$
ρ^0/ω	565–950	$40.6 \pm 3.3 \pm 2.1 \pm 4.1$
ϕ	950–1100	$45.4 \pm 2.9 \pm 2.5 \pm 4.5$
High mass	> 1100	$< 2.8\,(3.3)$
$D^0 \to K^+K^-\mu^+\mu^-$		
$m(\mu^+\mu^-)$ region	[MeV/c^2]	$\mathcal{B}$ [10^{-8}]
Low mass	< 525	$2.6 \pm 1.2 \pm 0.2 \pm 0.3$
η	525–565	$< 0.7\,(0.8)$
ρ^0/ω	> 565	$12.0 \pm 2.3 \pm 0.7 \pm 1.2$

Table 1.2. Branching fractions of $D^0 \to \pi^+\pi^-\mu^+\mu^-$ (top) and $D^0 \to K^+K^-\mu^+\mu^-$ (bottom) decays in different intervals of di-muon mass [190]. The uncertainties are respectively statistical, systematic and due to the limited knowledge of the normalization branching fraction.

1.7.1 Angular distribution

Being a four-body decay, the phase space can be described with five kinematical variables. Indeed the four-momenta of the 4 daughter particles define a set of 16 kinematical variables, which are subject to [191]:

- 4 constraints of the known masses,
- 4 constraints of the energy-momentum conservation,
- freedom to change the orientation of the D^0 rest frame, since it has no spin, thus removing the 3 Euler angles.

These constraints reduce then the independent variables from 16 to 5. Any choice of five independent variables can be used to parametrise the phase space, for example a set of five invariant masses. However the most natural one in this case is the Cabibbo-Maksymowicz (CM) parametrisation [192], composed of two invariant masses, two polar angles and one azimuthal angle:

- $m(h^+h^-)$, the invariant mass of the di-hadron system.
- $m(\mu^+\mu^-)$, the invariant mass of the di-muon system.
- $\cos(\theta_{h^+})$, the cosine of the helicity angle for the di-hadron system, where the helicity angle θ_{h^+} is defined as the angle between the momentum of the positive hadron in the rest frame of the di-hadron system with respect to the di-hadron flight direction as seen from the rest frame of the D^0. An equivalent definition to not mix two reference frames is: the

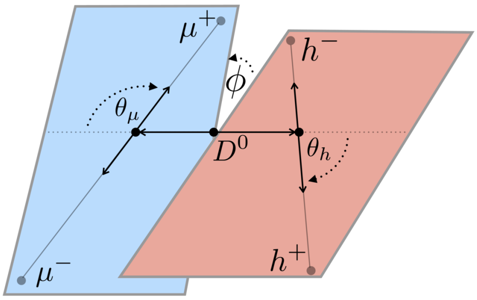

FIGURE 1.8. Scheme showing the angles chosen to parametrise the $D^0 \to h^+h^-\mu^+\mu^-$ phase space.

angle between the momentum of the positive hadron and the inverse of the momentum of the D^0 all defined in the di-hadron system. For the $\overline{D}^0$ the negative hadron is considered.

- $\cos(\theta_{\mu^+})$, the cosine of the helicity angle for the di-muon system, with the analogous definition of the hadronic one, but considering the positive muon and the di-muon system.
- ϕ, the angle between the two decay planes of the di-muon and di-hadron system in the D^0 rest frame.

A more complete treatment on the calculation of the kinematical variables can be found in the Appendix A, while a scheme of the parametrisation is shown in Fig. 1.8. The effective Hamiltonian $\mathcal{H}_{\text{eff}}$ and the corresponding matrix element $\mathcal{M}$ can be written in terms of the Wilson coefficients c_9^{eff}, c_7^{eff}, c_{10} and their primed versions, to take into account BSM effects, plus all the new terms $c_{S,P,T,T5}$ introduced in Sect. 1.6.3. The effective coefficients c_i^{eff} take into account also the perturbative calculation on the four-quark local operators, thus absorbing the LD effects from quark loops, and are then related to c_1 and c_2 [168]. In particular the c_9^{eff} coefficient contains both a weak phase, related to the CKM matrix elements, and a strong phase, related to the perturbative calculation of the four-quark operators, thus allowing a possibility of CP violation [193]. Squaring the matrix element $\mathcal{M}$ and summing over spins, it can be proven that the decay rate can be written in a compact form and can be factorised in simple angular terms, $c_{1,\ldots,9}$, which depend only on $\cos(\theta_\mu)$ and ϕ through trigonometric functions, and angular coefficients $I_{1,\ldots,9}$, which depends on the other kinematical variables, both explicitly and implicitly (through the transversivity amplitudes). The complete derivation can be found in [193]. The decay rate can be written as

$$d^5\Gamma = \frac{1}{2\pi}\left[\sum_{i=1}^{9} c_i(\theta_\mu,\phi)\, I_i(q^2,p^2,\theta_h)\right] \cdot dq^2 dp^2 d(\cos\theta_\mu) d(\cos\theta_h) d\phi, \tag{1.59}$$

where q^2 (p^2) is the invariant mass squared of the two muons (hadrons). The c_i functions are

$$c_1 = 1,\ \ c_2 = \cos 2\theta_\mu,\ \ c_3 = \sin^2\theta_\mu \cos 2\phi,\ \ c_4 = \sin 2\theta_\mu \cos\phi,\ \ c_5 = \sin\theta_\mu \cos\phi, \\ c_6 = \cos\theta_\mu,\ \ c_7 = \sin\theta_\mu \sin\phi,\ \ c_8 = \sin 2\theta_\mu \sin\phi,\ \ c_9 = \sin^2\theta_\mu \sin 2\phi. \tag{1.60}$$

The $I_{1,\dots,9}$ coefficients are given in terms of generalised tranversivity amplitudes, $H^{L/R}_{0,\|,\perp}$, and reported in details in Appendix A, in the approximation of no tensor or pseudoscalar operators and for vanishing lepton mass. Generally we can write the functional dependence as [194]

$$I_i = I_i(H^{L/R}_{0,\|,\perp}, \sin\theta_h). \tag{1.61}$$

The generalised amplitudes can be written as

$$H^{L/R}_{0,\|} = C^{L/R}_{-}(q^2) F_{0,\|}(q^2, p^2, \cos\theta_h), \qquad H^{L/R}_{0,\perp} = C^{L/R}_{+}(q^2) F_{0,\perp}(q^2, p^2, \cos\theta_h), \tag{1.62}$$

where $C^{L/R}_{\pm}$ are q^2-dependent SD coefficients, linear combination of the Wilson coefficients mentioned above, and $F_{0,\|,\perp}$ are the tranversivity amplitudes. Since they can be expanded in associated Legendre polynomials P^m_ℓ,

$$F_0 = \sum_{\ell=0} a^\ell_0(q^2, p^2) P^{m=0}_\ell(\cos\theta_h), \tag{1.63}$$

$$F_{\|,\perp} = \sum_{\ell=1} a^\ell_{\|,\perp}(q^2, p^2) P^{m=1}_\ell(\cos\theta_h) \sin^{-1}\theta_h, \tag{1.64}$$

it is clear that the I_i terms contain also an implicit dependence on $\cos\theta_h$ and $\sin\theta_h$, according to the Legendre expansion. The full angular dependence can be made explicit, if one consider a specific angular momentum, like in $B \to K^*(K\pi)\ell\ell$ decays [195, 196], or expanding the h^+h^- system up to a D-wave configuration, like in [194]. Consequently a new set of angular coefficients appears, that no longer depend on θ_h. They are usually indicated as $J_{ix}(q^2, p^2)$ in literature.

From the relations of the angular coefficients I_i in Appendix A it is possible to see that $I_{5,6,7}$, containing a relative sign between the left-handed and right-handed amplitudes, constitute SM null tests. This is a key feature of rare charm decays: as already pointed out, the process $c \to u\ell^+\ell^-$ due the GIM mechanism is dominated by interactions from $SU(3)_c \times U(1)_q$ (electromagnetic and strong), which are all vector-like, thus with equal chirality of the lepton currents. Intermediate pseudoscalar resonances decaying directly in the two muons, or effects due to the non-vanishing lepton masses, can constitute a source of background to the null tests $I^{SM}_{5,6,7} = 0$, but since they are higher order effects not appreciable with the current experimental accuracy, they pose no problems on null tests or on the search for BSM effects, which are needed to be of $\mathcal{O}(1)$. The observables $I_{5,6,8,9}$ are also odd under CP transformation and can be used to measure CP asymmetry [168].

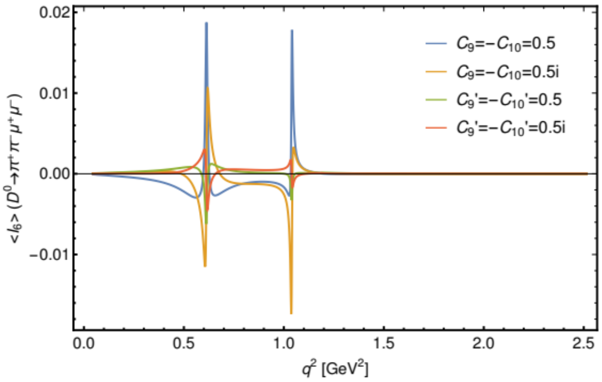

FIGURE 1.9. The observable $\langle I_6 \rangle$ as a function of q^2 for some NP models which have primed $C'_{9,10}$ Wilson coefficients, or same of order of magnitude between SM C_9 and C_{10}. A relative strong phase of π between ρ^0 and ω mesons is assumed.

1.7.2 Angular asymmetries

As already pointed out in the Sect. 1.6.3, the angular and *CP* asymmetries are useful observables to search for BSM effects. A full angular analysis, i. e. a full set of measurements of the coefficients I_i and $\overline{I}_i$, provides the full information to access to all the asymmetries. In particular we can define some angular asymmetries calculable directly through specific integration of the decay rate over the phase space. The first one is the forward-backward asymmetry A_{FB}, which quantify the difference in partial decay rates to produce a positive muon in the forward and in backward region with respect to the di-muon flight direction, which is proportional to I_6,

$$A_{\mathrm{FB}} = \frac{\Gamma(\cos\theta_\mu > 0) - \Gamma(\cos\theta_\mu < 0)}{\Gamma(\cos\theta_\mu > 0) + \Gamma(\cos\theta_\mu < 0)} \propto \langle I_6 \rangle. \tag{1.65}$$

We can measure A_{FB} in bins of q^2, which correspond on the other hand to measure the average values of I_6 as a function of q^2. The average quantity $\langle I_6 \rangle(q^2)$ can be calculated as

$$\langle I_6 \rangle(q^2) = \frac{1}{\Gamma} \int_{4m_\pi^2}^{(m_D-q)^2} dp^2 \int_{-1}^{+1} d(\cos\theta_h)\, I_6(q^2, p^2, \theta_h), \tag{1.66}$$

and similar expressions can be written for the average values of the other coefficients [168]. In some BSM scenarios with the presence of primed operators $\mathcal{O}'_{9,10}$, the observable $\langle I_6 \rangle$ shows large enhancements, especially near the resonance peaks, as shown in Fig. 1.9. Such resonance enhancement effect is explained in more detail in case of *CP* asymmetry in the next section. Other two known asymmetries are $A_{2\phi}$ and A_ϕ, which are proportional to I_9 and I_7, respectively

$$A_{2\phi} = \frac{\Gamma(\sin 2\phi > 0) - \Gamma(\sin 2\phi < 0)}{\Gamma(\sin 2\phi > 0) + \Gamma(\sin 2\phi < 0)} \propto \langle I_9 \rangle, \tag{1.67}$$

$$A_{\phi} = \frac{\Gamma(\sin \phi > 0) - \Gamma(\sin \phi < 0)}{\Gamma(\sin \phi > 0) + \Gamma(\sin \phi < 0)} \propto \langle I_7 \rangle. \tag{1.68}$$

It is important to note that $\sin\phi$ is a triple-product observable and it is $\hat{T}$-odd, being $\hat{T}$ the operator which reverses momenta and spin three-vectors but does not interchange final states into initial states,

$$\sin\phi = (\vec{n}_{\mu\mu} \times \vec{n}_{hh}) \cdot \frac{\vec{p}_{hh}}{|\vec{p}_{hh}|},$$

where $\vec{n}_{\mu\mu}$ and $\vec{n}_{hh}$ are normal unit vectors to the decay planes defined by the di-muon and di-hadron systems respectively. Then $A_{2\phi}$ and A_ϕ can be defined as triple-product asymmetries of the daughter particles momenta. They can be used to search for *CP* violation in an independent and complementary way with respect to usual *CP* asymmetry. A collection of analysis that used triple-product asymmetries to search for *CP* violation can be found in [197–204]. However they are not clean observables since they are defined mixing D^0 and $\overline{D}^0$ and could be affected by phases introduced in final state interactions. Defining $A_{2\phi}$, A_ϕ for D^0 decays only and $\overline{A}_{2\phi}$, $\overline{A}_\phi$ for $\overline{D}^0$ decays, a *CP*-violating clean observable can be defined as

$$\mathbf{A}_{CP}^{\hat{T}\text{-odd}} = \frac{1}{2}(A_\phi - \overline{A}_\phi). \tag{1.69}$$

The advantage in using this observable is that no large strong phases are needed to produce a sizeable asymmetry, since the functional dependence on the strong phase difference is a cosine,

$$\mathbf{A}_{CP}^{\hat{T}\text{-odd}} \propto \sin(\Delta\varphi)\cos(\Delta\delta)$$

while $A_{\mathrm{CP}} \propto \sin(\Delta\varphi)\sin(\Delta\delta)$ where φ and δ are the weak and strong phases respectively.

1.7.3 *CP* asymmetry and the role of resonances

In addition to these angular asymmetries, the *CP* time integrated asymmetry can be also measured,

$$A_{CP} = \frac{\Gamma(D^0 \to f) - \Gamma(\overline{D}^0 \to f)}{\Gamma(D^0 \to f) + \Gamma(\overline{D}^0 \to f)}. \tag{1.70}$$

Thanks to the presence of LD contributions, in regions of the phase space near resonances, the interference term between LD *CP*-conserving amplitude and SD *CP*-violating amplitude can produce an enhancement of *CP* asymmetry, whose value and signature is highly strong-phase dependent. This effect is know in literature as *resonance-catalysed* CP asymmetry [169, 205]. A similar effect can happen between LD SM-dominated amplitudes and SD NP amplitudes, allowing enhancements of angular asymmetries due to NP in regions near resonances, as seen in the previous section and in Fig. 1.9. Considering for example the ϕ resonance, as done in [205] in the case of $D^+ \to \pi^+\ell^+\ell^-$, we can write the amplitudes as

$$\mathcal{A}(D^0 \to \pi^+\pi^-\mu^+\mu^-) = \mathcal{A}_{LD}^{\phi} + \mathcal{A}_{SD}^{CPV}, \tag{1.71}$$

$$\mathcal{A}(\overline{D}^0 \to \pi^+\pi^-\mu^+\mu^-) = \mathcal{A}_{LD}^{\phi} + \overline{\mathcal{A}}_{SD}^{CPV}, \tag{1.72}$$

and can be proven that the corresponding asymmetry is

$$A_{CP} \propto \left(\cos\delta_\phi - \frac{q^2 - m_\phi^2}{m_\phi \Gamma_\phi} \sin\delta_\phi \right), \tag{1.73}$$

where δ_ϕ is the strong phase on the ϕ peak and Γ_ϕ is the ϕ width. Hence, when considering both the A_{CP} behaviour and the differential branching fraction scaling around the ϕ peak, the best effective experimental sensitivity is close to the peak if $\delta_\phi \sim 0$, but is slightly off the peak in the case of $\delta_\phi \sim \pm\pi/2$, being the *CP* asymmetry an odd function with respect to the peak. For this reason a useful strategy is to divide the peak in two bins when performing the experimental search, in order to not blur the possible *CP* asymmetry.

The LHCb collaboration has measured the angular asymmetries, A_{FB}, $A_{2\phi}$ and the time-integrated *CP* asymmetry A_{CP} in $D^0 \to \pi^+\pi^-\mu^+\mu^-$ and $D^0 \to K^+K^-\mu^+\mu^-$ with data collected from 2011 to 2016, corresponding to a an integrated luminosity of $5\,\text{fb}^{-1}$ [206]. The asymmetries are also measured as a function of the di-muon invariant mass and are consistent with the SM predictions,

$$\begin{aligned}
A_{FB}(D^0 \to \pi^+\pi^-\mu^+\mu^-) &= (3.3 \pm 3.7 \pm 0.6)\%,\\
A_{2\phi}(D^0 \to \pi^+\pi^-\mu^+\mu^-) &= (-0.6 \pm 3.7 \pm 0.6)\%,\\
A_{CP}(D^0 \to \pi^+\pi^-\mu^+\mu^-) &= (4.9 \pm 3.8 \pm 0.7)\%,\\
A_{FB}(D^0 \to K^+K^-\mu^+\mu^-) &= (0 \pm 11 \pm 2)\%,\\
A_{2\phi}(D^0 \to K^+K^-\mu^+\mu^-) &= (9 \pm 11 \pm 1)\%,\\
A_{CP}(D^0 \to K^+K^-\mu^+\mu^-) &= (0 \pm 11 \pm 2)\%.
\end{aligned}$$

In this thesis the expected asymmetries in $D^0 \to \pi^+\pi^-\mu^+\mu^-$ and $D^0 \to K^+K^-\mu^+\mu^-$ decays with data collected from 2015 to 2018 will be discussed. Thanks to the excellent 2017-2018 LHCb data taking condition and with an optimised selection strategy the number of selected $D^0 \to h^+h^-\mu^+\mu^-$ is doubled with respect to the previous study, despite the integrated luminosity being similar and corresponding to $\sim 5\,\text{fb}^{-1}$. The observed statistics paves the way for a first full angular analysis in multi-body rare charm decays, whose feasibility is studied and described in this thesis.

Chapter 2

THE LHCb EXPERIMENT AND ITS UPGRADE

The Large Hadron Collider beauty (LHCb) experiment [207] at the European Organization for Nuclear Research (CERN), in Geneva, is one of the main experiments in the world studying flavour physics with high precision, exploiting proton-proton collisions from the Large Hadron Collider (LHC) [208]. LHCb was built specifically to study *CP* violation and rare decays of hadrons containing beauty quarks, with the aim of searching indirectly for BSM effects. The excellent characteristics in terms of trigger, vertex and momenta resolution and the high charm production cross section have also allowed the experiment to be a powerful charm factory and to perform world leading measurements within charm physics.

2.1 The Large Hadron Collider

LHC [208] is the largest particle accelerator in the world. The accelerator is located in a circular underground tunnel, which previously housed the LEP accelerator, with a length of approximately 27 km and at a depth that goes from 50 m to 175 m. LHC consists of superconducting magnets and accelerating structures driving two beams of high-energy particles, protons and heavy ions, and make them circulating in opposed directions inside two vacuum pipes. The particles are grouped together in *bunches*, with nominal energies of 7 TeV per proton, and collide at center of mass energy of 14 TeV. The bunches are spatially and temporally spaced by 25 ns, and at the various collision points they collide (*bunch crossing*) at a frequency of 40 MHz. The filling pattern of LHC with the proton bunches is not completely uniform, since it reflects the filling scheme of the previous acceleration stages and has to take into account some additional empty space, required for the beam dump. For this reason the actual collision frequency is approximately 30 MHz. The nominal instantaneous luminosity is $10^{34}\,\mathrm{cm}^{-2}\mathrm{s}^{-1}$.

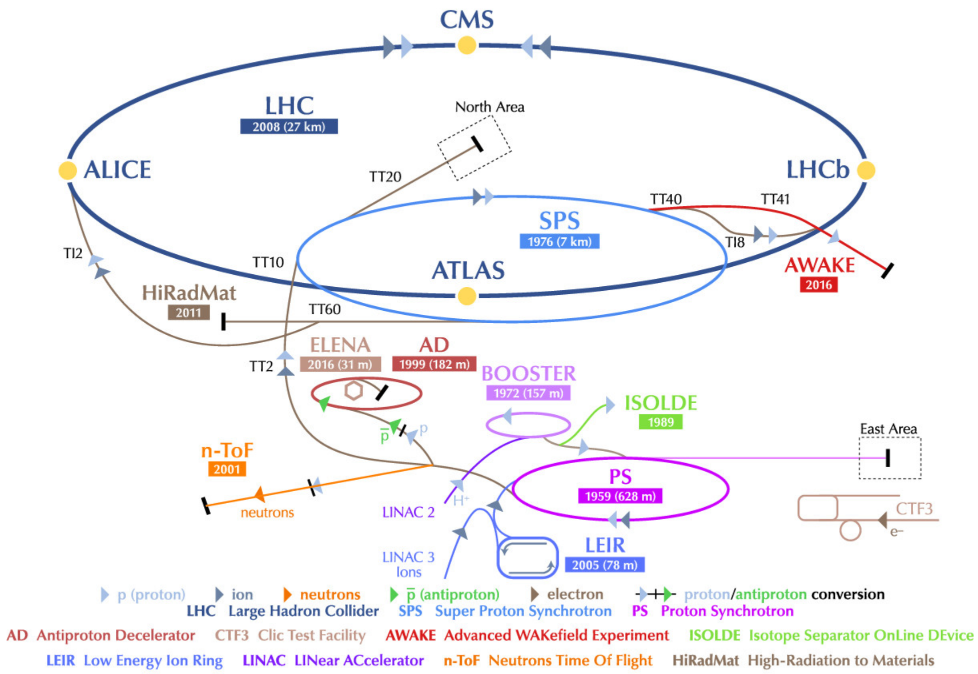

FIGURE 2.1. The CERN accelerator complex [209].

Superconducting magnets are kept at cryogenic temperatures of 1.7 K thanks to a cryogenic system using superfluid helium, in order to generate magnetic fields of the order of 8 T and thus be able to bend the beams. A system of multi-polar magnets is also present to focus the beams and properly drive them within the interaction areas, in which the two beams actually collide. In the LHC the beams are injected with an energy of 450 GeV, already accelerated through an acceleration chain, schematically illustrated in Fig. 2.1. The proton beam is initially accelerated up to an energy of 50 MeV by the linear accelerator LINAC2, and subsequently by a circular accelerator (called booster) up to an energy of 1.4 GeV. The protons are then injected into the Proton Synchroton (PS) where they reach an energy of 26 GeV and subsequently enter the Super Proton Synchroton (SPS), in which they are accelerated up to 450 GeV, ready to be finally injected into LHC to reach the final energies. Detectors and experiments are located around or near the interaction points. In particular the four main experiments are ATLAS, CMS, ALICE and LHCb. ATLAS and CMS experiments are focusing on direct search of NP, in particular searching for production of BSM particles, and study also the electroweak and Higgs sector of the SM. ALICE mainly investigates heavy ions physics and Quark Gluon Plasma. LHCb, as already mentioned, is dedicated to the heavy flavour physics and will be described in greater detail below. It acquires data at an instantaneous luminosity of $4 \cdot 10^{32}\,\mathrm{cm}^{-2}\mathrm{s}^{-1}$ because the hardware trigger efficiency is already saturated at this luminosity. Moreover, the lower luminosity means a lower maximum average number of interactions per bunch crossing, allowing a cleaner track and vertex reconstruction.

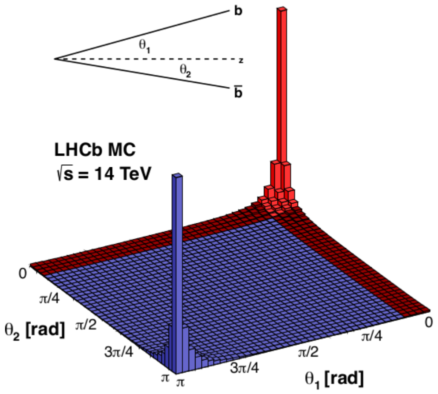

FIGURE 2.2. Simulation of polar angles distribution of the produced $b\bar{b}$ pairs at $\sqrt{s} = 14$ TeV. The LHCb acceptance is highlighted in red.

2.2 The LHCb detector

Thanks to the large production cross sections for $b\bar{b}$ and $c\bar{c}$ pairs, respectively of 72 (144) μb and 1.4 (2.6) mb at an energy of $\sqrt{s} = 7\,(13)$ TeV in the LHCb acceptance [210, 211], and the general excellent performance of the detector, LHCb has done precision tests on heavy flavour physics and continues to have a wide physics program based on *CP* violation, decay properties (amplitude and angular analysis) and search for NP in rare decays, both in beauty and charm.

The LHCb detector [207, 212] is a single-arm spectrometer, built in the forward region with respect to the proton-proton interactions. The forward geometry is optimised for heavy flavour physics, since hadrons containing heavy quarks are mainly produced, at high energies, in the forward or backward regions with respect to the collision point. In fact at high energy the $b\bar{b}$ pair production is dominated by gluon-gluon processes, since the gluon parton density functions are dominant. Since the two gluons predominantly carry different momenta, the resulting longitudinal momentum along the collision axis is dominant, and the corresponding $b\bar{b}$ pair is produced highly boosted along the beam direction, as shown in Fig. 2.2. The vertical section of the detector is shown in Fig. 2.3. The coordinate system of LHCb is right-handed: the z-axis is defined along the beam direction and points towards the muon chambers, while the y-axis is vertical and points upwards. The LHCb magnet produces a magnetic field that causes the charged particles to bend in the x-z plane (called bending plane), and not in the y-z plane (non-bending plane). The angular coverage ranges from 10 to 300 mrad in the bending plane and from 10 to 250 mrad in the non-bending plane, which is equivalent to a pseudorapidity coverage of $2 < \eta < 5$, where the pseudorapidity is defined as $\eta = -\ln(\tan(\theta/2))$, being θ is the angle with respect to the beam axis.

The instantaneous luminosity in a collider like LHC can be written in terms of the machine parameters as [213] $\mathcal{L} = N_p^2 n_b f / A_\perp^{\text{eff}}$, where N_p, n_b and f are respectively the number of protons

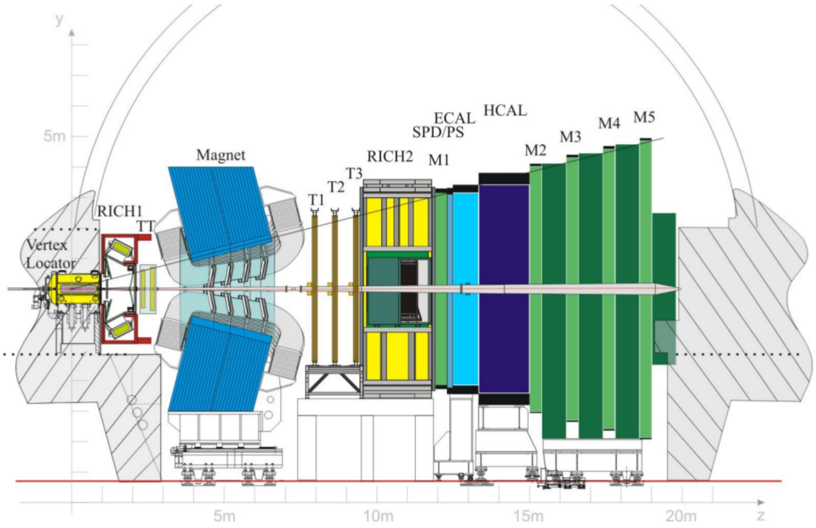

FIGURE 2.3. Scheme of the vertical section of the LHCb detector.

in a single bunch, the number of colliding bunches and the collision frequency, while $A_{\perp}^{\text{eff}}$ is the effective transverse colliding area, which can be estimated from the overlap of the beam spatial distributions. Since the number of protons decrease with time due to beam collisions and scattering within the beam pipe, the luminosity decreases itself with a lifetime of approximately $\mathcal{O}(10\ \text{h})$. As already anticipated, in the LHCb collision point the luminosity is continuously levelled and maintained at a lower constant value of $4.4 \cdot 10^{32}\,\text{cm}^{-2}\text{s}^{-1}$, tuning the transverse separation of the beams, thus constantly redefining the effective colliding area [214]. This choice allows LHCb to avoid as much as possible events with many Primary Vertices (PV), simplifying secondary vertices reconstruction due to the decay of heavy hadrons.

The PV is reconstructed by the VErtex LOcator (VELO) and the particles pass through the first Ring Imaging CHerenkov detector (RICH-1) and the first stage of the tracking stations, the Tracker Turicensis (TT). After these stations the particles pass through the magnet and, if charged, their trajectories are bended before reaching the second stage of the tracking system, the stations T1, T2, T3. Downstream there are other detectors composing the particle identification (PID) system: RICH-2, the electromagnetic (ECAL) and hadronic (HCAL) calorimeters, and the muon detector, composed of five muon stations, M1-M5. In the following the main and fundamental elements are briefly described.

2.2.1 Dipole Magnet

The magnet of LHCb [215] is a warm dipole magnet used, together with the tracking system, to measure the charged particles momenta through the measurements of the trajectories curvature. The opening angle is ±250 mrad vertically and ±300 mrad horizontally. The magnetic field is

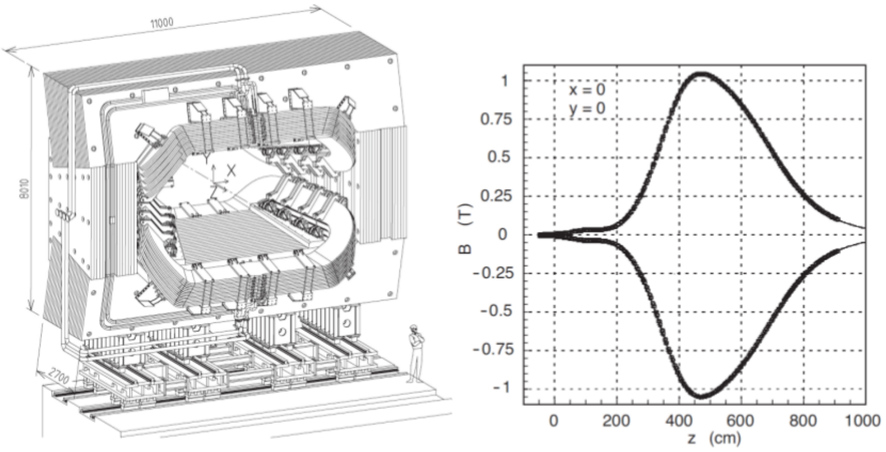

FIGURE 2.4. Drawing of the LHCb magnet (left) and the magnetic field along the z axis (right).

vertically oriented, and the particles trajectories are curved the horizontal plane. The magnet polarity is periodically reversed in order to control the systematic effects due to possible left-right asymmetry, as it is a crucial element for precision measurements of CP violation. The two conditions are named *MagUp* and *MagDown*. The magnet is made of 50 tons of pure conductor Al-99.7 cables, forming two trapezoidal coils, bent at 45 degrees with respect to the horizontal plane, and symmetrically arranged with respect to each other. The coils are included in a yoke to get the return flow of the field, consisting of steel plates. The nominal current is 5.85 kA and its own total resistance is 130 $m\Omega$ (at 20° C). The maximum value of the field is 1.1 T and an integrated value of 4 Tm, measured with an accuracy of $4 \cdot 10^{-4}$, and a non-uniformity of the order of 1%. The region subject to the field ranges approximately from $z = 2.5$m to $z = 7.95$m.

2.2.2 Tracking system

The tracking system, as already mentioned, is one of the most important and crucial detector system. It consists of the vertex detector (VELO), and four tracking stations: the Tracker Turicensis (TT) and the T1-T3 stations. The purpose of the tracking system is to provide information on the passage of the charged particles, in order to reconstruct the trajectories and estimate the momenta.

2.2.2.1 VELO

The Vertex Locator (VELO) [216] is placed around the interaction point of the two proton beams. The PV and the displaced Secondary Vertices (SV), due to decays of hadrons containing b and c quarks, are reconstructed from the coordinates of the hits in the detector, thus allowing the determination of flight distances, lifetimes and impact parameters. The detector consists of two identical halves placed around the beam, that can move in a radial direction with respect to it, along the y-z plane. In particular, if LHC is not in a stable beam condition, the halves are separated by 6 cm, while during collisions they are closed together, with a small overlap to maintain alignment and full acceptance coverage, as shown in Fig. 2.5. The position is then optimised for each LHC fill. Each half consists of 21 stations, each one formed by a pair of semi-circular silicon modules mounted back-to-back. In particular one type of module is composed of circular strips (Φ sensors) and the other one of radial strips (R sensors), so that their combination provides the coordinates r and ϕ of the point where the particle hits the station, while the third coordinate is derived from the station position along the line. The sensors are mounted on a support and contained in a vacuum vessel, which maintains the vacuum inside (about 10^{-4} mbar), providing also a separation from the Ultra High Vacuum of LHC (10^{-8} mbar), through a 0.3 mm thick layer of aluminium, the so-called RF foil, which faces the beam. The sensors and the readout electronics must operate at low temperatures and must also be radiation tolerant, since they operate at approximately 8 mm from the beam axis. Additional modules are installed upstream and constitute the pile-up veto system, used to measure the backward track multiplicity and to detect events with multiple primary interactions. Approximately the pitch varies from $40\,\mu$m to $100\,\mu$m for the two type of sensors, with the finer granularity close to the beam. The acceptance is the typical one of detectors placed before the magnet: particles coming from the primary vertex are detected in the interval $|z| < 10.6\,$cm, with pseudorapidity between 1.6 and 4.9, with at least three stations crossed by a particle within the angular coverage. Tracks reconstructed in the VELO are used to determine the PV, with a resolution of 13 μm in the transversal (x and y) direction and 71 μm in the longitudinal (z) direction, that degrades to $\sim$150 μm for secondary vertices, due to the smaller number of tracks. The impact parameter, i.e. the distance between the track's point of closest approach to the PV and the PV itself, is measured with a resolution of 44 μm in the transversal direction for particles with transverse momentum of 1 GeV, that reduces to 15 μm for larger transverse momentum [217].

2.2.2.2 Tracking stations

The tracking system consists of the TT, located between the RICH-1 and the magnet, and the T1-T3 stations beyond the magnet. The TT has an active area of 8.4m^2 and covers the entire acceptance of LHCb. It provides information for the reconstruction of low momentum tracks, which do not reach the other stations due to the deviation induced by the magnetic field, and to provides also information on the transverse momentum for tracks with a high impact parameter. Stations T1-T3 measure the x coordinate along the curvature plane, and two stereo coordinates, rotated with respect to the first of an angle of $\theta = \pm 5°$, so as to have information along the y direction. Since the density of tracks scales with the inverse of the square of the beam axis

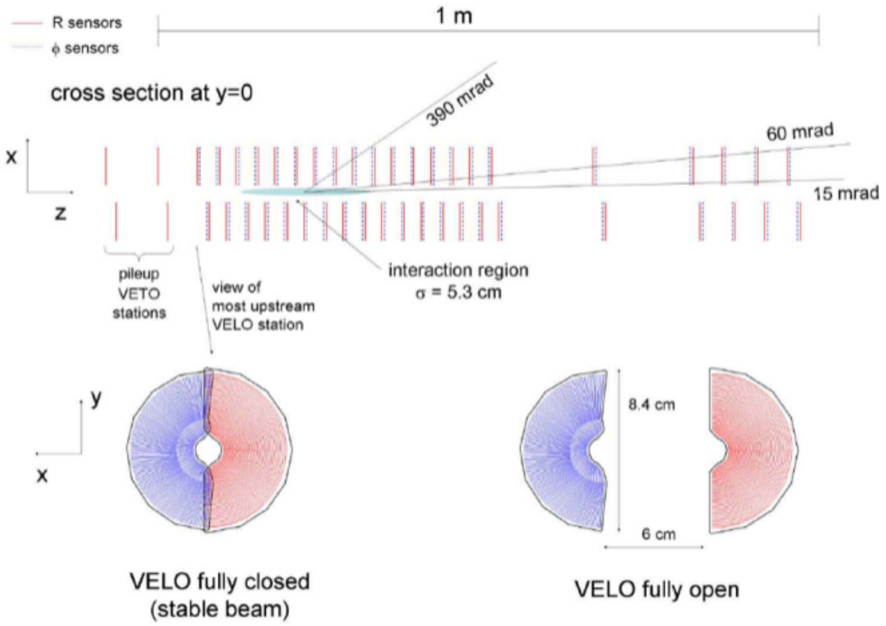

FIGURE 2.5. Scheme of the VELO layout, with R sensors in blue and Φ sensors in red. A representation of the two conditions of VELO fully closed and fully open is also shown (bottom).

distance, the tracking system is divided in several parts.

Silicon Tracker The Silicon Tracker (ST) [218] is composed of the TT station and the inner part of the T1-T3 stations, called Inner Tracker (IT), as shown in Fig. 2.7. It is made of silicon microstrips sensors, with a strip pitch of about 200 μm, providing a hit resolution of 50 μm and a fast time response. Each station is composed of four detection layers with a particular arrangement called x-u-v-x, as shown in Fig. 2.6. In the first and last layers the strips are vertical, while in the second and third layers (the u and v) the strips are rotated by a stereo angle by $-5°$ and $+5°$ respectively. This layout allows to get the best hit resolution and the reconstruction of all the three spatial coordinates without ambiguities.

- **Tracker Turicensis**: the TT is located upstream of the magnet and its size is 150 cm wide and 130 cm high. There are two type of detector modules where the sensor are split in two or three readout sections, which are then connected to a different number of sensor according to the granularity. Indeed in the region close to the beam pipe the granularity is higher. The main aim is to reconstruct decay products of long lived particles like K^0_S and Λ and of low momentum tracks which can go out of the acceptance due to the curvature by the magnetic field.

- **Inner Tracker**: the IT is located downstream of the magnet, covering the inner region

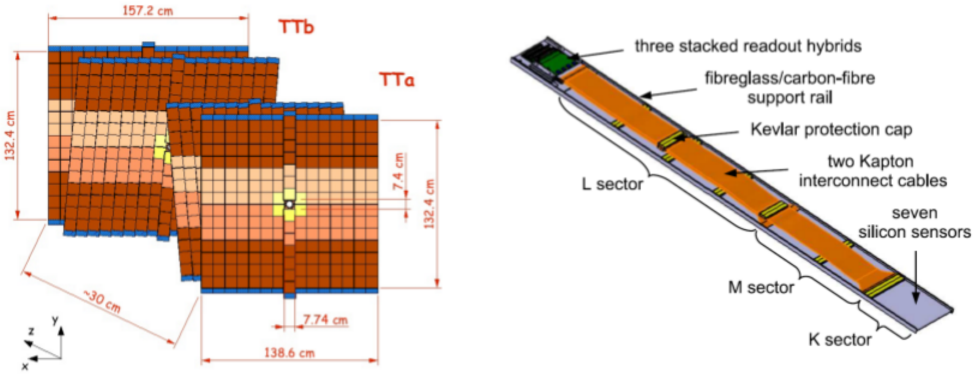

FIGURE 2.6. Left: view of the TT detector with the readout electronics in blue and the other readout sectors. Right: View of the TT module with three readout sections.

of the T1-T3 stations, where the occupancy is higher ($5 \cdot 10^5$ cm^{-2} s^{-1}) and an higher resolution is required. The size is 120 cm wide and 40 cm high. Each station is composed of four detector boxes surrounding the beam pipe, each one containing four layers of detectors in the x-u-v-x arrangement. About 20% of all produced charged tracks traversing the tracking system pass through this region.

Outer Tracker The Outer Tracker (OT) [219] covers the remaining outer regions of the T1-T3 stations. It is a drift chamber detector, designed as an array of gas-tight straw tube modules. Each stations is composed of four modules in the x-u-v-x configuration, and each module contains two monolayers of drift tubes, vertically oriented, with diameters of 5 mm and filled with a gas mixture of CO_2 (~30%) and Ar (~70%). A 25 μm thick anode wire is located at the centre of each straw, as shown in Fig. 2.7. The drift time across the tube is less than 50 ns and the spatial resolution is about 200 μm.

2.2.3 Particle Identification system

In the study of rare decays, since many decay modes have the same multiplicity and topology, possible contamination due to particle misidentification can be not negligible and can be even the dominant contributions with respect to other sources of background. For this reason Particle identification (PID) is an extremely important requirement in LHCb. The charged particles (e, μ, π, K, p) are identified by combining information from the two RICH detectors, from calorimeters and from the muon detector system.

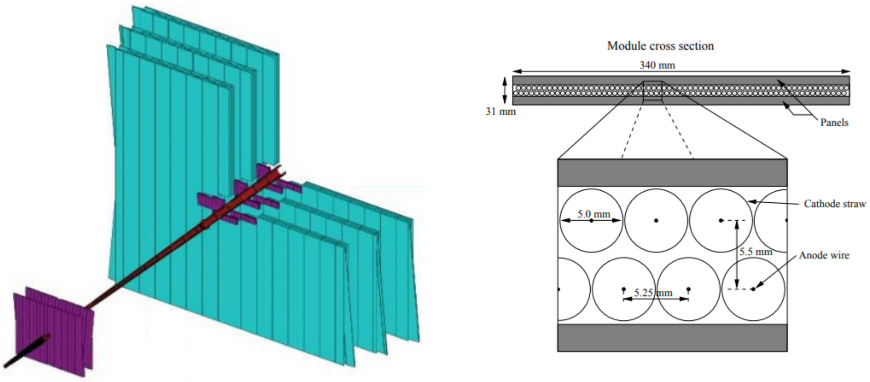

FIGURE 2.7. Left: scheme of the tracking system, with the OT (light blue), the beam pipe (brown) and the ST (violet). Right: section of a straw-tube in an OT module.

2.2.3.1 Ring Imaging Cherenkov detectors (RICH)

Two RICH detectors [220] are present in LHCb with the main purpose to separate kaons, pions and protons. A charged particle passing through a medium, called *radiator* in this case, faster than the speed of light in the medium, produces a cone of Cherenkov light whose opening angle θ_c depends on the medium refractive index, n, and the velocity v of the particle, as $\cos\theta_c = 1/(\beta n)$, where $\beta = v/c$. Combining this information with the momentum p, provided by the tracking system, it is possible to deduce the mass of the particle,

$$\cos\theta_c = \frac{1}{n}\sqrt{1+\left(\frac{mc}{p}\right)^2}.$$

The separation is shown in Fig. 2.9 (left). The photons in the visible spectrum (200-600 nm) emitted through the RICH radiator are reflected outside the detector acceptance by a combination of spherical and flat mirrors, and are finally detected by a matrix of $5 \cdot 10^5$ channels of segmented Hybrid Photon Detectors (HPDs), suitably shielded from the magnetic field. Due to the strong correlation between the polar angle of the particles and their momentum, the RICH consists of two detectors, to cover different regions of the polar angle, thus different momentum ranges. The combination of the two RICH detectors, shown schematically in Fig. 2.8, covers the entire range of momenta of the B and D meson decay products. Three different radiator media are used for this purpose.

- RICH-1: located upstream of the magnet and downstream of the VELO, uses as radiator C_4F_{10} gas ($n = 1.0014$) for intermediate momentum, covering the whole range of $1-60\,\text{GeV}/c$. It has an angular acceptance from ±25 mrad to ±300 mrad horizontally, and ±250 mrad vertically.

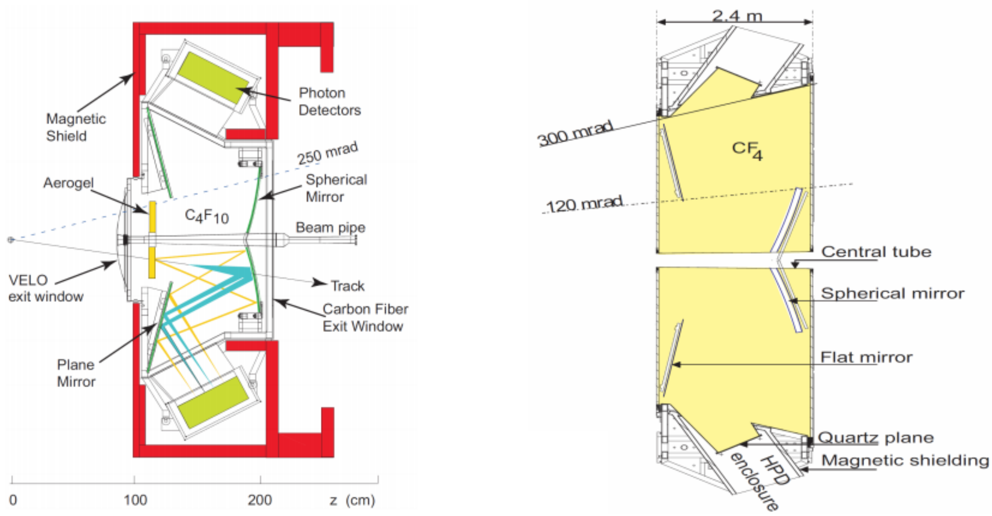

FIGURE 2.8. Schematic side view of the RICH-1 (left) and RICH-2 (right) detectors.

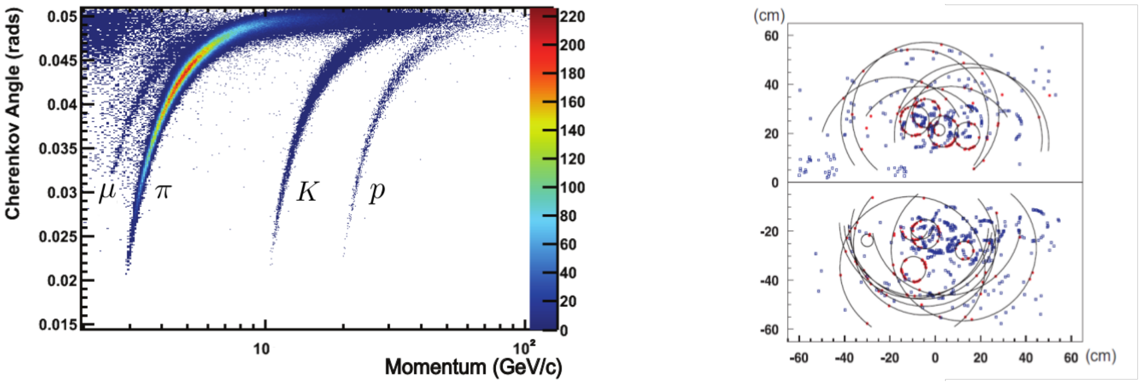

FIGURE 2.9. Left: Cherenkov angle versus particle momentum [221]. Right: a typical LHCb event in RICH-1 with Cherenkov rings interpolation.

- RICH-2: placed downstream of the magnet, uses as radiator CF_4 ($n = 1.0005$) for larger momentum, from 10 GeV/c to 100 GeV/c. The angular acceptance is smaller with respect to RICH-1, and goes from ±15 mrad to ±120 mrad horizontally, and ±100 mrad vertically.

2.2.3.2 Calorimeter system

The calorimeter system [222], located downstream of RICH-2, allows to identify electrons, photons and hadrons, and to measure their position, momentum and transverse energy. A particle passing through the calorimeters produces a shower, composed of charged and neutral particles that release their energy inside the system, in the absorbers or in the active materials. The overall quantity of light produced in the scintillation materials depends on the total energy released. The entire system consists of four sub-systems: a Scintillator Pad Detector (SPD), a PreShower detector (PS), which are separated by a lead converter, an electromagnetic calorimeter (ECAL) and an hadron calorimeter (HCAL). The four sub-systems consist of sampling devices with scintillating material, interspersed with absorber materials. The scintillation light is transmitted to the photomultipliers (PMT) through to WaveLength-Shifting (WLS) fibres. SPD and PS consist of a matrix of cells, which are composed of a 15 mm thick scintillators and a 12 mm-thick layer of lead. The SPD purpose is to identify charged tracks, while the PS discriminates photons and pions from electrons, in a fast way to use the information at hardware trigger level. The electromagnetic calorimeter (ECAL) is composes of shashlik cells, which consists of 66 alternating layers of 2 mm thick lead and 4 mm thick scintillator. It detects electrons and photons by measuring the electromagnetic showers caused by e^+e^- and γ. The sampling fraction of the ECAL cells and the high granularity allow to obtain a resolution of

$$\frac{\sigma(E)}{E} = \frac{9\%}{\sqrt{E}} \oplus 0.8\%,$$

where E is expressed in GeV. The first term is due to the statistical uncertainty on the energy deposit, while the second is a constant contribution. The hadronic calorimeter (HCAL) is a sampling calorimeter, with a non-standard structure, since the scintillating tiles are arranged parallel to the beam pipe. It is composed of 16 mm thick iron tiles and 4 mm thick of scintillator layers, for a total extension along z of 1.6 m. The resolution in energy is

$$\frac{\sigma(E)}{E} = \frac{69\%}{\sqrt{E}} \oplus 9\%,$$

with E expressed in GeV. The aforementioned structure of the calorimeter system allows to perform a separation between electrons, photons and hadrons as shown in Fig. 2.10. In particular:

- photons do not leave hits in the SPD station, but interact with the lead converter, creating an electromagnetic shower in the PS and ECAL;
- electrons have the same behaviour as the photons at the PS and ECAL level, but also leave hits in the SPD detector;
- hadrons are typically Minimum Ionising Particles (MIPs) in the SPD, PS, and in the ECAL (in the latter the energy deposit can be very variable). Basically all the energy is released in the HCAL.

2.2.3.3 Muon system

In many relevant decay channels within LHCb physics program there are muons in the final state. For this reason the performance of the muon detector is of crucial importance. Moreover,

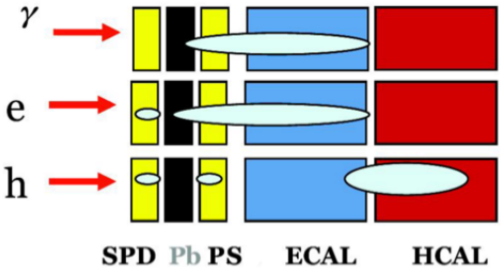

Figure 2.10. Schematic representation of the separation between photons, electrons and hadrons within the calorimeter system.

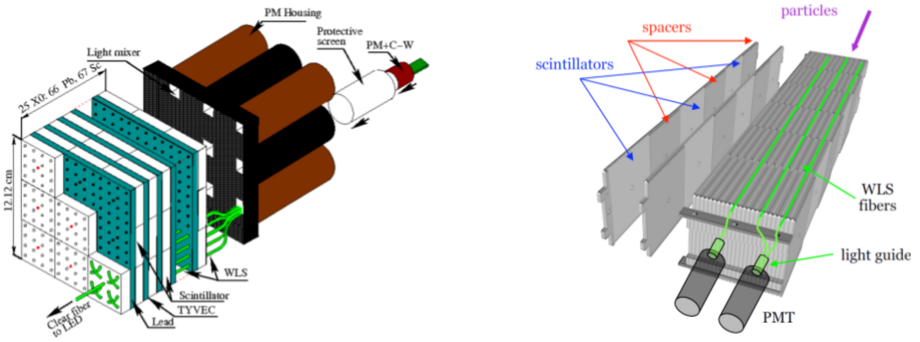

Figure 2.11. Illustrations of the ECAL cell (left) and HCAL cell (right) structures.

since the decays studied in this thesis have muons in the final states we will focus with more attention on this detector.

The muon detector [223–225] is placed downstream of the calorimeters, since the muons are the only charged particles that can pass through the calorimeters as minimum ionizing particles with a low energy loss. It is possible to detect muons with an efficiency greater than 95%, at a frequency of 10 MHz at the nominal luminosity of LHCb. This allows to use the information also for the hardware level trigger for muons with a p_T above a given threshold, as well as to separate muons from hadrons in the High Level Trigger. In particular, this property is very important for rare decays with muons in the final state, since purely hadronic decays with the same multiplicity and topology can happen at least 10^4 times more often than the rare decay considered.

Muon system layout

The detector consists of five rectangular stations, called M1-M5. The M1 station is located between RICH2 and the SPD calorimeter, while the M2-M5 chambers are located downstream of the hadronic calorimeter. Starting from M2, the stations are interspersed with iron absorbers 70 cm thick, to absorb particles other than muons. The stations are characterised by a projective

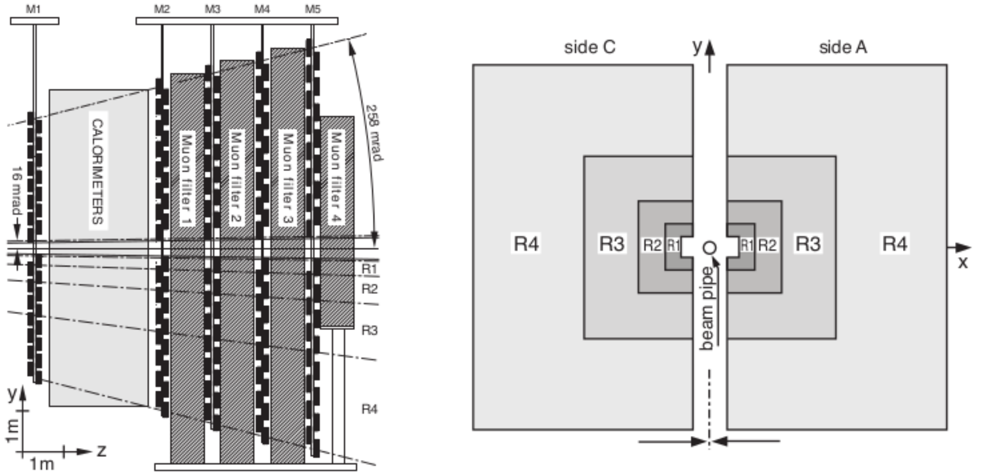

FIGURE 2.12. Side (left) and front (right) view of the LHCb Muon System. The R1-R4 projective scaling is also represented.

geometry, i.e. the transverse area increases along z in order to maintain the same angular acceptance. The last station, M5, has a dimension approximately of $10 \times 9\text{m}^2$. Each station is divided in four regions, called R1-R4, where R1 is the innermost, with dimensions that increase as the distance from the beam axis increases, with the ratios 1:4:16:64, as shown in Fig. 2.12. The whole detector is composed of 1380 chambers, 1368 Multi-Wire Proportional Chambers (MWPCs) and 12 triple GEM detectors (Gas Electron Multiplier). In particular each station is equipped with 276 MWPCs: 12, 24, 48 and 192 in R1, R2, R3 and R4 respectively, with the exception of the M1R1 region, which uses 12 GEMs, since they allow an higher granularity and a better responses for high particles occupancy, which in this region is about 500 kHz/cm^2.

Muon chambers internal structure

Due to the different geometries, resolutions and rate capability requirements, there are 20 types of chambers, with different size, segmentation and readout granularity. Nevertheless the internal geometry is practically the same for all MWPCs. In stations M2-M5 the chambers are equipped with four gas gaps 5 mm thick, in which the different gold-plated tungsten wires, with a diameter of 30 μm each, are placed with a spacing of 2 mm to form an anode plane, and kept at high voltage of about 2.6-2.7 kV. Each gap has its independent high voltage line. The cathode are instead made of FR4 fiberglass plates, equipped with a two-sided 35 μm thick copper coating. The various gaps are then put together, separated by polyurethane panels, and connected in order that the gas can flow in each gap with a single input and output line per chamber. The non-flammable gas used is a mixture of Ar/CO$_2$/CF$_4$ in the ratio 40/55/5. Two adjacent gaps define a readout independent layer, putting the two gaps in OR, and has an efficiency of 95% in a 20 ns window at a gas gain of $G \sim 10^5$. A four gaps chamber consists then of two layers with

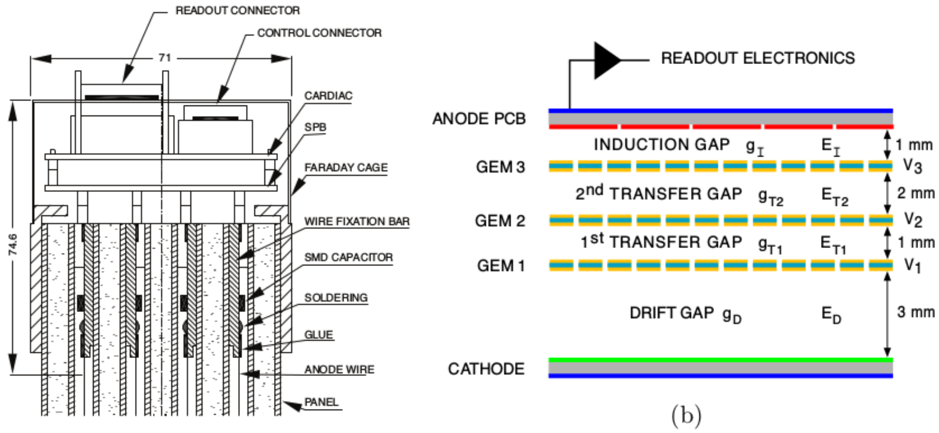

(b)

FIGURE 2.13. Left: schematic representation of a section of a four gap MWPC. Right: schematic drawing of the triple-GEM detectors, with the GEM foils, gas gaps and their corresponding dimensions.

independent readout. In station M1 the chambers are equipped with two gas gaps only, with an overall number of gaps of 4944 for the whole muon system. The structure of MWPCs is shown in Fig. 2.13 (left). More details on the principles of gaseous detectors can be found in [226].

Triple-GEM detectors [227, 228] were chosen for the innermost region, M1R1, to sustain the high rate, in terms of efficiency and radiation hardness. LHCb GEM chambers have an active area of 20×24 cm^2 each, and the following internal structure: a gas gap about 7 mm thick, contains an anode and a cathode plane and in the intermediate space three GEM foils are placed, with different spacing of the order of 1 or few millimetres. A single GEM consists of a 50 μm Kapton foil coated on each side by a thin (5 μm thick) layer of copper, and perforated with an high density of bi-conical holes, with an external (internal) diameter of 70 μm (50 μm) and a pitch of 140 μm. Applying a voltage of 350-500 V on each side provides an electric field into the holes as high as 100 kV/cm. The ionisation electrons, produced by the passage of a muon inside the gap, drift towards the GEM foils and are subject to an avalanche multiplication when traversing the holes, inducing a signal on the anode. Tests on prototypes have shown that the gas mixture Ar/CO$_2$/CF$_4$ in the ratio 45/15/40 allows to achieve a time resolution better than 3 ns and an efficiency above 96% in a 20 ns time window at a gain of $\sim 6 \cdot 10^3$. In LHCb two triple-GEM detectors are superimposed and their readout pads logically OR-ed. The structure of triple-GEM detectors is shown in Fig. 2.13 (right).

Muon chambers readout

The granularity of the detector, which defines the x and y coordinates to be used for the reconstruction, is determined by rectangular *logical pads*, which are made up by the readout electronics as explained in the following. The chambers are divided into *physical channels* (or

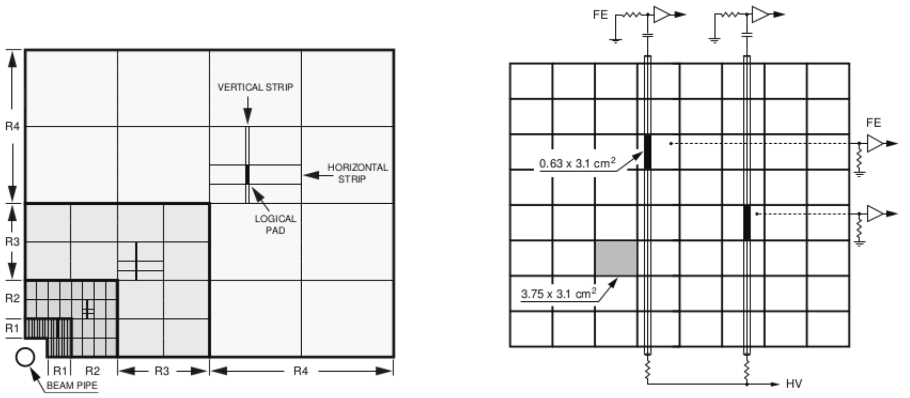

FIGURE 2.14. Left: front view of one top quadrant of stations M2-M3 showing the x and y logical strips per region, and the corresponding sectors. Right: example of mixed readout adopted in R1-R2 regions of M2-M3, in particular the case M2R1 is shown here. The logical pad (in black) is obtained by the coincidence between crossing vertical wire pads and cathode pads.

physical pads), whose size is constrained by construction reasons, and especially by specific electronics requirements, like the dead time and the noise acceptable levels on front-end electronics, linked to the rate on the pad and the electrical capacitance. For these reasons different readout solutions are adopted, with a physical granularity finer with respect to the required spatial resolution: in outer regions large wire pads are used, while in inner regions, like R1-R2 of M2, a mixed solution for the readout pad is used, shown in Fig. 2.14 (right), obtained by crossing cathode pads with narrow wire strips; in all the other internal regions small cathode pads are used. GEM chambers use anode pads only. Appropriate combinations of physical channels are used to form a total of 55296 rectangular *logical pads*. The segmentation of the logical pads in the R1-R4 regions scales with the ratio 1:2:4:8. Since the magnetic field curves the trajectories of the particles horizontally, the pads have a finer segmentation in the horizontal direction x, rather than in the vertical direction y, in order to provide a good estimate of the impulse at the first trigger level. The granularity in M4-M5 is coarser since the main purpose is to identify the most penetrating particles. In station M1, that experiences the largest occupancy, the logical pads are not further processed, but in the other regions several contiguous logical pads are further put in OR at readout electronics level, in order to build larger x and y logical *strips*, named *logical channels*. The logical pad can be then reconstructed by the crossing of the x-y strips. The length of x and y strips defines a rectangular *sector* that is used by the trigger, as can be shown in Fig. 2.14 (left). Although this strategy helps to highly reduce the bandwidth, the disadvantage is that if n muons cross the same sector, an order $\mathscr{O}(n^2)$ of ambiguities arise when reconstructing the logical pads from the crossing strips, an effect that produce the so-called muon *ghost tracks* in LHCb.

Muon readout electronics

The readout electronics can be divided in two main categories, according to the position of the boards: the front-end electronics, mounted directly on the chambers and hence required to be highly radiation tolerant, and the off-detector electronics, mounted on racks close to the stations but already outside the acceptance. The main purpose of the electronics is to readout the signal from the chambers, perform the appropriate transformations (shaping, discrimination, etc.), send the information to the Level-0 trigger and wait for its response and finally send the formatted data to the DAQ system. An important part of the electronics is used to control, configure and monitor both the front-end and the off-detector boards. All these steps are described in the following and are also schematically represented in Fig. 2.15.

- The Front-End Boards (FEB), called CARDIAC boards, are mounted directly on the external part of the muon chambers, shielded by a Faraday cage, and are equipped with with two CARIOCA chips and one DIALOG chip. The CARIOCA is an amplifier-shaper-discrimination (ASD) chip with 8 channels, equipped with a pre-amplifier that can handle the large variety of of detector input capacitance (20-220 pF) and the discrimination threshold can be set for each channel. The outputs of two CARIOCAs are received by the DIALOG, which performs the logical OR to build up the logical pad. The DIALOG can adjust the delays of its input thanks to a 4-bit TDC reaching a time alignement within 1.6 ns. Moreover it can set the CARIOCA channels thresholds, if requested by the Service Boards, described later. For the GEM a different version of the ASD chip, called CARIOCAGEM, on the CARDIACGEM, has been developed, to have a lower threshold and a longer shaping time. When the trigger sector spans more than one FEB, a special board called Intermediate Board (IB) has been developed with the aim to perform the OR of the physical channels. This happens in M2-M5, in all regions except R1.

- The signals processed by FEBs are then sent to 152 Off Detector Electronics (ODE) boards, housed in the same crates of the IBs. Each ODE has 192 logical channels as input which are processed by 24 SYNC chips. The SYNC chip is a digital chip which has 8 input channels, and is equipped with a 8 independent TDC used to measure the time phase of the arriving signals with respect to the corresponding bunch crossing period. All the SYNC mounted on the ODE use the same master clock, synchronous with LHCb clock, and provided by the Timing and Fast Control (TFC) system through the TTCrx interface. The signal within the SYNC can be then tagged with the corresponding bunch crossing identification number. The resulting information is sent to the Level-0 trigger every 25 ns and temporary stored in the L0 buffer for 4 μs waiting the L0 decision unit response. If positive, the formatted data are written in a FIFO for a final de-randomisation, to achieve a regular rate of 1.1 MHz, and are then sent to the muon DAQ boards, called TELL1, to proceed the acquisition.

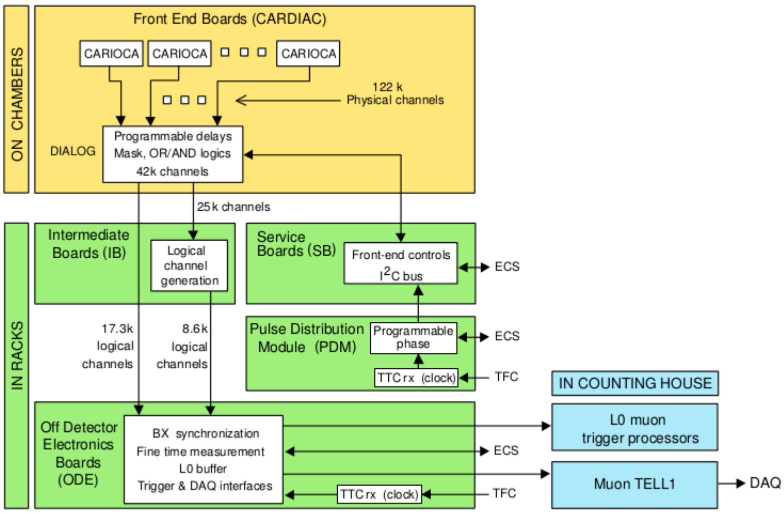

FIGURE 2.15. Scheme of the readout and control electronics chain of the LHCb Muon System.

- Both FEBs and ODEs can be monitored, controlled and configured through a control path, which consists of Service Boards (SB) and Pulse Distribution Module (PDM). The SBs are equipped with Embedded Local Monitoring Boards (ELMBs) based on 8-bit microcontrollers, that can be instructed to perform the communication with FEBs and ODEs through the I^2C protocol. There are a total of 156 SBs, housed in ten crates. Each crate contains a single PDM, used to generate low time-jitter pulses synchronous with the LHCb clock to perform the time alignment of the muon system.

2.2.4 Trigger and data processing algorithms

The purpose of the trigger is to select events of interest and keep a low rate of events to be saved, compatibly with the bandwidth and storage capacity. The actual bunch crossing rate of approximately 30 MHz does not allow to record all the events, therefore the trigger must be able to take a decision as fast as possible whether an event has to be rejected or not, maintaining high efficiency on interesting events for physics analyses and with a sufficient flexibility, in order to change easily the trigger parameters and configurations. The output rates of the different trigger stages varied a lot during the data taking period. At nominal luminosity the rate of visible interactions varied from 15 to 30 MHz (i.e. interactions with at least two produced charged particles reconstructible from the VELO and T1-T3 stations), while only a rate of 5-12 KHz of data can be saved to disk for offline analyses [229, 230]. In LHCb the trigger system [231, 232] is composed of two main levels: an hardware trigger, called Level-0 (L0) and a software trigger, called High Level Trigger (HLT). A precise trigger configuration, both hardware and software, is uniquely identified by a 32-bit hexadecimal code called TCK (Trigger Configuration Key).

2.2.4.1 Level-0 trigger

The L0 trigger is a hardware trigger based on the custom front-end electronics that operates synchronously with the bunch crossing at 40 MHz, reducing the event rate to 1 MHz. The trigger uses general event feature to perform the selection: in most of the B and D decays of interest the secondary particles are produced with large transverse momentum and transverse energy, information that is reconstructible from calorimeters and muon stations, while the VELO pile-up system provides an estimation of the number of primary interactions. The overall multiplicity of the events can be estimated by the number of hits in the SPD, which is required typically to be smaller than $\sim \mathscr{O}(500)$. In order to take into account this information and process them, the trigger is divided in three independent partitions, connected to the respective detector systems: L0 pile-up, L0 calorimeter and L0 muon. The final decision is the OR of the three independent decisions.

L0 calorimeter trigger

The L0 calorimeter uses the transverse energy in 2×2 cell blocks in ECAL and HCAL, defined as $E_T = \sum_{c=1}^{4} E_c \sin\theta_c$, where c is the cell index, E_c the deposit in each cell and θ_c the angle between the z axis and the line joining the cell to the nominal detector interaction region. According to this information and the one coming from PS and SPD the trigger performs the further decision and can flag the objects as "photon", "hadron" or "electron":

- Photon trigger (`L0Photon`): defined as the candidate with the highest ECAL only, E_T^{ECAL}, with also corresponding PS hits in front of the cluster and no hits in the aligned SPD cells. A typical threshold is $E_T > 2.7\,\text{GeV}$.
- Hadron trigger (`L0Hadron`): defined as the candidate with the highest E_T^{HCAL}. If there is an aligned cluster with the highest E_T^{ECAL} in ECAL the two values are summed. A typical threshold is $E_T > 4\,\text{GeV}$.
- Electron trigger (`L0Electron`): similar to `L0Photon` but with the additional requirement of at least one hit in the aligned SPD cells.

It is important to remark that the L0 thresholds varied a lot during the running period, following the evolving filling scheme of the LHC machine.

L0 Muon trigger

The muon trigger searches instead for muon candidates with transverse momentum greater than a given threshold, using the information of all the five muon stations. The search algorithm starts from the logical pads fired in M3, which define the starting points to search for other hits in the adjacent stations within a predefined Field of Interest (FoI). The muon system is segmented in 192 *towers* in which the processing unit searches for the tracks in parallel. The calculated p_T, with a resolution of 20%, is the used to take the final decision:

- Muon trigger (`L0Muon`): the candidate with a p_T greater than a given value, typically about $2.5 - 3\,\text{GeV}/c$.

- Di-Muon trigger (`L0DiMuon`): the square root of the product of the two largest p_T has to be greater than a given value, typically about $1.5\,\text{GeV}/c$.

2.2.4.2 High Level Trigger

Events passing L0 trigger lines are processed by the HLT. This is an entirely software trigger that works asynchronously with bunch crossing, on a platform network-based called Event Filter Farm (EFF), which consist of about 1800 nodes, each consisting of 24-32 logical processor cores, and an overall disk space of 10 PB. It is divided into two levels, called HLT1 and HLT2.

HLT1

This level carries out a partial event reconstruction, reducing the rate from 1 MHz to about 30 kHz, in particular selecting events with displaced vertices or with charged particles or photons with high p_T or E_T respectively. The event is processed on different HLT1 trigger selection lines, i.e. a series of parallel selection algorithms. Since the VELO reconstruction is fast but the full reconstruction for many tracks will take too much time the HLT1 reconstruction is practically divided in two steps. After the L0 confirmation, in the first stage VELO tracks [233] and PV are reconstructed, and information from the VELO are matched with that of tracking stations, allowing a refinement of the measurement of the transverse momentum p_T with respect to the L0 trigger and an estimation of the particle charge. The tracks are then fitted with a bi-directional Kalman filter [234] in order to account for effects like multiple scattering and ionisation energy loss, further refining the tracks parameters. In this way also the impact parameter of the tracks with respect to the PV can be determined, as well as secondary vertices positions, invariant masses and the flight directions, values that can be used to perform a first physics selection. Having a richer set of parameters with respect to L0, simple multivariate classifiers can be used to get a further improved selection performance with respect to simple cuts, in particular to select one and two tracks combinations (topological triggers) [235] with an associated good quality vertex. For muons, a quick identification is performed by comparing the VELO and T-station tracks with muon chamber hits. This information is used to apply cuts on the momentum, transverse momentum and the Impact Parameter χ^2, which is the difference in the χ^2 between a PV fit with and without the considered track. If the event is selected by at least one HLT1 line, it can be further processed by the second level, HLT2.

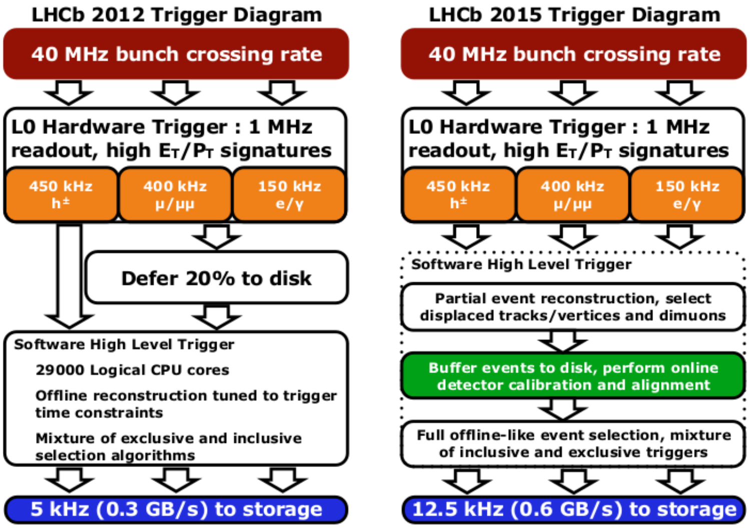

FIGURE 2.16. The LHCb trigger schemes for Run I (left) and Run II (right).

HLT2

The HLT1 output rate is low enough to perform a complete reconstruction of the event, including also information from RICH and calorimeters. This is performed by the HLT2 trigger level. It is composed of a series of selection algorithms (lines) that are applied in parallel to the events, similarly to the HLT1 case. The lines can be divided in two main categories: the inclusive topological lines, in order to select also partially reconstructed decays, and exclusive lines that select specific final states. The output rate is further reduced to 5-12.5 kHz, at which data are written to disk. In 2012 a configuration called "deferred HLT2" [236] has been used, in which 20% of the events accepted by the L0 trigger were temporarily saved in the local unused EFF disks, and processed subsequently during the LHC beam filling periods. This allowed a tracks reconstruction with less stringent selections, allowing also an improvement in the selection performance for rare decays. During Run II the increasing in luminosity and the consequently increased multiplicity leads to a more stringent selections. In this case all the events before HLT2 reconstruction are buffered to disk, while a precise real time alignment and calibration of the detector has been implemented between HLT1 and HLT2 [237]. The comparison of the HLT processing flow between 2012 and Run II is shown in Fig. 2.16.

2.2.4.3 Computing framework and Data processing

The different applications of LHCb for data reconstruction and analysis are designed on a common framework, called GAUDI [238]. The main purpose of this framework, based on C++, is to define a set of common interfaces for the various applications, keeping them decoupled from each other. Some of the most important applications are listed below:

- BRUNEL [239]: is the application for the offline tracks and full event reconstruction, starting from the tracks system hits and using information from RICH, calorimeters and the muon system..
- DAVINCI [240]: is the data analysis application of LHCb. Thanks to the hypotheses on the identification of particles and information on tracks and vertices, already present at reconstruction level, the entire decay chain can be built, combining reconstructed particles to define B or D mesons, or allowing manipulation of all the quantities available in the event. The last step of the data analysis is instead performed by analysts using the ROOT software, developed by CERN [241].
- MOORE [242]: is the application that applies the software trigger algorithms.
- GAUSS [243]: the event simulation program. The procedure of simulation first uses the Pythia program [244], to simulate the proton-proton collisions, the EvtGen program [245] for the particle decays, and subsequently Geant4 [246] to propagate the particles through a simulated version of the LHCb detector, containing information on the dimensions, materials and geometries of the detectors.
- BOOLE [247]: is the program for the final simulation phase and reproduces the digital response of the experiment, taking into account also possible dead channels, electronic noise or cross-talk. The output thus has the same format as the real data coming from the detector.

The information coming directly from the detector, from readout electronics response, is saved in files called RAW. The events are then reconstructed through the Brunel application and all the information is saved in files called "Data Summary Tape" (DST), which contains the full event information, such as reconstructed objects and raw data and typically takes around 150 kB of disk space. To reduce non-useful information for analysts, save disk space and also simplify the further analysis, a subsequent centralised procedure called *stripping* is implemented [248]. It consists of a series of offline selection algorithms, called stripping lines, characterised by loose selection cuts similar to those present in HLT2. The stripping lines are grouped into *streams* according to the type of analysis to which they are dedicated, and run in a centralised way. Since the stripping selection is applied to offline reconstructed variables, analysts had to take into account both the HLT and Stripping selections, which often concerned the same quantities but with different resolutions, due to the different reconstruction. For this reason, before the beginning of Run II a big effort has been done to optimise algorithms both in the online reconstruction at HLT level and in the offline one such that now the two reconstructions are identical, opening also the possibility to perform some physics analyses directly after HLT2 filtering. The candidates selected from a particular stripping line are saved in files usable by analysts in formats like DST, or μDST, which was designed to save disk space by storing only the information of the candidate of interest and discard the raw event, which takes around 10 kB per event.

The stripping procedure is important for another reason: it automatically flags the candidate particle of interest, like B or D mesons and the related daughters, as *signal* candidate. Since this flag is applied at offline level, it is interesting to retrieve the online objects at trigger level and check if they are fired by the signal candidate or not. This is explained in the next section.

2.2.4.4 Trigger decisions: TIS, TOS, Dec

In LHCb every unit of information used in the reconstruction, like detector channels, logical pads etc. has a unique numerical identifier, called LHCbID. Once an event is accepted by HLT1 and HLT2, and after the offline processing, the corresponding LHCbIDs are saved. After the stripping, the LHCbIDs of the signal candidate and its daughters can be compared to the ones of the trigger objects. This allows to perform various checks, for example if a particular trigger line was fired by the signal candidate or by the rest of the event or by a combination of the two. Three main categories, not mutually exclusive, can be defined [249]:

- Trigger On Signal (TOS): the trigger line has been fired by the signal candidate, regardless of the presence of the rest of the event. More precisely, a candidate is considered TOS with respect to a trigger line if the LHCbIDs of the final state particles of the trigger accepted decay overlap for more than 70% with the LHCbIDs of the final state particles of the offline signal candidate.

- Trigger Independent of Signal (TIS): the trigger line has been fired regardless of the presence of the signal. A candidate will be TIS with respect to a trigger line if, removing it from the event, the trigger continues to accept the event, i.e. another particle or set of particles is present in the event that is also accepted by the trigger. In this case the LHCbIDs of the triggered candidates overlap less than 1% compared to those of the offline candidate. Thus, requiring a signal candidate to be TIS on a particular line, leads to a signal sample that is unbiased with respect to that particular trigger selection.

- Trigger Decision (Dec): events that have passed the selection of triggers, regardless their classification with the TIS-TOS categories.

Since the TIS and TOS categories are not mutually exclusive, a candidate can be simultaneously TIS and TOS for a given trigger line. If a trigger line is fired on partial combination of the signal and the rest of the event the candidate can be nor TIS nor TOS. These categories are useful for calculating trigger efficiencies directly from data (TIS-TOS method [249]).

2.2.4.5 Main processing algorithms

We now explain in the following sections two main algorithms running at HLT and offline reconstruction level: the tracks reconstruction and the particle identification algorithm.

Tracks reconstruction

In the tracks reconstruction algorithm running in HLT1, information from the VELO, TT and T1-T3 stations are used to build the particle trajectories, starting from the individual hits. Different types of tracks are defined, as illustrated in Fig. 2.17 [233]:

- **Long Tracks**: they cross the whole tracking system, leaving hits in the VELO and in all the T stations after the magnet. Hence they have the most accurate momentum measurement, and typically the most important tracks used for for physics analyses. The momentum resolution for the long tracks is $\delta p/p \sim 0.5\%$ at low momentum, up to 1% at momentum of $200\,\mathrm{GeV}/c$.
- **Upstream Tracks**: they only pass through the VELO and TT stations. Generally they are of low momentum and are therefore bended out of the detector acceptance by the magnetic field. As they pass through the RICH1, emitting Cherenkov photons if $p > 1\,\mathrm{GeV}/c$, they can be used to study the background in the particle identification algorithms in the RICH. The momentum resolution is $\delta p/p \sim 15\%$.
- **Downstream Tracks**: they leave hits in TT and T stations only and are generated mainly by long lived particles like K_S^0 and Λ. The momentum resolution is $\delta p/p \sim 0.43\%$.
- **VELO Tracks**: tracks leaving hits in the VELO only, useful for reconstruction of the primary vertices. They correspond generally to particles generated at high angles.
- **T Tracks**: they leave hits in the T stations only downstream of the magnet and they are are generated mainly by secondary interaction.

The track finding and reconstruction is organised hierarchically, trying first to reconstruct long tracks, then using the remaining tracks to reconstruct downstream and upstream tracks. The procedure is divided into three main steps:

- Pattern recognition of the hits, produced by the passage of charged particles. In the VELO this procedure corresponds to create segments matching the hits lying on a straight line. In the tracking stations a first segment matching hits in T1 and T3 is created, and a subsequent calculation of possible hits in T2 under the hypothesis of parabolic trajectory is made. If the hits are found they are added to the previous defined segment. In order to search for long tracks a matching algorithm between VELO segments and tracking stations segments has to be used, based practically to extrapolation techniques.

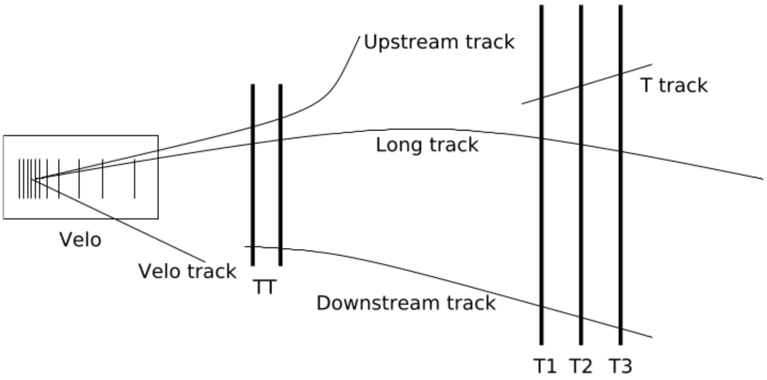

FIGURE 2.17. The LHCb trigger schemes for Run I (left) and Run II (right).

- A bi-directional Kalman filter [234] fit is applied, as explained in Sect. 2.2.4.2. This allows to take into account secondary interactions or energy loss, giving a better estimation of the tracks parameters.
- Removal of duplicate tracks, comparing them two by two. The comparison is done by checking the percentage of shared hits by the two tracks, and if this is greater than given threshold one of the two tracks is rejected, typically one with less hits or the worst χ^2.

A tracking efficiency can be defined as the probability of a full reconstruction of trajectory leaving hits in the full tracking system. The average efficiency is above 96% for muons or hadrons that have passed through the full tracking system without hadronic interactions, in the momentum range $5 - 200\,\mathrm{GeV}/c$ and within the pseudorapidity range of LHCb acceptance.

A track can also be reconstructed from random combination of hits, in which case the track is called *ghost*. A multivariate algorithm has been developed and its output variables are used to quantify the probability that a track is a ghost.

Particle Identification

PID algorithms use information from the whole detector to assign a mass hypothesis to the tracks, in particular information coming from calorimeters, RICH detectors and muon stations.

Consider a generic event, which can belong to a given category k, in this case the particle type, and consider that it is characterized by n variables x_i, for example track parameters, energy deposit in the calorimeter cells etc. We can define the likelihood $\mathscr{L}^k$ as $\mathscr{L}^k = \prod_i^n p_i^k(x_i)$, where $p_i^k(x)$ are in general probability distribution functions, generally extrapolated from simulations or from data calibration samples. Thus $\mathscr{L}^k$ quantifies the probability that an event with the measured experimental data x_i belongs to the category k. Given therefore a set of variables coming from the experimental data, it is possible to construct likelihoods for the different hypothesis and compare them. A definition often used is the following form (log-likelihood) to use sums instead of products:

$$\ln \mathscr{L}^k = \sum_i^n \ln p_i^k(x_i).$$

In particular we can define the delta-log-likelihood (DLL) variable, to quantify how much a hypothesis is more likely than the other:

$$DLL_{h_1/h_2} = \ln \mathscr{L}(h_1) - \ln \mathscr{L}(h_2) = \ln \left(\frac{\mathscr{L}(h_1)}{\mathscr{L}(h_2)} \right),$$

where h_2 and h_2 refer to different mass hypotheses of the track considered.

A global likelihood can be constructed in various ways, in order to combine the information of all the sub-detectors. The simpler way is to multiply the likelihoods deriving from RICH, calorimeters and muon system, accordingly to the mass hypothesis, as:

$$\mathscr{L}(K) = \mathscr{L}^{RICH}(K) \cdot \mathscr{L}^{Calo}(K) \cdot \mathscr{L}^{Muon}(\bar{\mu}),$$

$$\mathscr{L}(\pi) = \mathscr{L}^{RICH}(\pi) \cdot \mathscr{L}^{Calo}(\pi) \cdot \mathscr{L}^{Muon}(\bar{\mu}),$$

$$\mathscr{L}(\mu) = \mathscr{L}^{RICH}(\mu) \cdot \mathscr{L}^{Calo}(\bar{h}, \bar{e}) \cdot \mathscr{L}^{Muon}(\mu),$$

where the bar indicates the hypothesis of not being that particle. With these variables one can then build the global DLL variable. Another more powerful way is to combine the sub-detectors information with a multivariate algorithm, for example a Boosted Decision Tree (BDT) or a neural network (as the `ProbNN` variables used in the following analysis), exploiting also information from the tracking system.

Muon identification Since the muon identification is an important procedure on which the analysis described in this thesis is based, we describe it in more detail. The muon identification is basically composed of two main algorithms [250]: the `IsMuon` binary selection and the muon likelihood:

- `IsMuon`: being muons minimum ionising particles with momenta greater than 100 MeV/c and having a probability of 95% to reach M5 for momenta greater than 6 GeV/c, a loose binary selection can be defined based on the penetration of the muons through the muon stations. The output is *true* if a series of matched hits is found in a given FoI on adjacent stations, considering a variable number of stations according to the momentum, as described in Tab. 2.1. The aperture of the FoI also varies with the momentum as $FoI = a + be^{-cp}$, where parameters a, b and c are tuned from simulations, and different for each station and region. The average efficiency of `IsMuon` is $\sim 98\%$ and the average misidentification is $\sim 1\%$.
- A likelihood for muon and non-muon hypotheses can be calculated starting from the hits pattern around the extrapolated track trajectory. The empirical variable used to define

Momentum range	Muon stations
$3\,\mathrm{GeV}/c < p < 6\,\mathrm{GeV}/c$	M2 + M3
$6\,\mathrm{GeV}/c < p < 10\,\mathrm{GeV}/c$	M2 + M3 + (M4 or M5)
$p > 10\,\mathrm{GeV}/c$	M2 + M3 + M4 + M5

Table 2.1. Muon stations in which hits are required for a positive `IsMuon` decision, as a function of the momentum.

the likelihood is the D^2 variable: the average squared distance of the hits with respect to the extrapolated trajectory, weighted by the pad resolution,

$$D^2 = \frac{1}{N}\sum_i \left[\left(\frac{\Delta x^i}{\mathrm{pad}_x^i}\right)^2 + \left(\frac{\Delta y^i}{\mathrm{pad}_y^i}\right)^2\right],$$

where the index i runs over the stations, while $\Delta x^i = x^i_{\mathrm{closest}} - x^i_{\mathrm{track}}$ is the difference between coordinates of the closest hit to the track extrapolation point and that point itself (analogously for Δy^i) and finally $\mathrm{pad}^i_{x,y}$ are half of the logical pad size considered. A likelihood can then be defined as the cumulative probability on the D^2 distribution, from zero to the observed D^2_{obs}, where the distributions are pre-calibrated and thus take into account the differences between muon and non-muon hypotheses (the distribution is narrower and close to zero for true muons). The logarithm of the ratio between the likelihoods of muon and non-muon hypotheses is called *muDLL*.

The muon likelihood can then be combined with the ones from the other sub-detectors, there are two main ways to perform this procedure:

- Simple combined PID: as explained in the previous section, the likelihoods from calorimeters and RICH are simply multiplied. Commonly the DLL(μ-π) is used, defined as the logarithm of the ratio between the likelihoods of muon and pion hypotheses. This strategy however does not consider the full information coming from the detector, for example from tracking, and also the correlation between variables are not properly considered.

- Neural-Network based PID: to avoid the drawback of the simple combined PID an algorithm based on a neural network has been developed. It uses the various sub-detectors likelihood and also information from tracking system and ghost probability. The algorithm is trained on simulated samples, and the various output variables are called `ProbNN` [251].

Other variables can be defined to help the muon identification. One useful discriminating variable is called `nShared`: since the same hit in the muon stations can be used by `IsMuon` to build more than one track, a score of +1 on the variable `nShared` is assigned to the track for which the shared hit is more distant. Requiring `NShared`$= 0$ reduces the probability of hadron misidentification, especially in high multiplicity events.

2.3 LHCb upgrade

During Run I and Run II LHCb has successfully recorded an overall integrated luminosity of $8\,\mathrm{fb}^{-1}$, that allowed to perform a large number of high precision measurements in the context of heavy flavour physics, obtaining leading and outstanding results. However many key measurements remain statistically limited. Even the exploration research fields will benefit of a statistics improvements, since they will become high precision research fields, with many new possibilities in terms of observables [252].

LHCb has been operating at a levelled and reduced instantaneous luminosity of $4{\cdot}10^{32}\mathrm{cm}^{-2}\mathrm{s}^{-1}$, which is highly below the luminosity LHC can deliver. Indeed the main limitation is not coming from LHC but from the current LHCb readout and trigger architecture, which basically prevents to turn efficiently an higher luminosity into high precision measurements, and also from the radiation damage that most of sub-detector systems can experience, due the higher occupancy and event multiplicity. For this reason LHCb is undergoing a major upgrade to allow data taking operation at an increased luminosity of $2 \cdot 10^{33}\mathrm{cm}^{-2}\mathrm{s}^{-1}$, in which the detector readout will be performed at 40 MHz instead of the current 1 MHz, and the Level-0 hardware trigger will be completely removed, only doing online selection with a pure software trigger [253, 254]. In order to sustain this readout changes, increase the radiation hardness and be able to operate efficiently with an higher occupancy, mainly all the sub-detectors will be upgraded.

2.3.1 Physics motivation

In the context of search for physics BSM in the flavour sector, usually the studies can be divided in two main categories:

- Precision studies: this includes measurements of already known parameters with improved sensitivity, in order to get results with higher precision, allowing a more meaningful comparison with theory predictions.
- Exploration studies: this includes experimental observables still not accessible or which cannot be studied with interesting precision with the current experiment, but very sensitive to search for NP. In this case a $\sim 1/\sqrt{N}$ scaling, where N is the number of events collected, is not applicable. With an upgraded detector it is expected that some of the exploration studies will migrate in the context of precision studies.

Most of the LHCb physics results are dominated by statistical uncertainty. In case of CKM tests, like measurements of Unitary Triangle angles, charm physics and electroweak penguins physics, like studies of $B^0 \to K^*\mu^+\mu^-$, the ratio $\sigma_{\text{stat}}/\sigma_{\text{syst}}$ is regularly of the order $\mathscr{O}(1-5)$, except $\sin 2\beta$ and ϕ_s measurements for which the ratio can be up to 8 [255].

An example of an important precision study is the measurement of the γ angle of the Unitary Triangle of the CKM matrix, defined as $\gamma = \arg[-V_{ud}V_{ub}^*/V_{cd}V_{cb}^*]$, which can be studied *directly* through theoretically clean tree level processes, being known in the SM with negligible uncertainty of order $\mathscr{O}(10^{-6})$. The angle γ is the least-well-known angle of the Unitary Triangle, and a possible discrepancy between direct and indirect measurements would be a sign of NP. The current experimental value is $\gamma = (74^{+5.0}_{-5.8})^{\circ}$ with the full Run I and II dataset and combining several modes of the type $B \to Dh$. Prospects for the upgrade full dataset, an overall luminosity of $50\,\mathrm{fb}^{-1}$ lead to a possible precision of $\mathscr{O}(1^{\circ})$. Other examples of precision studies are the measurement of the angle ϕ_s of the Unitary Triangle to precision smaller than the theoretical one, since these kinds of measurements will strongly benefit of an increased statistics, as pointed out previously. Other precision studies involve the improvement of the recent measurement of CP violation in charm, with a precision below 10^{-4}, as well as reducing the uncertainty on the measured branching fraction of most observed decays. In particular, a crucial rare decay branching fraction measurement is the one of $B_s \to \mu^+\mu^-$ decay, for which an achievable precision of $0.15 \cdot 10^{-9}$ is estimated, since this will be approximately a factor 2 below the current theoretical uncertainty of $(0.3 \cdot 10^{-9})$ [252].

Examples of exploration studies are the search for $B^0 \to \mu^+\mu^-$ decay or the study of other kinematical observables in $B^0 \to K^*\mu^+\mu^-$ decay, as well as in charm multi-body rare decays.

It is important to note that in deriving prospects for measurements in upgrade condition, several assumptions are made: the proton beams will collide at $\sqrt{s} = 14\,\mathrm{TeV}$, with heavy flavour production cross-sections scaling linearly with $\sqrt{s}$; the instantaneous luminosity will be at least $2 \cdot 10^{33}\mathrm{cm}^{-2}\mathrm{s}^{-1}$ with a pile-up of $\nu = 7.6$; the polarity of the magnet will change with a regular frequency like in the current condition and finally a total sample of $50\,\mathrm{fb}^{-1}$ is considered.

2.3.2 Upgrade of LHCb readout system

One of the fundamental change in the LHCb upgrade is the drastic replacement of the current readout and back-end electronics, and most of the front-end one, in order to remove completely the Level-0 trigger and perform the full readout of the detector at 40 MHz, for all the proton-proton collision. The front-end electronics will thus run freely, sending data synchronously at 40 MHz to the back-end electronics, with a fixed latency [256–259]. The data will be buffered to disk, similarly to the current case, and a software trigger will perform the first selection and reconstruction, with a final output rate to storage of 2-5 GB/s. The upgraded trigger scheme is shown in Fig. 2.18. In fact the major limitation for an high luminosity operation is the current L0 configuration: for events without muons in the final state, the L0 trigger performs decisions based on the energy deposition measurement in the calorimeters, but increasing the luminosity at $2 \cdot 10^{33}$ $\mathrm{cm}^{-2}\mathrm{s}^{-1}$ would require to further increase the energy threshold to maintain the output rate at 1 MHz. In this condition the trigger yield is saturated and the thresholds are too high that signal events are rejected significantly, as shown in the Fig. 2.19. Being the readout upgrade a challenging and ambitious project, it was decided to develop the system with some fundamental requirements like flexibility, i.e. being able to modify parameters and configurations

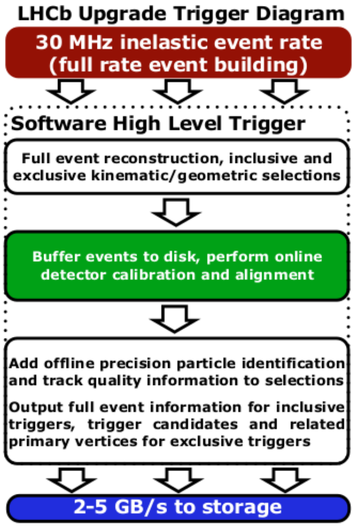

FIGURE 2.18. Trigger scheme for Run III in the LHCb experiment.

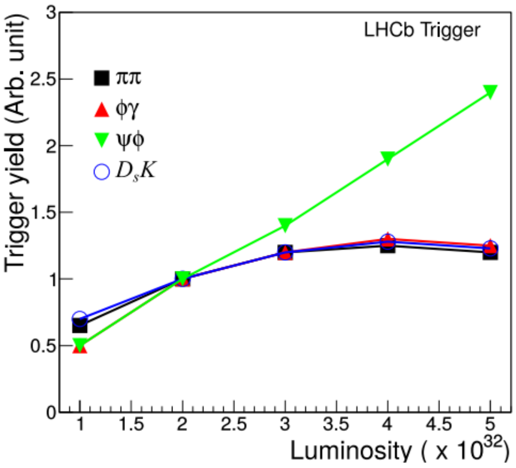

FIGURE 2.19. Expected trigger yields for different decays of B mesons, as a function of the instantaneous luminosity.

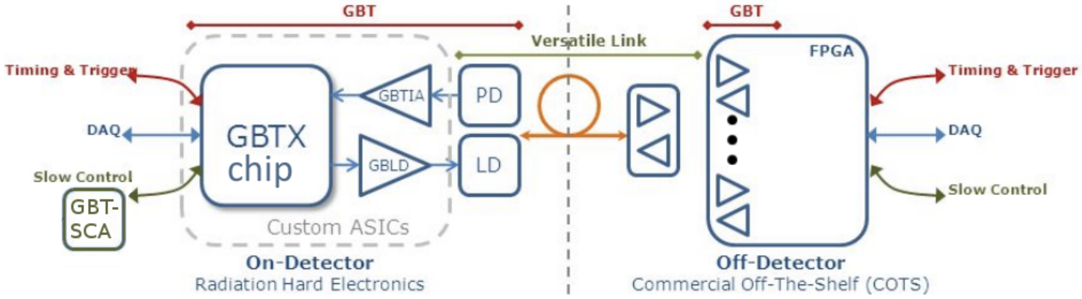

FIGURE 2.20. Schematic representation of the GBT chipset, with the optical link, the GBTx chip, the GBT-SCA and the GBT-FPGA.

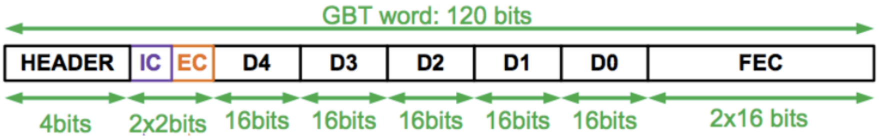

GBT word: 120 bits

HEADER	IC	EC	D4	D3	D2	D1	D0	FEC
4bits	2x2bits		16bits	16bits	16bits	16bits	16bits	2x16 bits

FIGURE 2.21. The 120 bits of the GBT frame and the internal division as foreseen by the GBT protocol.

in a quite easy way, and especially reliability and low cost. With this in mind the choice was to use, wherever possible, Commercial Off-the-Shelf (COTS) components, for examples FPGAs for the back-end electronics, and use high bandwidth bidirectional optical links with a common protocol. The bidirectional link are implemented through the GBT chipset [260], and its related components developed by the EP-ESE (the Electronic Systems for Experiments) group at CERN, both for data readout and for fast and slow control tasks. The GBT chipset is composed of the main chip, called GBTx, which prepare, encode and serialise the data frame to be sent through the optical link at 4.8 Gb/s, which is called Versatile Link [261]. Analogous operations of decoding and deserialisation are made by the GBTx when it receives the data frame as input. Other hardware components regards small chips for the optical driving (GBTIA and GBLD), the GTB-FPGA, which is an analogous of the GBTx but implemented as a firmware component to be loaded on FPGA, and the GBT-SCA [262], an ASIC widely used to configure and monitor the FE electronics via a set of several protocols such as JTAG, I^2C and SPI. The GBT data frame consists of 120 bits, sent and read back at 40 MHz, composed of: a 4 bits header for the frame lock; 2 bits for the internal GBTx configuration; 2 bits for the external slow control, to be collected by the GBT-SCA to instruct it for subsequent actions on front-end; five slots 16 bit wide each for the custom payload; and 32 final bits for the forward error correction (FEC). A scheme of the GBT chipset is shown Fig. 2.22, while in Fig. 2.21 the GBT data frame structure is shown. The structure of the LHCb Timing and Fast Control system (TFC), which is basically the main system on which the readout is based on, is drastically changed [257, 258].

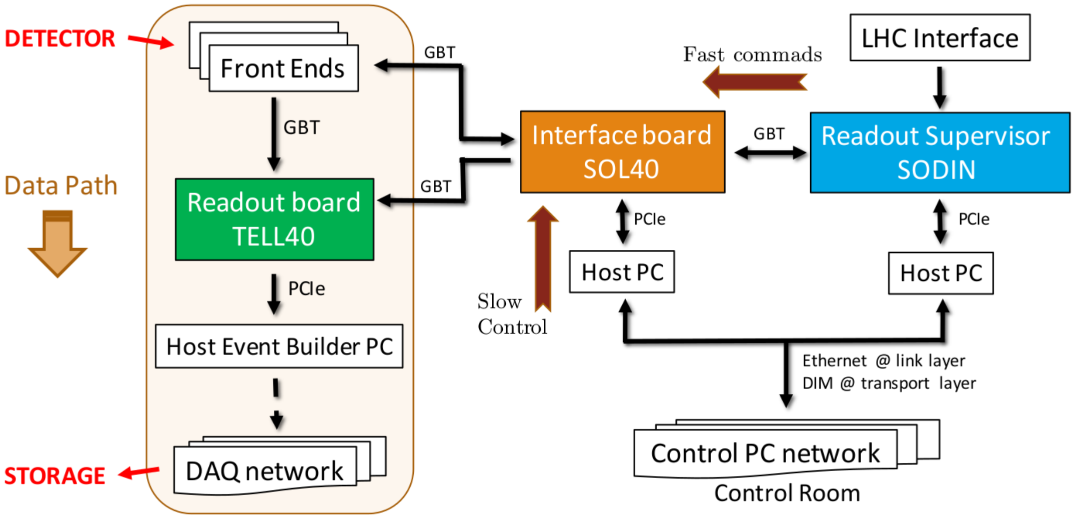

FIGURE 2.22. Schematic complete view of the readout architecture. In the yellow box on the left the data path is represented, from the FE to the storage, through the TELL40 boards. The FE electronics receives both the fast and slow commands from the SOL40 board, which is indeed interfaced to the SODIN and the ECS. The communication between the boards is implemented with the GBT chipset, while communication between boards and host PCs is done by PCIe buses.

It is composed of FPGA-based electronics boards, interfaced to the software control system via PCIe bus, and with front-end (and reciprocally with the other TFC boards) through the bidirectional optical links of the GBT chipset. Actually the board typology is unique, called PCIe40 [263–265], but the different FPGA firmwares (loaded on the Altera ARRIA 10) define the *flavour* of the board, and hence its specific functionality. A schematic view of the readout architecture is shown in Fig. 2.22. There are three different firmwares, namely:

- SODIN: it is the readout supervisor. Thanks to the LHC interface, it is able to distribute the LHC clock, and to generate synchronous and asynchronous commands to the full readout system (like resets, calibration commands etc.) and also to dispatch event data to the event building stage.

- SOL40: it is an interface board, responsible for interfacing both the fast synchronous commands, timing and clock information coming from SODIN, with the slow asynchronous commands coming from the ECS (Experiment Control System), integrating both into the same GBT frame, to be sent to FE boards. This allows to both control and monitor the FE over the same link.

- TELL40: replacing the current TELL1, it is responsible for the readout of the FE event fragments, which are sent to the DAQ to build the complete event.

As already pointed out, not only the readout system will be upgraded but most of the sub-detectors, which need an higher granularity and radiation tolerance, in particular for the tracking sub-detectors. The upgraded VELO [266] will be placed closer to the beam axis (5.1 mm) and particles will encounter less detector material (1.7% radiation lengths) before the intersection of the first tracking layer. Moreover the strip technology will be replaced with pixels of reduced thickness (200 μm). This will improve the impact parameter resolution of 40%, with a better tracking efficiency for low momentum particles and an improved decay time resolution. The current tracking stations will be replaced with the Upstream Tracker, upstream of the magnet, and the Scintillating Fiber tracker (SciFi), downstream of the magnet [267]. The UT will be composed of four tracking layers based on silicon strip in p^+-in-n and n^+-in-p technology. The SciFi will be structured in twelve detector layers, based on 2.4 m long plastic scintillating fibres with a diameter of 250 μm diameter, arranged on vertical direction, and readout by SiPMs placed on the top and bottom of the layers. The combination of these tracking sub-detectors will allow to reduce the number of ghost tracks by a factor 50-70%. For the RICH1 [268], the optical layout will be changed to handle the higher occupancy. In particular the spherical mirrors focal length will be increased by a factor $\sqrt{2}$ and the mirrors curvature radius will be also increased, improving the Cherenkov angle resolution and reducing the aberrations of the mirrors. The readout of both RICH detectors will be replaced by Multianode PMTs working at 40 MHz. The calorimeter will not undergo a big change: the removal of SPD and PS is foreseen for Run III since they are involved mainly in the L0 trigger, while current used PMTs will be kept with a reduced gain by a factor of 5, to keep the same mean anode current. A scheme of the new LHCb layout in upgrade condition is shown in Fig. 2.23.

2.3.3 Upgrade of Muon system and its readout electronics

In the upgrade condition the muon system must continue to ensure high reconstruction and identification efficiencies, with a corresponding low misidentification fraction, up to an integrated luminosity of $50\,\text{fb}^{-1}$ [268]. The limiting factor are clearly the higher intensity of charged and neutral particles, and the related radiation damage along the ten years of upgrade operation. Various tests have been done in order to study the operation under upgrade condition. In particular the MWPCs have been at the expected rate of the most irradiated chambers of M2, at the CERN Gamma Irradiation Facility (GIF), with a 100 GeV muon beam and a superimposed γ ray flux of 662 keV by a ^{137}Cs source, with variable intensity. The tests have shown no major deterioration in the performance, except for dead time effects. The four gaps redundancy system guarantees the required control of inefficiencies, while other possible problems, for example due to space charge effects, are of minor importance. These results have been also confirmed in special LHC test runs, at various luminosity values and bunch spacing, and the data have been then used to extrapolate the behaviour of all the regions and stations at the nominal upgrade conditions.

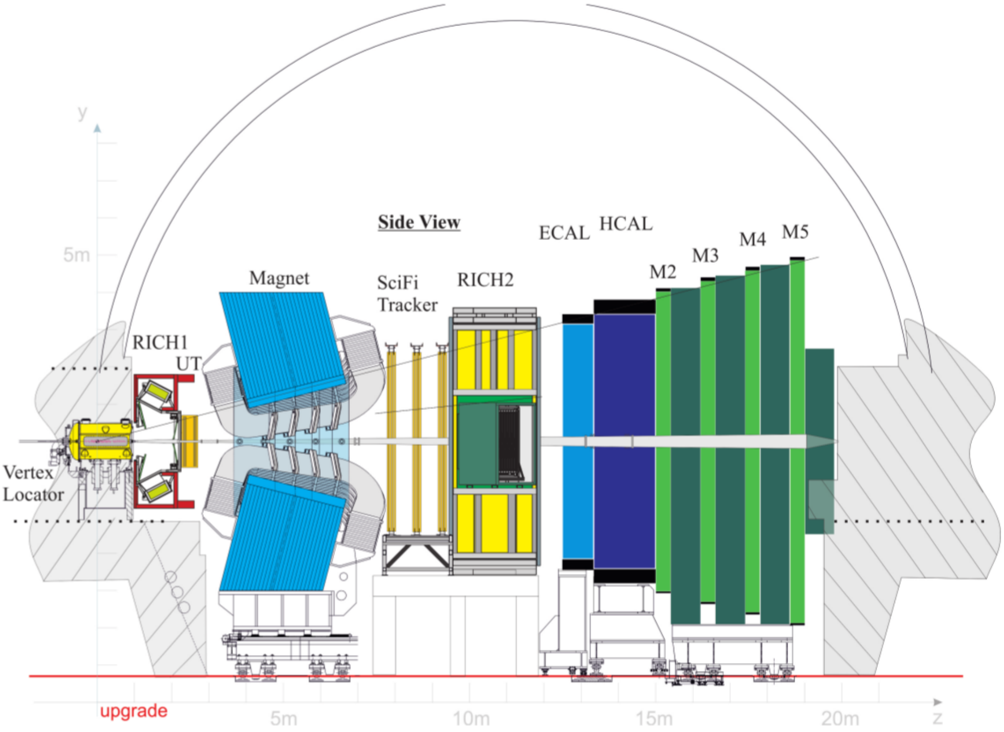

FIGURE 2.23. Side view of the upgraded LHCb experiment.

The radiation damage has been studied at GIF and at the ENEA Calliope Gamma Facility, with an accumulated charge of 0.45 C/cm with no perforce loss. Since this value corresponds to about 70% of the expected integrated charge over ten years of upgrade operation, the radiation damage of the chambers will become a sensitive matter after the Long Shoutdown 3 (LS3).

For all these reasons the muon system will not undergo important changes for the upgrade, since most of the detector already meet the requirement for working in upgrade conditions. The major changes are reported in the following:

- Removal of M1. Being the most shielded sub-detector, the muon system can tolerate the higher particle flux except in the M1 station, where the huge hit occupancy would make the hits association to the muon track segment practically impossible. Moreover, since the main purpose of M1 was to the get a better resolution of muon tracks p_T at L0 level, which is removed, then the M1 can be removed without a strong impact on the operation.

- Additional shielding behind HCAL. The hit rate in front of M2 is expected to very high, especially in the innermost regions, due the not sufficient absorption of particles produced in the showers behind HCAL and near the beam pipe. The high hit rate will cause inefficiencies, due to the dead time. For this reason an additional custom shielding, made of lead and tungsten, will be installed around the beam pipe and placed behind HCAL,

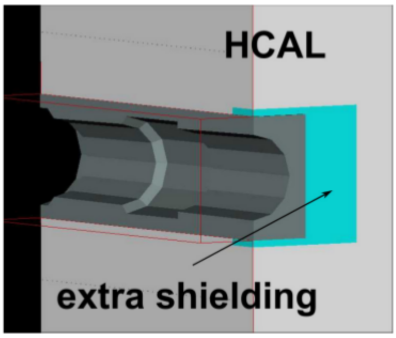

FIGURE 2.24. Schematic drawing of the extra shielding foreseen behind HCAL and around the beam pipe.

in order to ensure a more efficient absorption in front of the innermost regions of M2. A schematic view of the shielding is shown in Fig. 2.24.

- Removal of Intermediate Boards in M5R4. In most outer regions of the muon stations, M5R4, the logical pads results from the logical OR of 24 front-end channels and reach an area of 0.5 m^2. They already suffer also from back scattering by the cavern walls. In upgrade conditions the rate is too high and will cause severe inefficiencies beacuse of electronics dead time. For this reason the granularity will be increased, removing the IBs and performing directly the readout with new ODE boards.

Upgrade of Muon readout electronics

The current structure of the muon readout electronics is described in Sect. 2.2.3.3. This architecture is no longer suited to the requirements of the upgrade. The TDC information of the SYNC chips is in fact extracted at a rate of 1 MHz only and the current optical communication system, based on the GOL chipset, needs to be replaced with the new GBT chipset, as explained in the previous sections. For this reason it has been decided to replace the ODE, the SB and the PDM with new electronic boards (nODE, nSB and nPDM respectively), maintaining the present crates and power supply system, and guaranteeing a mechanical and electrical compatibility with existing system in order to perform and fast and reliable replacement. The new electronics allows to integrate the GBT chipset, thus with an automatic communication compatibility to the TFC and ECS system, to perform the TDC readout at 40 MHz, and to potentially increase the readout granularity with a simultaneous minimisation of the current number of readout links. A schematic representation of the new readout system in shown in Fig. 2.25, which is a specification to the muon case of the generic scheme in Fig. 2.22.

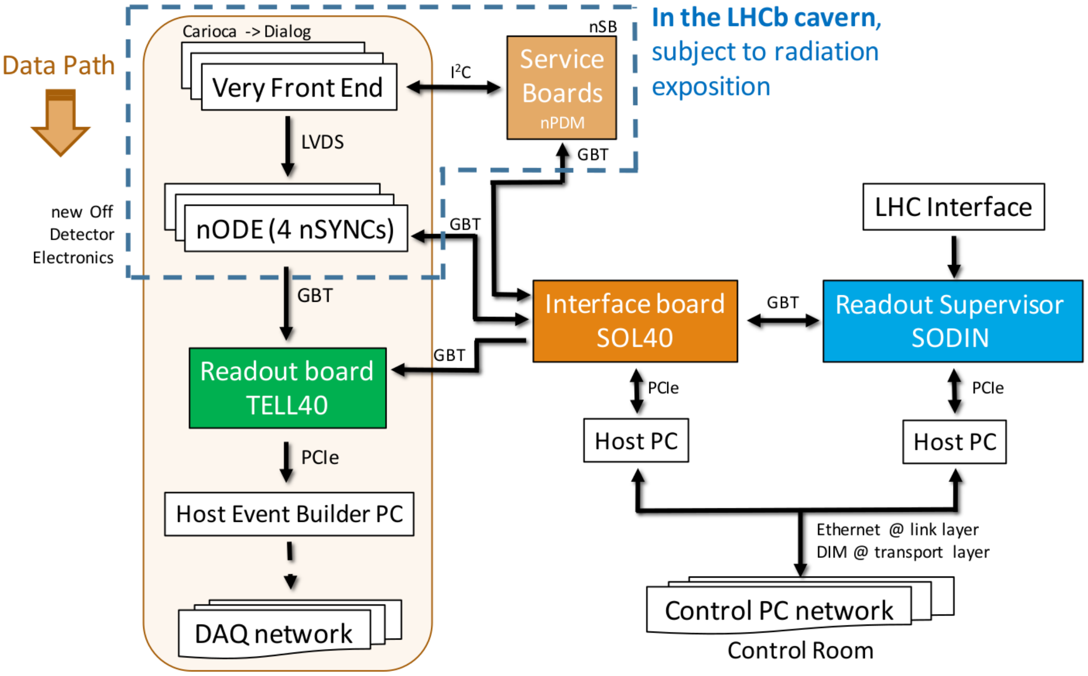

FIGURE 2.25. Schematic view of the muon readout architecture. In the yellow box on the left the data path is represented, from the CARDIAC boards, to the TELL40 boards, through the nODE boards. The nODE receives both the fast and slow commands from the SOL40 board, while the CARIDIAC boards are pulsed or configured through the nPDM and nSB, which communicate theirselves with the SOL40 boards, from which fast and slow commands can be received.

The nSYNC architecture

For the upgraded Muon Detector the nSYNC chip [269, 270], a custom ASIC in UMC 130 nm technology, has been developed as an evolution of the current SYNC chip [271]. The nSYNC architecture is composed of several functional blocks, schematically shown in Fig. 2.26. It receives, through 48 LVDS input channels, the digital signals coming from the FEBs of the muon chambers. In each channel the phase of the arriving signal with respect to the LHC 40 MHz clock is measured by a TDC. The main core of the TDC is a fully digital patented Digitally Controlled Oscillator (DCO), which produce a clock signal based on an input digital word. The TDC can work with several time resolutions, i.e. the number of slices on which the clock can be divided, from 8 to 32. The nominal resolution will be 16, corresponding to a time slice of 1.56 ns.

The phase measurement is activated by the incoming signal that triggers the DCO oscillation. The DCO clock periods are then counted by a fast counter, until the rise-edge of the master clock arrives and stops both the counter and the DCO. The measurement then corresponds to the counter output and can be stored in an output buffer. Since the DCO is composed of a digital delay chain, a systematic error is continuously accumulated during the measurements.

The dithering system add or remove a unit to the digital input word of the DCO, thus inverting the systematic error and preventing its accumulation. Since the DCO is not working continuously but only when a signal arrives, the digital input word for a given resolution has to be recomputed, with a particular procedure called *DCO calibration* in this context. After resolution is set, the automatic DCO calibration can be lunched, using an internal calibration signal generated at the beginning of the master clock cycle. A Finite State Machine (FSM) governs the calibrations stages and the dithering system, until the requested DCO digital word is computed.

Every 25 ns, the output data of each TDC consist of a binary flag (corresponding to the Hit/No-Hit information) and a 5 bits-wide word with the measured phase, if an hit is present. Each input channel is equipped also with an histogram facility block, composed of 16 counters (bins), in order to histogram the measured phases. The TDC output data are sent in parallel through a programmable-length pipeline, that allows to align the hits with different delay time but coming from the same bunch-crossing. This allows to uniquely associate the 12 bits-wide bunch-crossing identification number (BXid) to all the data and pack eventually these information together. Finally nSYNC creates an extended frame, composed of an Header, the 48 bits-wide Hit-Map and the TDC data. While the Hit-Map is always sent non zero suppressed, the TDC data are instead subject to a (bypassable) zero suppression algorithm: only the first non-empty TDC data are added to the frame, up to a maximum of 12 TDC data according to the chosen resolution and the output frame length. Therefore the same Hit-Map is used both for its intrinsic physics content and for the TDC data address decoding, allowing an optimization of the bandwidth usage and a reduction in the number of links. The last eight bits of the frame are dedicated to the Hamming code, used to correct single-errors or detect double errors possibly occurred during data transmission, a feature that can be anyway disabled to increase the TDC occupancy. The final data frame of the nSYNC, 112 bits-wide, is shown in Fig. 2.27, fitted in the payload available space of the GBT frame. Due to the data occupancy and taking into consideration the expected error rate of the versatile link, the so-called *wide-bus* solution was chosen, i.e. use the FEC space to extend the nSYNC payload.

The output communication between the nSYNC and GBTx chip is done using 14 LVDS links, at a data rate of 320 Mb/s. The data pass through an intermediate asynchronous FIFO to interface the two clock domains. The high frequency clock is generated internally using a PLL with the 40 MHz clock as reference. Moreover, there is a 8 steps programmable output pipeline to allow the correct alignment from the receiver side. The 40 MHz clock and all the other synchronous fast commands sent by the TFC system, such as calibration, reset or synchronization commands, are received through the GBTx master chip. Asynchronous slow commands, like configuration commands, are received a GBT-SCA chip mounted on the nODE board. The GBT-SCA is interfaced on one side with the Master GBTx through an e-link at 80 Mb/s, and on the other side with the nSYNC with an I^2C bus, as shown in Fig. 2.26. The e-link is a radiation-hard low-power electrical link, developed by CERN for data transmission over

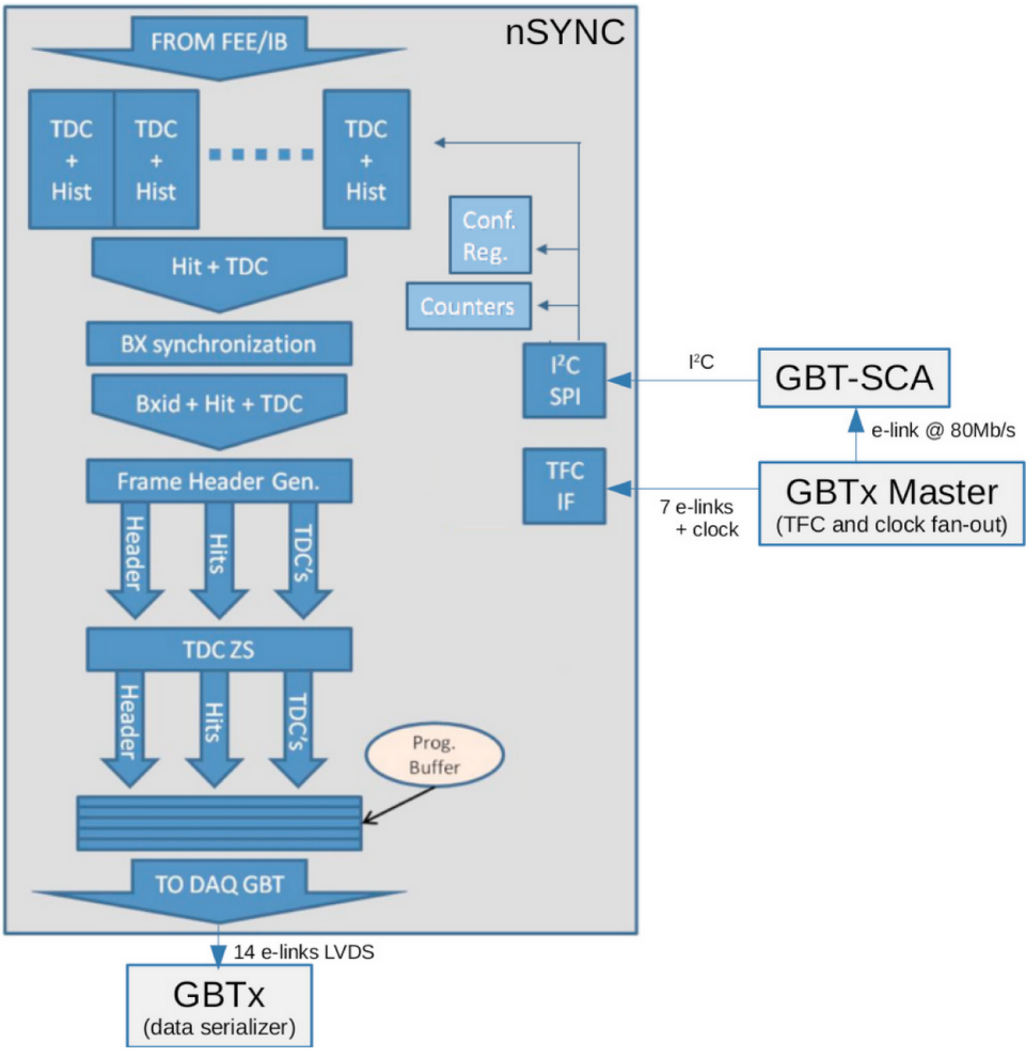

FIGURE 2.26. Schematic view of the nSYNC architecture and its interface with the GBT chipset.

PCBs or electrical cables, with the main purpose to provide a link between front-end electronics and the GBTx chip. Since it is LVDS compatible, the nSYNC uses LVDS links on the data output to the GBTx.

The radiation hardness features of the nSYNC will be explained in more detail in the next chapter.

The nODE architecture

The main component of the new readout is the new Off-Detector Electronics Board (nODE) [268, 269] that will be equipped with 4 nSYNC chip. Only a single type of nODE board is foreseen for all muon stations and regions. The nODE has 192 input channels that receive LVDS

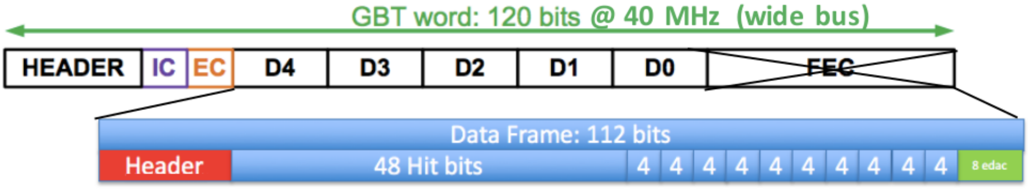

FIGURE 2.27. The 112 bits of the nSYNC frame and its inclusion in the GBT frame in wide-bus mode, i.e. using the FEC bits space as a payload extension.

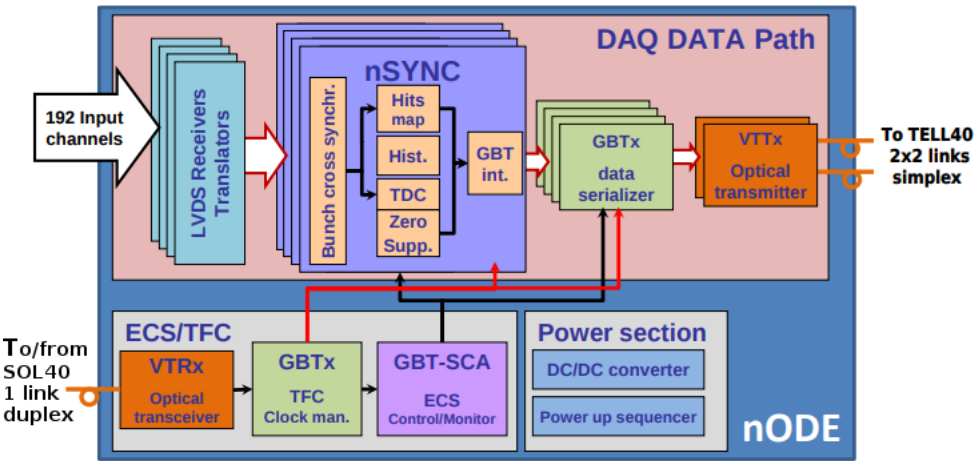

FIGURE 2.28. Schematic structure of the nODE boards with all the components.

signals from the FEBs, that are then dispatched in groups of 48 to the 4 nSYNC chips present on it. The nODE is then equipped in five GBTx chip: one is the so-called *master GBTx*, which is linked to the PCIe40 board (SOL40 firmware) through one optical dual link, using an optical transceiver (VTRx), and thus receive the master clock, the TFC and ECS information, while the aim of the other four GBTx, called *slave*, is to receive the output data from their own nSYNCs and serialise it out to the optical links, thanks to dual optical transpitter (VTTx). The structure of the nODE is indeed modular, in the sense that each nSYNC communicates to its own GBTx chip only, using an e-link (LVDS) data rate of 320 Mb/s. The slow control and configuration of the board regards configuration of GBTx and nSYNC chips, voltages monitoring etc. and it is assured by two GBT-SCA chips, that are interfaced with the Master GBTx on one side, and with the target devices on the other sides. The current crate and power system, that will be maintained in the upgrade. is based on the MARATON system and it is characterised by three power lines, with voltages from 2 V to 7 V. Since the various nODE components require different power voltages (1.2 V, 1.5 V, 1.8 V, 2.5 V and 3.3 V), a dedicated power section with radiation tolerant DC-DC converters is also implemented on the nODE. A schematic structure of the nODE board is shown in Fig. 2.28.

nSB and nPDM boards

The PDM and SB boards will be replaced by new boards, that will perform the same current operations but within the new upgrade readout architecture. Both the nPDM and nSB are based on the GBT chipset: the nPDM receive the TFC/ECS information through the optical link and the corresponding GBTx chip. Then the communication from GBTx to the various GBT-SCA on the several nSB present in the crate is possible thanks to a new backplane, thus dispatching the e-links from the nPDM to the nSB boards. On the nSB a radiation tolerant Actel FPGA, based on flash technology, is implemented to provide some external additional logic. The usage of a faster data link with respect to the current one (CANbus) allows the removal of the local microcontrollers and ELMBs, and all system operations will be performed directly via software.

CHAPTER 3

FUNCTIONAL AND IRRADIATION TESTS OF UPGRADED MUON READOUT ELECTRONICS

In this chapter the tests on the new readout electronics of the upgraded muon system will be described. Before the production of the nSYNC chips and the nODE boards, various tests were carried out to characterise the prototypes. Firstly, the electrical behaviour was tested, then a test setup was prepared to study the functional blocks performance, with a special focus on the TDC. Finally both nSYNC and nODE were tested, using a framework that simulates the new LHCb readout environment. Furthermore, the nSYNC chip was tested under radiation, using proton beams and X-rays in order to verify the correct operations. Possible degradation of performance, during the irradiation and after an absorbed equivalent dose to the one that will be absorbed in 10 years of upgrade operations were investigated.

3.1 Pre-production functionality tests

The final version of the nSYNC chip prototype was received in March 2017. The nSYNC chip was mounted on a test Printed Circuit Board (PCB), shown in Fig. 3.1, which allowed to test the LVDS Input/Output (I/O) connectivity block and read and write the configuration memory through the I^2C interface. The board was equipped with a quartz oscillator to emulate the LHC master clock and some pin-outs were used to redirect externally several nSYNC internal signal, like the 320 Mbps clock used on the output stage. The experimental setup consisted of:

- Power supply Hameg, model HM7042, to supply the 3.3 V to the nSYNC for the I/O interface, and the 1.2 V for the nSYNC core.

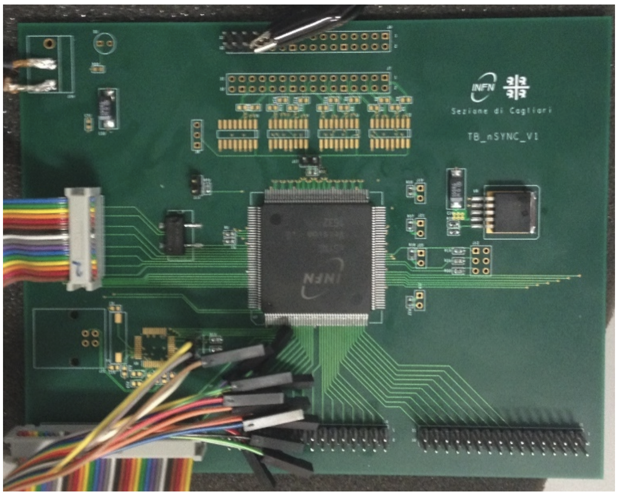

FIGURE 3.1. Top view of the nSYNC test PCB.

- Tektronix Logic Analyzer, model TLA7012 equipped with digital probes connected to the LVDS output channels of the nSYNC test board.
- A digital pattern generator by The Moving Pixel Company, model PG3A. This is used to generate the digital input signals, emulating the ones arriving from the FEBs of the muon chambers. The instrument is equipped with the P300 and P370LV input probes by the same company.
- Oscilloscope LeCroy WaveRunner 104 XMi, used mainly to check the analog signal integrity of the clock and the LVDS output signals.
- The USB-to-I^{2}C elite tool: a commercial device to send I^{2}C commands from a program on the PC. It is equipped with a series of libraries that can be used to build up a custom software program, as done for the radiation tests.

TDC functionalities

One of the main test was performed on the TDC functionalities, that had been already tested as an isolated prototype right after its development. The Digitally Controlled Oscillator (DCO) automatic calibration procedure, explained in Sect. 2.3.3, is tested launching the calibration for all channels at all resolutions. The corresponding DCO digital words as a function of the chosen resolution for each channel, or as a function of the channel number at fixed resolution, form a set of curves that are hereafter referred to as *DCO calibration curves*. The tests showed the right DCO code value for all resolutions and uniformity between different channels. Some variability is shown at resolutions between 20 and 27, that does not affect the TDC performance

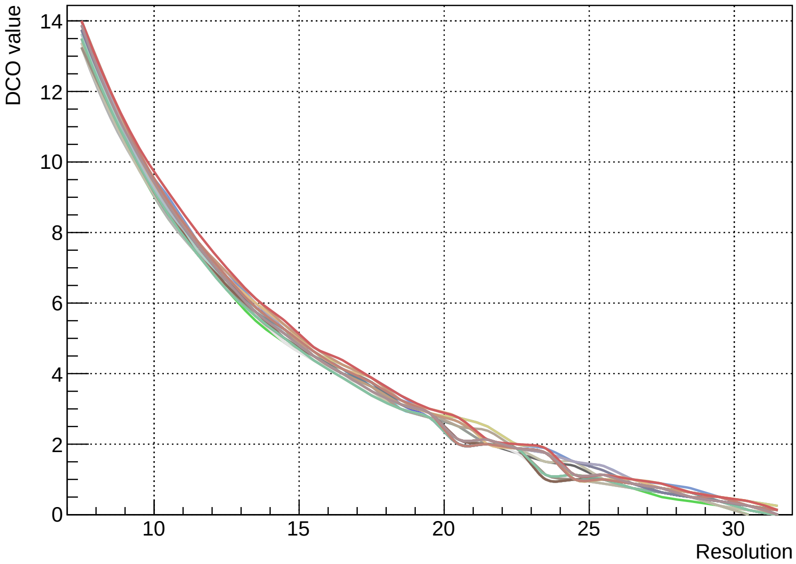

FIGURE 3.2. DCO calibration curve showing the calibrated DCO code values as a function of TDC resolution. The different colours represent the 48 channels.

and is it does not affect the LHCb operation, since the nominal resolution is 16. The curves are shown in Fig. 3.2 and Fig. 3.3.

Further test of the TDC uniformity were performed by impulsing all TDC channels with a synchronous input using the digital pattern generator. Using an adjustable time delay with respect to the master clock, all the channels were pulsed every 10 ps with 10 pulses, in order to scan the full time interval (0-25 ns) and check the channels uniformity. Ideally, the expected hit counts have to be uniformly distributed with an average (over channels) of ~ 1560 counts per bin. In particular, two effects can occur when the channels receive a digital signals from FEBs, or from the generator in this case:

1. Missing hit: a signal arriving on an input channel is missed, and the TDC does not perform any measurement. This missing hit inefficiency was measured to be 0.4%.

2. Wrong clock cycle association: when the input signal arrives right at the rising edge of the master clock, it can be associated with the subsequent clock cycle. This leads to a migration of hits from the first bin to the last one, as shown in the extreme bins in Fig. 3.4 (left), and the integral between the first and last bins confirm such effect. The average number of counts per bin obtained by the test is consistent with the one expected, and the wrong clock cycle assignment was estimated to be of 2% in this test, which reduced to 0.5% with an high statistics sample. This feature, expected from the post-layout simulations, is

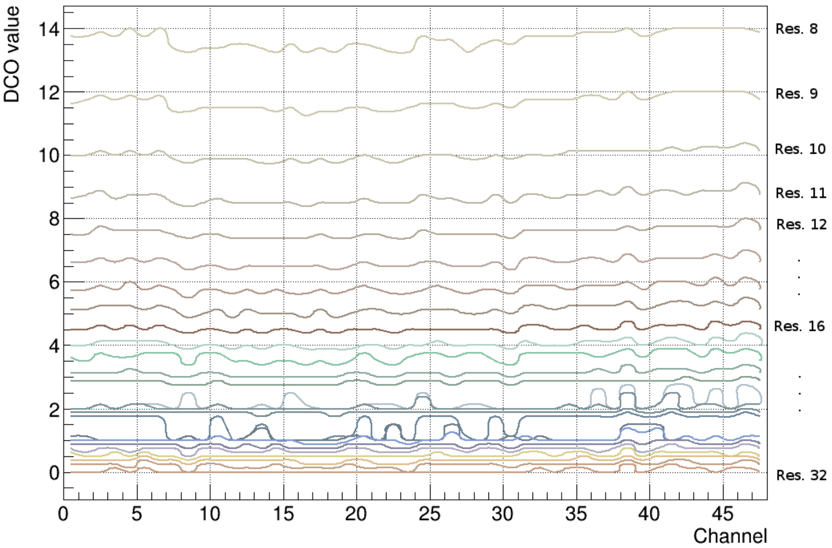

Figure 3.3. DCO calibration curve showing the calibrated DCO code values as a function of channel number. The different colours represent the 25 possible resolutions, from 8 to 32.

due to the timing constraint around the clock rising edge in the TDC input stage and it is well in agreement with what was observed on the TDC prototype.

These two effects have negligible impact on the LHCb Muon System overall efficiency.

Input/Output and configurations blocks

The other functional blocks tested are the output interface and the TFC/ECS interface. The test results are briefly reported in the following:

- GBT output interface: the LVDS output signals of nSYNC, that have to be received by the subsequent GBT, were tested with the oscilloscope to verify the signal integrity and the correct voltage levels, and with the Logic Analyzer to check the correctness of the data frame sent by the nSYNC. The LVDS signals were found compliant with the standard specification and the communication worked as expected at 320 Mb/s.

  The nSYNC is able to send a Pseudo Random Binary Sequence (PRBS) on the GBT output interface, that can be used to acquire an eye diagram of the LVDS signals, as shown in Fig. 3.4(right). The diagram is obtained by overlaying different segments of the stream driven by the 40 MHz master clock. Overlaying many bits thus produces a diagram that can be used to inspect the quality of the data transmission, by observing for example the diagram opening and width.

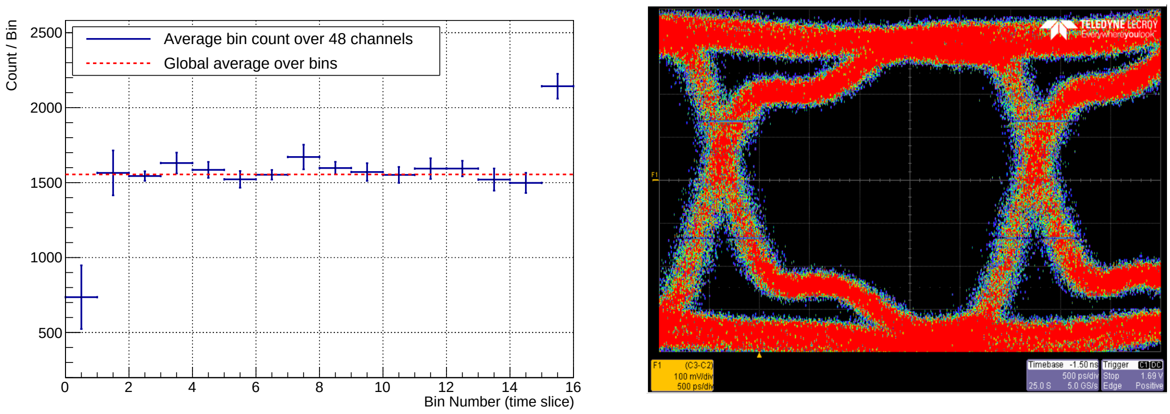

FIGURE 3.4. Left: the 48 channels average counts per bin is shown, after sending 10 synchronous input signals every 10 ps to each channel, scanning the 25 ns time interval. The wrong clock cycle association is affecting the first and last bin. Right: example of the eye diagram of a single channel, acquired sending a Pseudo Random Binary Sequence on the output lines is shown.

The acquired diagram shows a good aperture of $\sim$ 2.1 ns and a jitter of $\sim$ 400 ps, demonstrating the good driver quality. The crossing percentage is slightly above 50%.

Moreover, the nSYNC frame building capability in normal mode, i.e. when the nSYNC sends in output the normal data frame containing the Hit Map and the TDC measurements, was successfully tested pulsing the input channels with the pattern generator.

- TFC/ECS interface: the nSYNC chip receives 7 different fast synchronous commands from the TFC system. They are briefly listed in the following:
  - Synch: used to synchronise the nODE↔TELL40 communication. If a Synch command is received the nSYNC sends in output a special data frame composed of the BXid field (12 bits) plus a sync pattern of 16 bits (the rest is set to zero). The sync pattern is stored in configuration registers and can be changed via the ECS.
  - Snapshot: used to sample the monitoring internal counters of the nSYNC in special registers, accessible through the ECS interface;
  - Calib 0: used to launch the DCO automatic calibration;
  - Calib 1: this command is used to reset the internal error flags registers;
  - NZS Mode: this commands activates the Non Zero suppression of TDC data;
  - FE reset: used to reset state machines, buffers and data transmission stages of the nSYNCs. It has no effect on the configuration, status and monitor registers and BXid counter;

  - BXid reset: reset the BXid internal counter. This command is received for each LHC orbit to pre-load the internal 12-bit BXid of the nSYNC to a value stored in a static register and writeable via ECS.

  All this commands were sent to the nSYNC thanks to the TFC interface present on the test PCB using the pattern generator, and it was found that they are received correctly and act as expected.

  The nSYNC is also equipped with ~ 60 configuration registers that can be read and written through the I^2C interface. With a custom LabVIEW [272] program all the registers were written and read back successfully and the configuration applied as expected.

3.1.1 Preliminary chain test with nSYNC and MiniDAQ

As explained in Sect. 2.3.2, the upgraded readout system is based on the PCIe40 board, containing the FPGA Arria 10 on which three different firmwares can be loaded in order to get a SODIN, a SOL40 or a TELL40 board. The LHCb readout group provides a development kit, called MiniDAQ [273], allowing the first testing and debugging of front-end electronics, integrating it in a readout framework similar to the final one. Two versions of MiniDAQ were developed:

- MiniDAQ_1: is not based on the PCIe40 board but on another board called AMC40, containing the Stratix V GX FPGA and 32 GBT optical I/O links up to 10 Gb/s. The board is supplied and interfaced with another custom board called AMC_TP (Test Pad), which provides the power supply and the clock input using an internal oscillator (at 80.158 MHz) or an external clock through a SMA connector. The board is equipped with a express computer-on-module (COM) in order to control the AMC40 and interface with the FPGA memory banks.

- MiniDAQ_2: based on the PCIe40 and the Arria 10 GX FPGA, and with 48 optical I/O GBT links, as the final design. The board is mounted on a PC through the PCIe GEN3 bus, allowing a communication with a bandwidth up to 110 Gb/s.

Both these standalone systems are based on a special single firmware, which contains a simplified version of all the three firmwares on which the readout system is based. This allows to interface a front-end to a single board which actually emulates the readout system. The MiniDAQ kit includes also a software control system in WinCC-OA, to be installed in a PC and connected via Ethernet to the MiniDAQ, in order to provide the ECS for the SODIN, SOL40 and TELL40 of the MiniDAQ. The ECS software can be easily integrated with custom routines and panels in order to extend the control to the front-end under test. Most of the tests discussed later were done using the MiniDAQ_1 system, which is schematically shown in Fig. 3.5. The communication between the PC and the MiniDAQ exploits a particular protocol at application layer, called Distributed Information Management (DIM) [274], developed at CERN to provide a network

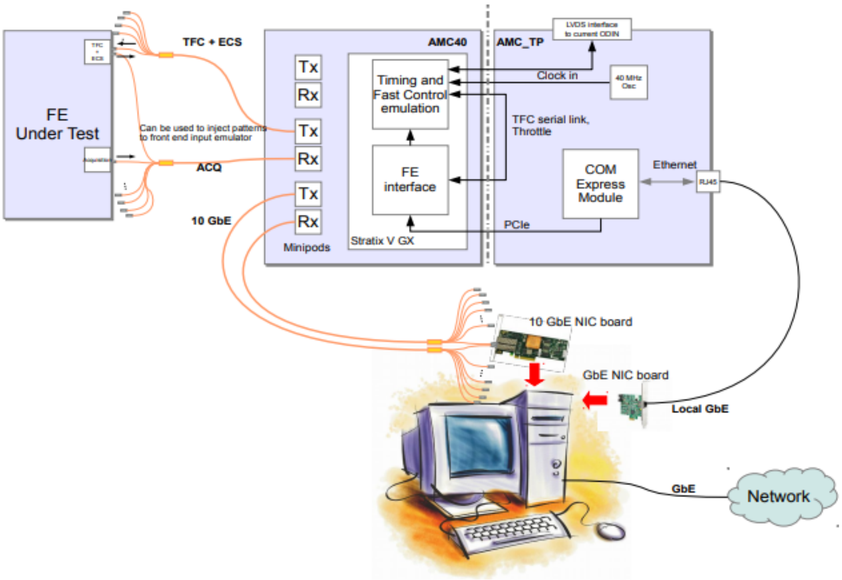

FIGURE 3.5. Schematic representation of the MiniDAQ_1 setup, with the AMC40 and AMC_TP boards. The PC is connected through the local Gigabit Ethernet (GbE) to the COM express module, which is able to instruct properly the FE interface of the FPGA, reading and writing its memory. Another 10 GbE connects the PC and the Tx/Rx minipods in order to access directly the data at TELL40 stage.

transparent inter-process communication layer. It is based on services request/offer between a client and a server. The services are requested by the client only once and they are subsequently automatically updated by the server when needed. This allows to avoid the Remote Procedure Call (RPC), largely used at application layer, when a continuous point-to-point and synchronous communication is necessary.

The first communication test between the nSYNC chip and the GBT-SCA was done using the MiniDAQ_1 system. A schematic view of the experimental setup is shown in Fig. 3.6, the experimental setup is composed of:

- nSYNC test board, already described in the previous section.
- MiniDAQ hardware setup, described previously. The AMC_TP board is powered at 12 V DC using an external power supply. The AMC40 is then automatically powered at 12 V and 3.3 V by the Power Management block of the AMC_TP.
- Versatile Link Demo Board (VLDB) [275]: it is a demo board to provide the GBT chipset to front-end electronics. It gathers the Versatile link main chips and modules: GBTx, GBT-SCA, VTRx/VTTx and the radiation-hard DC-DC converter. In this way the nSYNC test board, described in the previous section, can be connected to the VLDB board and interfaced with the GBT-SCA, without having to integrate the nSYNC within the nODE.

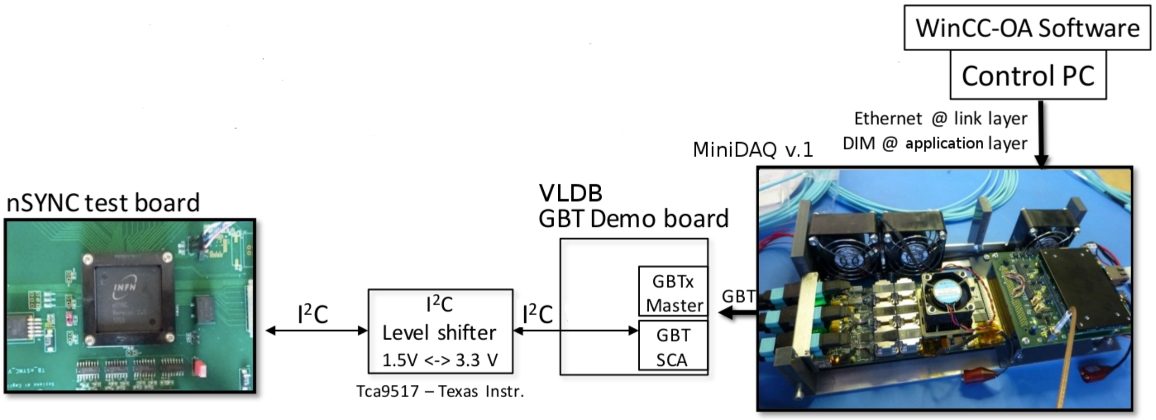

FIGURE 3.6. Schematic view of the nSYNC chain test. The nSYNC test board is connected to the I^2C bus of the GBT-SCA chip, present on the VLDB board (through the I^2C level shifter).The master GBTx of the VLDB is connected through the optical fibre to the AMC40 optical interface.

- I^2C levels shifter, model TCA9517 by Texas Instrument. This component was necessary because the first version of the GBT-SCA I^2C interface worked with 1.5 V levels, while the nSYNC interface works at 3.3 V.

A custom WinCC-OA library and a set of panels were developed in order to instruct the SOL40 to send the I^2C commands, through the GBT-SCA chip, to the nSYNC, testing successfully, for the first time, the communication between nSYNC and miniDAQ, effectively operating the nSYNC within the LHCb readout system. In particular the read/write operations on configuration registers and the read-only operations on internal nSYNC counters were successfully tested. The DCO calibrations were also properly launched.

3.1.2 Chain test with nODE and MiniDAQ

After the production of the first nODE prototype, shown in Fig. 3.7, a series of test was done to study its functionalities and performances. The master GBTx was successfully configured through USB-to-I^2C dongle provided by the CERN GBT group. The GBT optical link was tested by generating a PRBS pattern from the GBTx and acquired with an oscilloscope LeCROY SDA 816Zi-B, with 16 GHz of bandwidth and a sample rate of 40 GS/s, through an optical-to-electrical converter LeCroy mod.OE425. A continuous data stream of 200 μs at 40 GS/s allowed to produce the GBT link eye diagram of the nODE, showing an aperture of $\sim 50\%$ at a bit error ratio (BER) $< 10^{-16}$ and an average jitter of 110 ps at BER$< 10^{-13}$. The same test was performed with a 9 dB attenuator and three breakouts on the fibre, still showing acceptable horizontal and vertical openings of $\sim 35\%$ at a BER$< 10^{-16}$ and an average jitter of 122 ps at BER$< 10^{-13}$. Furthermore, the GBTx optical link was tested: the nODE master GBTx was

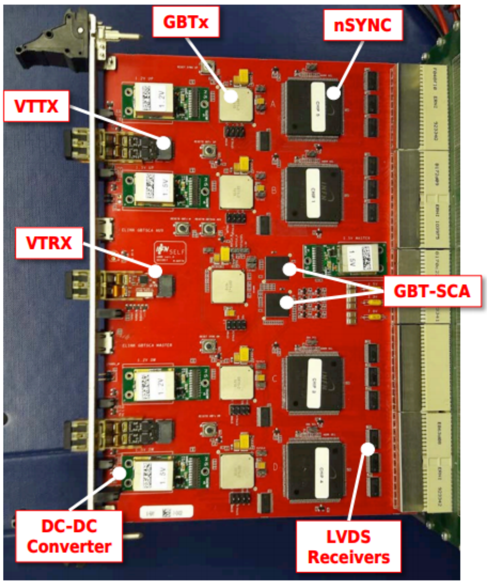

FIGURE 3.7. Picture of the first nODE prototypes, with the main components highlighted.

programmed to send a fixed pattern to a VLDB board, and the internal checker of the GBTx present on the VLDB was used to check bit errors. The test run without errors for 24 hours, with a BER$< 10^{-24}$ with a Confidence Level of 99%.

A major role was played in the chain test of the nODE with the MiniDAQ1 system, in which all the TFC/ECS and data paths functionalities were studied. The nODE board was connected to the MiniDAQ_1 through the master optical link (TFC/ECS path) and the other four optical links for data transmission, as shown in Fig. 3.8. The custom WinCC-OA library and set of panels was upgraded and integrated in order to configure the four nSYNC, use the GPIO bus of the GBT-SCA to reset the nSYNC and also monitor the different voltages present in the board through the ADC of the GBT-SCA. The main WinCC-OA panel, developed for the nODE test within the MiniDAQ control system, is shown in Fig. 3.9. In particular the main test performed on the nODE in this configuration are:

- TFC path: the master GBTx was configured in its default status (transceiver mode) and from the ECS custom panels the TFC commands were sent to the nODE, thus to every nSYNCs, continuously for two hours. The test was carried out with a 9 dB attenuation on the optical link. The corresponding nSYNC internal counters monitored the number of received TFC commands and a snapshot command was sent periodically to sample the counter values, in order to access them via ECS. Thus after a single test run, the snapshot command allowed to check the proper alignment of the four nSYNC, and to cross-check the number of sent TFC commands from the MiniDAQ control system and the ones actually received by each nSYNC.

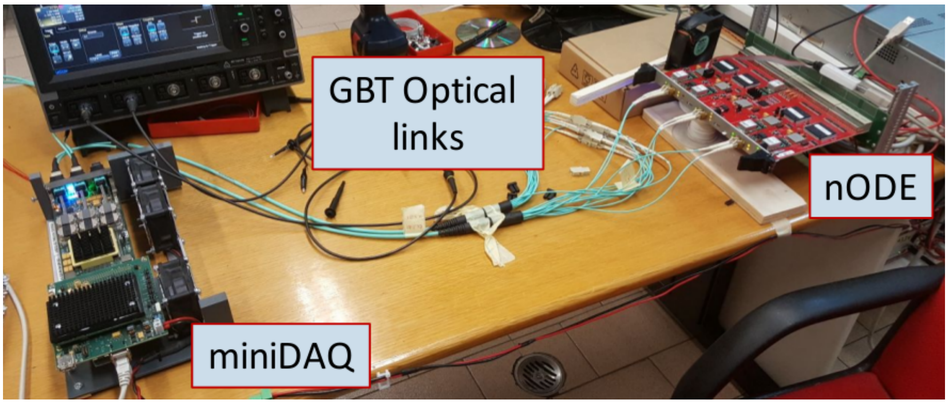

FIGURE 3.8. Picture of the first connection between the nODE prototype and the MiniDAQ system, similarly to Fig. 3.5 in which the role of FE is done by the nODE board.

- ECS path: with the master GBTx in transceiver mode, slow control commands were sent to the nODE from the MiniDAQ through our custom panels in WinCC-OA. The functions instruct the SOL40 to code properly the command for the target GBT-SCA into the GBT data frame, and the GBT-SCA subsequently acts on the nSYNC or the other GBTx, for example performing I^2C read/write operations. Each I^2C bus was tested performing 1024 read/write operations on configuration registers of nSYNC (via the auxiliary GBT-SCA) and the slave GBTx via the main GBT-SCA. No errors were detected. The GPIO was successfully configured both in input and output to monitor internal nSYNC status or perform the hard reset on the chips. The main GBT-SCA chip is used also to perform voltage measurements throughout its ADC lines, which were successfully used to monitor all power supply voltages: 7 V, 2.5 V, 3.3 V, 1.2 V, 1.5 V.

- DATA path: the slave GBTx were configured in transmitter mode and their clock is provided by the master GBTx, since it provides the clock generated after the recovery from the optical link. The nSYNC sends data to the GBTx through the LVDS output channels at 320 Mbit/s. The data from nSYNC can be misaligned with respect to the GBTx and several ways to align them exist: a programmable delay at the nSYNC output level ca be used to compensate the misalignment of the serial data stream, and also a fixed delay for all the channels can be added in order to shift the entire stream by multiple of the clock cycle; also a programmable phase shifter block of the slave GBTx chips can be used to align the phase of the clock used to strobe the data stream. Therefore, before starting the test of the links, the slave GBTx best sampling point and the correct data stream phase was determined. This procedure is very important at each nODE start-up, because the phases between the various clock are each time at different random values, despite the clocks being generated by the same source, from the master GBTx. An automatic procedure at ECS level has to be developed in order to adjust the delays at each start-up. After that, the slave GBTx was tested at optical link only, setting it to send a PRBS pattern that was verified from the MiniDAQ side. A similar second test was performed starting from the nSYNC that generated the PRBS pattern at each channel, also cross-checked at MiniDAQ level. A third test concerned the nSYNC-TELL40 communication, where the SYNC command of the TFC was used to synchronise the communication, verifying for the first time the right lock of the data stream. Within the MiniDAQ firmware, a custom VHDL block to check the PRBS data stream arriving through the optical link was integrated by the LHCb electronics Frascati group, allowing to check the presence of errors on the PRBS decoding. The slave GBTx PRBS test described above run without errors for ~ 48 hours, resulting in a BER $< 10^{-14}$ with a Confidence Level of 99%. The same test was replicated for 2 hours with 9 dB attenuation on fibre without errors. Concerning the nSYNC PRBS data stream, all 56 links were tested for ~ 64 hours without errors, where each link reached BER $< 10^{-13}$ with a Confidence Level of 99%. An eye diagram at e-link level was acquired with an active probe on the receiver side and the same oscilloscope mentioned before (LeCROY SDA 816Zi-B). The eye diagram features were found to be compatible to the ones found using the nSYNC test board only.

These tests were presented at the Production Readiness Review at CERN in Ocotber 2017 in order to start the production procedure of the nSYNC and nODE.

3.2 Introduction to radiation damage of electronics

Although the readout system of the muon detector will not be placed in a strongly radiated area, it will have to work for ten years of LHCb upgrade activity in an environment with non-negligible radiation level. The nODE board is made up entirely of radiation hard devices that can tolerate the radiation doses foreseen for upgrade activities, but the nSYNC chip, being of recent development, needs to be characterised from the point of view of its radiation hardness. For this reason a series of tests were performed to verify the performance of the nSYNC chip, both using proton beams and X-rays. Before describing the tests, some concepts and observables that are necessary for the subsequent discussion are now introduced.

3.2.1 Units and radiation environment

In the LHC collisions a high fluence of high energy particles is produced, where the fluence is the time integrated flux, measured in particles/cm^2. The particles interact with the detector materials, the electronics, all the infrastructure and the cavern walls. In particular the silicon semiconductors are affected by two main radiation damage effects:

- Ionisation damage: when a charged particle passes through the semiconductor it releases energy through electromagnetic interaction, creating electron-hole pairs that can diffuse,

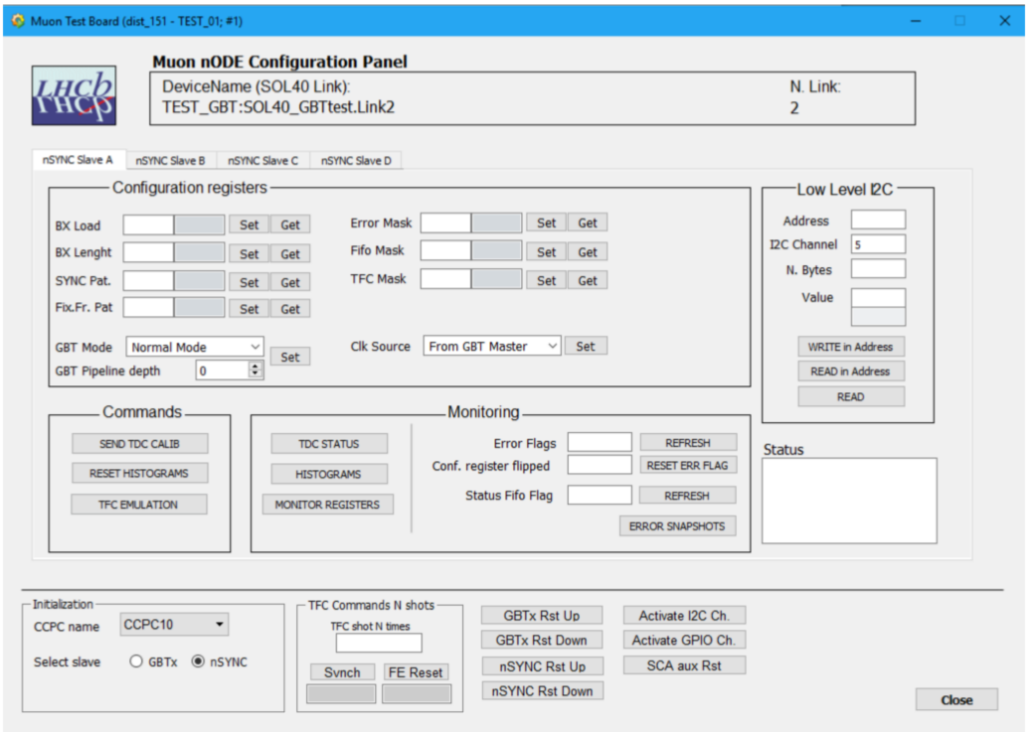

Muon Test Board (dist_151 - TEST_01; #1)

Muon nODE Configuration Panel

DeviceName (SOL40 Link): TEST_GBT:SOL40_GBTtest.Link2

N. Link: 2

GBT Mode: Normal Mode

GBT Pipeline depth: 0

Clk Source: From GBT Master

I2C Channel: 5

CCPC name: CCPC10

Select slave: ○ GBTx ● nSYNC

Figure 3.9. WinCC main panel of the software developed to test the nODE and nSYNC functionalities within the MiniDAQ control system. For each nSYNC the main configuration registers can be accessed, with a special space for low level I^2C communication. The main commands like calibration, reset and TFC emulation can be easily sent, while another space is dedicated to the monitoring (TDC calibrated DCO values, histograms content, error counters, etc.).

drift under local fields or be trapped. This modifies the electrical properties of the device in terms of current consumption, time response, introducing abnormal transient and dangerous currents or change the digital behaviour. Ionisation damage depends mainly on the absorbed energy per unit volume (dose), expressed in rad ($1\text{rad} = 100\,\text{erg/g}$) or gray ($1\text{Gy} = 1\text{J/kg} = 100\,\text{rad}$).

- Displacement damage: an incoming particle can release part of its energy in collisions with atomic nuclei, thus displacing silicon atoms from their lattice positions, creating single point defects or a tree of vacancies and interstitials. This mechanism leads to silicon bulk damage, with a modification of the electrical properties of the crystal.

The order of magnitude of total ionising dose for ten years of activity in a typical detector environment at LHC ranges from 10 Mrad in the most irradiated regions to few krad at distances where usually the off-detector electronics is installed. The ionising spectrum is largely dominated by gamma rays with energies up to few MeV, but also protons and pions contribute in some specific areas. Neutrons are also present with a spectrum similar to the gamma rays but with a large low energy component. The neutron fluences ranges from $\mathcal{O}(10^{14})\,\text{cm}^{-2}$ in the innermost regions to $\mathcal{O}(10^{10})\text{cm}^{-2}$ within the cavern. Hadrons with energy greater than 20 MeV (a typical quantity used to quantify the radiation levels), like protons or pions, are in general present with fluences one order of magnitude less than that of neutrons.

3.2.2 Radiation effects on silicon devices

Some concepts useful to study the radiation damage on readout electronics are now introduced, explaining in particular the main radiation damage mechanisms mentioned before.

Displacement damage

An incident particle or photon can transfer enough momentum to a silicon atom to displace it from its lattice site, creating a vacancy (V) and an interstitial (I), called *Frenkel pair*. The kinetic energy necessary to dislocate the atom is about 25 eV. Even though this energy is quite low, the collision kinematics imposes higher energy for the incoming particles: for neutrons the energy threshold is about 10 keV, for electrons/positrons is 125 keV and for photons 250 keV. For this reason X-rays and gamma rays below this energy do not cause direct displacement, but they can generate an appreciable quantity of Compton electrons, that could interact with silicon atoms and produce displacement damage. Thus the damage can depend on the photon spectrum and on the shielding materials near the target considered. A 1 MeV neutron can transfer from 60 to 130 keV, displacing a high number of silicon atoms: the first ones are called knock-on-atoms (PKAs) and have very high energy. They will subsequently displace other atoms, forming a displacement tree, as shown in Fig. 3.10, that is in general difficult to characterise, due to the high mobility of vacancies and interstitials. Generally the vacancies are highly active from the electronic point of view: for example the di-vacancy (V-V) system, the one most known, has many electronic levels in the forbidden gap of silicon, and the interaction between the V-V system and intrinsic impurity complexes (phosphorous, boron, oxygen, germanium etc.) present in the lattice can shift such energy levels in a multitude of different configurations. These additional levels leads to trapping, hole/electron capture and electron/hole emission to their corresponding conduction bands, therefore generating intrinsic thermal noise and increase the leakage current, with an exponential reduction of minority-carrier lifetimes and diffusion lengths with respect to the irradiation fluence. Due to the high mobility, the defects can recombine as a function of time and of temperature, a phenomenon called *annealing*. The annealing curves, for example for the current consumption, are generally not described by a single exponential with respect to time, and show a saturation value, usually called *unannealable* component, related to permanent damage in silicon. In some cases the damage becomes more severe with respect to time (the so-called reverse annealing), due to diffusion of defect species from clusters with unstable configuration.

The displacement damage is linked to the non-ionising energy loss (NIEL) of particles through matter*, that is not proportional to the total energy absorbed, but to the energy and type of the incident particle. Since NIEL was studied for a wide range of energies and particle types, generally one can estimate the displacement damage for a specific particle and energy relatively to another energy and particle type, applying the same proportion of their NIEL (procedure called NIEL *scaling* or *rule*). Violation to this principle was observed and for a more detailed study also the defect formation has to be taken into account.

In neutron interactions, the dominant process for NIEL is the elastic scattering with nuclei, for an incoming energy range between 50 keV and 14 MeV. It is worth to note that a *ionising* damage can be associated also to neutron irradiation, since it is related to the ionisation energy loss by the PKAs. For neutrons the two contributions are generally of the same order of magnitudes.

For protons and heavy charged particles, the dominant processes for producing displacement at high energy (above 20 MeV) are strong elastic and non-elastic interactions, while at energies below 10 MeV the dominant process is the Coulomb scattering with the nuclei. In this case it is important to note that charged particles dissipate energy through ionisation, causing the excitation and ionisation of atoms close to the trajectory. This energy loss mechanism is highly dominant with respect to NIEL.

A useful unit of measure was introduced to quantify the damage caused by NIEL: the *1 MeV equivalent neutron fluence*, defined as the fluence of 1 MeV neutrons producing the same damage in a detector material as the one produced by an arbitrary particle fluence with a specific energy distribution.

Total Ionising Dose (TID) effects

The ionisation energy loss is usually called *total ionising dose* or simply *total dose*. The charged particle passing through matter interact electromagnetically with the electrons in the medium and they can acquire enough energy that electron-hole (e-h) pairs can be produced. The charges are then free to drift under the local fields and eventually be trapped. This mechanism is very important in MOS devices, since the energy required to create the e-h pair is relatively small also in the insulator (18 eV in SiO_2) and the charges are easily trapped. From the point of view of radiation damage effects, one of the most important mechanism is the trapping near the interface SiO_2-silicon, that can drastically change the electrical properties of MOS transistor in CMOS based electronics and integrated circuits. Holes produced by ionisation can slowly drift towards the SiO_2-Si interface and be trapped in the oxide. Since they cannot be excited back into the conduction band by thermal processes, because the required energy is too high, they

---

*NIEL involves both energy dissipation through atom displacements and through lattice vibrations without any displacement.

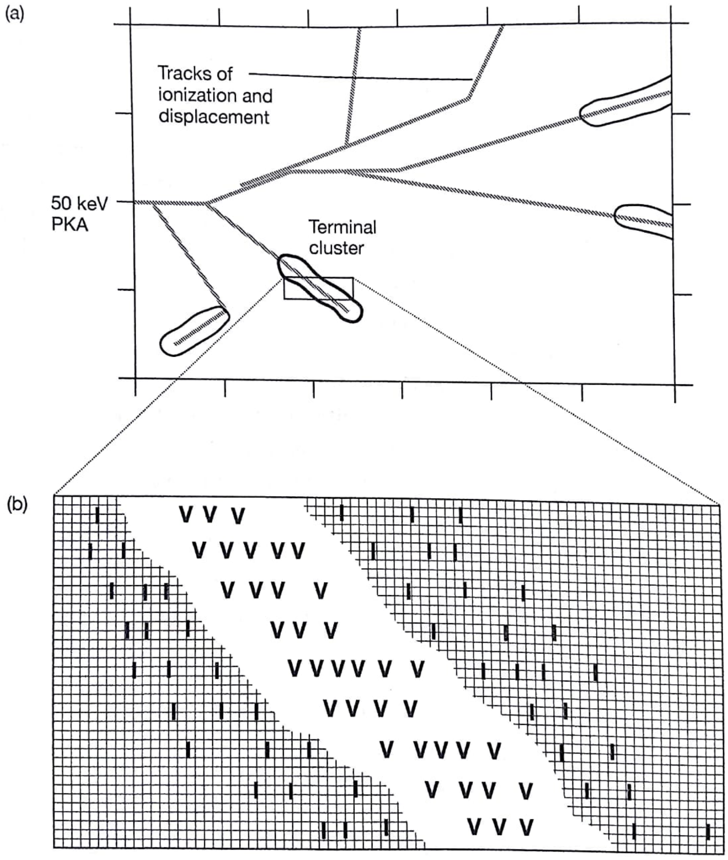

Figure 3.10. Picture of atomic displacement on Si crystal by an energetic PKA. The PKA has a typical range of 100 nm at 50 keV. Figure taken from [276].

start to accumulate during irradiation, building up a charge layer. This layer, always positive, exactly at the transistor gate, shifts the gate voltage required to maintain a given current flow.

Typically the trapped holes in the SiO_2 bulk (5-20 nm from the Si interface) remains long-lived. Near the Si interface (2.5-5 nm) there is a layer of unstable interface-traps, whose net charge depends on the Si doping type. In this layer the probability of electron tunnelling from Si is high enough that recombination with holes from the oxide bulk can occurs, thus leading to a slow annealing mechanism. A schematic view of these layers can be seen in Fig. 3.11. The effect is highly dependent on the bias conditions: irradiated CMOS devices with no bias show a significant lower degradation. A dependence on temperature is also known, where higher temperature enhances degradation although always remaining under threshold for holes annealing, which happens at about $\sim 90°C$. As already mentioned, the electrical consequence are several and important. The main effects are the lowering of transconductance, the distortion of drain-gate current properties, the gate voltage shift and the degradation of time response.

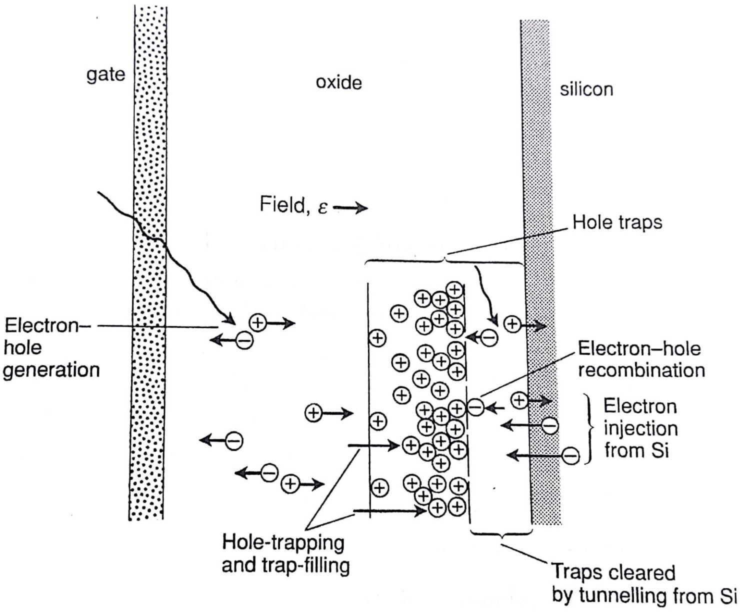

FIGURE 3.11. Scheme of the charge build-up mechanism under radiation, in which the effect of tunneling near the Si interface is visible. Figure taken from [276].

3.2.3 Single Event Effects

Single Event effects are a special case of ionisation effects that can occur due to a single impact of an energetic particle. They can be classified in several categories according to the produced effects.

Single Event Upset

The Single Event Upset (SEU), also named *soft error* or *bit-flip*, is the change of state of a bistable element due to the released charge by an energetic heavy ion ($Z \geq 2$) ionisation. The affected electronic devices are the digital ones like SRAM, DRAM, FLASH memories, FPGA and microprocessors. The generation mechanisms that lead to a SEU are two:

- Direct ionisation. A particle with $Z \geq 2$ can produce enough e-h pairs along its passage due to ionisation. The e-h produced in the bulk are mainly subject to recombination, but the ones produced near a junction or within the depletion zone are separated and collected by the local electric field, leading to a current spike. This is generally named Single Event Transient (SET). If the charge is high enough, the spike can potentially trigger the digital status change of the component and in that case it is called SEU. The collection region can extend outside the normal depletion zone due to a phenomenon called *funneling* and it is shown in Fig. 3.12. This causes the current spike to have a fast component of $\mathcal{O}(\text{ps})$ and a slower component of $\mathcal{O}(\text{ns})$.

- Indirect ionisation. The incoming particle interact with the Si atom and produce heavy ions in the collisions, that will subsequently produce a charge sufficient to induce a SEU with direct ionisation. This mechanism is the dominant one for incoming neutrons and protons, because they do do not create enough charges to directly cause a SEU. A possible process is the proton-Si strong inelastic collision that can produce a recoiling proton, an α particle and a recoiling magnesium ion. A wide variety of these types of reactions can take place depending on their energy thresholds, especially if the incident particles spectrum is not monochromatic and composed of neutrons, protons and gamma rays, like the typical LHC radiation spectrum. Thermal neutrons also can cause SEU, since the capture reaction with boron (widely used in semiconductors as dopant and in passivation layers) produces α particles and lithium.

The capability of an incident ion to produce enough e-h pairs to trigger a SEU depends on the linear energy transfer (LET) and the sensitive volume. LET is just the mass stopping power, measured in $\mathrm{MeVcm^2mg^{-1}}$, and defined as

$$\mathrm{LET} = \frac{1}{\rho}\frac{dE}{dx},$$

where x, E are respectively the position and the energy of the particle producing directly the ionisation (thus does not apply to neutron or proton energy) and ρ is the material density. In order to actually trigger a SEU a charge greater than a given threshold called *critical charge* (Q_c) has to be released in a *sensitive volume* (SV), a critical region with a typical depth of few microns in which the prompt current or voltage change can induce the digital status change of the device. The size of the sensitive volume and the voltage difference to trigger a SEU are of fundamental importance and the critical number of electrons can vary by many orders of magnitude according to the transistor size and chosen technology. The technology evolution towards smaller geometries leads to a decrease of sensitive volume and consequently of critical charge, resulting in a increased SEU vulnerability.

The SEU exposure can be empirically measured with the so-called SEU cross section, usually as a function of LET, and measured in $\mathrm{cm^2}$. It is defined as the number of observed SEU per unit of fluence,

$$\sigma(\mathrm{LET}) = \frac{N_{\mathrm{SEU}}}{\Phi},$$

where Φ is the fluence of incoming particles. The value of N_{SEU} can be an integrated quantity (number of SEU observed for an entire chip) or can be normalised to the total number of sensitive bits. In the latter case the cross section quantify the vulnerability of a given device developed with a specific technology. While increasing the LET the cross section saturates to a specific value called saturated cross section.

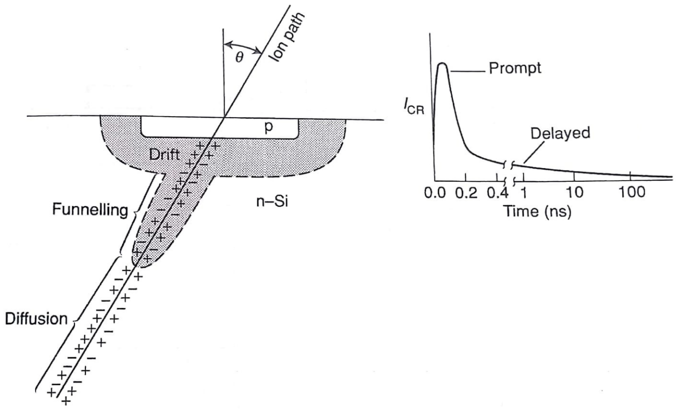

FIGURE 3.12. Scheme of e-h creation due to a ion passing through the device. The corresponding current pulse with the fast and slow components is shown on the right. Figure taken and modified from [276].

Single Event Latch-up

A Single Event Latch-up (SEL) is a potential destructive single event effect in which a very high current flows within a transistor circuit due to a single ionisation effect. In bulk CMOS structure there are parasitic p-n-p and n-p-n transistors that can couple together to form a parasitic thyristor device. The thyristor is similar to a diode, conducting when the gate receives a current trigger and continuing to conduct until the gate is reverse biased. Under normal operation the parasitic thyristor is "off", but, for a sufficiently large ionising pulse, it can be triggered in an "on" condition. The positive feedback causes the device to remain in low impedance state, so this single event effect is potentially destructive for the device. Other non-destructive single event effects have been observed and studied in detail. A condition known as *"snapback"*, affecting n-channel transistors, is characterised by a three-layer avalanche activation with positive feedback and thus recoverable under normal operations. Another similar non-destructive effect, known as *soft latch-up*, leads to a general stuck of the device, recoverable only under a power cycle.

3.3 Expected radiation levels for LHCb upgrade

The nODEs will be mounted near the muon stations, outside the detector acceptance, as shown in Fig. 3.13 (left). In order to compute the expected radiation levels for LHCb upgrade, the most irradiated regions are taken into account, i.e. those near the M2 station. In LHCb coordinate system these correspond to

$$x = \pm 5\,\text{m}, \quad -1\,\text{m} < y < 1\,\text{m}, \quad z = 15.2\,\text{m}.$$

The radiation levels in the LHCb underground environment can be studied with simulations and verified with periodic measurements. The simulations are based on the FLUKA package [277], which is a general purpose software of particle transport and interactions with matter. Using a detailed description of detector geometry, the radiation field can be simulated with a good accuracy and allows the estimation of charged hadrons and neutrons fluence values and the total ionisation dose. The same software was used to predict radiation levels during the LHCb upgrade operations. For the muon detector some considerations are needed

- The muon towers structure is not accounted for in the simulation geometry, thus any shielding effect from them is also missing.
- A general systematic was observed: simulation values for dose tend to be lower than measurements in most parts inside the acceptance. The missing tower structure can compensate this systematic trend in the nODE crates regions. Indeed radiation level measurements took during Run I suggest that the simulation was quite accurate in the ODE crates region.

Taking these considerations into account, the LHCb simulations group recommends anyway to apply a safety factor 2 to all the estimated fluence and dose values.

The radiation level in ODE crates regions is not so critical, being about $20-40$ times smaller than the one present in FEB regions. Using the aforementioned simulations, the radiation levels obtained for 10 years of upgrade operation (this period will be called 1 equivalent LHCb upgrade in the following) in the most irradiated nODE regions are the following[†]:

- TID: 130 Gy average, with a maximum TID < 200 Gy.
- Ionisation dose rate: $\sim 6 \cdot 10^{-7}$Gy/s.
- Fluence of hadrons with energy greater than 20 MeV: $2 \cdot 10^{11}/\mathrm{cm}^2$.
- Fluence of 1 MeV neutrons equivalent: $2 \cdot 10^{12}/\mathrm{cm}^2$, with the corresponding NIEL dose of 0.65 Gy.

All the values above include already a safety factor of 2. The output of the FLUKA simulation for TID is shown in Fig. 3.13(right). The FLUKA output values are the local TID, measured in Gy, and the local fluences, measured in cm^{-2}. The values are normalised per single proton-proton collision, therefore the results were scaled considering the nominal upgrade luminosity and an operation time period of ten years. In order to cross-check the correct calculation, the values were compared with the ones from the current LHCb operation, already calculated by the simulation group, and rescaled by the luminosity, showing consistent results.

[†] All the doses in Gy are referred to absorbed dose in silicon. Any reference to other materials will be explicitly pointed out.

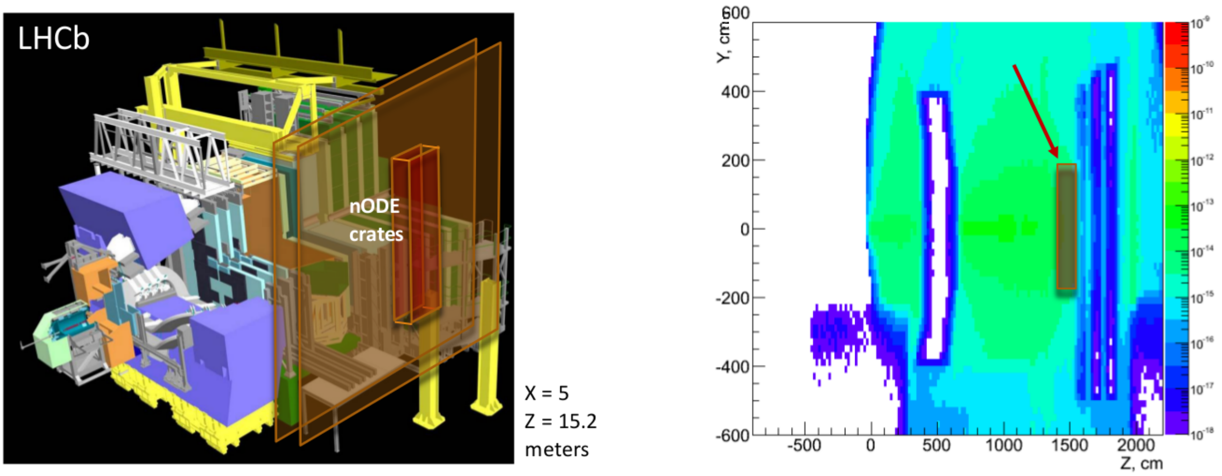

FIGURE 3.13. Left: a schematic view of the LHCb detector and the approximative positions of the nODE racks near M2, where the radiation levels are more important. Right: Output of the FLUKA simulations for TID, measured in Gy/collision, with the interesting regions highlighted in dark red.

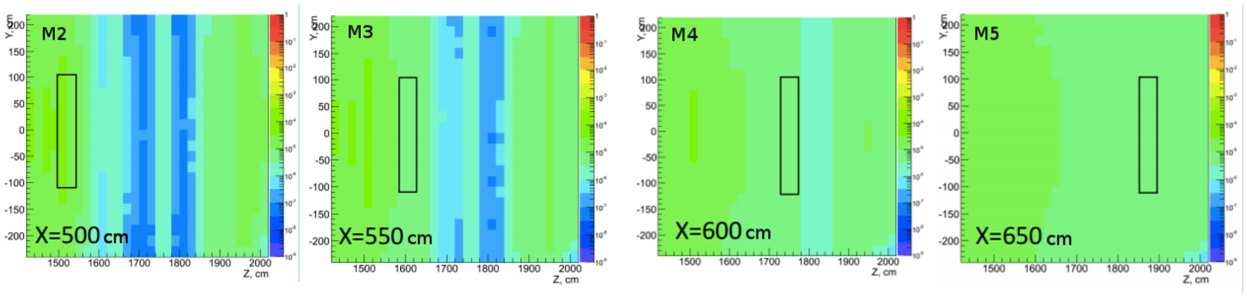

FIGURE 3.14. Output of the FLUKA simulations for hadrons fluence, measured in hadrons per collision per cm^2, in the interesting regions near each station.

The doses are also estimated near the other stations, by simply shifting the corresponding x and z coordinates and leaving y the same. These values together with the M2 region are reported in Tab. 3.1, while their corresponding TID values are also shown in Fig. 3.14. It is interesting to note that in M5 the fluences are a bit larger that in M4, due to the scattering of the incoming particles with the cavern wall behind M5, which constitute a non negligible source of low energy background.

Station	LHCb coordinates [m]	Average TID [Gy]	Hadrons fluence $E > 20\,\mathrm{MeV}$ [cm^{-2}]	1 MeV neutrons equivalent fluence [cm^{-2}]
M2	$x = \pm 5, \quad z = 15.2$	130	$2 \cdot 10^{11}$	$2 \cdot 10^{12}$
M3	$x = \pm 5.5, \ z = 16.4$	60	$6.6 \cdot 10^{10}$	$1.7 \cdot 10^{11}$
M4	$x = \pm 6, \quad z = 17.6$	53	$6.3 \cdot 10^{10}$	$1.4 \cdot 10^{11}$
M5	$x = \pm 6.5, \ z = 18.8$	48	$7.4 \cdot 10^{10}$	$2 \cdot 10^{11}$

TABLE 3.1. Values for average TID, hadrons and 1 MeV neutrons equivalent fluence for the different interesting regions in all the four stations.

3.4 nSYNC radiation hardness

Sub-micron UMC CMOS processes are one of the preferred technologies for the development of radiation tolerant ASIC. The nSYNC chip was developed in UMC 130 nm technology, and designed equipped during the design of two main radiation hardness features to mitigate the SEU occurrence:

- Triple Modular Redundancy (TMR): in order to protect a single bit of memory, the bit information is stored into three different registers, and the actual output is obtained using a digital logic that checks the majority of the three values. In case of a bit-flip in one of the three bits, the flipped register is refreshed with the majority value at the next clock cycle. In this way the circuit can tolerate a single bit-flip without changing its output and therefore without causing any malfunctioning. Only in case of a double bit-flip in two of the related registers the output value will be wrongly refreshed. The disadvantage of this solution is the increase of the circuit area and in the switching power by about a factor three. For this reason only the most critical registers, such as the first input stage of TFC commands and the configuration registers are protected by the TMR.

- Hamming code: it consists of an algorithm to perform the parity check of a digital word. The algorithm first performs the parity check and add extra bits to the word at specific positions. The protected data can be then extracted by a logic, named Error Detection And Correction (EDAC), able to recalculate the parity of the entire word, including the previously added check bits. The EDAC algorithm is able to establish if there was one or two errors and, in case of single error, to correct it. With respect to TMR, the advantage is that there is not a significant increase in the circuit area and in the power consumption, but the drawback is that not all the bits are protected and in case of double errors (on a large number of bits) the errors can not be corrected. All the internal counters for monitoring operations, the internal buffers and the output FIFO are protected by the Hamming code and EDAC system.

Other types of error can occur within the chip logic and are properly monitored internally. A

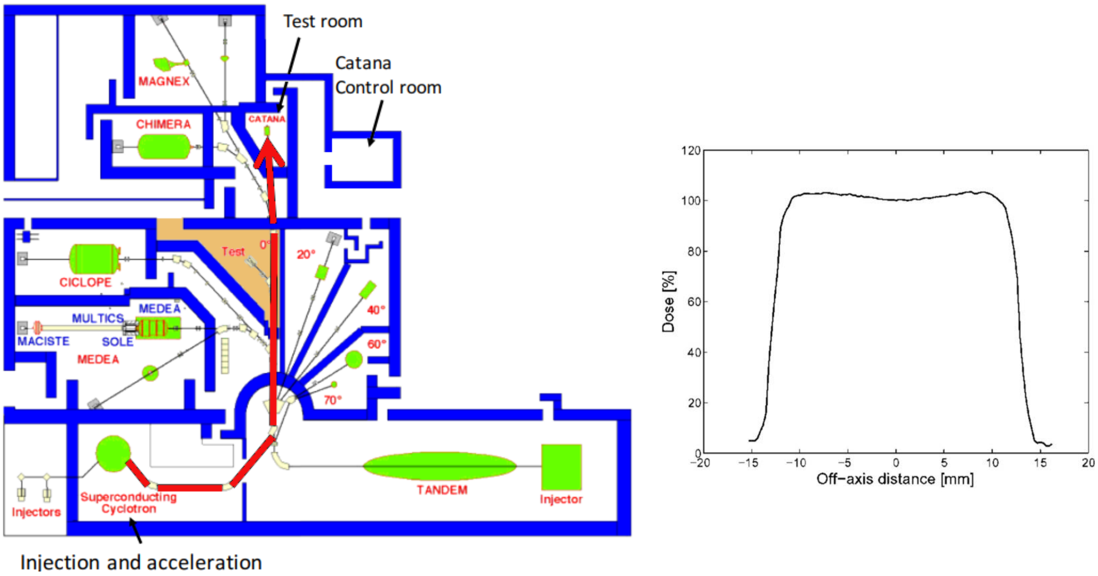

FIGURE 3.15. Left: Schematic view of the LNS complex, with the beam line for the CATANA test room highlighted in red. Right: Lateral beam profile without collimator.

set of six flags was implemented to signal these errors, monitoring for example the number of errors detected by the EDAC and by the TMR system.

3.5 Irradiation with proton beam

3.5.1 The proton facility

The irradiation tests were carried out with proton beam at the CATANA (Centro di AdroTerapia Applicazioni Nucleari Avanzate) facility, at the Istituto Nazionale di Fisica Nucleare (INFN) - Laboratori Nazionali del Sud (LNS), in Catania (Italy). The facility is dedicated to the radiation treatment of ocular diseases using a 60 MeV proton beam, accelerated by the INFN-LNS superconducting cyclotron. The beam line is shown in Fig. 3.15. In the CATANA room the beam pipe terminates and the accelerated protons exit in air through a 50 μm Kapton window. Two tantalum foils are placed upstream and downstream the exit window in order to perform a two steps beam broadening and to obtain the optimal homogeneity in terms of lateral dose distribution. The second tantalum foil, 25 μm thick, downstream of the exit window, is also used as Secondary Emission Monitor (SEM): the emission of secondary electrons, produced when the primary beam pass through the foil, generate a current that is converted in a voltage, V_{th}, proportional to the beam current. The proton energy is of 60 MeV and the flux is $5.69 \cdot 10^8$protons cm^{-2}s^{-1}. A collimator of 15 mm diameter is used to define the beam spot, to keep guaranteeing an homogeneous lateral profile.

The choice of using a 60 MeV protons beam is justified by the fact that the probability curve

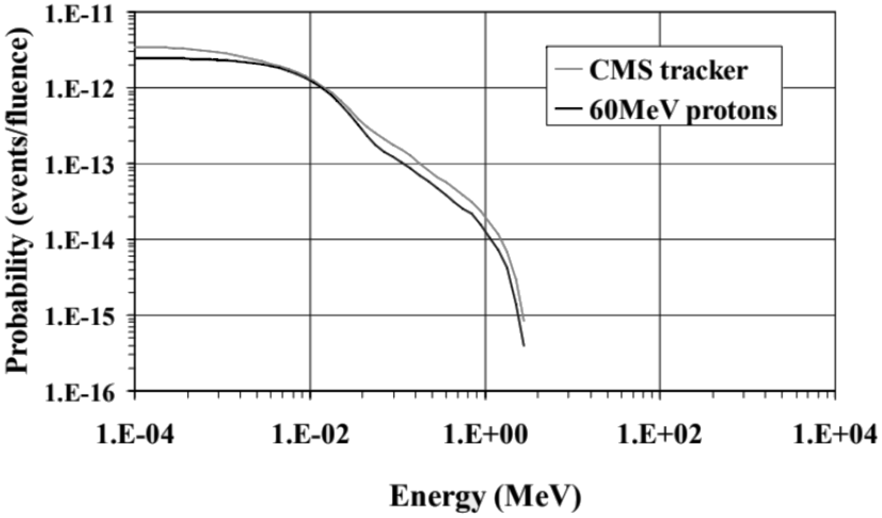

FIGURE 3.16. Probability per unit of flux to deposit an energy equal or larger than E_{dep} in the sensitive volume, as a function of E_{dep}, for a typical LHC environment (CMS tracker) and using a 60 MeV proton beam. Plot taken from [278].

to cause a SEU with respect to the deposited energy in the sensitive volume is very similar to the one obtained for a typical LHC environment, as can be seen in Fig. 3.16, in which the probability per unit of flux to deposit an energy equal or larger E_{dep} is shown as a function of E_{dep} [278, 279].

3.5.2 Experimental setup and test plan

Before the radiation test, several dry run tests were performed to optimise the experimental setup, to develop and test the data acquisition system and to check the absence of any types of errors. The experimental setup is composed of:

- The nSYNC test board. Three different chips were tested under proton irradiation, while in addition several others were used for the dry test run in our local laboratory.
- Two Keithley Source Meter (2400 and 2410 model), were used to provide the 3.3 V and 1.2 V voltages to supply the I/O and the core of nSYNC respectively. They were also used to measure the respective current consumption remotely.
- An oscilloscope Tektronix TDS3054B: used to monitor the 320 MHz PLL jitter and the signal integrity of one of LVDS output channel.
- The USB-to-I^{2}C elite tool: already used for nSYNC pre-production test, it was used to send directly I^{2}C commands to the nSYNC test board from a remote PC using the custom DAQ software explained below.

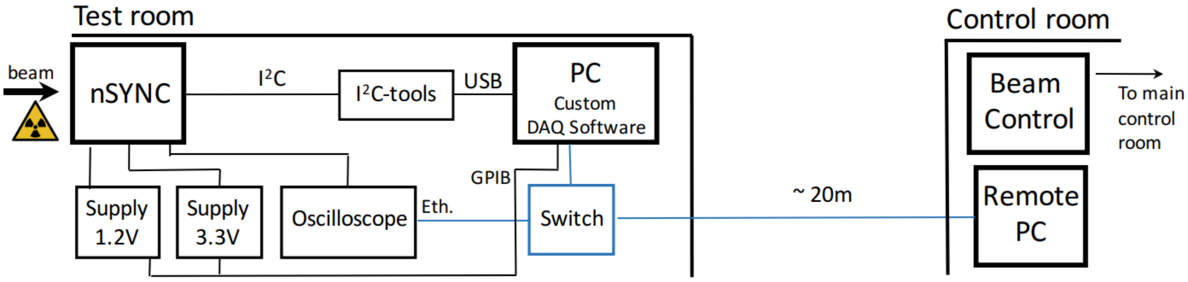

FIGURE 3.17. Scheme of the experimental setup connections.

- An ethernet switch and a General Purpose Interface Bus (GPIB), in order to connect respectively the oscilloscope and the power supplies to the same PC and be able to control the whole experimental setup within a unique DAQ software. In particular the connection between the power supplies and the PC was done with a National Instrument GPIB-USB-HS interface.

During the irradiation test the main PC was left inside the test room, and controlled remotely using another PC connected to a local network, as shown schematically in Fig. 3.17.

DAQ custom software

The DAQ system was developed with the aim to centralise all the control, monitoring and data acquisition in a unique complete custom system. Thanks to the proprietary libraries and interface for the oscilloscope and the I^2C tools, and using simple GPIB instructions for the power supplies communication, a single DAQ software was written in LabVIEW. It is composed of a set of custom libraries for the most fundamental operations, a front panel for the user interface, shown in Fig. 3.20, and the main diagram block in which all the code was implemented. The DAQ system is able to perform many operations, in particular:

- set the voltage supplies, monitor periodically the power consumption for both the 3.3 V and 1.2 V supplies, since the trend vs. time is indicative of the TID damage;
- read periodically the error flags (introduced in the previous section), the corresponding error-triggered snapshots for all the counters or read directly the error counters on request;
- read periodically the DCO calibration code for all the 48 channels, since they are not error-protected and are fundamental to estimate the SEU cross section. The possibility to start the DCO calibration for all the channels at all resolution was also implemented, both on request or periodically. The trend of the DCO values with respect to resolution is also shown on the front panel for a quick view;

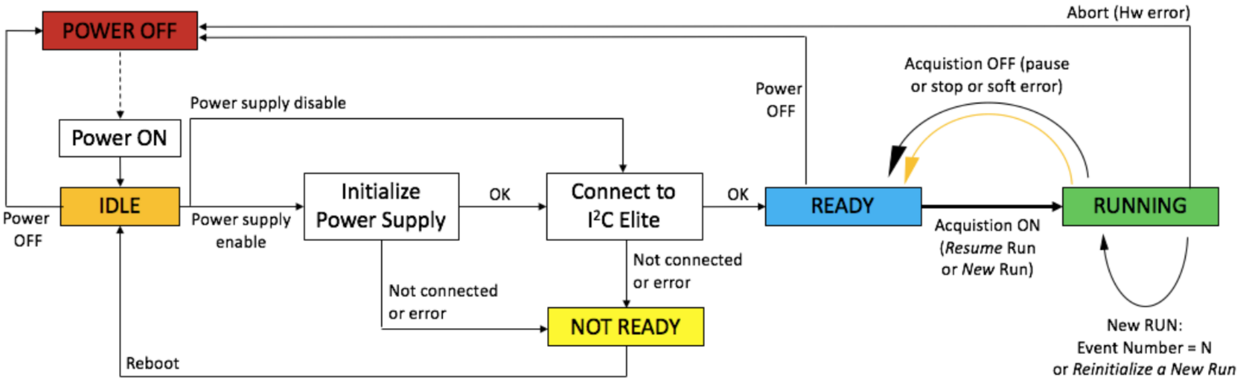

FIGURE 3.18. Scheme of the 5 states FSM of the DAQ software. After the power ON, the FSM goes into the IDLE state in which the main hardware components are not yet initialised. If they initialise correctly the status becomes READY to launch the run.

- read and save periodically all the values stored in the histogram registers, since they correspond to 2304 bytes not error-protected and are useful to estimate the SEU rate;
- read and save periodically all the TMR protected configuration registers, useful to check the TMR correction. A low level I^{2}C read and write operation was also implemented to perform such operation on configuration and command registers if needed, for example to change the output pattern to be read by the oscilloscope;
- monitor the PLL period jitter and the output LVDS driver stability requesting periodically the measurements to the oscilloscope.

The software is composed of a fast loop continuously running that waits for user actions. The main actions such the start of the run, pause etc. are linked to an internal FSM described in the following and shown in Fig. 3.18. A second asynchronous loop that performs the main operations sequentially, shown in Fig. 3.19, was implemented. As anticipated the software is based on a FSM with 5 different states in order to switch easily between the implemented functionalities, run initialisation of the instruments and especially to perform a reliable error handling and recovering. The nSYNC board was aligned in front of the beam using an optical system. The experimental setup is shown in Fig. 3.21, while the nSYNC test board in front of the beam collimator is shown in Fig. 3.22.

Test Procedure

As already mentioned, three chips were tested with proton beams, the first one for dose rate calibration and software debugging, while the other two for the final analysis, showing consistent results. For each chip, the test was divided in 7 runs. In the first 5 runs the beam intensity

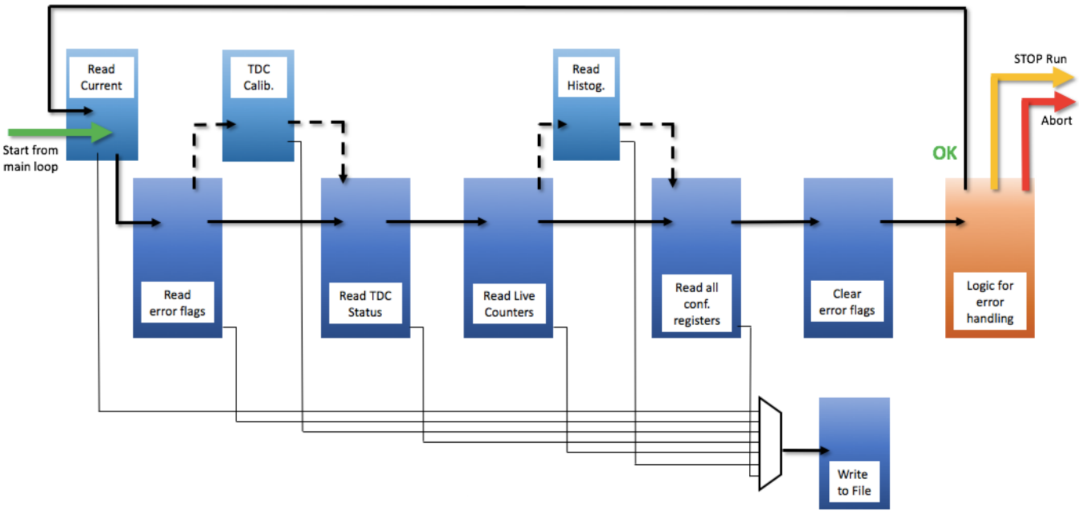

FIGURE 3.19. Scheme of the sequential procedure of the acquisition loop. The TDC calibration and the download of the histograms can be disabled or activated periodically when needed. The final logic for error handling is used in the FSM logic to decide if staying in the running status.

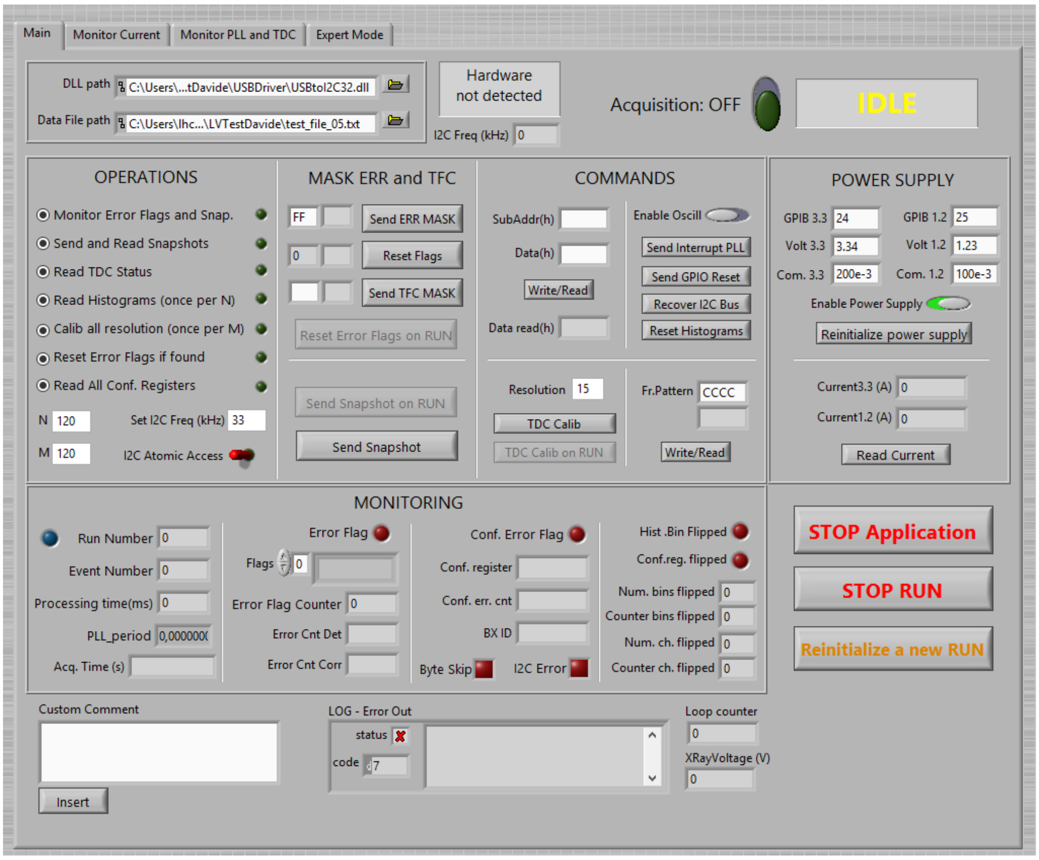

DLL path C:\Users\...tDavide\USBDriver\USBtoI2C32.dll

Data File path C:\Users\lhc...\LVTestDavide\test_file_05.txt

Hardware not detected

I2C Freq (kHz) 0

Acquisition: OFF

IDLE

○ Monitor Error Flags and Snap.
○ Send and Read Snapshots
○ Read TDC Status
○ Read Histograms (once per N)
○ Calib all resolution (once per M)
○ Reset Error Flags if found
○ Read All Conf. Registers

N 120

M 120

Set I2C Freq (kHz) 33

I2C Atomic Access

FF

0

SubAddr(h)

Data(h)

Data read(h)

Enable Oscill

Resolution 15

Fr.Pattern CCCC

GPIB 3.3 24

GPIB 1.2 25

Volt 3.3 3.34

Volt 1.2 1.23

Com. 3.3 200e-3

Com. 1.2 100e-3

Enable Power Supply

Current3.3 (A) 0

Current1.2 (A) 0

Run Number 0

Event Number 0

Processing time(ms) 0

PLL_period 0,000000(

Acq. Time (s)

Error Flag

Flags 0

Error Flag Counter 0

Error Cnt Det

Error Cnt Corr

Conf. Error Flag

Conf. register

Conf. err. cnt

BX ID

Byte Skip

I2C Error

Hist .Bin Flipped

Conf.reg. flipped

Num. bins flipped 0

Counter bins flipped 0

Num. ch. flipped 0

Counter ch. flipped 0

Custom Comment

LOG - Error Out

status ✗

code 7

Loop counter 0

XRayVoltage (V) 0

FIGURE 3.20. Picture of the main front panel of the DAQ software.

FIGURE 3.21. Left: picture of the final experimental setup within the CATANA room, in particular the nSYNC test board and the oscilloscope are shown. Right: The main control PC, the two power supplies and the various connections are shown.

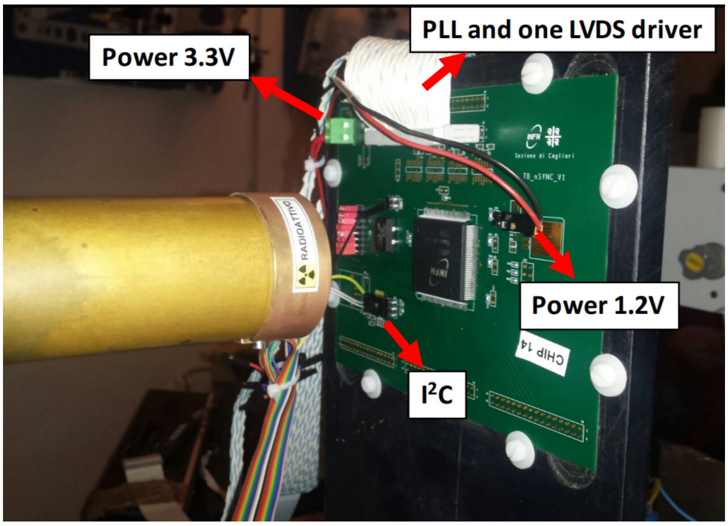

FIGURE 3.22. Picture of the nSYNC test board in front of the beam collimator. The I^{2}C bus, the power connections and the probes for the PLL and LVDS drivers are highlighted.

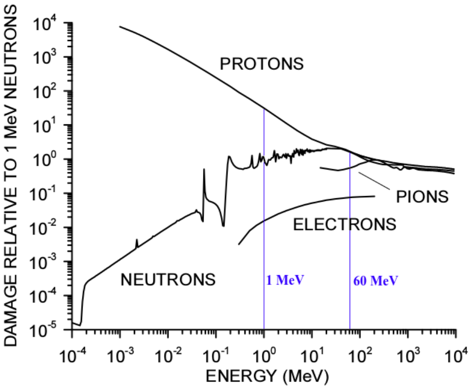

FIGURE 3.23. Displacement damage as a function of energy for neutrons, protons, pions and electrons. The Y axis was rescaled to represent the relative damage with respect to 1 MeV neutrons.

Runs	Dose rate [Gy/s]	Integrated TID [Gy]	Integrated proton fluence
1-5	0.08	400	$3.65 \cdot 10^{11}$
6	0.08	800	$7.29 \cdot 10^{11}$
7	0.8	800	$1.09 \cdot 10^{12}$

TABLE 3.2. Summary of the fluence and dose values integrated during the proton irradiation test.

allowed a TID of 80 Gy/run with an irradiation rate of 0.08 Gy/s, therefore integrating a total of 400 Gy and an overall fluence of $3.7 \cdot 10^{11}\text{cm}^{-2}$. The sixth run was longer, integrating 400 Gy at the same rate, while in the seventh the rate was increased by a factor 10, integrating other 400 Gy. The run details are summarised in Tab. 3.2. The final protons fluence is then of $1.1 \cdot 10^{12}\text{cm}^{-2}$, while the overall TID is of 1200 Gy, which approximately corresponds to the dose absorbed in 10 equivalent LHCb upgrades, i.e. in 100 years of upgrade operations.

Using the Screened Relativistic NIEL calculator [280], a proton fluence of $1.1 \cdot 10^{12}\text{cm}^{-2}$ was used to estimate the NIEL dose deposition in Si, which corresponds to NIEL $= 0.72\,\text{Gy}$. Applying the NIEL scaling rule, the fluence of the corresponding 1 MeV neutrons equivalent that produces the same NIEL can be estimated to $2.3 \cdot 10^{12}\text{cm}^{-2}$. Being the expected 1 MeV neutrons fluence in one LHCb upgrade of $2 \cdot 10^{12}\text{cm}^{-2}$ and corresponding to NIEL $= 0.65\,\text{Gy}$, the proton irradiation allowed to test the nSYNC for a displacement damage of the same order of magnitude of the one integrated in one equivalent LHCb upgrade. This is also confirmed by the trend of displacement damage for different species with respect to energies, as shown for example in Fig. 3.23, when 60 MeV protons and 1 MeV neutrons are characterised approximately by the same displacement damage, assuming the same fluence for both the species.

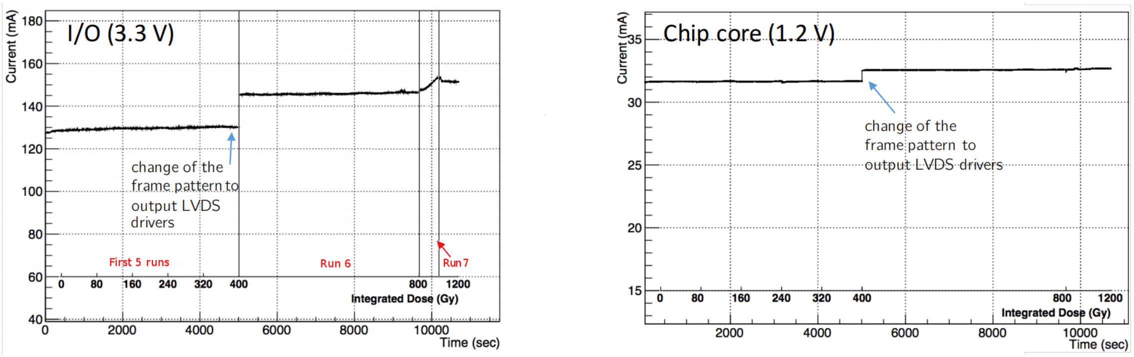

FIGURE 3.24. Current consumption on the I/O ring (left) and the chip core (right) for the first chip tested, covering the whole irradiation test. The increasing trend is not visible at this scale, except in the last run. The intermediate step is due to a different frame pattern on the LVDS output, which causes a natural greater current consumption.

3.5.3 Results

The results of the irradiation test are presented for current consumption, the PLL stability, the TDC calibration curves and the SEU studies. Only the plots for one chip are shown as an example.

Effects of TID on current consumption

The typical nSYNC current values for the I/O interface range between 80 and 120 mA, depending on the LVDS output load, and about 30 mA for the chip core. During the entire radiation tests the currents remained stable. The change in the LVDS output fixed pattern after the fifth run leads to an increased power consumption due to the LVDS drivers, as can be seen from the step observed after the fifth run in Fig. 3.24. One soft latch was observed for the first preliminary chip tested with no failure and no consequences in terms of chip functional stability. Moreover, no SEL was observed for all the chip tested. The increase in the current trend due to the integrated TID is evident on the I/O ring current only, and can be seen in Fig. 3.25. In particular in the first run, at low dose rate, the current increases of 1.2% in about three equivalent LHCb upgrade, thus 0.8% in one equivalent upgrade. In the last run, at higher dose rate, the increase is of 1.3% in one equivalent upgrade. In this run the annealing trend can also be observed. The chip core does not show instead any significant increase on these tests. These cumulative effects are also compatible with those obtained from independent test using X-Ray radiation as explained later.

Performance of PLL and LVDS driver

The clock generated by the PLL was monitored to measure the possible jitter increase with respect to the integrated dose. The same measurement was done on one LVDS output, sending

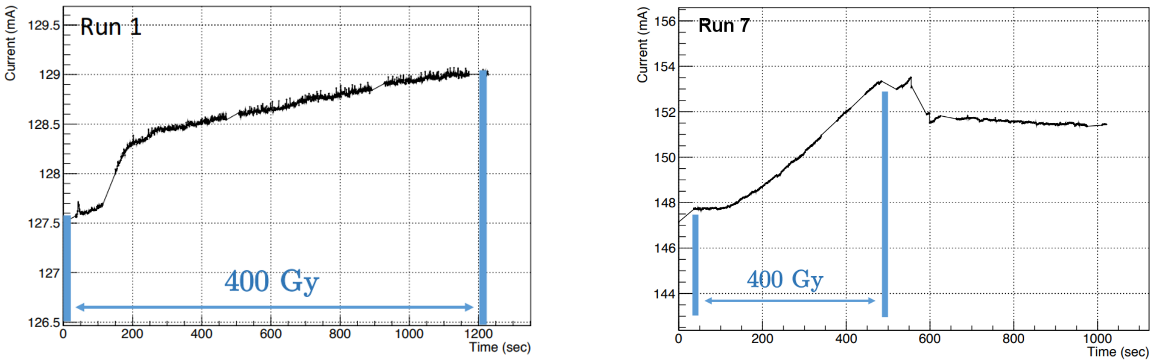

FIGURE 3.25. Current consumption on the I/O ring for the first chip tested during the first run (left) and the last run (right). In the last run, after the irradiation stops, some fluctuations of the current are present due to changes in the internal functionalities, related to the communication with the chip. After that, a decreasing current trend of the annealing is clearly observed.

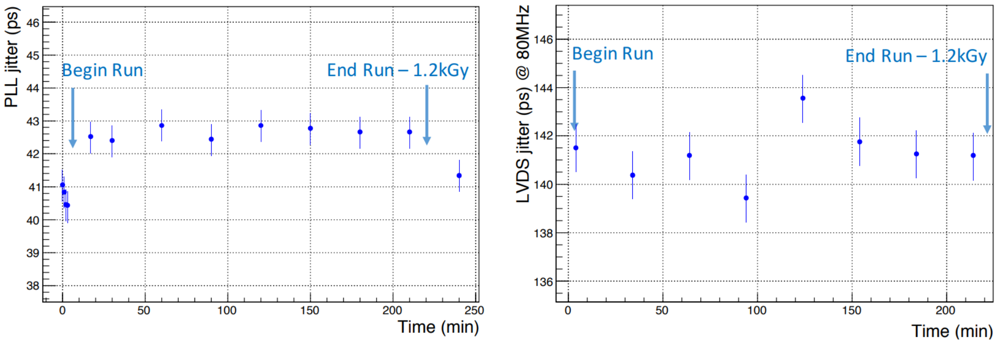

FIGURE 3.26. Left: PLL jitter as measured by the oscilloscope before, during and after the irradiation test. A slight increase in the jitter of ∼ 2 ps is clearly evident. Right: output LVDS jitter measured by the oscilloscope before, during and after the irradiation test. Maximum fluctuations of order of ∼ 4 ps are present but no particular trend was observed.

a periodic signal to the output interface, emulating a clock with a fixed pattern on the output data frame. No instability or unexpected behaviour for both signals was observed during the full test and for all chips, neither any cumulative effect. A rise in the PLL jitter of about 2 ps, corresponding to ∼5%, was observed with beam, while the LVDS signal jitter did not show an increasing trend but fluctuations of about 4%, as shown in Fig. 3.26.

TDC performance - DCO calibration

To test the TDC performance with respect to TID, in absence of front-end input signals, the internal automatic DCO calibration procedure was used. The calibration was launched periodically for each channel and for each resolution, and the corresponding DCO values, stored in read-only registers, were read back through the I^2C communication. The values as a function

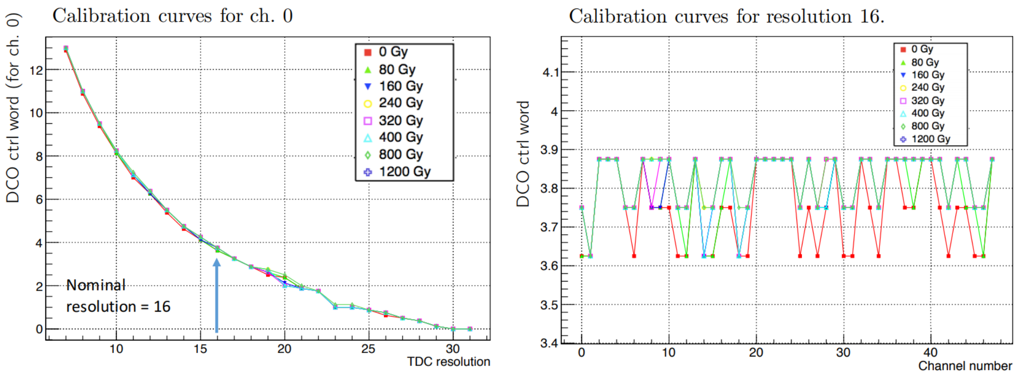

FIGURE 3.27. Left: DCO control word as a function of chosen resolution for the channel n.0 of the first nSYNC tested. Right: DCO control word as a function of the channel number at the nominal resolution for the first nSYNC tested. Each curve is obtained for different TID. The curve corresponding to a TID of 0 Gy is slightly at lower DCO values with respect to the other curves, however this trend is within the dithering correction and it is considered negligible.

of the resolution chosen and channel number, at increasing TID, were then studied offline. The calibration curves are super-imposable with no evident trends at increasing TID for all the chips tested, as shown in Fig. 3.27 (left). A small trend can be seen in some channels of one chip only (Fig. 3.28), but it is considered not to be significant since it is of the same order of the dithering correction. At the LHCb nominal resolution (16), a small trend is observed just after the first irradiation step and for some specific channels only, where the experimental points tend to higher DCO values, as shown in Fig. 3.27 (right). The increase is within the dithering correction also in this case, thus not representing an issue for normal operation at LHCb.

SEU studies and cross sections

The number of SEU was measured by reading periodically the nSYNC registers through the I^2C interface, in particular by counting offline the bin-flip occurrences and by reading the internal error counters. Knowing the fluence values at each end of run, the trend of number of observed SEUs, N_{SEU}, at each run with respect to the corresponding fluence, Φ , was obtained. The SEU cross section can thus be easily estimated as the angular coefficient of a linear fit on these curves. This procedure, instead of simply performing the ratio between the final N_{SEU} and the total fluence, has the advantage of taking into account possible statistical fluctuations and allows to check how the cross section remains at a constant value during the irradiation. The following values for the cross section are the average of the results obtained from the two chips under test, while the uncertainty is half the difference between the two values. Four functional blocks were analysed separately:

- TDC: For each input channel, after the DCO calibration, the TDC status is stored in

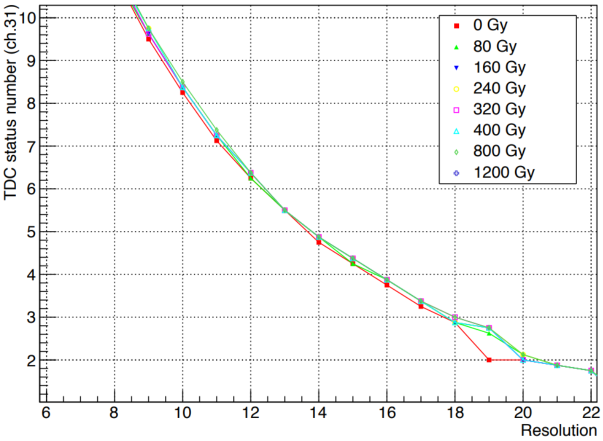

FIGURE 3.28. DCO control word as a function of chosen resolution, for the channel n.31 of the first nSYNC tested. Each curve is obtained for different TID. The curve corresponding to a TID of 0 Gy is slightly at lower DCO values with respect to the other curves, however this trend is within the dithering correction and it is considered negligible for the TDC functionality.

2-bytes wide unprotected registers, which were readout periodically every second. A SEU is then immediately observable as a permanent bit-flip. The average cross section for these registers, which correspond to 90 bytes in total, is $(5.8 \pm 0.9) \cdot 10^{-11}$ cm^2. Multiplying this value for the expected hadrons fluence in 10 years of LHCb upgrade activity and for about 600 nSYNC, results in 6800 SEU for the whole muon detector, corresponding to less than 2 events per day. It is important to note that this number has no impact on LHCb operations, since the TDC values are only used for time alignment, thus with no effect whatsoever in the LHCb data quality. The number of TDC SEU as a function of fluence for the chip 1 can be seen in Fig. 3.29 (left).

In order to further check possible channels vulnerabilities, the number of SEU per channel number was studied. The statistics was too low to perform a detailed study but no particular trend was observed: the SEU were widespread over all channels, without holes or group of channels more vulnerable than others.

- Histograms: the same measurement was performed for the histogram registers, corresponding to the biggest memory block of not protected 2.3 kbytes. The values were downloaded every 2 minutes. The resulting average cross section is $(0.95 \pm 0.08) \cdot 10^{-9}$ cm^2, corresponding to about 30 events/day for the whole muon system. In this case it is worth to note that the histogram facility is used only for time alignment purpose and not during normal data taking, thus this rate has no practical effect on LHCb normal operations. Moreover, assuming that there is a SEU affecting one bin, the correct histogram shape can be inferred from the other bins and the SEU can be spotted out. The number of SEU as a function of fluence for chip 1 can be seen in Fig. 3.29 (right).

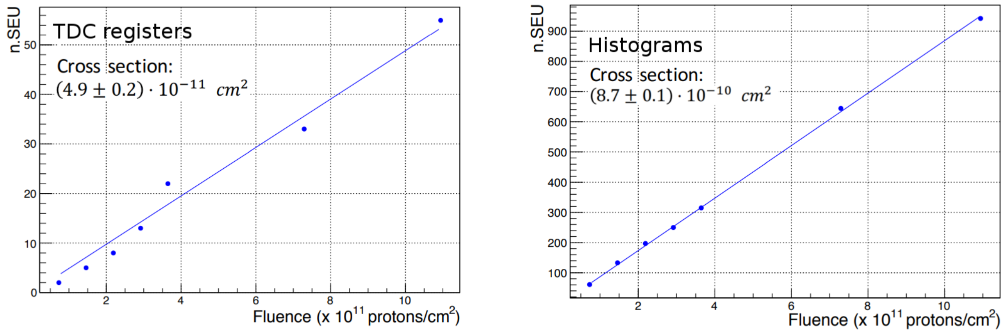

FIGURE 3.29. Number of SEU in the TDC not-protected registers (left) and the not-protected histogram registers (right). The plot and cross sections shown refer to the first chip tested.

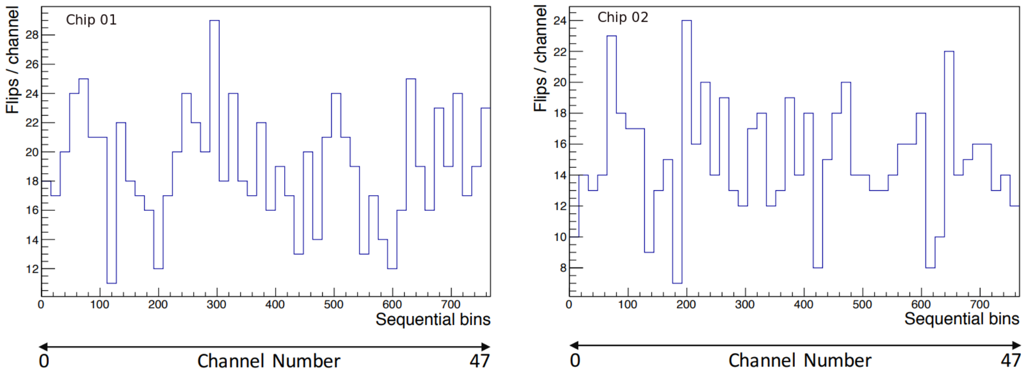

FIGURE 3.30. Number of bit-flips as a function of all the bins (3 bytes wide) for all the 48 histograms, for the first chip tested for a proton fluence of $1.09 \cdot 10^{12}$. The bins are ordered in a sequential way, starting from channel 0. No holes or blocks of channels more vulnerable than others are observed.

The same vulnerability study done on TDC registers was repeated also for the histogram block, for which the statistics is higher. As shown in Fig. 3.30, the number of SEU with respect to the channel number is counted, grouping together the corresponding 16 counters (3 bytes/counter). No particular trend was seen, with the SEU distributed over all bins.

- Configuration registers and TFC: the measurements were done also for the functional blocks protected by TMR system, which correspond to 195 bytes, reading continuously the TMR error internal counters and also cross-checking the contents of the configurations registers periodically. The TMR system detected several errors and never failed the correction: this corresponds to a detected SEU cross section of $(7.7 \pm 0.8) \cdot 10^{-11}$ cm^2, equivalent to about 2.5 events/day for the whole muon system, and an upper limit of $8 \cdot 10^{-13}$ cm^2 for the not corrected one. The number of TMR corrected SEU as a function of fluence for the chip 1 can be seen in Fig. 3.31 (left).

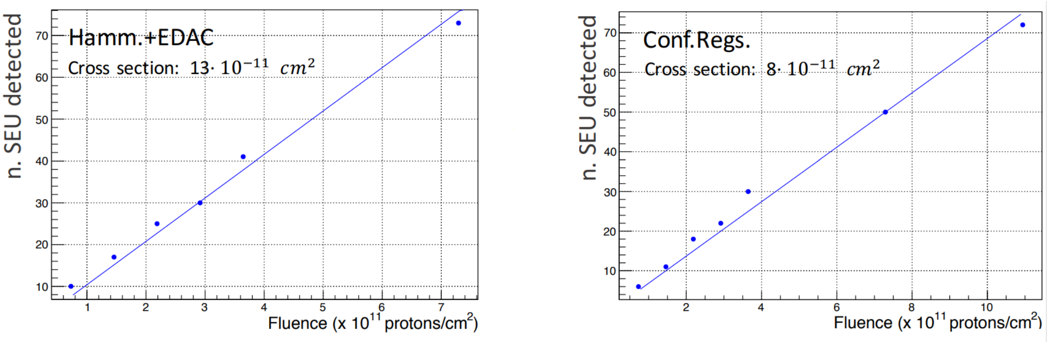

FIGURE 3.31. Number of detected SEU in the EDAC protected registers (left) and the TMR protected configuration registers (right). The plot and cross sections shown refer to the first chip tested.

- Internal logic Hamming protected: assuming that errors detected by the EDAC system are SEU, the SEU cross section can be computed also for the internal logic protected by the Hamming code and the EDAC. The internal logic was monitored thanks to the internal error counters, which counted both the total errors occurred and the number of corrected ones. Their difference allows to count the number of the double errors in the same digital word, which leads to a not correction, that was observed in less than 3% of the total number of detected errors. The latter corresponds to a detected SEU cross section of $(13 \pm 3) \cdot 10^{-11}$ cm^2, while the not corrected errors cross section is $(3 \pm 1) \cdot 10^{-12}$ cm^2. The related expected error rate is 0.1 events/day for the whole muon system. The number of EDAC total SEU as a function of fluence for the chip 1 can be seen in Fig. 3.31 (right).

For TDC, histograms and TMR-protected blocks, a normalisation of the cross sections to the overall number of involved bits can be calculated. The importance of these quantities is related to the fact that, in principle, apart fluctuations, the normalised values have to be the same, since they only depend on the memory cell type and the chosen technology. The normalised values are all indeed compatible on every nSYNC tested:

$$\sigma_{\text{TDC}}/\text{bit} = (0.80 \pm 0.10) \cdot 10^{-13}\,\text{cm}^2,$$
$$\sigma_{\text{Hist}}/\text{bit} = (0.52 \pm 0.04) \cdot 10^{-13}\,\text{cm}^2,$$
$$\sigma_{\text{TMR}}/\text{bit} = (0.49 \pm 0.05) \cdot 10^{-13}\,\text{cm}^2.$$

We conclude that these measurements characterise the radiation resistance of the UMC 130 nm technology. The weighted average value of the SEU cross section per bit is

$$\sigma/\text{bit} = (0.53 \pm 0.04) \cdot 10^{-13}\,\text{cm}^2.$$

Functional Blocks	Cross section σ events/cm^{-2}	Events in 10 years (150 nODE)	Events per day (150 nODE)	Cross section σ per bit events/(bit·cm^{-2})
Internal logic (all errors detected)	$(13 \pm 3) \cdot 10^{-11}$	$\sim 1.5 \cdot 10^4$	~ 4	-
Internal logic (double errors)	$(3 \pm 1) \cdot 10^{-12}$	$\sim 5 \cdot 10^2$	~ 0.1	-
TDC	$(5.8 \pm 0.9) \cdot 10^{-11}$	$\sim 6.8 \cdot 10^3$	~ 1.8	$(0.8 \pm 0.1) \cdot 10^{-13}$
Histograms	$(0.95 \pm 0.08) \cdot 10^{-9}$	$\sim 1.2 \cdot 10^5$	~ 30	$(0.52 \pm 0.04) \cdot 10^{-13}$
Config and TFC (all TMR corrected)	$(7.7 \pm 0.8) \cdot 10^{-11}$	$\sim 9.4 \cdot 10^3$	~ 2.5	$(0.49 \pm 0.05) \cdot 10^{-13}$
Config and TFC (TMR failures)	$< 8 \cdot 10^{-13}$ @ 95% C.L.	< 90	< 0.02	-

Table 3.3. Final cross section results, averaged between the two tests, for all the nSYNC functional blocks. The estimation of the expected events per day and in 10 years of upgrade operation are shown. The normalised cross sections per bit are also showed.

3.6 Irradiation with X-Ray

To study in more details the effect of accumulated TID, also an irradiation test using X-rays was performed, using an X-Ray facility at the LHCb group laboratory at Physics Department in Cagliari [281].

3.6.1 Experimental setup and X-Ray tube calibration

The experimental setup and the DAQ system used for this test is the same used for the protons irradiation test, described in Sect. 3.5.2, while the other instruments used are:

- X-Ray tube from the company PANalytical, used in the past to check uniformity on triple-GEM and shown in Fig. 3.32 (right). It is equipped with a Fe anode, a short fine focus focal spot with diameter of 7 mm and a 250 μm thick beryllium output window.

- Power supply for X-Ray tube, an HV generator (model XLF) specifically customised for our setup, by the Spellman company. The generator can provide a voltage output up to 20 kV and a current up to 60 mA.

- Water cooling system, equipped with a small pump and set of tubes to provide a continuous and stable flux of cooling water with a minimum flow of 3.5 l/min.

- A double-axis electric actuator placed in front of the tube at fixed distance from it, in order to correctly align a target device with the X-Ray spot in transverse plane, with a position accuracy of 50 μm.

FIGURE 3.32. Left: the safety shielded enclosure with the X-Ray tube and the moving system inside. Right: picture of the X-Ray tube and the moving system.

- Safety interlock system: the X-Ray tube and the moving system are placed inside a safety shielded enclosure, shown in Fig. 3.32 (left), made of iron and glass walls, that can be opened on one side for user operations. This shielded enclosure reduces the outer radiation level to that compatible with natural background. A water flow sensor, two electro-mechanical switches for the door closure and a user key-enable switch are all connected to a single system that provides an interlock signal for the HV generator, in order to switch off the HV within 0.1 seconds in case the water flow is too low or the door is opened.

Before using the X-Ray facility to irradiate the chip two important procedures were performed:

- Some chips were sent to the MASER Engineering company, which offers reliability test and failure analysis services for semiconductors and electronics, in order to decapsulate and expose the chip die, as shown in Fig. 3.33. In this way the dose absorbed by the silicon can be estimated more accurately, since the exact size and composition of the package above the die is not known with high precision, leading to possible uncertainties on the actual dose absorbed by the silicon.
- A careful and precise calibration of the X-Ray tube energy rate, as a function of distance and depth in silicon was done, in order to estimate correctly the absorbed dose and TID on the irradiated nSYNC.

X-Ray spectrum studies

The first procedure to get the X-Ray dose calibration was to study the X-Ray spectrum, and correct it from two main effects: the efficiency of the detector used to acquire it and the air

FIGURE 3.33. Picture of the nSYNC package and the exposed die after the decapsulation.

attenuation due to the distance between the detector and the tube exit window. The spectrum was acquired with an Amptek XR-100 CR detector, equipped with a thermoelectrically cooled 300 μm thick Si-PIN photodiode, together with the PX4 digital pulse processor as a multichannel analyzer (MCA). The Si detector is equipped with a 25 μm thick beryllium input window. For the spectrum acquisition a 5 mm thick brass collimator was used, with diameter of 1 mm, and the detector was placed at approximately 950 mm from the X-Ray source. In the emission spectrum, shown in Fig. 3.34, there are clearly three peaks above the Bremsstrahlung structure, two of them due to the Fe anode fluorescence: two merged peaks of $K_{\alpha 1}$ and $K_{\alpha 2}$ at 6396 eV and the K_β peak of 7058 eV. The third peak is due to the silicon detector fluorescence, corresponding to the K_α Si escape peak at 4656 eV. The three peaks found were fitted with gaussian distributions, in order to obtain the peak positions and calibrate the multichannel scale in energy.

Due to the finite thickness of the detector, part of the higher energy X-Ray photons are not absorbed in it. For this reason the spectrum measured was corrected for the energy-dependent detector efficiency, $\varepsilon(E)$, in order to obtain the actual emission spectrum. The efficiency can be defined as

$$\varepsilon(E) = 1 - e^{-(\mu(E)/\rho) x \rho}, \tag{3.1}$$

where $\mu(E)$ is the attenuation coefficient in silicon measured in cm^{-1} and function of the photon energy, x is the detector thickness, ρ the material density and the ratio μ/ρ is defined as the mass attenuation coefficient. In order to find an accurate parametrisation of the ratio μ/ρ the NIST data [282] for the X-Ray attenuation coefficient in silicon as a function of photon energy are fitted in the range 2-30 keV with a four-parameters exponential function, considering a third-degree polynomial dependence in the exponent. In this energy range, most of the photons interact through photoelectric effect, and above 10 keV the 300 μm-tick detector efficiency decreases quite rapidly. For all the energy bins, the acquired spectrum was then corrected rescaling with the efficiency in Eq. (3.1). Another possible detector related effect is the absorption of low energy photons by the 25 μm beryllium window. This effect was found to be negligible (intensity reduction ~0.3%) due to the small window thickness and the low value of Z for beryllium.

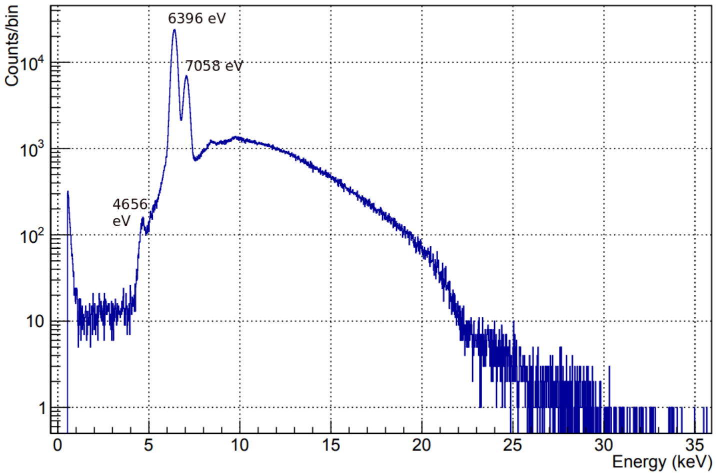

FIGURE 3.34. Measured X-Ray spectrum, with the three peaks used to perform the energy calibration.

Since the silicon detector was placed at approximately 950 mm from the X-Ray source, the photon beam attenuation due to the air is not negligible, and it is necessary to correct the acquired spectrum to obtain the real emission spectrum. The attenuation factor is $e^{-(\mu(E)/\rho)x\,\rho}$ where in this case $\mu(E)$ is the attenuation coefficient in air, ρ is the air mass density and x corresponds to 950 mm. A similar procedure to the previous one was done, fitting the NIST data [282] for attenuation of X-Rays in air with the same fit model, and the spectrum was again rescaled. The result of both the detector efficiency and air absorption correction is shown in Fig. 3.35. Energies below 5 keV were not considered, since for these low energy photons the absorption probability in 950 mm of air is approximately 1, and it is no longer possible to define a correction factor.

Since the spectrum is characterized by a large amount of low energy (6-7 keV) X-Ray photons, the absorbed dose in silicon is not uniform in depth, with a large fraction of energy deposited in the first $\sim$50 μm of the target, in which typically the active electronics logic is located. This could potentially lead to an underestimation of the dose. In order to harden the spectrum and get a more uniform absorbed dose the possibility to filter the X-Ray beam using Al filters was studied. In order to determine the photon attenuation, two reference energies were considered: the K_α and K_β Fe fluorescence peaks, at 6396 eV and 7058 eV respectively. Filters made of 1, 2, 4, 8, 16 thin Al foils were used and, for each measurement, the number of entries in the peaks bins, corresponding to the two reference energies chosen, were counted. The number of entries, as a function of the number of Al foils, was fitted by a simple exponential. The fit also allowed to estimate the foil thickness, 13.1 ± 0.2 μm for both the measurements. The fit was also repeated on the NIST data [282] for the X-Ray attenuation in aluminum in the range 2-30 keV in order to simulate the aluminum filtering effect starting from the measured unfiltered spectrum. Qualitatively the spectra are in good agreement for all the measurements, within

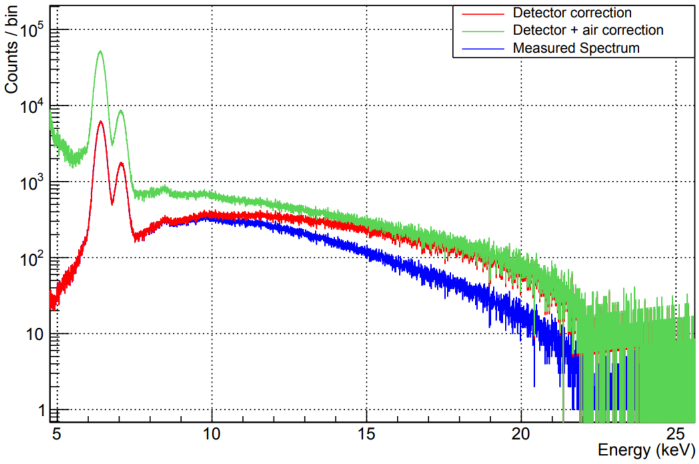

FIGURE 3.35. Comparison between the measured X-Ray spectrum (blue), the one corrected for the detector efficiency only (red) and the one with also the air absorption correction (green).

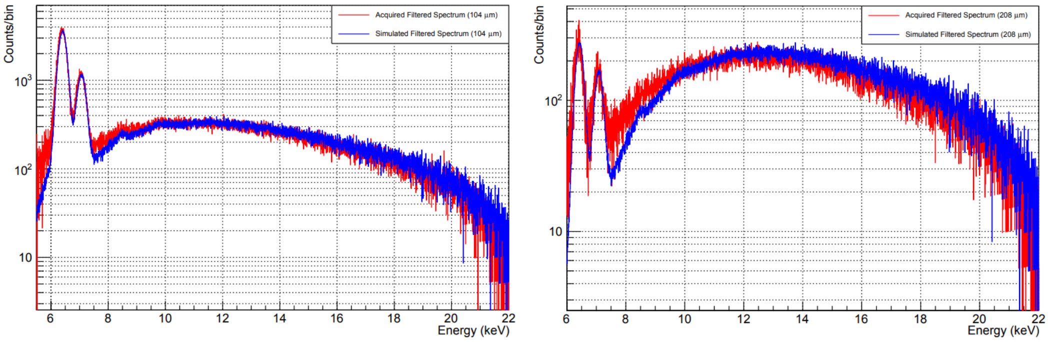

FIGURE 3.36. Comparison between the simulated Al-filtered X-Ray spectrum (blue) and the measured one (red), for 104 μm thick Al filter (left) and 208 μm thick (right). In the latter case the spectrum is highlu hardened, being the low energy peaks reduced by an order of magnitude.

a 5% of the simulated filter thickness, as shown in Fig. 3.36. This procedure allowed to use a simulated spectrum to compute the doses for a wider range of thickness, up to 300 μm.

X-Ray dose calibration

The dose calibration was performed using a 10x10 mm^2, 300 μm thick, unsealed Si-PIN diode from Hamamatsu (model n. S3590-09). in order estimate the dose rate the diode was reverse biased at 100 V and monitored the current in DC mode, using a Keithley 6517A electrometer. The PIN diode was placed at 3 mm from the exit window of the tube, so that the X-Ray spot was entirely contained inside the diode active area. Due to the package shape, the active area was located at 3.5 mm from the tube.

The alignment of the diode was a crucial and delicate procedure, since a small misalignment with respect to the X-Ray spot will cause an underestimation of the dose. The XY moving system was used to properly align the diode in front of the tube, by searching a current plateau along both axes, and eventually by fixing the position in the plateau center.

Supposing 1 W power deposition in silicon and considering 3.6 eV to create one electron-hole pair, the maximum (ideal) X-Ray sensitivity of the silicon is can be estimated, $\mathcal{S} = 0.277A/W$. The dose rate D can be therefore calculated as:

$$D = \frac{I}{\mathcal{S} \cdot M}, \tag{3.2}$$

where I is the PIN diode current and M the target mass in which the dose is absorbed. The mass is calculated considering the silicon density, the diode thickness and the X-Ray spot area. This method provides a lower limit to the dose, because an ideal sensitivity and an ideal measurement of the X-Ray spot are considered. Since the spot itself is intrinsically not defined enough to perform a more precise radius measurement, the measured dose values are considered within a precision of 10%. The diode current measurements were repeated using Al filters of 100, 200 and 300 μm at different X-Ray tube currents, in order to verify the linearity of the diode response, as shown in Fig. 3.37 (left).

At the maximum tube current of 40 mA and without Al filters and at 3.5 mm far from the output window, the maximum dose rate is approximately of 1.29 kGy/min, while with 300 μm of Al the maximum estimated dose is approximately of 66 Gy/min. These values are consistent with typical high-dose rates of modern X-Ray tubes.

One important effect taken into account in this procedure was the variation of the dose with distance. The X-Ray spot indeed shows an elliptical shape and an average aperture angle of $3.70° \pm 0.15°$, estimated using radiochromic films by the Gafchromic company (model XR-QA2 and EBT3). Thus, even if the entire spot is contained within the active area of the diode, the same power is deposited in a bigger volume while increasing the distance, reducing the absorbed dose (which depends on the total mass involved, as shown in Eq. (3.2)). The dose scales with distance as

$$D(x) = D(0)\frac{R_h(0)\, R_v(0)}{R_h(x)\, R_v(x)}, \tag{3.3}$$

where $D(x)$ is the dose at distance x, while $R_{h,v}$ are the x-dependent horizontal and vertical spot radii respectively. The scaling dose curves are shown in Fig. 3.37 (right). Thus, the previous dose rates becomes, at zero distance, 1.47 kGy/min without Al filters, and 75 Gy/min with 300 μm of Al filter.

The air attenuation introduces another dose suppression factor: this is negligible (absorption less than 4%) for distances smaller than 10 cm, but becomes more important for higher distances. At 50 cm the air attenuation introduces a factor 0.44 for the unfiltered spectrum, and up to a factor 0.85 for the 300 μm of Al. This was carefully taken into account during electronics irradiation test, in order not to overestimate the dose absorbed by the sample under test.

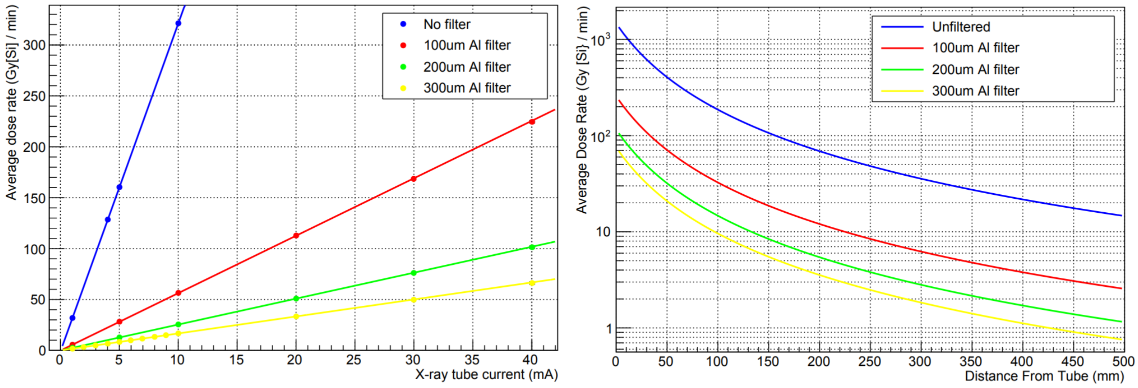

FIGURE 3.37. Left: average dose rate, in Gy/s, in the Si-PIN detector as a function of the X-Ray tube current, for different Al filter thicknesses. Right: average dose rate, in Gy/s, as a function of the distance from the tube, for different Al filter thicknesses.

X-Ray dose profile in silicon

The spectra acquired at different filter thickness were used to compute the dose absorbed in the silicon with respect to depth, named *dose profile*. To compute the energy deposited, consider a beam of monochromatic photons of energy E, directed along the x axis through a silicon target, and a small layer of thickness δ, located at depth x inside the target itself. The energy deposited in the layer is:

$$E_{\mathrm{dep}} = N_{\mathrm{ph}}(E) \cdot E \cdot e^{-\mu(E)/\rho\,(x\rho)} \cdot (1 - e^{-\mu(E)/\rho\,(\delta\rho)}), \tag{3.4}$$

where $N_{\mathrm{ph}}(E)$ is the number of photons, with energy E, emitted by the X-Ray tube; the first exponential is the fraction of photons reaching the x depth, while the second factor $(1 - e^{(\cdots)})$ is the absorption efficiency in the layer of thickness δ. At a particular depth x, a sum over all the contributing energies, by weighting $N_{\mathrm{ph}}(E)$ with the X-Ray tube emission spectrum, can be computed, properly correcting for the detector efficiency and air attenuation at a particular distance. This leaded to the final deposited energy in the δ-layer at x depth, which was then divided by the layer mass to find the final local dose. This computation was repeated for the whole x range, finding the final dose profile inside 300 μm of silicon, as shown in Fig. 3.38 in the specific case of zero distance from the tube. In our considerations the δ layer is simply the bin width of the dose profile histogram. Since the spectrum measurements were relative, also the preliminary dose profile computation was relative. The vertical scale was calibrated using the information of the absolute dose measured by the Si-PIN detector, rescaled by the air attenuation, distance dose scaling and Al filtering effects. From the dose profile it is clear that most of the energy is absorbed in the first $\sim$ 50 μm of the target, effect highly reduced by using Al filters. The final dose rate tables as a function of silicon depth, distance and Al filter thickness can all be found in [281].

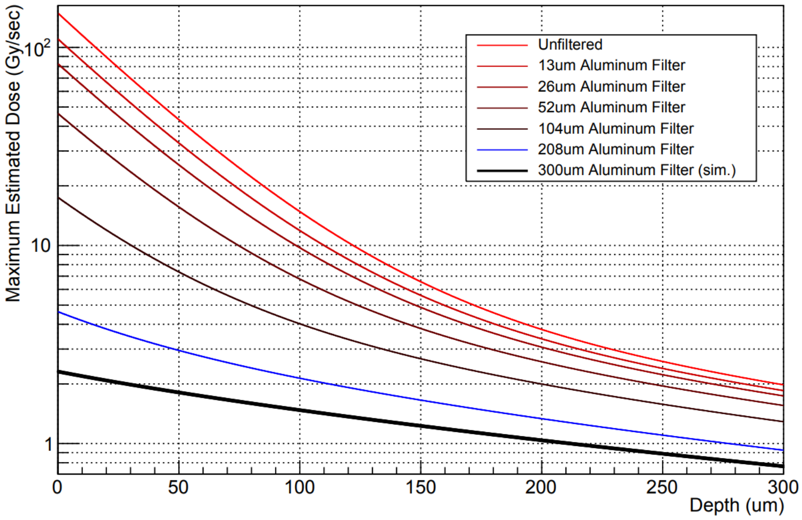

FIGURE 3.38. Maximum local estimated dose rate, in Gy/s, as a function of the depth in silicon, in μm, for different Al filters. A 100 μ thick Al filter is able to reduce the local dose rate at the surface by an order of magnitude, and in the bulk (at 150 μm) by a factor ~ 2.

Combinations of various parameters allow to get a dose rate range from fractions of Gy/min and up to 1.4 kGy/min. Therefore typical maximum integrated dose values considered for the muon system readout electronics in LHCb upgrade can be achieved for irradiation times of about one hour.

3.6.2 Results

Five chips were tested: two of them were decapsulated, while the other ones were used to optimise the experimental setup and the DAQ system. One of the decapsulated chip was mounted on the nSYNC test PCB by means of a Zero Insertion Force (ZIF) socket. The second chip was instead soldered on a second test board, with the design optimised in order to perform a possible test even nearer the source. To properly align the nSYNC die with the X-Ray spot, a set of radiochromic films was used and the position was adjusted until the spot was exactly above the chip die. An example of the usage of the radiochromic film is shown in Fig. 3.39 (right).

In the first tests an Al filter of 100 μm was used. The average dose in 300 μm of irradiated silicon was computed averaging the dose profile shown in Fig. 3.38 and the scaling with respect to the source-target distance was computed. At 25 mm the average dose is reduced by a factor 2 with respect to zero distance, reducing from approximately 200 Gy/min to 100 Gy/min (considering a 10% of accuracy on the dose values). In the first run the chip was irradiated for a maximum time of 16 minutes, integrating at 100 Gy/min a TID of 1.6 kGy corresponding to a TID for 12 LHCb equivalent upgrades. The current consumption for I/O ring and the chip core was monitored during the test and shown in Fig. 3.40. No failure behaviours were

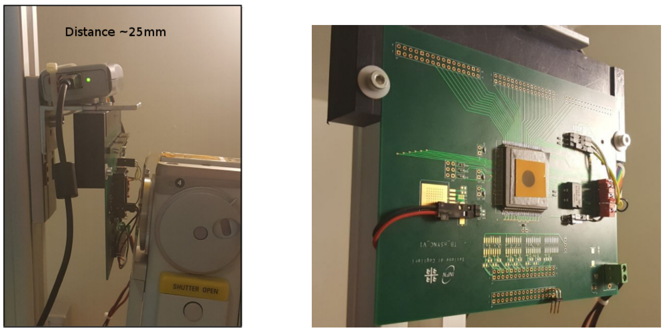

FIGURE 3.39. Left: picture of the nSYNC test board mounted in front of the X-Ray tube at a distance of 25 mm. Right: picture of the nSYNC test board with the radiochromic film above the chip package, used for alignment purpose. The dark X-Ray spot on the film is visible.

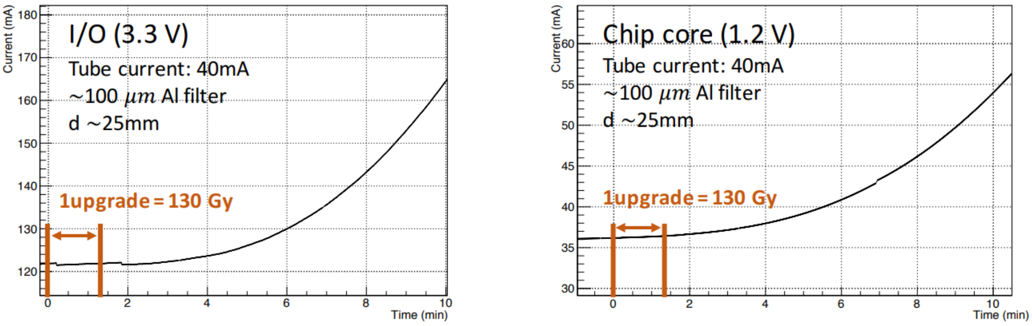

FIGURE 3.40. Current for the I/O ring (left) and the chip core (right), for the test on the first chip. One equivalent LHCb upgrade is highlighted in orange. The nSYNC was at 25 mm far from the X-Ray source and a 100 μm thick Al filter was used.

seen during the entire test. The current increasing in one equivalent LHCb upgrade (130 Gy) is about 3% at low TID values, i.e. during the first irradiation time, for the I/O ring. The chip core current showed also a clear increase of 1.5% at low TID. Both the current consumption showed a current increase of about 10% at higher TID values, demonstrating how the ionisation damage is a cumulative effect. Nevertheless it is important to point out that the higher TID values reached on these tests corresponds to many LHCb equivalent upgrades, therefore the more realistic values considered for the TID damage are those at low integrated TID. On the same chip the annealing was monitored for one week. After this period the currents decreased back to approximately the same starting values of ~77 mA on the I/O and ~36 mA on the chip core. The same chip was then irradiated again to perform a stress test, integrating a final dose of 3 kGy, corresponding to 23 LHCb equivalent upgrades. No failure behaviour was observed: the internal functionalities like I^2C communication, setting and reading configuration, DCO calibration performed without errors or functionalities loss.

A second similar run was done with the other decapsulated chip, irradiating it for 10 minutes

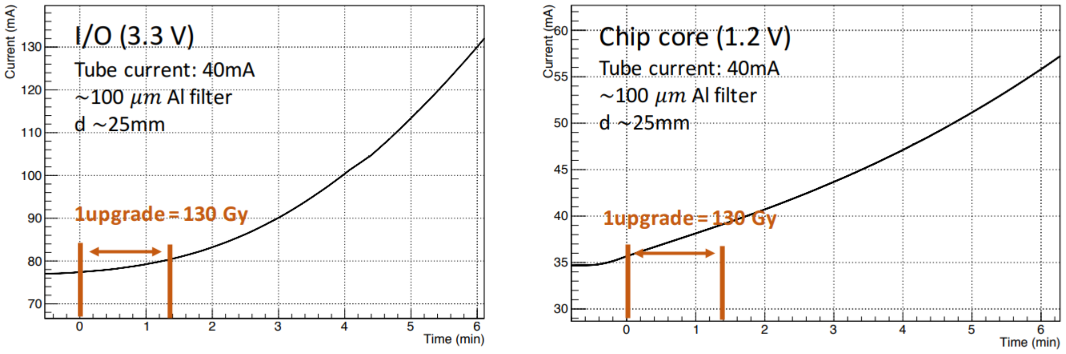

FIGURE 3.41. Current for the I/O ring (left) and the chip core (right), for the test on the second chip. One equivalent LHCb upgrade is highlated in orange. The nSYNC was at 25 mm far from the source and a 100 μm thick Al filter was used.

at 100 Gy/min, thus integrating approximately up to the TID of more than 7 LHCb equivalent upgrades. The results are similar to the previous test, with an increasing of 3.9% of the I/O current at low integrated TID. In this case the chip core presented a stronger and more linear power consumption increase, up to 8% at low integrated TID. This can be due to intrinsic differences between the chips during the production, or differences during the decapsulation procedure, that is certainly an invasive and potentially damaging procedure.

It is interesting to note that the measured current consumption increments (in percentage) are systematically higher than the ones obtained from the protons irradiation test. Indeed that a clear dependence on the dose rate can be observed, as shown in Fig. 3.42. Since the average dose rate during the upgrade operations are very low ($6 \cdot 10^{-7}$ Gy/s) with respect to the ones used in these tests, it is expected that the current consumption will increase less than 1%, both for the I/O ring and the chip core.

3.7 Summary

In the irradiation tests using 60 MeV protons beam the nSYNC showed an excellent performance, with no failure behaviour or SEL after an integrated TID 10 times larger the one expected in 10 years of LHCb upgrade operations. The chip current increase remains below 5%, as well as the clock jitter variation, in one equivalent LHCb Upgrade. The SEU cross sections were also measured and do not show any dangerous errors rate for LHCb nominal operation. Even though the irradiation test was performed to verify and validate the chip functionalities for LHCb upgrade before starting its production, also the cross section normalised per bit was measured to be $(0.53 \pm 0.04) \cdot 10^{-13}$ cm^2: this important achievement is the first result for SEU cross section of the UMC 130 nm technology. It is important to remark that protons do not have enough high LET to produce SEU by direct ionisation, but only though secondary produced ions. Obtaining the ions LET spetrum in Si or SiO$_2$ starting from a monochromatic beam of protons is a general

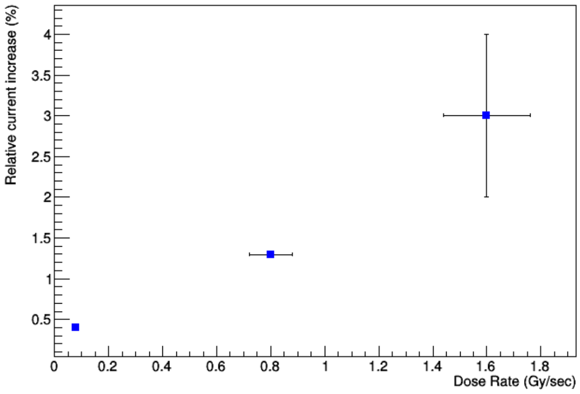

Figure 3.42. Current increment in the I/O nSYNC, in percentage, with respect to the dose rate. The first two points refer to the protons irradiation test, the last one refers to the X-Ray test, in which a wider range was observed (2-4%). A 10% of dose rate uncertainty was taken into account.

known problem, difficult to treat analytically. It can be investigated through simulations, which show that a wide spectrum of LET, in the range 1-14 MeV cm^2/mg, is produced in silicon [283]. For this reason our measured cross sections is equivalent to an average of the cross sections at different LET. From a technology characterisation point of view, further tests of the UMC 130 nm with ions beam at fixed LET will help to reproduce the cross section curve and estimate the saturated cross section.

CHAPTER 4

STUDY OF $D^0 \to h^+h^-\mu^+\mu^-$

SELECTION AND YIELDS DETERMINATION

In this chapter the analysis strategy for the study of $D^0 \to h^+h^-\mu^+\mu^-$ decays, with $h = K, \pi$, is described with particular focus on the candidates selection and yields determination. The first step consists in reconstruction and selection of events in order to increase the fraction of D^0 signal candidates with respect to background. For this purpose, the variables used in the selection are described, and the multivariate analysis methods is introduced. The data and simulated samples are discussed together with the selection requests applied at trigger and offline. Finally, the procedure for choosing the optimal selection is outlined.

4.1 Analysis strategy

The number of $D^0 \to h^+h^-\mu^+\mu^-$ signal candidates is obtained by analysing the invariant mass spectrum of the final state particles in the mass region of D^0. It was decided to consider the decay chain $D^{*+}(2010) \to D^0\,\pi^+$, performing a so-called *tagged* analysis, since it is possible to *tag* the flavour of the D^0 meson at production from the charge of the pion, but there are other important reasons that justify this choice, discussed in more details in Sect. 4.1.1. The selection of signal candidates is based on hardware and software trigger requests, some loose selection cuts on kinematic and angular variables, which constitute the stripping and preselection stage, and final cuts on multivariate variables. Once the final selection is applied the number of signal candidates is obtained by fitting the invariant mass spectrum with probability density functions (pdf) for the signal and the background components. The pdf are used to perform a background subtraction procedure and obtain the distributions for the 5D phase space, described by the Cabibbo-Maksymowicz parametrisation, already discussed in Sect. 1.7.1. This procedure is one of the most delicate, since the presence of background coming from particle misidentification can invalidate the assumptions on which the background subtraction is based, as discussed later. Since for a multi-body decay the angular asymmetries may vary as a function of the phase space position, knowing the reconstruction and selection efficiency variation across the phase space is essential and has to be properly taken into account. This variation is determined from simulation.

A basic amplitude model is built in order to simulate the phase space distributions of $D^0 \to h^+h^-\mu^+\mu^-$ decays along with the main known resonances, taking properly into account the coherent sum of amplitudes and thus their possible interference. The next step is then to build up a complete set of pseudoexperiments in which a simulated D^0 mass spectrum and its corresponding simulated phase space distributions are added up to the real background samples taken from data, in order to obtain a realistic simulated sample with signal and real background components. After the efficiency correction and the background subtraction procedures, the angular distributions are fitted with the angular model. This allows to check whether the final distributions are in agreement with the simulated ones, effectively testing the reliability of the angular fit.

4.1.1 Tagged analysis

As already anticipated, the D^0 candidates are selected by the decay chain $D^{*+}(2010) \to D^0\,\pi_{\rm s}^{+}$*. Decaying strongly, the D^{*+} meson decays instantaneously near the PV, and since the D^0 flavour oscillations are slow, the charge of pion can tag the flavour of the D^0 meson at production. The pion $\pi_{\rm s}^+$ is called *soft* because it has a low momentum (average of $\sim 5\,\text{GeV}$), since the decay $D^{*+} \to D^0\pi_{\rm s}^+$ is characterised by a low Q-value. The fraction of the D^0 from the D^{*+} decay mode is roughly

$$\frac{N(D^{*+} \to D^0\,\pi_{\rm s}^+)}{N(D^0)} = \frac{f(c \to D^{*+})}{f(c \to D^0)} \cdot \mathcal{BR}(D^{*+} \to D^0\,\pi_{\rm s}^+) \sim 0.27, \tag{4.1}$$

where $f(c \to D^{*+})$ and $f(c \to D^0)$ are the charm fragmentation fractions to D^{*+} and D^0 respectively[284] while $\mathcal{BR}(D^{*+} \to D^0\,\pi_{\rm s}^+)$ is the branching fraction of the $D^{*+} \to D^0\,\pi_{\rm s}^+$ decay [13]. The visible fraction reduces approximately to ~ 0.10 due to the reconstruction efficiency of the soft pion [285].

In addition to the flavour tag, there are two advantages to use this decay chain, using an observable defined as $\Delta M = m(D^{*+}) - m(D^0)$. The nominal ΔM value of 145.426 MeV is near the kinematical threshold at the pion mass, 139.57 MeV, at which the distribution goes to zero, thus helping to reject the combinatorial background, that has typically higher ΔM values. This background is typically due to wrong combinations of a real D^0 with one of the many pions produced in the high-energy collision, or of a real $\pi_{\rm s}^+$ with an unrelated D^0 meson. Since

---

*Unless explicitly stated, charge conjugated modes are included implicitly.

these candidates contribute to the combinatorial background even in the observable $m(D^0)$, a selection in ΔM helps in increasing the purity. The other advantage is that the resolution effects in $m(D^{*+})$ and $m(D^0)$ partially cancel out in the difference because of the correlation of their four-vectors, so the signal peak in ΔM is typically narrower than the one in $m(D^0)$ $(0.5-0.6$ MeV).

4.2 Expected backgrounds

In order to select the signal candidates efficiently with high purity, it is necessary to study the types of backgrounds that contribute to the invariant mass spectrum. These fall under two main categories: combinatorial backgrounds and physical backgrounds, in which real decays can enter in the invariant mass spectrum due to wrong particle identification or partially wrong track association. In particular the following sources of background can be defined:

- **Combinatorial background**: it is due to the reconstruction of the decay from the association of random tracks. It is mainly composed of random combinations of real $hh\mu\mu$ particles, but it can be also due to random combinations in which the final state particles are misidentified. It is characterized by a small dependence in $m(hh\mu\mu)$ and ΔM.

- **Misidentified (misID) background** $D^0 \to h_1^+ h_2^- h_3^+ h_4^-$: it is due to the four-body decay of D^0 where two final state particles are misidentified as opposite charged muons. These particles come from a real D^0 meson and create a peak in the $m(hh\mu\mu)$ and ΔM distributions. Since the wrong mass is associated to the two decay products, the peak is shifted with respect to the real D^0 peak. The most dangerous background of this type is due to the decay $D^0 \to h^+h^-\pi^+\pi^-$, where the two pions are misidentified as muons, creating a peak at exactly the same value of signal in ΔM distribution, but shifted to lower masses by ~12 MeV in the $m(hh\mu\mu)$ distribution. This is the most important background and its visible rate is non negligible, since the branching fraction of the decay is $\mathcal{O}(10^4)$ higher than the signal one, despite the misidentification probability being $\mathcal{O}(10^{-5})$. Other backgrounds of this type are $D^0 \to h^+h^-K^+K^-$ and $D^0 \to h^+h^-K^-\pi^+$ decays, whose peak in $m(hh\mu\mu)$ distributions is displaced to even lower invariant masses due to the larger mass difference between K and μ, thus properly selecting the $m(hh\mu\mu)$ range of interest their contribution can be considered negligible.

- **Radiative background**: it is due to the $D^0 \to \pi\pi\eta(\mu\mu\gamma)$ decay, which has a branching fraction three order of magnitudes higher than the signal one. Neglecting the photon momentum, a study of this decay on a previous $D^0 \to \pi^+\pi^-\mu^+\mu^-$ LHCb analysis [188] showed it forms a peak at the nominal D^0 mass, due to low energy photons, with a long left tail. Most of the candidates lie in the η bin (the $m(\mu\mu)$ binning scheme is explained in Sect. 4.5.3), in which no significant yield was observed in the latest $D^0 \to \pi^+\pi^-\mu^+\mu^-$ analysis [190].

- **Barionic background**: a possible source of background that emulates the complete chain $D^{*+} \to D^0\pi_s^+$ is the decay $\Lambda_c(2595)^+ \to \Sigma(2455)^0\pi^+$ with the subsequent decay $\Sigma(2455)^0 \to \pi^-\Lambda_c^+(pK^-\pi^+)$. The most dangerous combination is when two final state pions are misidentified as muons or the proton is misidentified as a muon and the kaon as a pion, because in this configuration the candidates can enter in the ΔM spectrum too. Cutting on the PID variables of the final state particles to reveal this background (`ProbNN`$\mu < 0.5$ for both muons, with also `ProbNN`$K > 0.2$ and `ProbNN`$p > 0.2$ for hadrons) showed no significant excess with respect to a flat combinatorial background †. Therefore this background is considered negligible.

- **Secondary D^{*+} decays**: due to a real $D^0 \to h^+h^-\mu^+\mu^-$ decay where the D^{*+} is not prompt, i.e. does not come from the PV, but from a B meson decay like $\overline{B}^0 \to D^{*+}\mu^-\overline{\nu}_\mu$. It is considered a source of background for the A_{CP} asymmetry measurement, since secondary D^{*+} mesons exhibit a different production mechanism and a different production asymmetry than primary ones. Due to the B meson flight distance, the D^0 decay vertex is significantly displaced from the PV and this feature can be used to estimate the secondary decays fraction.

- **Random soft pion**: this background is due to an association between a real D^0 meson and a random low-momentum pion to form a fake D^{*+} candidate. It causes also a random $D^0/\bar{D}^0$ flavour tagging.

- **Ghost soft pion**: this background is caused by a wrong soft pion reconstruction, due to the association of VELO tracks of a real soft pion with unrelated hits in the tracking station. The most affected variable in this case is the pion charge, leading to a wrong D^0 flavour tagging. Thanks to multivariate discriminant, the ghost track probability, this background can be reduced to a negligible level.

4.3 Data and simulated samples

The data samples of the proton-proton collisions collected at a center of mass energy of 13 TeV during the Run II (2015-2018) are used, corresponding to an integrated luminosity of 5.7 fb^{-1}. The generation of the simulated data uses the software packages described in Sect. 2.2.4.3: the proton-proton collision is simulated in a vacuum, with the consequent production of a certain number of primary particles. In each event there is at least one meson of interest that decays in the requested mode, while the others decay in other modes, according to their branching

---

[†] The `ProbNN` variable is discussed in the Sect. 2.2.4.5

Sample	Statistics (MagUp/MagDown)
	2015
$D^0 \to K^+K^-\mu^+\mu^-$	2512621/2501720
$D^0 \to \pi^+\pi^-\mu^+\mu^-$	2497831/2503909
	2016
$D^0 \to K^+K^-\mu^+\mu^-$	7493417/7491750
$D^0 \to \pi^+\pi^-\mu^+\mu^-$	7497706/7493137
	2017
$D^0 \to K^+K^-\mu^+\mu^-$	9990304/9990550
$D^0 \to \pi^+\pi^-\mu^+\mu^-$	9989961/9981127
	2018
$D^0 \to K^+K^-\mu^+\mu^-$	9985695/10424194
$D^0 \to \pi^+\pi^-\mu^+\mu^-$	9986017/9991077

TABLE 4.1. List of simulated samples used in the analysis and the corresponding statistics at generator level.

fractions. Of all the particles produced in the generation phase, only those inside the acceptance of the LHCb detector are kept. The response of the entire detector is simulated and the final dataset are produced, in the same format as the real data, so that they can be processed by the software trigger, reconstructed and selected in the stripping phase. The samples for each year are divided according to the direction of the magnetic field during the data taking period: *MagUp* and *MagDown*. The same subdivision is provided for the MC samples as well. In Tab. 4.1 the number of events generated for each sample, divided by year and magnet polarity, is shown. In the simulation the signal decays are generated as a non-coherent mixture of resonant and non-resonant contributions, in both di-muon and di-hadron final states. The non-resonant contribution is described by a simple four body phase space decay, with a flat distributions over all angles but non-flat distributions in the di-muon and di-hadron spectra. This assumption is a good approximation given the low expected statistics in data.

4.4 Variables used in the selection

In addition to kinematic variables such as the momentum p, the transverse momentum p_{T} or invariant masses, other important variables are used in the selection. Since some of them are obtained through a fit procedure during the reconstruction phase, the selection request can be made not on the actual value of the variable but on the associated reduced χ^2 of the fit.

- Vertex χ^2/dof [†]: the decay vertex of a particle is reconstructed via to a fitting procedure starting from the final state tracks. Therefore the associated χ^2 is obtained, which indicates

---

[†] dof is the acronym of *degree of freedom*.

the degree of confidence on the origin of the daughter particles from the same vertex. A typical requirement is $\chi^2/\text{dof} < \mathcal{O}(10)$.

- Track χ^2/dof: since each track is obtained from a fit of the detector hits positions, a χ^2 is associated to each track and can be used to remove ghost tracks.
- Impact parameter (IP) with respect to the PV: it is the minimum distance between a reconstructed track and the PV. This variable is useful to distinguish particles coming from the PV or from short lived resonances produced at the PV, from particles coming from a secondary vertex, due to the decay of a longer lived particle like B mesons, since on average they have a bigger IP. Typical selections on this variable are made on the χ^2, called χ^2_{IP}, defined as the variation of the χ^2 per degree of freedom of the PV fit done with and without the considered particle. A better signal-background separation is obtained selecting on χ^2_{IP} instead of the IP value, since it takes into account also the uncertainties coming from the first measured point in the track.
- Flight distance (`FD`) and χ^2_{FD}: it is the distance between the decay vertex of a particle and the vertex in which it originates. For this variable a better separation is also obtained by imposing the selection on the χ^2 called χ^2_{FD}. It is defined as

  $$\chi^2_{\text{FD}} = (\vec{r}_{\text{PV}} - \vec{r}_{\text{DV}})^{\text{T}} \Sigma^{-1} (\vec{r}_{\text{PV}} - \vec{r}_{\text{DV}}),$$

  where $\vec{r}_{\text{PV}}$ and $\vec{r}_{\text{DV}}$ are the position of the primary and decay vertex, while Σ^{-1} is the inverse of the covariance matrix of their measurements.
- Cosine of the pointing angle (`DIRA`): it is defined as the cosine of the angle between the particle's flight direction (obtained joining the origin and the decay vertex) and the particle momentum direction. In the case of the D^0 in our case this variable can be written as

  $$\frac{\vec{p}_{D^0} \cdot (\vec{r}_{\text{PV}} - \vec{r}_{\text{DV}})}{|\vec{p}_{D^0}||\vec{r}_{\text{PV}} - \vec{r}_{\text{DV}}|}$$
- Distance of closest approach (`DOCA`): it is defined as the minimum distance between two trajectories, which can be used to reject particles that do not come from the same vertex. For multi-body decays the selection is done on the largest `DOCA` (named `MAXDOCA`) of all the tracks combinations.
- D^{*+} isolation variable (D^{*+}-cone p_{T} asymmetry): it takes into account how much a particle, in this case the D^{*+}, is isolated. It is defined as

  $$A = \frac{p_{\text{T}}(D^{*+}) - \sum_i (p_{\text{T}})_i}{p_{\text{T}}(D^{*+}) + \sum_i (p_{\text{T}})_i},$$

  where the sum runs over all the tracks inside a cone with radius $R = \sqrt{(\Delta\eta)^2 + (\Delta\phi)^2} = 1.5$ rad around the D^{*+} track, not counting the tracks which are not part of the signal candidate decay chain. If the D^{*+} is completely isolated and no other tracks are found in the cone then $A = 1$, otherwise $A < 1$.

4.5 Selection

Having defined the main variables, the selection procedures carried out on the data samples and on MC will be described in this section, concluding with the study of the optimisation of the final selection.

4.5.1 Trigger requirements

The $D^0 \to h^+h^-\mu^+\mu^-$ signal can be triggered either by the hardware trigger L0, and by the software trigger HLT. In particular at HLT2 trigger level, specific lines were written to select these channels. Muon triggers have been developed for high transverse momenta, the selection is not optimal for our signal, since muons from $D^0 \to h^+h^-\mu^+\mu^-$ have average momenta of $p \sim 10 - 20\,\mathrm{GeV}$ and transverse momenta $p_\mathrm{T} \sim 1.5\,\mathrm{GeV}$, however efficiencies remain sufficiently high.

- At L0 trigger, at least one of the two muons is required to be triggered as `TOS` on the `L0Muon` trigger line. For a definition of the `TOS` category the reader can refer to Sect. 2.2.4.4.

- At HLT1 level four trigger lines are considered: `Hlt1TrackMVA` and `Hlt1TwoTrackMVA` for the D^0 candidate, and `Hlt1TrackMuon` and `Hlt1TrackMVAMuon` for the muons. The lines for single track are based mainly on requirements for p_T and χ^2_IP, while the two-tracks lines are based also on requirements for the secondary vertex quality, like its χ^2_vertex, the two-tracks mass and p_T etc. Also a MatrixNet classifier is used to assign a score to the secondary vertex and quantify its compatibility with a heavy hadron decay vertex [235, 286]. The final choice is to require the D^0 candidate to be `TOS` on `Hlt1TrackMVA` or `Hlt1TwoTrackMVA`, or at least one of the two muons to be `TOS` on `Hlt1TrackMuon` or `Hlt1TrackMVAMuon` line.

- At HLT2 trigger level for each decay mode the D^0 candidate is required to be `TOS` on the exclusive line named `Hlt2RareCharmD02{KK,PiPi}MuMu`. The HLT2 selection is very similar to the offline one made at stripping level, except that in 2015 and 2016 no D^{*+} candidate was built at HLT2 level, while it was added in the definition of 2017 and 2018 lines. For this reason the trigger requirement is made on the D^0 for 2015 and 2016 and on the D^{*+} for 2017 and 2018.

Trigger fiducial cuts

Relevant behaviour of the trigger system is that usually the thresholds and the configuration of a particular trigger line remains constant when applied on the MC, but may vary for

Year	L0Muon_PT threshold (ADC counts)
2015	57
2016	37
2017	29

TABLE 4.2. L0Muon_PT requirements applied offline on data.

trigger applied on data, since the trigger configuration (identified by the TCK number, already mentioned in Sect. 2.2.4) is often changed and adapted during the data taking, due mainly to rate adjustments. Thus some of the thresholds, both at L0 and HLT1 levels, must be made consistent to get a good data-MC agreement. At the L0 trigger level the selections made on transverse momenta are based on measurements with a worse resolution with respect to the corresponding offline measurements, and are defined in terms of ADC counts. For the `L0Muon` line only the three highest impulse trigger objects are saved, without any direct reference to the candidates subsequently reconstructed offline. All the different trigger configurations used in Run II during data taking and in the simulations are reported in Appendix B, together with the main L0 and HLT1 line thresholds. For `L0Muon` p_{T} thresholds, the correct alignment is to require that on data the p_{T} of the `L0Muon` objects are larger than the threshold fixed on the simulation of the corresponding year, in order to assure that the candidates are properly treated in the simulation. These requirements are reported in Tab. 4.2.

For HLT1 the fiducial cuts have to be applied only in 2016, when the most important changes on the line configurations were applied. In fact in 2015, 2017 and 2018 the HLT1 thresholds were identical to those applied on the corresponding MC so no inconsistencies are expected. First of all, some of 2016 data are removed because of the tight thresholds, named *thr*, of the `TwoTrackMVA` line, that correspond to the values applied on the MatrixNet classifier. Thus it was decided to remove the TCKs 0x11371609, 0x1137160E for 2016 MagDown, and 0x11351609 and 0x11361609 for 2016 MagUp, corresponding approximately to $\sim 30\%$ of the overall collected 2016 sample. The HLT1 lines `TrackMVA` and `MuonTrackMVA` used in this analysis, are characterised by a 2D hyperbolic cut on p_{T} and χ^2_{IP}, which depends by a parameter denoted b in the following as well as in the tables in Appendix B. The parameter b changes as a function of the TCK. The 2D cut is given by

$$\log \chi^2_{\mathrm{IP}} > \frac{1.0}{(p_{\mathrm{T}}[\,\mathrm{GeV}] - 1.0)^2} + \frac{b}{25} \cdot (25 - p_{\mathrm{T}}[\,\mathrm{GeV}]) + \log(7.4). \tag{4.2}$$

For the `TrackMVA` line a tight value of b is not a problem since it happens in the TCKs already removed. For `TrackMuonMVA` the iperbole cut has been implemented in order to apply the selection on data with $b = 1.1$ for all the 2016 TCKs that did not foresee that selection. The fiducial cuts for the `TrackMuon` line tighten the selections on the χ^2_{IP}, the track ghost probability and the muon p_{T}, in order to be consistent with the selections applied on MC. For

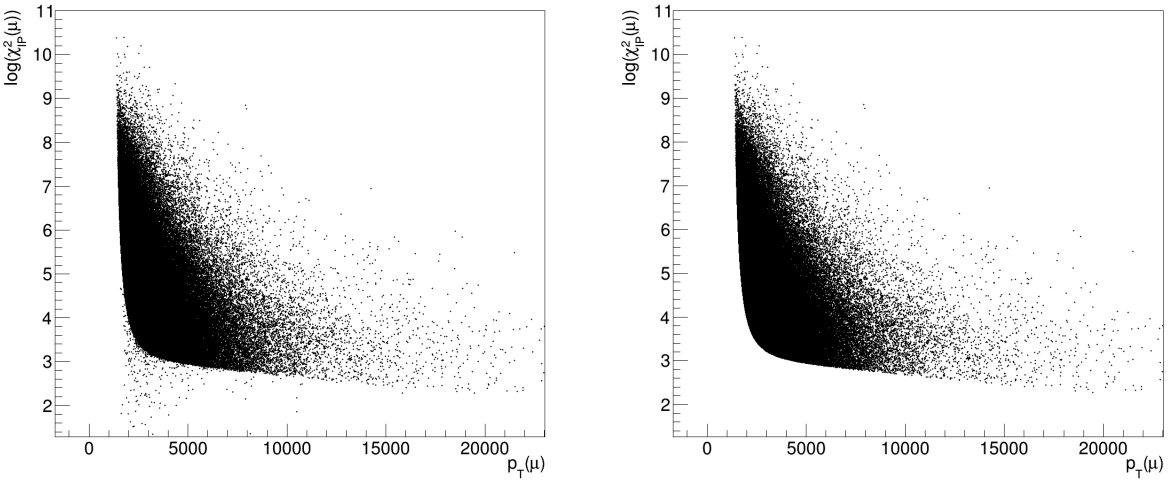

FIGURE 4.1. Scatter plot of the $\log(\chi^2_{\mathrm{IP}}(\mu_1))$ with respect to $p_{\mathrm{T}}(\mu_1)$ before the `TrackMuonMVA` fiducial cut (left) and after the fiducial cut (right), for the 2016 $D^0 \to \pi^+\pi^-\mu^+\mu^-$ data sample after the stripping selection and with only `TrackMuonMVA_TOS` on μ_1 required.

Line	Fiducial cut
`TrackMuonMVA`	χ^2_{IP}- p_{T} cut with $b = 1.1$
`TrackMuon`	$\chi^2_{\mathrm{IP}}(\mu) > 35$ $p_{\mathrm{T}}(\mu) > 1.1\,\mathrm{GeV}$ `mu_TRACK_GhostProb` < 0.2
`TwoTrackMuon`	Removal TCKs with tight *thr*

TABLE 4.3. Trigger fiducial cuts applied on 2016 data sample.

the `TwoTrackMVA` line, the ghost probability and the p_{T} threshold have not been changed since they are applied to all possible two-tracks combinations of the four tracks composing the D^0 candidate, and are difficult to reproduce offline. It is important to note that a tightened cut $p_{\mathrm{T}}(D^0) > 2$ GeV is applied anyway at stripping level.
The final trigger fiducial cuts applied on 2016 data sample are reported in Tab. 4.3.

4.5.2 Stripping selection

Specific stripping lines were developed for the exclusive selection of $D^{*+} \to D^0(\to h^+h^-\mu^+\mu^-)\pi_{\mathrm{s}}^+$ candidates. The selection is organised in a hierarchical way:

- in the first step all the events with a reconstructed PV are selected and the four charged particles, reconstructed as long tracks (μ and K or π), are searched for to form the

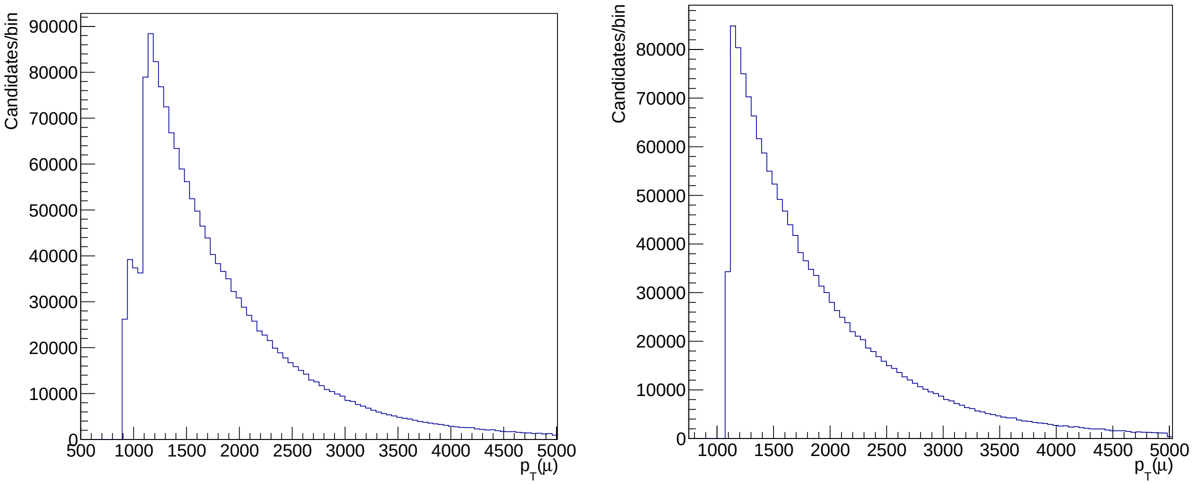

FIGURE 4.2. Distribution of $p_\mathrm{T}(\mu_1)$ before the `TrackMuon` fiducial cut (left) and after the fiducial cut (right), for the 2016 $D^0 \to \pi^+\pi^-\mu^+\mu^-$ data sample after the stripping selection and with only `TrackMuon_TOS` on μ_1 required.

D^0 candidate. On these tracks loose cuts on the momentum, $p > 3\,\mathrm{GeV}/c$, transverse momentum, $p_\mathrm{T} > 300\,\mathrm{MeV}/c$, and track quality, $\chi^2_\mathrm{track}/\mathrm{dof} < 3$ are requested. It is also required for the tracks not to be compatible with those coming from the PV by imposing $\chi^2_\mathrm{IP} > 3$ and at least one of the tracks with $\chi^2_\mathrm{IP} > 9$. The tracks have to form a common vertex, thus the largest DOCA has to be smaller than 0.3 mm. For kaons a loose PID condition is requested with $\mathrm{DLL}_K > -5$, while `isMuon` flag is required for muons. A stronger PID selection for muons is done on top of the full selection chain and properly optimised with a multivariate discriminant selection to suppress the two main source of backgrounds, the full hadronic D^0 four body decay and the combinatorial background.

- The four tracks are used to build up a D^0 candidate, on which other requirements can be applied. The D^0 decay vertex is fitted and has to be of high quality, satisfying $\chi^2_\mathrm{vertex} < 20$, and detached from the PV by imposing $\chi^2_\mathrm{FD} > 30$. The D^0 candidate has to come from the PV and not from other secondary decay. This is achieved by requiring $\chi^2_\mathrm{IP} < 36$ and a `DIRA` > 0.9998. The invariant mass of the candidate has to be within $\pm 100\,\mathrm{MeV}/c^2$ around the known D^0 mass, and cuts on the (transverse) momentum to be greater than (2)3 GeV/c are applied to suppress combinatorial background.

- The last step consists in pairing the D^0 candidate with a low momentum pion with good track quality ($p_\mathrm{T} > 2\,\mathrm{GeV}/c$ and $\chi^2_\mathrm{track} < 3$) to form the D^{*+}. The DOCA between the two particles has to be smaller than 0.3 mm and the corresponding vertex fit has to be of good quality ($\chi^2_\mathrm{vertex} < 20$). Kinematical requirements on the built D^{*+} help to reduce

Particle	Variable	Requirement
K, π, μ	p	$> 3\,\mathrm{GeV}/c$
	p_T	$> 300\,\mathrm{MeV}/c$
	χ^2_IP	> 3
	χ^2_track	< 3
μ	`isMuon`	True
K	DLL_K	> -5
D^0	p	$> 3\,\mathrm{GeV}/c$
	p_T	$> 2\,\mathrm{GeV}/c$
	m	$m_\mathrm{PDG} \pm 100\,\mathrm{MeV}/c^2$
	χ^2_vertex	< 20
	χ^2_FD	> 30
	χ^2_IP	< 36
	`DIRA`	> 0.9998
	`MAXDOCA`	< 0.3 mm
	χ^2_IP of at least one daughter	> 9
D^*	p_T	$> 2\,\mathrm{GeV}/c$
	χ^2_vertex	< 20
	`DOCA`	0.3 mm
	ΔM	$> 137.4\,\mathrm{MeV}/c^2$
		$< 164.4\,\mathrm{MeV}/c^2$
π_s	p_T	$> 120\,\mathrm{MeV}/c$
	χ^2_track	< 3
	n. of PV	≥ 1

TABLE 4.4. Stripping selection requirements.

the combinatorial background, in particular selecting a ΔM mass range ($137.4\,\mathrm{MeV}/c^2 - 163.4\,\mathrm{MeV}/c^2$) and a D^{*+} p_T greater than $2\,\mathrm{GeV}/c$.

All the cuts implemented in stripping selection are reported in Tab. 4.4.

4.5.3 Offline Preselection

A loose preselection is applied on top of the stripping in order to further reduce the combinatorial background. In particular, for the final state particles (K, π, μ) a cut on the Artificial Neural Network (`ANN`) variable for ghost probability is applied, `ProbNNghost` < 0.3, to reduce the amount of artificial ghost tracks. A tighter requirement is applied on the π_s^+, `ProbNNghost` < 0.05. In order to reduce misidentification, kaons and pions from the D^0 are requested to satisfy loose PID criteria (`ProbNNK` > 0.2 and `ProbNNpi` > 0.2 respectively), while for muons also the `NShared` variable is required to be zero (for the `NShared` variable definition the reader can refer to

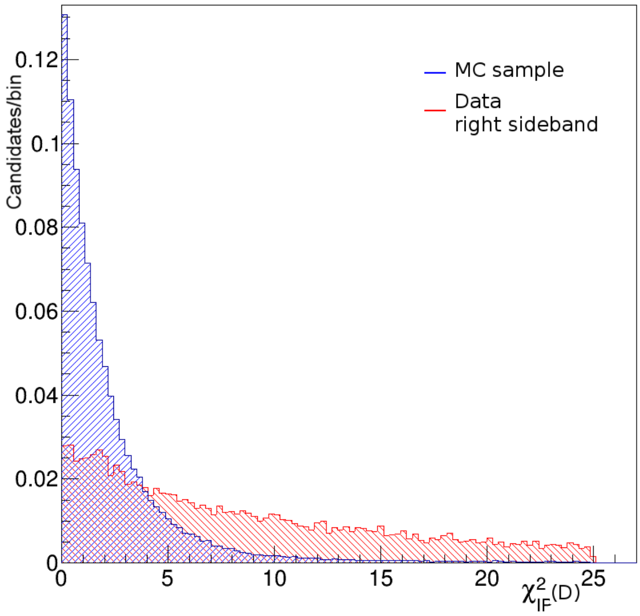

FIGURE 4.3. Normalised χ^2_{IP} distributions for 2017 $D^0 \to \pi^+\pi^-\mu^+\mu^-$ candidates, from MC sample (blue) and data right sideband (red) defined by $m(D^0) > 1890\,\text{MeV}/c^2$, after the trigger, preselection and ΔM cut.

Sect. 2.2.4.5). A very efficient selection on signal, able to reduce the combinatorial background, is based on the tightening the D^0 χ^2_{IP} cut with respect to the one applied at stripping level, as shown in Fig. 4.3. This cut is efficient to reduce the background even on top of the ΔM cut, since it reduce the amount of secondary decays that lie in the signal region in ΔM. In the following some important concepts and procedures are described in more details, in particular concerning a full re-fit of the decay chain to extract variables with improved resolutions, definition of D^0 and $m(\mu\mu)$ mass ranges and a specific *truth matching* procedure done on the simulation.

Decay Tree Fitter

After the stripping selection, the decay chain is complete but has been built with a fast bottom-up approach. A particular procedure called Decay Tree Fitter (DTF) is available in LHCb [287, 288] and is used in this analysis. This algorithm takes in input a complete decay chain and allows to parametrise it in terms of kinematical, angular and geometrical parameters, and fit them simultaneously. The parameters can be subjected to constraints, imposing measured quantities, fixing invariant masses or positions. This leads to better resolutions in terms of vertex positions, flight distances, masses and momenta. Two different DTFs are implemented:

1. A fit with the D^{*+} constrained to come from the PV.

2. A fit requiring, in addition to the previous constraint, a fixed nominal mass for the D^0.

Observable	Interval [MeV/c^2]
$m(D^0)$	1800 - 1950
ΔM	144.5 - 146-5

TABLE 4.5. Mass ranges for $m(D^0)$ and ΔM on data.

The latter method is useful to perform the 5-D D^0 decay phase space analysis, since all the calculated momenta are inside the physical phase space and no resolution-induced smearing at the phase space borders arises. Each DTF algorithm provides also its corresponding χ^2_{DTF}: a loose fiducial cut on the first DTF of $0 \leq \chi^2_{\text{DTF}} \leq 150$ is applied at this preselection stage. In addition the ΔM observable considered in the analysis is the one obtained from the first type of DTF fit.

Mass Ranges

The number of candidates will be subsequently determined from a fit to the D^0 invariant mass spectrum. For this reason it is used a large mass window at high masses, with respect to the nominal mass of the D^0, to properly determine the distribution of the combinatorial background. On the other hand a less wide range at low masses has been chosen to be able to exclude the tail of the distribution due to the $D^0 \to h^+h^-K^-\pi^+$ doubly misidentified background, but to be able anyway to accurately determine the distribution of the $D^0 \to h^+h^-\pi^+\pi^-$ doubly misidentified background. A stringent cut on the ΔM variable allows to reduce a large part of the combinatorial background. A cut of $\pm 3\sigma$ around the nominal ΔM value is chosen, where σ corresponds to the typical signal peak resolution observed in ΔM, of the order of $0.3\,\text{MeV}/c^2$. The chosen mass ranges are reported in Tab. 4.5.

$m(\mu\mu)$ binning scheme

As explained in Sect. 1.7.1, the angular coefficients can strongly depend on the phase space position, and in particular on the di-muon invariant mass, where they can be enhanced by resonances. For this reason, and to obtain a cleaner comparison to theoretical predictions, the analysis has to be performed in regions of $m(\mu\mu)$. A total of five main regions can be defined: three of them corresponding to regions of the main di-muon resonances, η, ρ/ω and ϕ, and two other bins for low and high mass regions. Being the phase space smaller, for the $D^0 \to K^+K^-\mu^+\mu^-$ mode three bins can be defined. In order to take into account the resonance-catalysed asymmetry effect, where the asymmetry change sign at the pole of a resonance, a finer binning scheme can be defined, where the two main bins corresponding to ρ/ω and ϕ are subdivided in two symmetrical bins each. The final $q^2(\mu\mu)$ binning scheme is reported in Tab. 4.6.

	$m(\mu\mu)$ [MeV/c^2]				
Decay mode	low mass	η	ρ/ω	ϕ	high mass
$D^0 \to K^+K^-\mu^+\mu^-$	< 525	525-565	> 565	-	-
$D^0 \to \pi^+\pi^-\mu^+\mu^-$	< 525	525-565	565-780, 780-950	950-1020, 1020-1100	> 1100

Table 4.6. Definition of the di-muon mass binning scheme used in the analysis.

Simulation truth matching

In the simulated samples some of the selected candidates might be partially reconstructed or might contain ghost tracks. A particular procedure was developed in LHCb in order to perform a matching, at decay chain level, between the reconstructed and actually generated particles, comparing the hits in common between a reconstructed track and those produced by the generated particle. Starting from the final state tracks the information on the matching is then propagated to the intermediate reconstructed particles. There are several categories, numbered by the `BKGCAT` variable, that allows to classify the different kinds of partial reconstructions, which take into account, for example, whether at least one of the tracks is a ghost, or whether two different reconstructed particles are matched to the same generated particle, etc. The required truth matching accepts three categories:

- `BKGCAT` = 0: called signal, the decay chain in generation is identical to the reconstructed one, meaning that all the daughters and intermediate particles are correctly matched.
- `BKGCAT` = 10: called semi-signal, meaning that the final state particles are properly matched but there are different intermediate states.
- `BKGCAT` = 50: called low-mass background, it corresponds to the signal with also emission of photons due to radiative energy loss.

4.5.4 Soft pion acceptance asymmetry

Regions of the phase space with large acceptance asymmetries can introduce higher-order effects in D^0 angular distributions, since a possible asymmetry can enhance some of the angular coefficients discussed in Sect. 1.7.1. A well-known source of acceptance asymmetry arises from the detection and reconstruction of the soft pion. In particular, two effects can occur that lead to a maximal detection asymmetry in specific regions:

- soft pions of opposite charge and similar momentum are bent by the magnetic field into opposite directions. For low p_x and p_y, it is possible that one soft pion can be deflected on the opposite side, remaining in the LHCb acceptance, but the other one can be completely bent out and exit the LHCb acceptance without passing through the T stations. Then

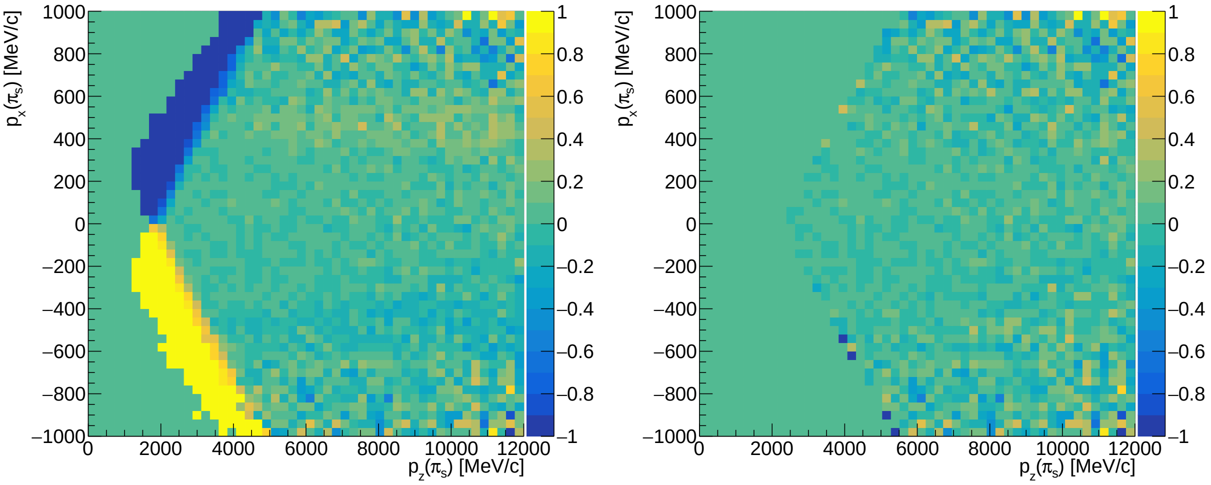

FIGURE 4.4. Raw asymmetry $A = (N_{\pi^+} - N_{\pi^-})/(N_{\pi^+} + N_{\pi^-})$ for $D^0 \to \pi^+\pi^-\mu^+\mu^-$ candidates in Run II *MagDown* MC sample, as a function of the soft pion p_x and p_z, before the fiducial cuts (left) and after the fiducial cuts (right).

the 3D distribution (p_x, p_y, p_z) of reconstructed π_s^+ and π_s^- are asymmetric. This effect is shown in Fig. 4.4.

- for low p_y (but the effect is visible also at higher p_y), i.e. for soft pions that lie close to the horizontal plane containing the beam pipe, and for specific p_x intervals, the pions can be bent into the beam pipe, reaching a region of the T-stations that is not instrumented, and therefore not be detected. This effect depends on p_x and p_z, and on the charge of the pions, as shown in Fig. 4.5. In the plots the raw asymmetry $A = (N_{\pi^+} - N_{\pi^-})/(N_{\pi^+} + N_{\pi^-})$ is shown for each p_x-p_z bin, where $N_{\pi^\pm}$ are the number of positive or negative soft pions.

In order to reduce these effects some fiducial cuts can be made, excluding specific intervals of the soft pion phase space that lie in the regions mentioned above. In particular, following [206, 289], the regions to be removed have to meet the following criteria:

- $|p_x| \geq a(p_z - p_0)$ for the first mentioned effect, where $a = 0.317$ and $p_0 = 2400\,\text{MeV}/c$;
- if $|p_y/p_z| < 0.02$ then $(p_1 - b_1 p_z) < |p_x| < (p_2 + b_2 p_z)$ for the beam pipe effect, where $p_1 = 418\,\text{MeV}/c$, $p_2 = 497\,\text{MeV}/c$, $b_1 = 0.01397$ and $b_2 = 0.016015$.

The distributions of ΔM and $m(hh\mu\mu)$ for $D^0 \to \pi^+\pi^-\mu^+\mu^-$ and $D^0 \to K^+K^-\mu^+\mu^-$ candidates after the trigger, preselection and soft pion fiducial requirements are shown in Fig. 4.6.

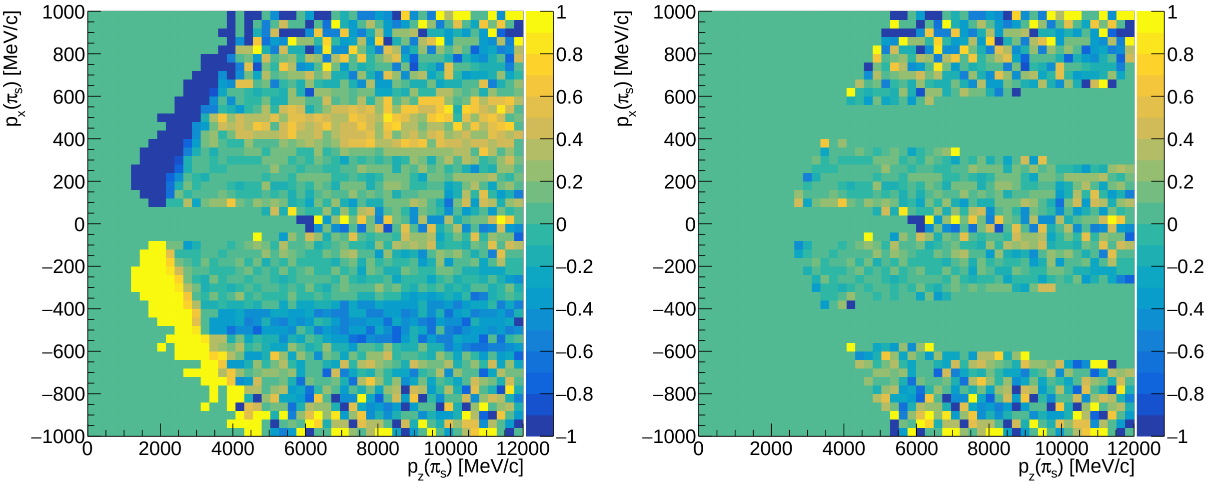

FIGURE 4.5. Raw asymmetry for $D^0 \to \pi^+\pi^-\mu^+\mu^-$ candidates in Run II *MagDown* MC sample, as a function of the soft pion p_x and p_z with the condition $|p_y/p_z| < 0.02$, before the fiducial cuts (left) and after the fiducial cuts (right).

4.5.5 Multivariate offline selection

In order to further suppress the combinatorial background and preserve high signal efficiency, a method that exploits all the correlations between kinematical and geometrical variables has to be used. In this study a multivariate analysis (MVA) classifier, in particular a Boosted Decision Tree (BDT) with a gradient boosting has been used. The classifier is available in the Toolkit for Multivariate Analysis (TMVA) package [290].

The BDT is trained adding up all the Run II datasets, using the preselected and truth-matched simulated sample as signal, and the preselected data right sideband as background, where the right sideband is defined by the events with $m(D^0) > 1890\,\text{MeV}/c^2$. This region contains events that are compatible with combinatorial background only, being sufficiently far away from the signal and misidentified backgrounds invariant mass regions. The BDT is trained before the ΔM cut to exploit a background sample with higher statistics.

In general, apply a MVA selection, especially a BDT, to a subsample which has been previously used to train the MVA classifier itself might cause a bias, since the classifier can separate the signal and background categories more efficiently on that subsample, an effect called *overtraining*. The presence of overtraining can be checked by comparing the BDT distributions of the training sample and of a different independent subsample, called test sample. In order to avoid any bias, even in case of no overtraining, it has been chosen to not apply the MVA to the subsample used in the training.

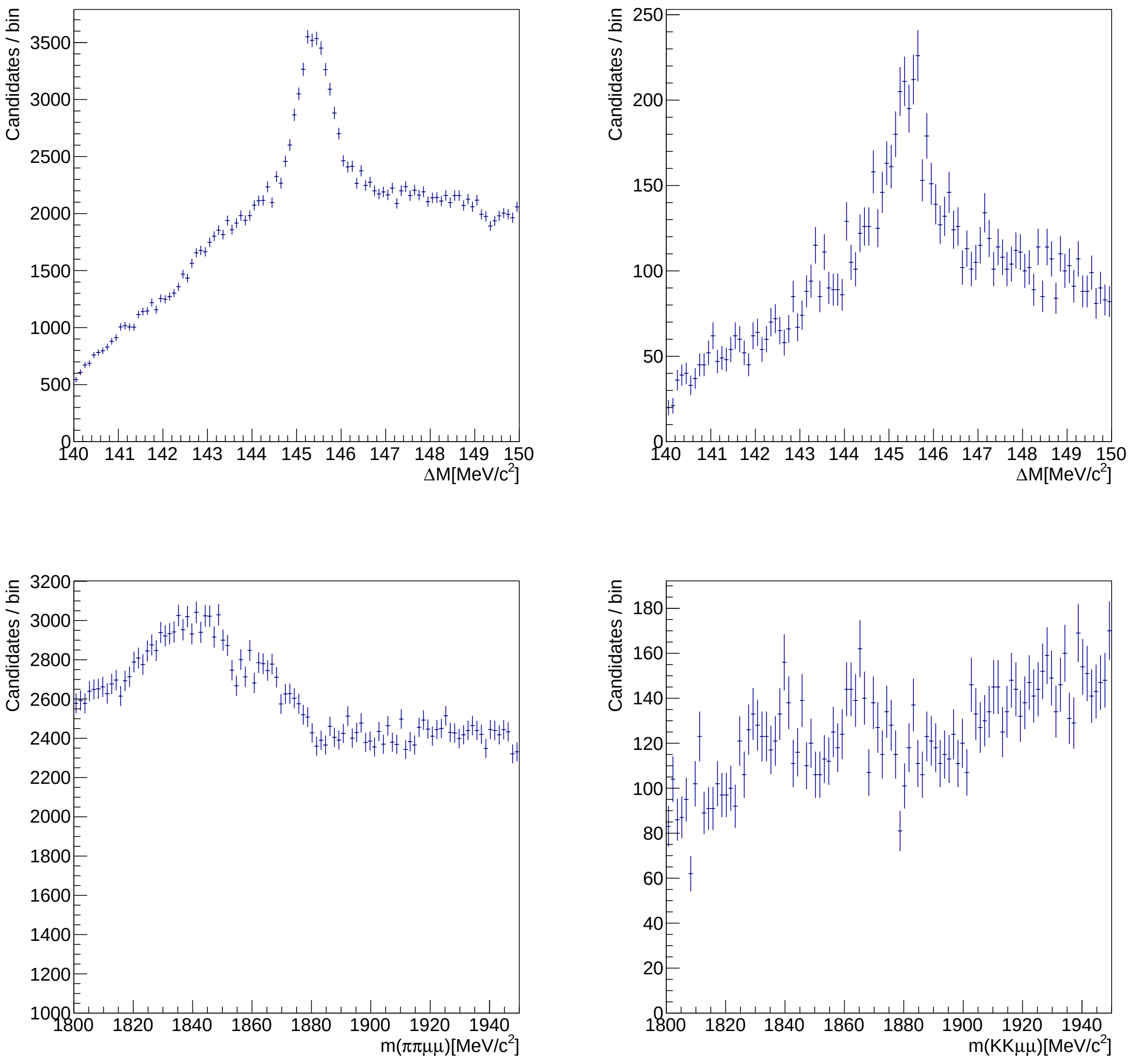

FIGURE 4.6. Distribution of ΔM (top) and D^0 invariant mass (bottom) for $D^0 \to \pi^+\pi^-\mu^+\mu^-$ (left) and $D^0 \to K^+K^-\mu^+\mu^-$ candidates (right) after the trigger, preselection and soft pion fiducial cuts requirements, except for the ΔM cut.

For this reason the initial training sample is divided in two subsamples, according to the parity of the `EventNumber`, an integer quantity that counts the events within the same LHCb run. Thus two training procedures are done, on the even and the odd sample, and finally the even-trained BDT is applied on the odd sample and viceversa. The training and application procedure is performed separately for the $D^0 \to \pi^+\pi^-\mu^+\mu^-$ and $D^0 \to K^+K^-\mu^+\mu^-$.
The variables used in the training are the following:

- largest distance of closest approach of the D^0 daughters (D^0 `MAXDOCA`),
- logarithm of the D^0 $\chi^2_{\rm FD}$, $\log \chi^2_{\rm FD}(D^0)$,
- logarithm of the cosine of D^0 pointing angle, $\log {\rm DIRA}(D^0)$,
- $\chi^2_{\rm vertex}$ of the D^0 decay,
- momentum of the $\pi^+_{\rm s}$, $p(\pi^+_{\rm s})$,
- transverse momentum of the $\pi^+_{\rm s}$, $p_{\rm T}(\pi^+_{\rm s})$,
- the D^*-cone $p_{\rm T}$ asymmetry.

Another undesired effect is the *sculpting* of the D^0 mass spectrum, or the di-muon and di-hadron spectrum. This can happen because the BDT can in principle learn to separate signal and background categories based also on the phase space position or the specific invariant mass considered. Supposing to have a purely combinatorial background sample and to cut on the BDT parameter to suppress it; a fake peak might arise in the expected mass region for the signal, because in that region the events are considered to be more *signal-like* by the BDT. In order to avoid this effect, the variables have to be chosen carefully in order to reduce the correlation between the BDT output and the set of the main variables used in the analysis: the D^0 invariant mass, the di-hadron and di-muon masses and the angular variables. The correlation has been reduced not using the D^0 final state particles momenta or transverse momenta in the set of training variables.
The BDT output variable is defined between -1 and 1. Stringent cuts at high values allow to select the signal rejecting the background, but also lead to a lower signal efficiency, so it is necessary to find an optimal point for the application of the cut, as described in the Sect. 4.5.6. In Fig. 4.7 and Fig. 4.8 the BDT distributions of the $D^0 \to \pi^+\pi^-\mu^+\mu^-$ and $D^0 \to K^+K^-\mu^+\mu^-$ *even* samples respectively are shown. The BDT of the signal and background samples are compared between the training and the test samples, and no significant difference is observed, which suggest a negligible overtraining effect. Similar and consistent results are observed for the *odd* samples. The Receiver Operating Characteristic (ROC) curves are also shown, which allow to determine the quality of the BDT selection showing the signal efficiency versus the background rejection for a given BDT classifier. An example of the input variable distributions separately for signal and background in case of $D^0 \to \pi^+\pi^-\mu^+\mu^-$ is shown in Fig. 4.9.

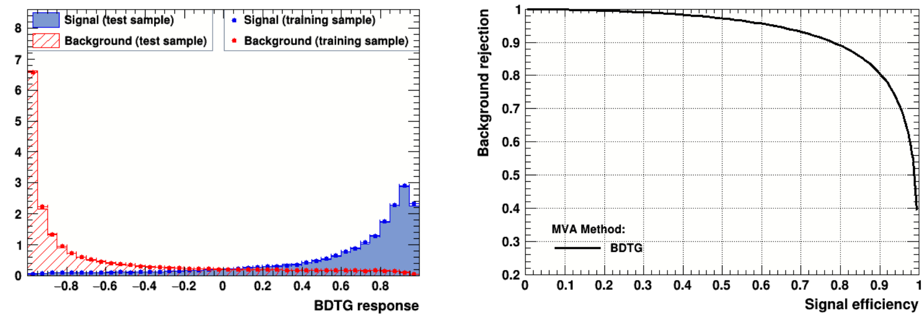

FIGURE 4.7. Left: ROC curve of the BDT classifier trained on even data samples for $D^0 \to \pi^+\pi^-\mu^+\mu^-$. Right: BDT distributions for the signal (blue) and background samples (red) and comparison between the ones for the training samples (points) and test samples (bars).

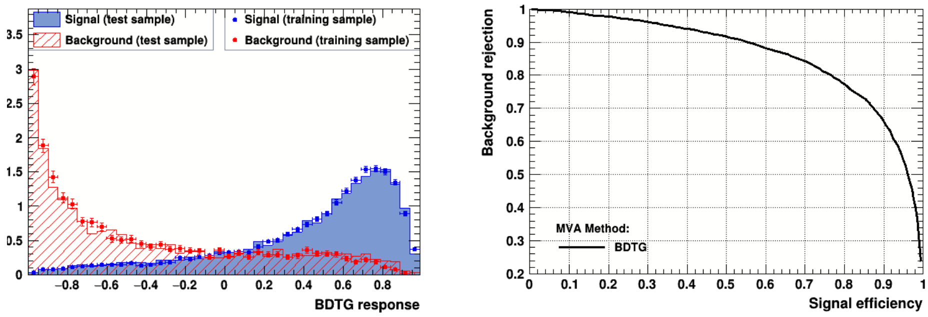

FIGURE 4.8. Left: ROC curve of the BDT classifier trained on even data samples for $D^0 \to K^+K^-\mu^+\mu^-$. Right: BDT distributions for the signal (blue) and background samples (red) and comparison between the ones for the training samples (points) and test samples (bars).

4.5.6 Final selection optimisation

In addition to the BDT selection to suppress the combinational background, a selection on the ProbNNμ variable of both muons is performed to reduce the doubly misidentified background $D^0 \to \pi^+\pi^-\pi^+\pi^-$. ProbNN$\mu$ is defined between 0 and 1: values closer to 1 select candidates with higher probability of being real muons. The optimisation of the final cuts both on the BDT and the ProbNNμ is also carried out simultaneously. For the optimisation procedure it is necessary to choose a *figure of merit* that quantifies the goodness of the selection itself. One possible choice is the ratio $\mathcal{S} = N_{\text{sig}}/\sqrt{N_{\text{sig}} + N_{\text{bkg}}}$, as a function of the selection, where N_{sig} and N_{bkg} are the number of signal and background events in the considered mass region. Since the aim of the study is to perform an angular fit, whose model is described by coefficients that are proportional to angular asymmetries, like A_{FB}, the chosen figure of merit (to be minimised) is the uncertainty on the raw asymmetry, δA, where A is defined as

$$A = \frac{N_+ - N_-}{N_+ + N_-}, \tag{4.3}$$

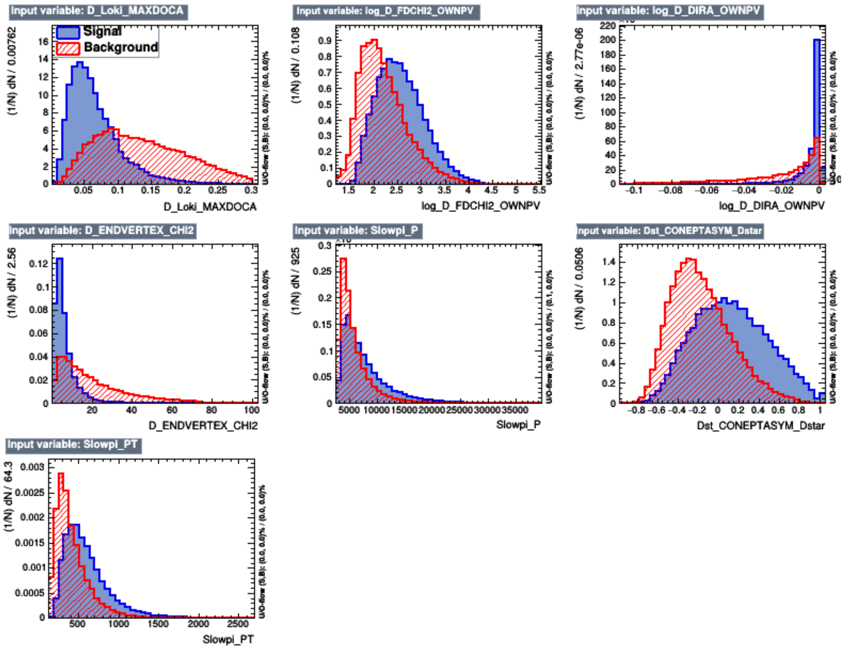

FIGURE 4.9. Distributions of the BDT input variables for signal (blue) and combinatorial background (red) for the $D^0 \to \pi^+\pi^-\mu^+\mu^-$ sample.

where the N_+ and N_- are the number of events of two randomly disjoint subsamples on which a simultaneous fit is done, with a procedure described in Sect. 4.7.2, and where A is a fit parameter. The optimisation is performed by scanning the BDT-ProbNNμ plane with cuts like BDT $> x$ and ProbNN$\mu > y$, separately for $D^0 \to \pi^+\pi^-\mu^+\mu^-$ and $D^0 \to K^+K^-\mu^+\mu^-$ for the whole Run II sample, as shown in Fig. 4.10. A common selection to the two decay modes is chosen:

$$\text{BDT} > -0.6,$$

$$\texttt{ProbNN}\mu > 0.6.$$

4.6 Correction for phase space dependent efficiency

The decay $D^0 \to h^+h^-\mu^+\mu^-$ can occur through several intermediate resonant states (that will be discussed later) which therefore occupy different regions of the phase space. Since reconstruction and selection can introduce efficiency and resolution effects as a function of the phase space region, an artificial change in the relative observed contributions of the resonant states can be observed. Furthermore, since the angular asymmetries also depend on the considered region, their measurements can be affected by biases. For this reason, a correction must be applied. The phase space can be parametrised as described in Sect. 1.7.1. Ideally the most natural procedure would be to divide the 5-dimensional phase space into sufficiently small bins so that

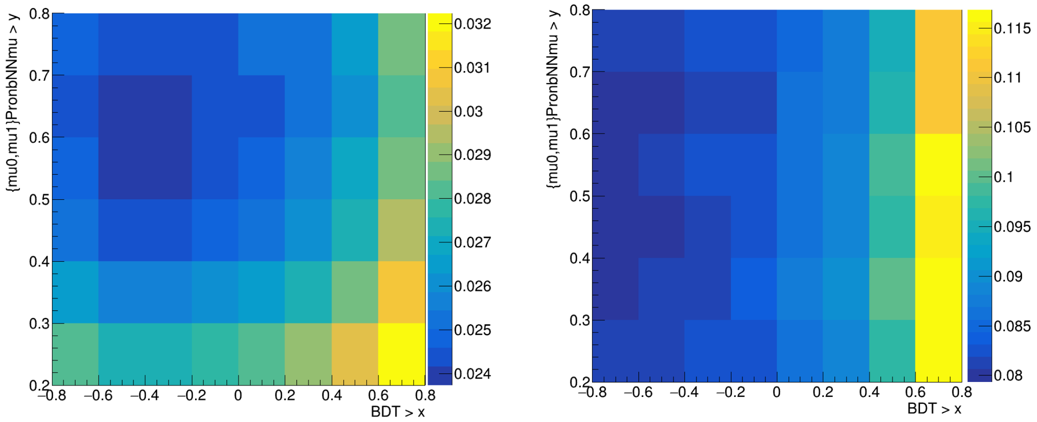

FIGURE 4.10. Scan of the uncertainty on the raw asymmetry on a randomly tagged sample in the two dimensional space of minimum BDT and ProbNNmu requirements for $D^0 \to \pi^+\pi^-\mu^+\mu^-$ (left) and $D^0 \to K^+K^-\mu^+\mu^-$ Run II data.

one can consider a constant efficiency within them, and calculate in each one a weight w, defined as the ratio between the number of candidates at the MC generation phase and the number of candidates after the reconstruction and complete selection. However the statistics is too limited to carry out a 5-dimensional binning. Another method recently developed [291] is to perform multidimensional efficiency correction with a MVA techniques. In particular, a BDT with gradient boosting is used, which is trained with two samples, both from MC simulations: one of which corresponds to the generator level decay, and the other to the reconstructed and selected decay. Any difference between the two is due to the effects of acceptance and resolution. In this case the BDT is not used to classify signal and background, but generated and reconstructed events. The ratio between the two BDT distributions, indicated as $\mathtt{BDT}^{\mathrm{gen}}$ and $\mathtt{BDT}^{\mathrm{sel}}$, therefore provides an estimate of multidimensional efficiency. Qualitatively, the BDT captures the 5-dimensional correlations and supplies a single output variable, on which the corrections can be made in bins as described above, instead of performing it in the 5-dimensional space. The assumption of the method is that reweighing the BDT variable, to make it equal to that of the generator level, automatically leads to a proper reweight of the input variables. The value of the per-candidate weight, to be applied on data, corresponds to the inverse of the per-candidate efficiency value:

$$w_i = \frac{1}{\varepsilon_i} = \left(\frac{\mathtt{BDT}^{\mathrm{sel}}_{i\in k}}{\mathtt{BDT}^{\mathrm{gen}}_{i\in k}} \right)^{-1}, \tag{4.4}$$

where i is the event index, and the notation $i \in k$ indicates that the i-th event falls into the k bin in which the ratio between the BDT distributions is computed. It is important to note that in this case only the efficiency variation on the phase space, and not in its absolute value, has to be considered. The BDT reweighter for $D^0 \to K^+K^-\mu^+\mu^-$ and $D^0 \to \pi^+\pi^-\mu^+\mu^-$ samples are shown in Fig. 4.11, with the ratio described by Eq. (4.4).

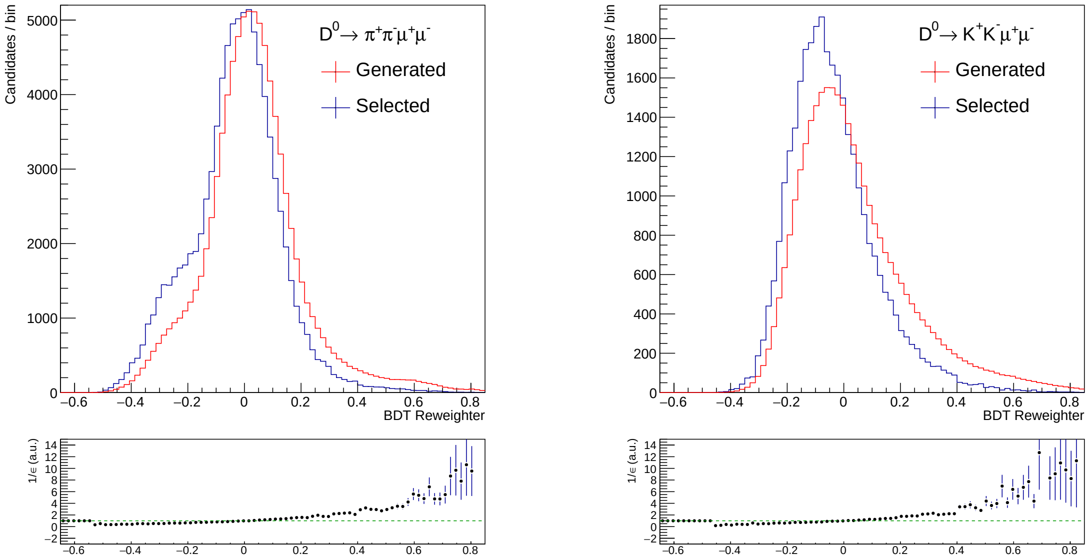

FIGURE 4.11. Output distributions of the BDT reweighter for $D^0 \to \pi^+\pi^-\mu^+\mu^-$ sample (left) and $D^0 \to K^+K^-\mu^+\mu^-$ (right) for simulated events at generator level (red) and fully selected (blue). The bottom panels show the ratio between the number of events of the two samples in each BDT bin, thus it is the inverse of the efficiency.

The chosen input variables to train the BDT are the two invariant masses $m(hh)$ and $m(\mu\mu)$ and the angular variables $\cos\theta_{\mu^+}$ and $\cos\theta_{h^+}$. The distribution on the angle ϕ is not affected by efficiency variation and it is also uncorrelated with the other variables, so it is not included as input variable. Nevertheless to check the efficiency variations the observable $\sin 2\phi$ is also shown. The efficiency variations of the input variables are shown in Fig. 4.12 and Fig. 4.13, where in addition the relative efficiency of the observable $\sin 2\phi$ is reported, showing a flat behaviour.

Assuming that the efficiency variation is similar for each year (assumption that has to be checked), an average correction for the full Run II can be applied. The training is then performed using the full Run II MC sample, with proportion between the years equal to the luminosity proportion in data. In order to avoid the overtraining the sample is randomly divided in four subsamples, three of them are using for the training and the BDT is applied on the fourth, and so on with the other combinations; when applied on data one of the four BDT classifiers is randomly chosen. The binning on the BDT variable to perform the reweighing procedure is characterised by a variable scheme: the bin width is chosen to get a constant number of selected candidates in each bin, thus avoiding large weight uncertainties in regions with too few selected candidates. As shown in Fig. 4.14 and Fig. 4.15 the selected-generated agreement after the reweighing procedure is sufficiently good. There are some regions, in particolar at low and high di-muon and di-hadron mass where the agreement is not optimal, due to the limited statistics of the selected sample.

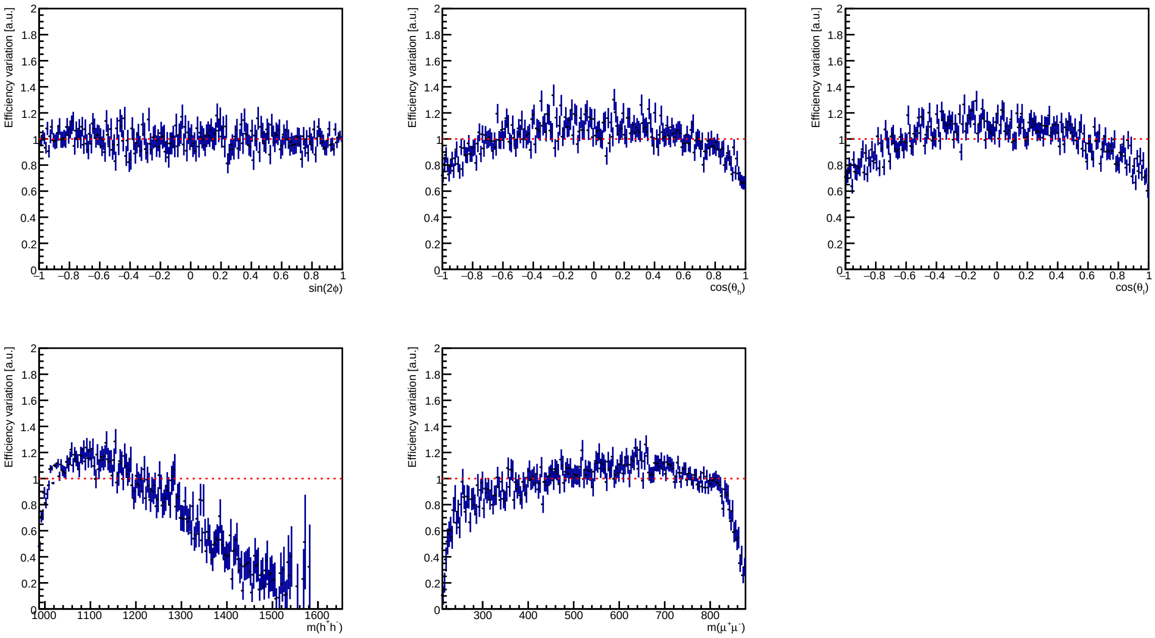

Figure 4.12. Efficiency variation as a function of the phase space variables for $D^0 \to K^+K^-\mu^+\mu^-$ candidates.

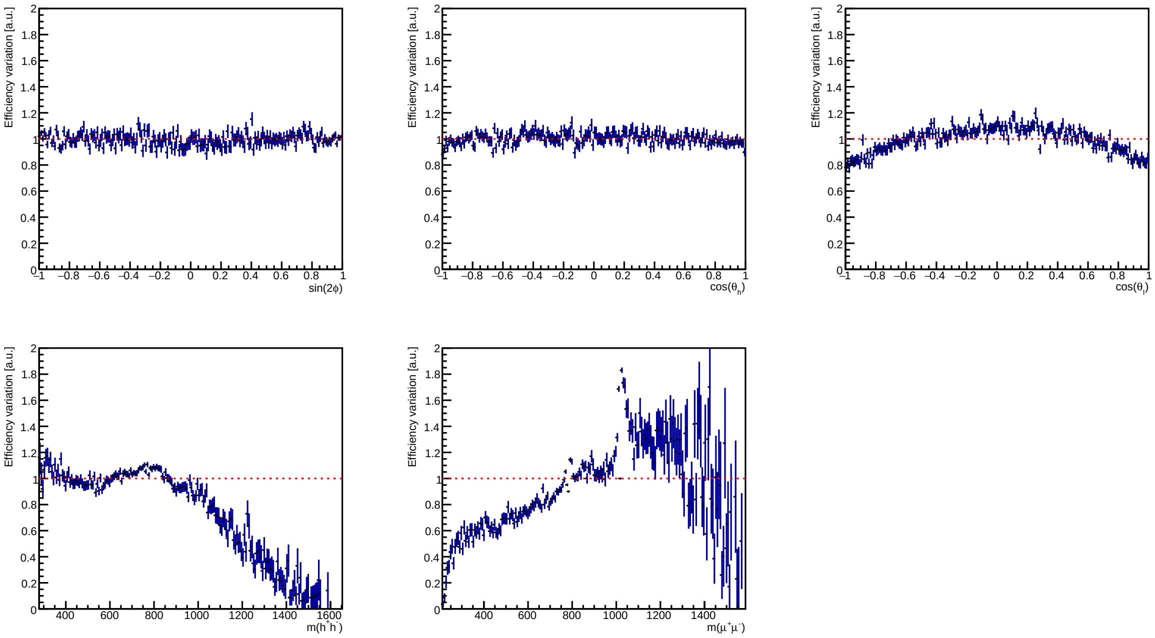

Figure 4.13. Efficiency variation as a function of the phase space variables for $D^0 \to \pi^+\pi^-\mu^+\mu^-$ candidates.

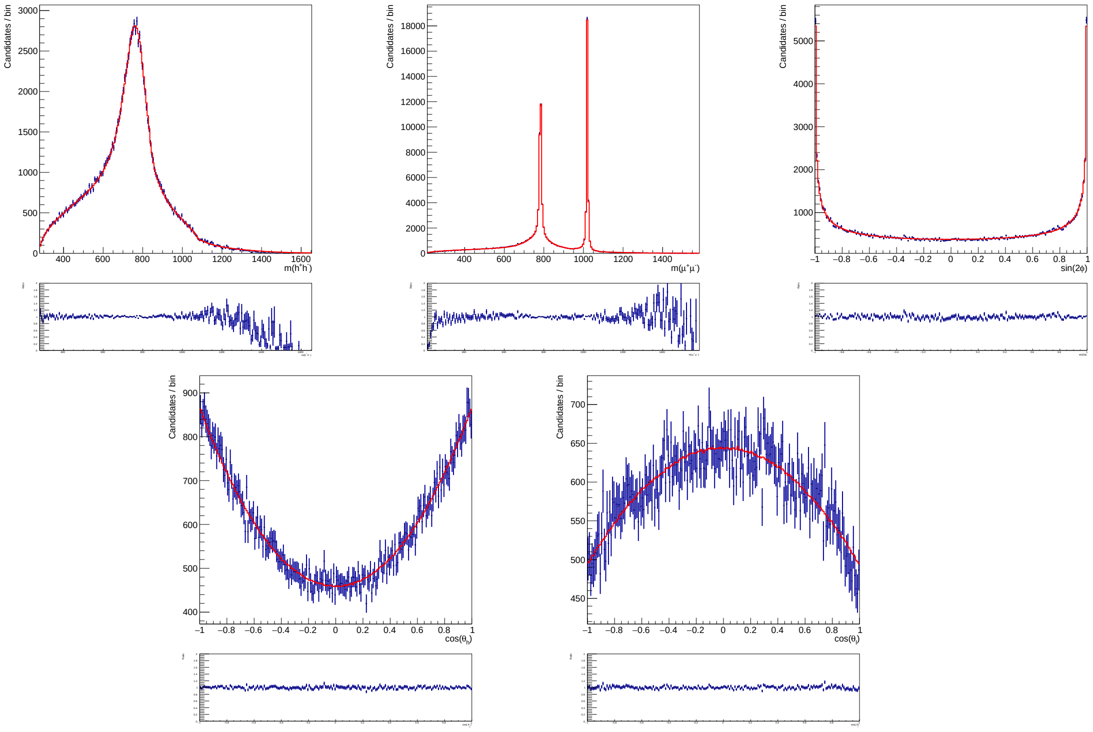

FIGURE 4.14. Phase-space distributions of simulated $D^0 \to \pi^+\pi^-\mu^+\mu^-$ candidates at generator level (red) and fully selected and efficiency corrected (blue). The bottom panels show the ratio between the two distributions.

From a statistical point of view, resampling a dataset, or equivalently reweight it, leads to a reduction of the statistical power of the original sample, where the statistical power is the probability that a statistical test based on a sample with a given size is able to reject a null hypothesis, where an alternative hypothesis is true. In the case of a reweighted sample, the more the weights are widespread the more the loss of statistical power is important. In order to take into account this effect, the weighted yield N_w of the dataset with original size N can be rescaled by a global effective weight $w_{\text{eff}} = \sum_{i=1}^{N} w_i / \sum_{i=1}^{N} w_i^2$, to obtain the effective yield

$$N_{\text{eff}} = w_{\text{eff}}\, N_w = \frac{(\sum_{i=1}^{N} w_i)^2}{\sum_{i=1}^{N} w_i^2}, \tag{4.5}$$

in case of equal weights $N_{\text{eff}} = N$. As shown in the BDT and weights distributions in Fig. 4.11, a large weight with a corresponding large uncertainty is assigned to candidates with high BDT values, due to the too low statistics in the corresponding BDT bins for the selected sample. This leads to a huge loss of statistical power for the reweighted sample. Since the fraction of candidates with $BDT > 0.6$ is less than 0.2% of the total sample and since they corresponds to candidates located at the border of the phase space it was decided to not reweight them, this is equivalent to consider the corresponding bins as empty. The effective size of the two samples are reported in Tab. 4.7.

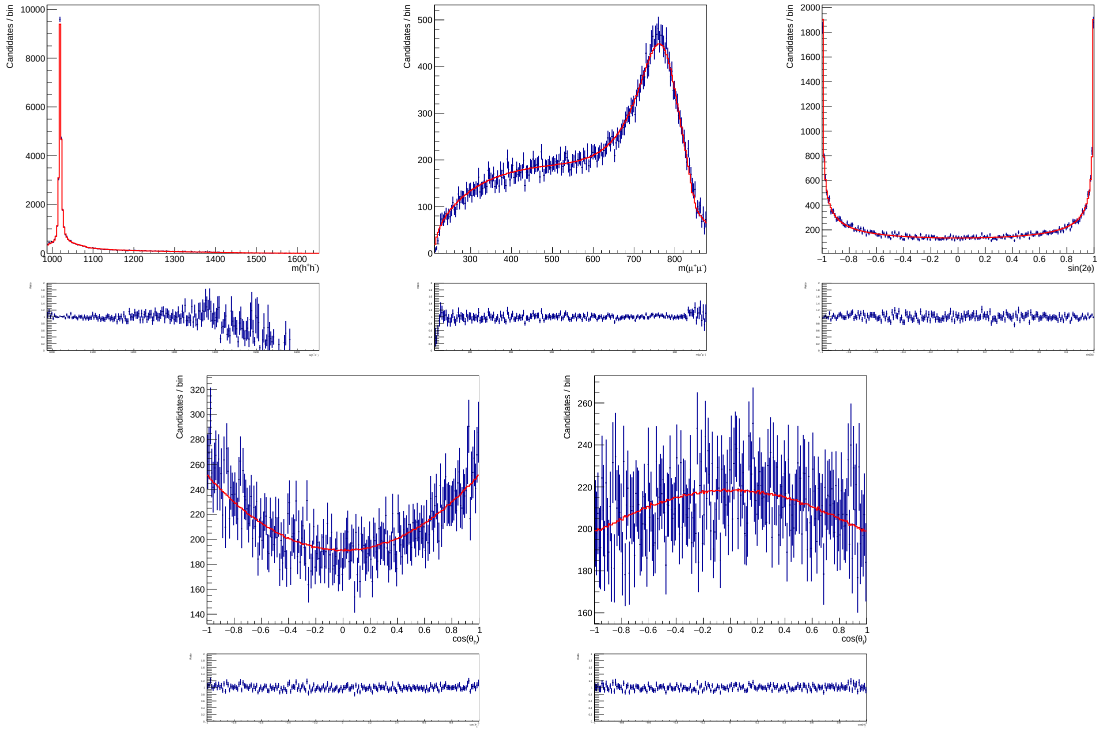

FIGURE 4.15. Phase-space distributions of simulated $D^0 \to K^+K^-\mu^+\mu^-$ candidates at generator level (red) and fully selected and efficiency corrected (blue). The bottom panels show the ratio between the two distributions.

Channel	N_{original}	N_{original}	ratio
$D^0 \to K^+K^-\mu^+\mu^-$	431	306	0.71
$D^0 \to \pi^+\pi^-\mu^+\mu^-$	5881	4330	0.74

TABLE 4.7. Effective sample size for $D^0 \to K^+K^-\mu^+\mu^-$ and $D^0 \to \pi^+\pi^-\mu^+\mu^-$ after the reweighting procedure.

4.7 Extraction of signal and background yields

The number of observed $D^0 \to h^+h^-\mu^+\mu^-$ candidates is obtained by a Maximum Likelihood (ML) fit, explained in more details in Appendix C (also in case of extended ML and weighted dataset), of the invariant mass distribution $m(hh\mu\mu)$. As already pointed out different background sources can enter in the $m(hh\mu\mu)$ spectrum. The most important ones are the combinatorial background and the doubly-misID $D^0 \to h^+h^-\pi^+\pi^-$. The random soft pion background forms a peaking distribution at the right mass in the $m(hh\mu\mu)$ spectrum, since the π_s^+ is associated to a true D^0, but can be anyway reduced with the ΔM cut, since the fake reconstructed D^{*+} has a random mass. The background from secondary D^{*+} cannot be reduced neither in ΔM nor in $m(hh\mu\mu)$ spectrum, but requiring a small IP for D^0 candidates, since the secondary D^{*+} come from a displaced secondary vertex and thus are characterised by a larger IP with respect to the prompt sample. The barionic and radiative background mentioned before are negligible and no dedicated PDF is considered. Therefore the total PDF is composed of three components:

- the signal PDF for $D^0 \to \pi^+\pi^-\mu^+\mu^-$ and $D^0 \to K^+K^-\mu^+\mu^-$ decays;
- the double-misID peaking background due to $D^0 \to h^+h^-\pi^+\pi^-$ decays;
- the combinatorial background.

The shapes of the PDFs of each component are determined using simulation samples, for the signal, and control samples for the double misID background. The combinatorial background can in principle be left free to float in the final fit, but the shape was anyway preliminary studied on data sidebands in order to get a final stable fit. The shapes are determined merging the whole Run II samples, but in regions of di-muon mass (considering the binning scheme explained in Sect. 4.5.3) in order to take into account the different muons kinematical properties; in particular the misID background can be characterise to PDF shape differences in different di-muon mass regions.

4.7.1 PDF determination

In this section the determination of the PDFs for the three components using simulations or data control samples is discussed.

4.7.1.1 Signal PDF

The signal PDF is determined on $D^0 \to K^+K^-\mu^+\mu^-$ and $D^0 \to \pi^+\pi^-\mu^+\mu^-$ MC samples, after the full selection and the truth-matching request. Since no significant shape difference was observed during the years, the study is done on the full Run II sample. The chosen PDF is a single-side Hypatia distribution, which is a generalisation of the Crystall Ball (CB)[†], and gives an excellent description of mass resolution non-Gaussian tails. The single-side Hypatia has the following form

$$I(m;\, \mu, \sigma, \lambda, \xi, \beta, a, n) \propto \begin{cases} A/(B + m - \mu) & \text{if } m - \mu < -a\sigma, \\ ((m-\mu)^2 + \delta^2)^{\frac{1}{2}\lambda - \frac{1}{4}}\, e^{\beta(m-\mu)}\, K_{\lambda - \frac{1}{2}}(\alpha\sqrt{(m-\mu)^2 + \delta^2}) & \text{otherwise.} \end{cases}$$

where K_ν is the modified Bessel function of the second kind, the parameter δ and α are defined as

$$\delta = \sigma\sqrt{\xi K_\lambda(\xi)/K_{\lambda+1}(\xi)},$$
$$\alpha = \sigma\sqrt{\xi K_{\lambda+1}(\xi)/K_\lambda(\xi)}/\sigma,$$

[†] A distribution composed of a gaussian core and a simple exponential left tail.

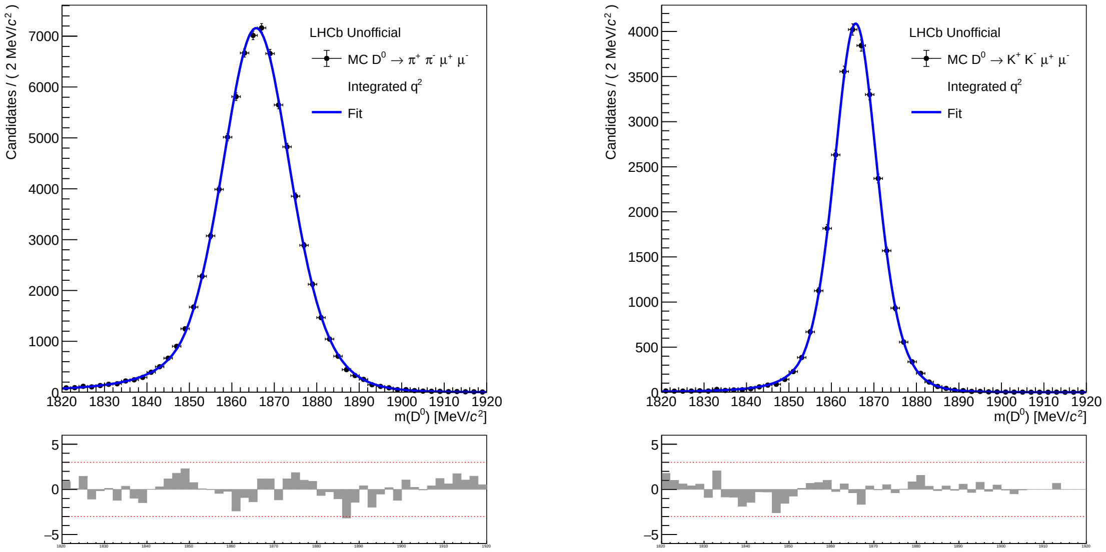

FIGURE 4.16. Fit to the D^0 mass distribution of simulated $D^0 \to \pi^+\pi^-\mu^+\mu^-$ (left) and $D^0 \to K^+K^-\mu^+\mu^-$ (right) candidates after the full selection.

and the parameters A and B are obtained by imposing continuity and differentiability on the connection point $m = \mu - a\sigma$. The parameters μ describes the most probable values for the distribution core, while σ describes the mass resolution. Similarly to the CB function, the left tail is able to describe radiative energy loss or badly reconstructed events, but in addition the core can describe the resolution effect with a variable per-event variance. The parameters ξ and β are always fixed to zero, while the other parameters μ, σ, λ, a and n are determined from the fit. An example of the fit to the D^0 mass distribution of simulated $D^0 \to \pi^+\pi^-\mu^+\mu^-$ and $D^0 \to K^+K^-\mu^+\mu^-$ candidates is shown in Fig. 4.16 in case of integrated $m(\mu^+\mu^-)$.

4.7.1.2 Double misID background

The D^0 invariant mass distribution of the doubly misID background is determined from data control samples of $D^0 \to h^+h^-\pi^+\pi^-$, where two opposite pions are reconstructed as muons. After assigning the wrong mass hypothesis the DTF procedure is repeated with the new hypothesis, in order to get the DTF variables in a similar condition as in the $D^0 \to h^+h^-\mu^+\mu^-$ data. For the $D^0 \to K^+K^-\pi^+\pi^-$ sample the choice of the two pion is unambiguous, while for $D^0 \to \pi^+\pi^-\pi^+\pi^-$ two random opposite charged pions are considered.

Ideally one wants to apply the same selection as in data, to study exactly the same shape as in the $D^0 \to h^+h^-\mu^+\mu^-$ spectrum. Unfortunately this cannot be done because it will result in a too low statistics and also would reveal the real signal $D^0 \to h^+h^-\mu^+\mu^-$ contained in the selected $D^0 \to h^+h^-\pi^+\pi^-$ sample. For this reason the `ProbNN`μ cut is applied only on one of

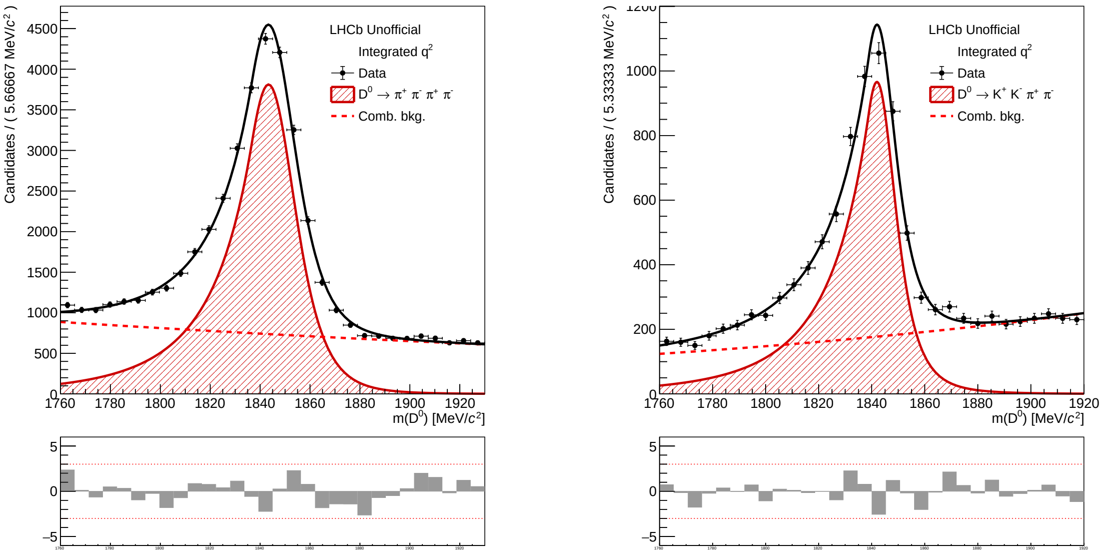

FIGURE 4.17. Fit to the D^0 mass distribution of data samples of hadronic $D^0 \to \pi^+\pi^-\pi^+\pi^-$ (left) and $D^0 \to K^+K^-\pi^+\pi^-$ (right) decays after the selection, where two oppositely charged pions have muon mass assigned and one of those has also muon PID requirements on `ProbNN`μ.

the two pions with muon mass assigned, in particular with the one with the opposite charge with respect to the π_s^+. A similar argument must be applied to the trigger selection, which contains PID requirements at all stages. Thus it is decided to not apply any trigger requests on this sample, while the rest of the selection (from preselection to BDT) is applied in the same way as in the final sample.

Cutting on `ProbNN`μ for one pion reveals the misidentified background of our interest. It is characterised by a peak at about 20 MeV/c^2 lower mass than the nominal D^0 mass, and shows a longer low-mass tail due to decays in flight $\pi \to \mu\nu$, where a fraction of the energy is not taken into account due to the undetected neutrino. Also the misID shape is parametrised by a single-side Hypatia, since it describes quite well the left tail. In the same spectrum there is the combinatorial background, described by an exponential function $f_{\text{comb}} \propto e^{-\gamma m}$, where γ and the yield are free to float in the fit. An example of fit to the D^0 mass distribution of data samples of $D^0 \to \pi^+\pi^-\pi^+\pi^-$ and $D^0 \to K^+K^-\pi^+\pi^-$ after the misidentification of two pions is shown in Fig. 4.17 in case of integrated $m(\mu^+\mu^-)$.

4.7.1.3 Combinatorial background

The combinatorial background is described by an exponential PDF. In order to determine the slope, a fit a combinatorial sample only is done on the data sidebands, independently for $D^0 \to K^+K^-\mu^+\mu^-$ and $D^0 \to \pi^+\pi^-\mu^+\mu^-$ and in $m(\mu\mu)$ bins. The data are selected with a

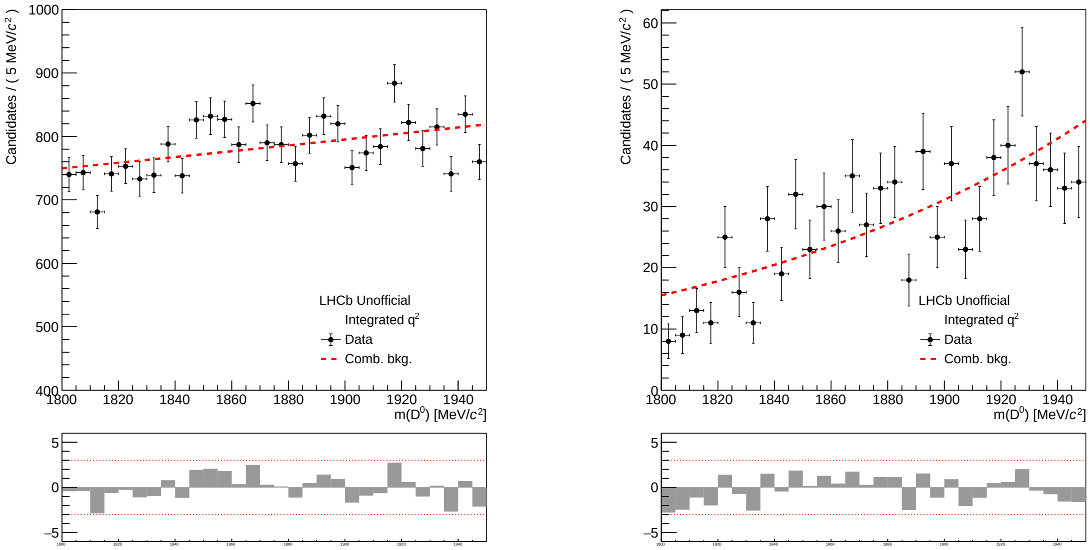

FIGURE 4.18. Fit to the D^0 mass distribution of data samples of $D^0 \to \pi^+\pi^-\mu^+\mu^-$ (left) and $D^0 \to K^+K^-\mu^+\mu^-$ (right) decays in ΔM sideband.

similar selection of the final sample, except for the specific selection of the sideband, defined by $\Delta M > 160\,\mathrm{MeV}/c^2$, $BDT < 0$ and `ProbNN`$\mu > 0.4$. An example of fit to the D^0 mass distribution of combinatorial backgrounds is shown in Fig. 4.18 in case of integrated $m(\mu^+\mu^-)$.

4.7.1.4 Determination of signal and background yields from data

The PDFs introduced in the previous sections are used to perform the ML fit on fully selected Run II candidates in each di-muon mass region. In order to take into account a possible disagreement of the real shapes with respect to the ones studied previously on simulated and control samples, the width of signal and misID shapes are not fixed, but are fitted with a gaussian constraint, using as central value and width the nominal value and uncertainty obtained from the studies on simulation and control samples. The effective weighted yields in each di-muon mass bin are reported in Tab. 4.8, while the unweighted ones are reported in Tab. 4.9. The fits on the di-muon mass integrated samples are shown in Fig. 4.19 for $D^0 \to \pi^+\pi^-\mu^+\mu^-$ and $D^0 \to K^+K^-\mu^+\mu^-$ samples, while the fits in each di-muon mass regions are shown in Fig. 4.20 and Fig. 4.21 for for $D^0 \to \pi^+\pi^-\mu^+\mu^-$ and $D^0 \to K^+K^-\mu^+\mu^-$ samples respectively.

4.7.2 Expected asymmetries

In the approximation of small asymmetries, their values can be estimated with the observed statistics by performing a simultaneous ML fit on the D^0 invariant mass spectrum, splitting randomly the sample in two independent subsamples, thus emulating the splitting by the D^0

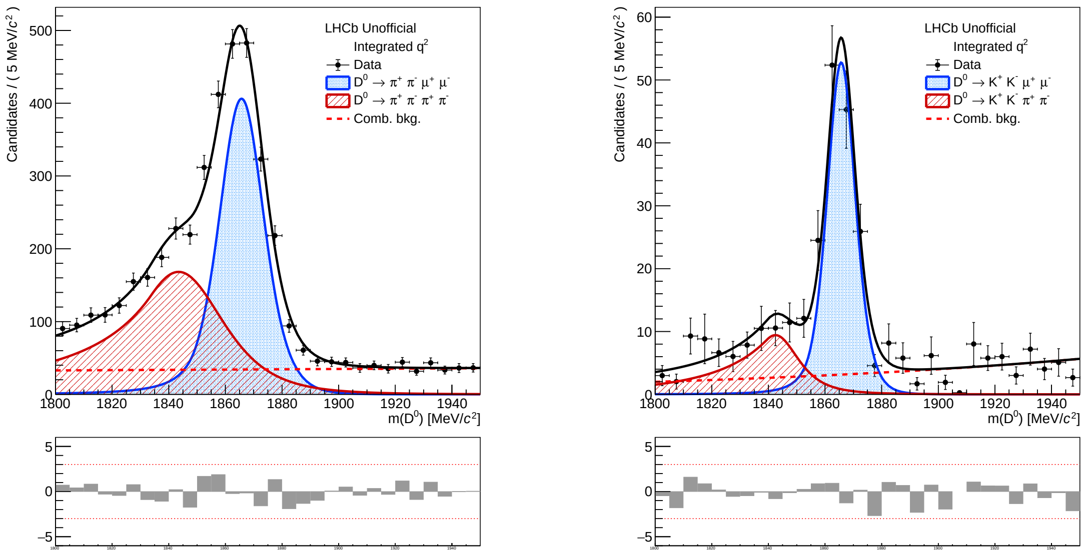

FIGURE 4.19. D^0 mass distributions and fit overlaid, for fully selected Run II $D^0 \to \pi^+\pi^-\mu^+\mu^-$ and $D^0 \to K^+K^-\mu^+\mu^-$ integrated in $m(\mu\mu)$.

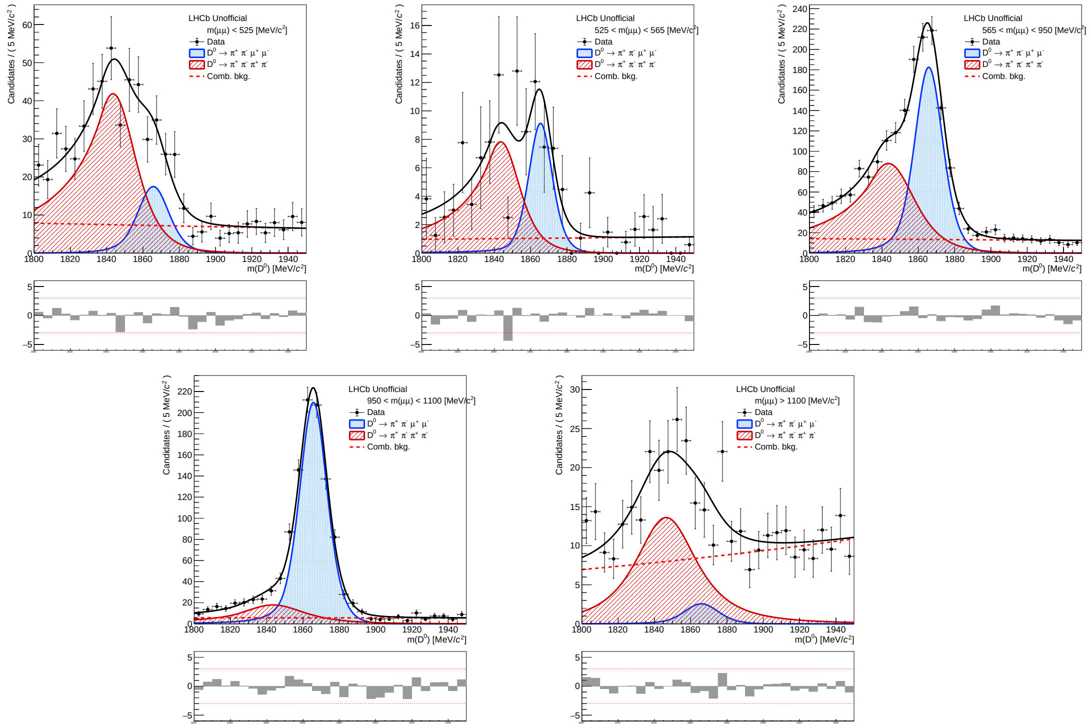

FIGURE 4.20. D^0 mass distributions and fit overlaid, for fully selected Run II $D^0 \to \pi^+\pi^-\mu^+\mu^-$ in $m(\mu^+\mu^-)$ bins. The fits on the full ρ/ω and ϕ bins are reported.

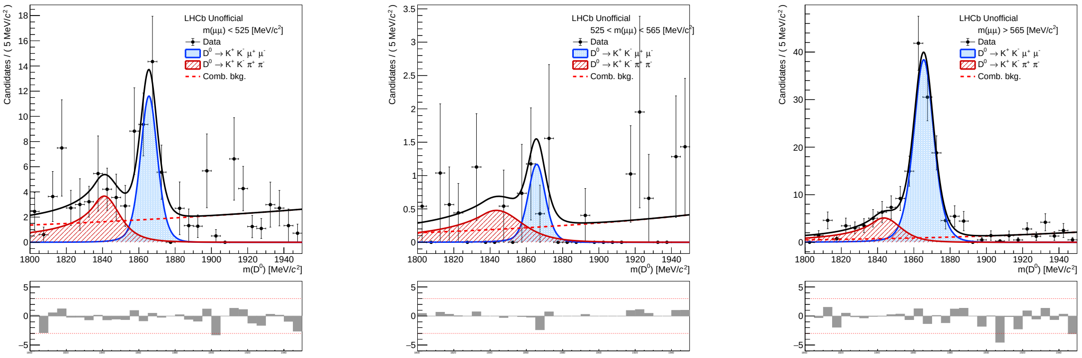

FIGURE 4.21. D^0 mass distributions and fit overlaid, for fully selected Run II $D^0 \to K^+K^-\mu^+\mu^-$ in $m(\mu^+\mu^-)$ bins.

Channel		$m(\mu^+\mu^-)$ MeV/c^2	N_{sig}	N_{misID}	N_{comb}
$D^0 \to \pi^+\pi^-\mu^+\mu^-$	full range		1730 ± 63	1569 ± 91	1031 ± 58
	low mass	< 525	82 ± 21	343 ± 27	215 ± 28
	η	$525 - 565$	32 ± 11	56 ± 16	32 ± 9
	ρ/ω (left)	$565 - 780$	564 ± 30	425 ± 33	267 ± 27
	ρ/ω (right)	$780 - 950$	241 ± 27	283 ± 33	147 ± 20
	ρ/ω (full)	$565 - 950$	769 ± 34	785 ± 39	399 ± 31
	ϕ (left)	$950 - 1020$	460 ± 22	80 ± 27	99 ± 17
	ϕ (right)	$1020 - 1100$	424 ± 22	73 ± 17	75 ± 15
	ϕ (full)	$950 - 1100$	865 ± 44	176 ± 41	170 ± 23
	high mass	> 1100	13 ± 3	130 ± 28	263 ± 30
$D^0 \to K^+K^-\mu^+\mu^-$	full range		143 ± 18	58 ± 9	105 ± 16
	low mass	< 525	29 ± 7	22 ± 8	58 ± 11
	η	$525 - 565$	2 ± 1	3 ± 1	6 ± 2
	high mass	> 565	115 ± 10	33 ± 7	34 ± 7

TABLE 4.8. Effective weighted yields as result of the ML fit on the D^0 mass spectrum for fully selected Run II $D^0 \to \pi^+\pi^-\mu^+\mu^-$ and $D^0 \to K^+K^-\mu^+\mu^-$.

Channel	$m(\mu^+\mu^-)$ MeV/c^2		$N_{\rm sig}$	$N_{\rm misID}$	$N_{\rm comb}$
$D^0 \to \pi^+\pi^-\mu^+\mu^-$	full range		2565 ± 68	2001 ± 71	1315 ± 58
	low mass	< 525	85 ± 17	336 ± 25	180 ± 22
	η	$525 - 565$	34 ± 8	46 ± 10	30 ± 8
	ρ/ω (left)	$565 - 780$	712 ± 34	515 ± 35	273 ± 27
	ρ/ω (right)	$780 - 950$	304 ± 34	440 ± 29	210 ± 24
	ρ/ω (full)	$565 - 950$	995 ± 43	925 ± 45	506 ± 37
	ϕ (left)	$950 - 1020$	736 ± 33	206 ± 30	123 ± 20
	ϕ (right)	$1020 - 1100$	756 ± 31	158 ± 72	121 ± 19
	ϕ (full)	$950 - 1100$	1468 ± 45	372 ± 38	261 ± 28
	high mass	> 1100	19 ± 10	210 ± 41	384 ± 35
$D^0 \to K^+K^-\mu^+\mu^-$	full range		207 ± 16	96 ± 14	128 ± 15
	low mass	< 525	41 ± 8	32 ± 8	59 ± 10
	η	$525 - 565$	5 ± 2	5 ± 3	8 ± 3
	high mass	> 565	172 ± 16	53 ± 12	50 ± 10

TABLE 4.9. Raw yields not efficiency corrected as result of the ML fit on the D^0 mass spectrum for fully selected Run II $D^0 \to \pi^+\pi^-\mu^+\mu^-$ and $D^0 \to K^+K^-\mu^+\mu^-$.

flavour for a CP asymmetry measurement or by the value of $\cos\theta_\mu$ for the $A_{\rm FB}$ measurement. All the PDF shape parameters are in common beetween the two samples, except the yields that are fitted separately. The value of the asymmetry and its uncertainty can be obtained directly from the fit as a common parameter:

$$A = \frac{N_+ - N_-}{N_{\rm tot}} \tag{4.6}$$

where N_+ and N_- are the yields of the signal component for the two subsamples, while $N_{\rm tot}$ is the total signal yield. The uncertainty on the raw asymmetries for a $D^0 \to \pi^+\pi^-\mu^+\mu^-$ and $D^0 \to K^+K^-\mu^+\mu^-$ are reported in Tab. 4.10. Using the full Run II sample will lead to a reduced uncertainty on the expected asymmetry, approximately by a factor 2 and 1.5 for $D^0 \to \pi^+\pi^-\mu^+\mu^-$ and $D^0 \to K^+K^-\mu^+\mu^-$ respectively, with respect to the current measurements.

4.8 Summary and future prospects

The complete selection of $D^0 \to \pi^+\pi^-\mu^+\mu^-$ and $D^0 \to K^+K^-\mu^+\mu^-$ candidates has been described using the Run II data, corresponding to an integrated luminosity of $4.9\,\text{fb}^{-1}$, considering the 2016 removed subsamples because of tight trigger requirements. The improved and optimised selection for Run II allows an improvement on the expected asymmetry precision with respect to the previous analysis of a factor of 2 and 1.5 for $D^0 \to \pi^+\pi^-\mu^+\mu^-$ and $D^0 \to K^+K^-\mu^+\mu^-$ respectively. A further improvement is therefore expected including the Run I data, which corresponds to approximately 20% of the currently used Run II sample, assuming the same selection

Channel	$m(\mu^+\mu^-)$ MeV/c^2		ΔA
$D^0 \to \pi^+\pi^-\mu^+\mu^-$	full range		2.5%
	low mass	< 525	20%
	η	$525 - 565$	20%
	ρ/ω (left)	$565 - 780$	5.1%
	ρ/ω (right)	$780 - 950$	7.3%
	ρ/ω (full)	$565 - 950$	4.3%
	ϕ (left)	$950 - 1020$	4.5%
	ϕ (right)	$1020 - 1100$	4.0%
	ϕ (full)	$950 - 1100$	3.1%
	high mass	> 1100	–
$D^0 \to K^+K^-\mu^+\mu^-$	full range		7.5%
	low mass	< 525	18%
	η	$525 - 565$	–
	high mass	> 565	8%

TABLE 4.10. Raw expected precision on asymmetry measurements in each di-muon mass bin for the fully selected Run II candidates of $D^0 \to \pi^+\pi^-\mu^+\mu^-$ and $D^0 \to K^+K^-\mu^+\mu^-$.

efficiency obtained in [206]. Other studies are still in progress to measure the asymmetries A_{CP}, A_{FB}, $A_{2\phi}$ and A_ϕ. In particular the measurement of the A_{CP} raw asymmetry must be corrected for the nuisance asymmetries due to the production asymmetry of D^{*+} with respect to D^{*-} and to the detection asymmetry of the soft pion. These two quantities can be taken into account and properly subtracted with the same strategy used in [206], selecting the complete Run II sample of $D^0 \to K^+K^-$ and knowing the real A_{CP} asymmetry of this channel, thus obtaining

$$A_d(\pi_{\text{s}}^+) + A_P(D^{*+}) = A_{CP}^{\text{raw}}(D^0 \to K^+K^-) - A_{CP}(D^0 \to K^+K^-)$$

after a proper equalisation of the D^{*+} kinematics between this channel and the $D^0 \to h^+h^-\mu^+\mu^-$ decays, which takes into account also differences in π_{s}^+ kinematics due to their high correlation.

The MC simulations were widely used for the study of the efficiency variation across the phase space and in the determination of signal PDFs. However, MC-data disagreements are present and must be investigated. Preliminary studies on the Cabibbo-favored sample $D^0 \to K^-\pi^+\mu^+\mu^-$ showed a good agreement for the most important variables used in the analysis, except for the events multiplicity and some of the PID variables. In the latter case, studies are in progress in order to correct the variables directly on the simulated sample using a LHCb data driven method based on calibration samples [292] Furthermore, various sources of systematic uncertainties must be investigated. The main sources are

- Fit procedure and determination of the PDFs used for the various components. This source of systematic uncertainty is directly linked to the statistics of simulated and control samples used in the determination of PDFs and it is therefore expected to be reduced compared to previous studies.

- Uncertainties in the correct determination of the efficiency variation across the phase space. The uncertainty can be studied varying the selection requirements on the training BDT samples and compare the resulting asymmetries with the ones in the standard configuration. In this case it is expected that the different and optimised trigger request will make the determination of the efficiency variation more stable with respect to previous analysis. Moreover, since the efficiency determination is based on simulations only, a prior MC corrections for any MC-data disagreement automatically will reduce the systematic uncertainties associated with the efficiency variation determination.
- Other systematics due to detector resolution effects and not accounted background sources.

We expect total systematic uncertainties lower than 1%, therefore a still small role when compared to the statistical ones reported in Tab. 4.10.

CHAPTER 5

DEVELOPMENT AND VALIDATION OF THE ANGULAR FIT FOR $D^0 \to h^+h^-\mu^+\mu^-$

In this chapter the angular fit is described. The strategy is to build an amplitude model first with the main expected contributions for the $D^0 \to \pi^+\pi^-\mu^+\mu^-$ and $D^0 \to K^+K^-\mu^+\mu^-$, in order to emulate a realistic phase space population on which the angular model can be tested. In the pseudo-experiments, the background subtraction from the invariant mass fit and the phase space dependent efficiency are included to take into account any possible systematic effect induced by those procedures.

The amplitude and angular models are implemented using the Hydra [293] framework, an header-only C++11 compliant framework designed to perform common data analysis tasks on parallel platforms. It is important to note that without a parallel computing implementation the generation of high statistics 5-dimensional phase space distributions or an angular fit are not feasible due to the large computation time. Thus an important role has been played in developing custom libraries to extend the Hydra framework functionalities and allowing to perform the phase space distribution generation and the angular fit. [*]

5.1 Development of a basic amplitude model

The partial decay rate of a particle in its rest frame to a four-body final state is

$$d\Gamma = \frac{(2\pi)^4}{2M} |\mathcal{M}|^2 \, d\Phi_4(P, p_1, ..., p_4), \tag{5.1}$$

---

[*] For example generating 3 millions of $D^0 \to \pi^+\pi^-\mu^+\mu^-$ candidates in the 5-dimensional phase space with a single thread on intel-i7-7700HQ takes about 19.4 ms, while with the GPU on nVidia GTX1050 takes about 2.5 ms. Using even more performing boards, such as nVidia GeForce GTX Tesla P100 or GeForce GTX Titan Z speed-ups up to a factor 100 are observed in MC generation and data fit.

where M and P are the mass and the four-momentum of the decaying particle respectively, $\mathcal{M}$ is the Lorentz-invariant matrix element of the process, $d\Phi_4$ is the element of the four-body phase space and $p_1, ..., p_4$ are the daughters four-momenta. The decay amplitude $\mathcal{M}$ can be phenomenologically modelled in terms of quasi-two-body decays, a description that is called *isobar model* and developed to describe three-body hadronic decays, where two final state particles come from a strong decay of an intermediate state. The interaction between these two final states and the third particle, called the *bachelor* particle, is described by higher order terms and it is often called a *re-scattering* process. This model can easily be extended to four-body decays, where three main topologies can be identified:

1. Non-resonant topology: in which the initial particle decays into the final state without intermediate resonances. In the case of multi-body D decays the corresponding non-resonant amplitude is often parametrised as a complex constant, obtaining a decay rate distributed as the phase space. In B meson decays, the non-resonant amplitude is also parametrised with smooth empirical functions that well describe experimental observations, being unlikely that the amplitude remains constant over the larger phase space. [294]. The SM contribution of the non-resonant topology is highly suppressed for the $D^0 \to h^+h^-\mu^+\mu^-$ decay, as reported in Tab. 5.1, and it is therefore not implemented in the amplitude model.

2. Resonant quasi-two-body topology: in which the initial particle decays into two intermediate states, each of which in turn decays into two final state particles. These processes are the most important ones for this analysis, and are indicated as $D^0 \to R_1R_2$, with $R_1 \to h^+h^-$ and $R_2 \to \mu^+\mu^-$, and with $h = \pi, K$. It is also possible to have a single intermediate state, in di-muon or di-hadron system, while the other system remains non-resonant: $D^0 \to R_1\mu^+\mu^-$, $D^0 \to R_2h^+h^-$. As reported in Tab. 5.1 in the case of $D^0 \to \pi^+\pi^-\mu^+\mu^-$, these higher order processes are suppressed at least by an order of magnitude with respect to the two-resonance case, and are therefore not implemented in the amplitude model, as discussed later in Sect. 5.1.3.

3. Resonant cascade topology: where the initial particle decays in a intermediate state and a bachelor particle, $D^0 \to R_1'h_1$, and the intermediate state in turn decays into another bachelor particle and an intermediate state, $R_1' \to R_2h_2$, that finally decays into the remaining two final states, $R_2 \to \mu^+\mu^-$.

Other higher order contributions can occur, involving for example final states re-scattering or cascade topology with three-body decays. They are not considered in this study since their effects is negligible with respect to the two main resonant topologies mentioned above, considering the low statistics of the data sample and the aim of the amplitude model.

Since the configuration of spin and angular momentum can be complicated, the so-called *helicity formalism* is used, which allows a proper treatment of angular configurations taking into

Decay mode	Branching fraction	
$D^0 \to R_1(\pi^+\pi^-)R_2(\mu^+\mu^-)$	10^{-6}	[190]
$D^0 \to R_1'^{\pm}[R_2(\mu^+\mu^-)\pi^{\pm}]\pi^{\mp}$	$10^{-7} - 10^{-6}$	[13]
$D^0 \to \pi^+\pi^- \, R_2(\mu^+\mu^-)$	10^{-7}	[13]
$D^0 \to \mu^+\mu^- \, R_1(\pi^+\pi^-)$	10^{-7}	[157]
$D^0 \to \pi^+\pi^-\mu^+\mu^-$ (ph.space)	$10^{-10} - 10^{-9}$ (SM)	[168]

TABLE 5.1. List of possible decay topologies for the $D^0 \to \pi^+\pi^-\mu^+\mu^-$ decay.

account the spin of final states and intermediate particles. It is worth noting that the cascade topology shows a further difficulty due to the fact that the decay of the first resonance foresees a second resonance as a daughter, which may have a large width, that in turn influences in a non-trivial way the width of the mother resonance. How to deal with this issue will be discussed later.

5.1.1 Resonant contributions

As pointed out in the previous section, the decay $D^0 \to h^+h^-\mu^+\mu^-$ can proceed through two main resonant topologies: quasi-two-body and cascade topology. In the case of the cascade topology, only the decay $D^0 \to a_1(1260)\pi$ with $a_1(1260) \to \rho^0(\mu\mu)\pi$ contributes to the $\pi\pi$ decay channel, while no contributions of this topology is expected in the KK mode.

The quasi-two-body decay is the richest since many resonances in principle can contribute. A complete list of resonances decaying in $\pi^+\pi^-$, K^+K^- and $\mu^+\mu^-$ are listed in Tab. 5.2. Not all the combinations between the h^+h^- resonant states and the $\mu^+\mu^-$ ones are possible, due to the kinematical constraint of the D^0 mass and conservation of angular momentum. The possible spin-parity and orbital angular momentum configurations are:

- $D^0 \to 0^+\,0^-$ (S-wave);
- $D^0 \to 1^-\,0^-$ (P-wave);
- $D^0 \to 0^+\,1^-$ (P-wave);
- $D^0 \to 1^-\,1^-$ (S, P, D-waves);
- $D^0 \to 2^+\,0^-$ (D-wave);
- $D^0 \to 2^+\,1^-$ (P, D-waves).

Since higher angular momentum configurations are suppressed (explained in more detail in Sect. 5.1.3) only the main contributions are introduced in the amplitude model. The list of simulated processes is reported in Tab. 5.3.

J^P	KK res.	$\pi\pi$ res.	$\mu\mu$ res.
0^+	$f_0(980)$, $a_0(980)$, $f_0(1370)$	$f_0(980)$, σ, $f_0(1370)$	
0^-			η
1^-	$\phi(1020)$	ρ^0, ω, $\rho^0(1450)$	ρ^0, ω, $\phi(1020)$
2^+	$f_2(1270)$, $a_2(1320)$	$f_2(1270)$	

TABLE 5.2. Resonances that can contribute to $D^0 \to \pi^+\pi^-\mu^+\mu^-$ and $D^0 \to K^+K-\mu^+\mu^-$.

Decay mode	Amplitude contribution
$D^0 \to \pi^+\pi^-\mu^+\mu^-$	$D^0 \to [\rho/\omega\ \rho/\omega]_{\mathrm{S}}$, $\rho/\omega \to [\mu^+\mu^-]_{\mathrm{S}}$, $\rho/\omega \to [\pi^+\pi^-]_{\mathrm{P}}$
	$D^0 \to [\rho/\omega\ \phi]_{\mathrm{S}}$, $\phi \to [\mu^+\mu^-]_{\mathrm{S}}$, $\rho/\omega \to [\pi^+\pi^-]_{\mathrm{P}}$
	$D^0 \to [a_1(1260)^{\pm}\ \pi^{\mp}]_{\mathrm{P}}$, $a_1(1260)^{\pm} \to [\rho\pi^{\pm}]_{\mathrm{S}}$, $\rho \to [\mu^+\mu^-]_{\mathrm{S}}$
$D^0 \to K^+K^-\mu^+\mu^-$	$D^0 \to [\phi\ \rho/\omega]_{\mathrm{S}}$, $\rho/\omega \to [\mu^+\mu^-]_{\mathrm{S}}$, $\phi \to [K^+K^-]_{\mathrm{P}}$

TABLE 5.3. List of amplitude contributions simulated in the amplitude model.

5.1.2 Helicity formalism

The helicity formalism is a general approach to describe in a correct and consistent way the final state angular distributions in multi-body relativistic scattering or decay process. The basic idea is that the decay amplitude can be factorised into two-body decay amplitudes, of the form $a \to bc$, where for each decay a reference frame with the mother at rest can be defined. The rotational invariance of helicities allows to define a set of relativistic two-particle state with definite total angular momentum, angular momentum projection and helicities. Using the conservation of angular momentum is then possible to write each amplitude by factorising out the angular variables and a dynamic factor from the helicity two-particle states brackets.

More quantitatively, for each $a \to bc$ process a coordinate system with A at rest can be defined with the z axis as the spin quantisation axis. The quantum states involved can be written in the following way:

- Initial state: in the J, M base can be written generically as $|A\rangle = |J_a, M_a\rangle$, with J total angular momentum and M its projection on the z axis.
- Two-particle final state: they are emitted back to back in A rest frame, with momentum p for each particle and along a direction defined by a polar angle θ and azimuthal angle ϕ. The reference frame can be rotated in order to align the new z' axis along the emitted particles, as required by the helicity formalism. A generalised rotation operator in three dimension can be defined using the Euler angles as $\mathcal{R}(\phi, \theta, 0)$. The state can be then written generically in the plane-wave base as $|bc\rangle = |p, \theta, \phi, \lambda_b, \lambda_c\rangle$, where λ_b and λ_c are the angular momentum projections onto the z' axis and thus coincide with the b and c helicities. This state is a linear combination of J, M states, in particular J will remain

> the same due to the angular momentum conservation, but M can change since a new quantisation axis z' is defined:
>
> $$|p,\theta,\phi,\lambda_b,\lambda_c\rangle = \sum_{J',M'} \sqrt{\frac{2J+1}{4\pi}}\, D^{J}{}_{M,\lambda_b-\lambda_c}(\phi,\theta,0)\, |p,J',M',\lambda_b,\lambda_c\rangle. \tag{5.2}$$
>
> The Wigner D-matrices $D^J_{M,M'}(\alpha,\beta,\gamma)$ are the expectation values of the three-dimensional rotation operator into the J, M basis, thus qualitatively they measure the probability amplitude of passing from M to M' after a rotation $\mathcal{R}(\alpha,\beta,\gamma)$ for a state with angular momentum J.

Indicating with U the time evolution operator, the amplitude can be finally written as

$$\mathcal{M}_{a\to bc} = \langle p,\theta,\phi,\lambda_b,\lambda_c|U|J_a,M_a\rangle = \sqrt{\frac{2J+1}{4\pi}}\, D^{J_a}{}_{M_a,\lambda_b-\lambda_c}(\phi,\theta,0)\, \mathcal{A}_{\lambda_b,\lambda_c}, \tag{5.3}$$

where $\mathcal{A}_{\lambda_b,\lambda_c}$ is a dynamical factor which takes into account the quantum couplings to those specific helicities. This factor contains all the QCD dynamics and the non-perturbative effects.

If there is a subsequent decays, like $b \to de$, a procedure similar to the one described above is used to build the amplitude $\mathcal{M}_{b\to de}$ that must multiply the first one and so on. For a four-body decay $a \to b(de)c(fg)$ a possible contribution of the amplitude is

$$\mathcal{M}_{a\to b(de)c(fg)} = \mathcal{M}_{a\to bc}\, \mathcal{M}_{b\to de}\, \mathcal{M}_{c\to fg}. \tag{5.4}$$

Since many intermediate states can contribute in a four-body decay $a \to b(de)c(fg)$, all the possible interfering contributions have to be summed coherently, while all the processes which can be discriminated by a final state measurement, for example depending on final state helicities, have to be summed incoherently.

The complete derivation of the amplitude formalism of the $D^0 \to h^+h^-\mu^+\mu^-$ decays can be found in Appendix D, in which other technical aspects are discussed. Using the notation previously introduced with $D^0 \to R_1R_2$ for the quasi-two-body topology and $D^0 \to R_1'(R_2h_2)h_1$ for the cascade topology, the final function (proportional to the decay rate) can be written as

$$\mathcal{S} = \sum_{\lambda_{\mu^+},\lambda_{\mu^-}=\pm 1/2} \left| \sum_j \left[\mathcal{H}^{D^0\to R_1R_2}_{\lambda_{\mu^+},\lambda_{\mu^-}}\right]_j + \sum_k \left[e^{i\Delta\lambda_\mu\alpha_\mu}\, \mathcal{H}^{D^0\to R_1'h_2}_{\lambda_{\mu^+},\lambda_{\mu^-}}\right]_k \right|^2, \tag{5.5}$$

where the sums in j and k refer to possible resonances states that contribute to the first and second topology respectively, λ_μ is the muon helicity and the sum in λ_μ is incoherent since the muons helicities are measurable and identify states that do not interfere. The $\mathcal{H}^{D^0\to R_1R_2}_{\lambda_{\mu^+},\lambda_{\mu^-}}$ amplitude implicitly contains the coherent sum over the intermediate resonant helicities, λ_R, which are equal for both the di-muon and di-hadron resonances in the quasi-two-body topology. The $\mathcal{H}^{D^0\to R_1'h_2}_{\lambda_{\mu^+},\lambda_{\mu^-}}$ amplitude implicitly contains the sum over the di-muon resonant helicity only,

λ_{R_2}, since the $a_1(1260)^{\pm}$ helicity is null for the conservation of angular momentum in the D^0 decay.

Since the definition of the spin quantisation axes depend on the decay chain considered, there can be a mismatch of the helicity states between the two topologies. If dealing with helicities of intermediate states, this possible axis misalignment has no consequences after the coherent sum over all possible helicity values. However, for final state particles like muons, the helicities λ_μ depend on the decay chain considered. For this reason one helicity state of one topology has to be expressed as a combination of states defined in the other topology, with a rotation,

$$|\lambda_1\rangle = \sum_{\lambda'} D^J_{\lambda,\lambda'}(\phi,\theta,0)^*|\lambda'\rangle. \tag{5.6}$$

The exponential $e^{i\Delta\lambda_\mu\alpha_\mu}$ in Eq. (5.5) is indeed used to properly align the muon spin quantisation axes between the two topologies. The detailed calculation can be found in Appendix D.

5.1.3 Helicity couplings and lineshape factor

As seen previously, the factors $\mathcal{A}_{\lambda_b,\lambda_c}$ are general couplings which contain all the dynamics. In particular for a generic decay $r \to a(\to bc)X$ where a is a resonance, the factor for the $a \to bc$ decay can be written as

$$\mathcal{A}_{\lambda_b,\lambda_c} = A_{\lambda_b,\lambda_c}\,\mathcal{R}(m_{b,c}), \tag{5.7}$$

where A_{λ_b,λ_c} is a complex number taking into account the couplings to helicity, while $\mathcal{R}(m_{b,c})$ describes the decay amplitude distribution as a function of the invariant mass $mm_{b,c}$ and daughter momentum. It is usually written as

$$\mathcal{R}(m_{b,c}) = \mathcal{L}(m_{b,c}|m_0,\Lambda_0)\cdot B'_{L_a}(q,q_0,d)\left(\frac{q}{q_0}\right)^{L_a}\cdot B'_{L_r}(p,p_0,d)\left(\frac{p}{p_0}\right)^{L_r}, \tag{5.8}$$

where $\mathcal{L}(m(b,c)|m_0,\Lambda_0)$ is a distribution in the $m_{b,c}$ spectrum (called a lineshape factor), with m_0 and Λ_0 the nominal mass and width of the resonance respectively. The $B'_{L_a}(q,q_0,d)$ factor is the Blatt-Weisskopf barrier factor, explained below, with $q = |\vec{q}|$ and $q_0 = |\vec{q}_0|$ the momentum of one daughter in the resonance rest frame, considering the measured resonance mass and the nominal resonance mass at the pole, respectively, while p and p_0 are the corresponding quantities of the resonance a in its mother rest frame. The quantity d is a scale that quantifies the radius of the decaying particle, typically set to 3 GeV$^{-1} \sim 0.6$ fm. The quantities L_a and L_r are the orbital angular momentum of the daughters in the mother rest frame and of the resonance in its mother rest frame, respectively.

The helicity couplings A_{λ_b,λ_c} are unknown complex numbers and are used as free parameters of the model. Since within the helicity formalism the parity conservation is not automatically taken into account, in contrast to the angular conservation, it can be imposed for all the strong or electromagnetic decays with the relation

$$A^R_{-\lambda_b,-\lambda_c} = \mathcal{P}(a)\mathcal{P}(b)\mathcal{P}(c)(-1)^{s_b+s_c-s_a} A^R_{\lambda_b,\lambda_c} \tag{5.9}$$

where s is the spin and $\mathcal{P}$ is the intrinsic parity of the particle. This also helps reducing the number of possible free parameters in the model.

Blatt-Weisskopf barrier factors

The Blatt-Weisskopf factors are used as centrifugal barrier factors, since they take into account the difficulty to create particles with high orbital angular momentum configuration. They depend on the scale d and on the momentum p and p_0 of the daughters in their mother rest frame as calculated at the measured resonance mother mass and the nominal mass respectively. The first three barrier factors are

$$B'_0(p, p_0, d) = 1, \tag{5.10}$$

$$B'_1(p, p_0, d) = \sqrt{\frac{1+(p_0d)^2}{1+(pd)^2}}, \tag{5.11}$$

$$B'_2(p, p_0, d) = \sqrt{\frac{9+3(p_0d)^2+(p_0d)^4}{9+3(pd)^2+(pd)^4}}, \tag{5.12}$$

$$B'_3(p, p_0, d) = \sqrt{\frac{225+45(p_0d)^2+6(p_0d)^4+(p_0d)^6}{225+45(pd)^2+6(pd)^4+(pd)^6}}. \tag{5.13}$$

Relativistic Breit-Wigner

A typical lineshape used to describe the mass distribution of a narrow and isolated resonance is the Relativistic Breit-Wigner (RBW)

$$\mathcal{BW}(m|m_0, \Lambda_0) = \frac{B'_L(q, 0)}{m_0^2 - m^2 - im_0\Lambda(m, L)}, \tag{5.14}$$

where the running width of the resonance is

$$\Lambda(m, L) = \Lambda_0 \left(\frac{q}{q_0}\right)^{2L+1} \left(\frac{m_0}{m}\right) B'^2_L(q, q_0). \tag{5.15}$$

In this expression q is a function of m, the measured resonance mass, and of the fixed daughter masses m_1 and m_2. However if one of the daughters is not a stable particle the expression is no longer valid, since another implicit dependence on the daughter kinematics is present. This is the case of the decay of the second topology $D^0 \to a_1(1260)\pi$ with $a_1(1260) \to \rho^0(\mu\mu)\pi$. A general approach to get a correct resonance width is to compute it as an integral over the phase space of the three-body decay $a_1(1260) \to \mu\mu\pi$. Since in our case the aim is just to build a realistic model to mimic the angular distributions starting from the amplitude contents, the results of a recent amplitude analysis on $D^0 \to \pi^+\pi^-\pi^+\pi^-$ and $D^0 \to K^+K^-\pi^+\pi^-$ using CLEO-c data [295] are used to interpolate the running width and mass of the $a_1(1260)$ state, and eventually use these interpolations within the amplitude model.

ρ-ω interference

Since ρ and ω mesons are not pure eigenstate of isospin, a mixing between the two states via strong interaction is possible. This effect has been studied in the past starting from the charged pion form factor. In order to take into account this phenomenon, the Bernicha formalism [296] is used to write

$$\mathcal{L}_{\rho-\omega} = \mathcal{BW}_\rho + \delta e^{i\varphi}\,\mathcal{BW}_\omega, \tag{5.16}$$

where $\mathcal{BW}$ is the relativistic Breit-Wigner for the ρ and ω while δ and ϕ are the modulus and phase of the complex number that quantify the mixing.

Model approximations

As previously pointed out, the amplitude model developed in this section is subject to several approximations, since it is not built to perform an amplitude analysis, given the far too low statistics. First of all many possible resonant contributions are not described since their relative branching fraction is at least one order of magnitude lower than the main resonant contributions visible with the current statistics, like three-body contributions $D^0 \to R(hh)\mu^+\mu^-$ or $D^0 \to h^+h^-R'(\mu\mu)$ [13, 157]. The former in particular has to be described by the K-matrix formalism [297], in order to take into account the re-scattering on the h^+h^- system, that can couple to several channels. An example are the $\pi\pi/KK$ S-wave contributions, that can couple to $\pi\pi$, $K\bar{K}$, $\pi\pi\pi\pi$, $\eta\eta$ and $\eta\eta'$ channels and include several poles like $f_0(980)$, $f_0(1300)$, $f_0(1500)$, $f_0(1200-1600)$ and $f_0(1750)$. The couplings in principle are process-dependent and this will result in a large number of free parameters. Another approximation is using a relativistic Breit-Wigner for all the resonances. It is known that the RBW does not describe correctly large or overlapped resonances. An example is the broad $\rho(770)^0$ state, for which the Gounaris–Sakurai parametrisation [298] is commonly used.

5.2 Background subtracted $m(hh)$ and $m(\mu\mu)$ distributions

Both the distributions of the invariant masses $m(hh)$ and $m(\mu\mu)$ and the angular variables are contaminated by the combinatorial and the misidentified backgrounds. In order to isolate the signal distributions only it is necessary to perform a background subtraction starting from D^0 invariant mass fit, in which the signal and backgrounds distributions are known, and use this information to unfold the signal from the backgrounds in the distribution of the phase space variables. The sPlot technique is used to perform this procedure. The method is based on a extended ML fit on the D^0 invariant mass distribution (called discriminating variable) using the PDFs discussed in the previous chapter to describe the different contributions. From the fit the sPlot method calculates per-candidate weights, called sWeights or ${}_sW$ for each component of the total PDF, that can be used to build a weighted distribution on the other variable (called control variable) on which the various components behaviours are not known. In this case for each candidate three sets of weights are calculated: for the signal component, and for the combinatorial and for the misID background component. For a specific component n, the weight for the candidate e is calculated as

$$ {}_sW_n(y_e) = \frac{\sum_{j=1}^{M} \mathbf{V}_{nj} f_j(y_e)}{\sum_{k=1}^{M} N_k f_k(y_e)}, \tag{5.17} $$

where M is the number of categories (3 in our case), N_k is the yield of the k-th component, $\mathbf{V}$ is the resulting covariance matrix of the ML fit, f_j are the PDFs of the various species used in the fit, while y is the variable on which the fit is performed, the D^0 invariant mass in our case. One of the property of the method is that the weights are calculated such that their sum over the events for a specific component is its corresponding total yield

$$ \sum_{e=1} {}_sW_n(y_e) = N_n, \tag{5.18} $$

and for each event the sum of the weights over the different categories is equal to 1. One of the most important assumption of the method is that the discriminating variable (within each component) has to be uncorrelated with the control variable, in order that all the visible correlations can be traced back to the proportions of different components only. In our case this is true for the signal and combinatorial background components, but can be false in principle for the misID background, since the probability of misidentification may be not constant within the phase space, and this can be correlated with the reconstructed D^0 mass.

The background subtracted $m(hh)$ and $m(\mu\mu)$ distributions are shown in Fig. 5.1 and Fig. 5.2 for $D^0 \to \pi^+\pi^-\mu^+\mu^-$ and $D^0 \to K^+K^-\mu^+\mu^-$ respectively. The distributions are used to tune the parameters of the amplitude model in terms of resonant components fractions and ρ-ω mixing parameters, since a ML fit of the amplitude model on the phase space distributions is not possible, due to the amplitude model approximations and the possible instability of the fit because of the low statistics and the high number of free parameters.

The distributions of the simulated $m(h^+h^-)$, $m(\mu^+\mu^-)$, $\cos\theta_{\mu^+}$ and of the angle ϕ using the amplitude model are shown in Fig. 5.3 and Fig. 5.4 for the $D^0 \to \pi^+\pi^-\mu^+\mu^-$ and $D^0 \to K^+K^-\mu^+\mu^-$ models respectively.

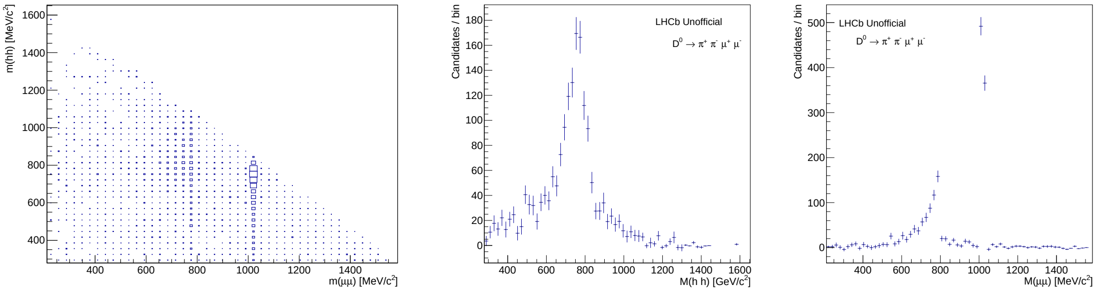

FIGURE 5.1. Distributions of $m(\mu^+\mu^-)$ vs. $m(\pi^+\pi^-)$ (left) and the relative projections (two plots on the right) after the sPlot background subtraction for the fully selected Run II $D^0 \to \pi^+\pi^-\mu^+\mu^-$.

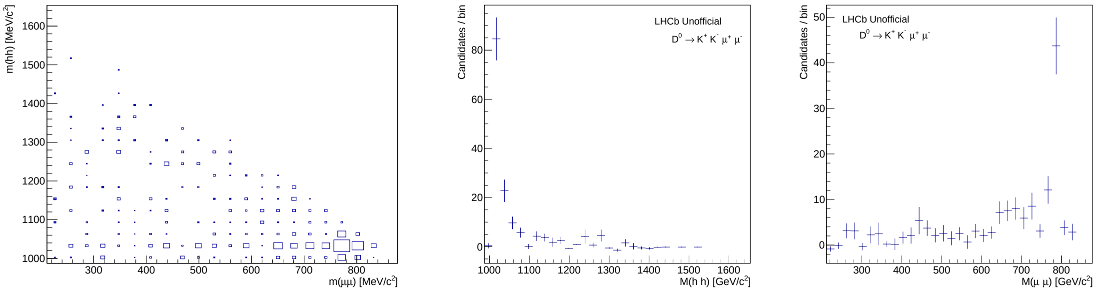

FIGURE 5.2. Distributions of $m(\mu^+\mu^-)$ vs. $m(K^+K^-)$ (left) and the relative projections (two plots on the right) after the sPlot background subtraction for the fully selected Run II $D^0 \to K^+K^-\mu^+\mu^-$.

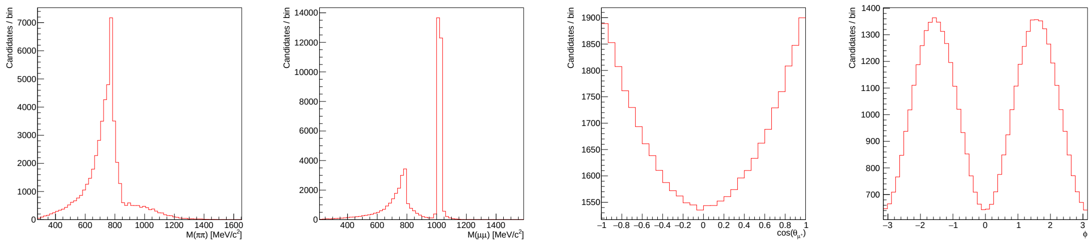

FIGURE 5.3. Distributions of $m(\pi^+\pi^-)$, $m(\mu^+\mu^-)$, $\cos\theta_\mu$ and ϕ (from left to right respectively) of the simulated $D^0 \to \pi^+\pi^-\mu^+\mu^-$ amplitude model.

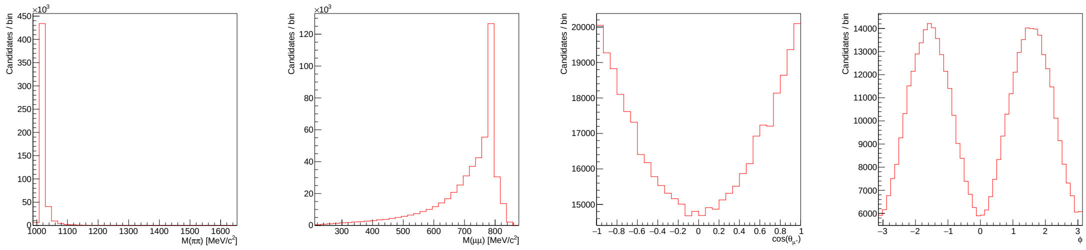

FIGURE 5.4. Distributions of $m(K^+K^-)$, $m(\mu^+\mu^-)$, $\cos\theta_\mu$ and ϕ (from left to right respectively) of the simulated $D^0 \to K^+K^-\mu^+\mu^-$ amplitude model.

5.3 Development of the angular fit

The angular ML fit procedure will be done in two dimensions, on the $\cos\theta_\mu$-ϕ plane, thus using the decay rate parametrisation introduced in Eq. (5.19), and reported here for reference [168],

$$d^5\Gamma = \frac{1}{2\pi}\left[\sum_{i=1}^{9} c_i(\theta_\mu,\phi)\, I_i(q^2,p^2,\theta_h)\right]\cdot dq^2 dp^2 d(\cos\theta_\mu) d(\cos\theta_h) d\phi. \tag{5.19}$$

If the fit is performed integrating in $m(\mu^+\mu^-)$ spectrum, the average values of the coefficients $\langle I_i\rangle$ are obtained as fit parameters, while if it is done in regions of $m(\mu^+\mu^-)$ one can probe the behaviour as a function of $m(\mu^+\mu^-)$ near the main resonances.

It is important to note that the absolute values of the coefficients can be obtained with an absolute branching fraction measurement. Since we are interested only in their behaviour as a function of $m(\mu\mu)$ and since the SM null physics test are not affected by a finite scale factor, the fit will be performed by rescaling all the coefficients by I_1 which is by definition a constant term (or by $\alpha\cdot I_1$, where α is a constant), thus a flat component over the phase space. The final PDF is

$$pdf = 1 + \frac{1}{2\pi}\sum_{i=2}^{9} c_i(\theta_\mu,\phi)\, I'_i(q^2,p^2,\theta_h), \tag{5.20}$$

where I'_i are now eight parameters, where $I'_i \propto I_i/I_1$. The previous parametrisation is analogous to fixing $I_1 = 2\pi$ in the fit. It is important to note that in each $m(\mu^+\mu^-)$ region the true value of I_1 can vary, hence the values I'_i obtained with independent fits in each bin does not reproduce the true behaviour of the single coefficient $I_i(m(\mu\mu))$ as a function of $m(\mu^+\mu^-)$, but only the relative trend with respect to the local I_1. In order to retrieve the $I_i(m(\mu\mu))$ function a simultaneous fit over all the $m(\mu^+\mu^-)$ regions must be performed. In this case also the SM null test is not affected by this local rescaling, since a non-null value is the signal of a non-null I_i true value.

5.4 Validation of the fit with pseudoexperiments

Before performing the angular fit on Run II data a careful test of the stability and reliability of the fit must be performed. A complete simulation chain is developed in order to introduce all the analysis steps that can introduce systematics effects on the fit procedure. The simulation chain consist of the following steps:

1. The signal PDF in the D^0 invariant mass spectrum as obtained by the ML fit on data is sampled in order to generate a set of N D^0 mass values of hypothetical N candidates of $D^0 \to h^+h^-\mu^+\mu^-$.
2. The previously tuned amplitude model (or directly the angular model as explained later) is used to generate the phase space distributions for the N candidates of $D^0 \to h^+h^-\mu^+\mu^-$, with fixed D^0 mass. It is worth remarking that this condition is the same as in real data, in which the phase space variables are obtained from the DTF algorithm with D^0 constrained mass. Then for each candidate, a D^0 mass generated at the previous step is associated to build a complete set of variables for the signal: invariant mass, affected by resolution, and phase space variables. At this step the simulated dataset has no efficiency effect applied.
3. The phase space dependent efficiency is added, applying the nominal inverse of the correction weight, as obtained by the phase space dependent efficiency correction described in Sect. 4.6.
4. At this point the background is added. In order to preserve the physical correlations between variables the background is not simulated but it is taken from real data, in particular from the $D^0 \to h^+h^-\pi^+\pi^-$ control samples where two pions of opposite charge are previously misidentified as muons before the `DTF` fit. In this way a large dataset of misID and combinatorial backgrounds is obtained and added to the previously simulated signal dataset, preserving the signal-to-background fraction as observed in real data. The control sample and its selection is the same used to determine the background PDF, then fitted in the D^0 mass spectrum, as described in Sect. 4.7.1.2.
5. Since the background dataset is affected by the phase space dependent efficiency, at this point the correction on the overall dataset is applied. In order to avoid a perfect cancellation of the efficiency previously added for the signal, the correction weight is extracted in each bin of the reweighter BDT from a gaussian distribution centred at its nominal value and using the error of the BDT bin content as standard deviation.
6. The D^0 invariant mass fit is then performed on the full dataset to extract the signal sWeights.
7. The sPlots corresponding to the background subtracted $\cos\theta_\mu$ and ϕ distributions are fitted with the angular model.

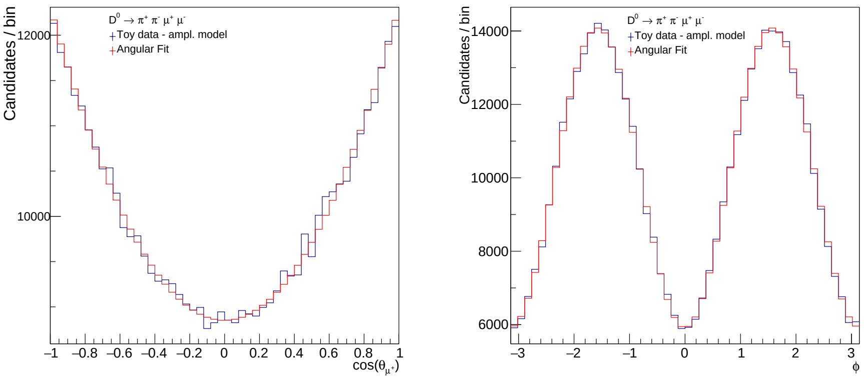

FIGURE 5.5. Example of angular fit, integrated $m(\mu^+\mu^-)$, on ϕ and $\cos\theta_{\mu^+}$ observables in case of an high statistics $D^0 \to \pi^+\pi^-\mu^+\mu^-$ simulated sample using the amplitude model.

8. The fitted angular parameters are then compared with those used at the generation level to check that the fit does not introduce any bias in the determination of the angular parameters and correctly estimate the uncertainties.

The study using these pseudo-experiments is composed of two main steps:

- Bias study: the phase space distributions generated using the amplitude model are fitted one single time with the angular model; the corresponding fitted coefficients $I_{2,\dots,4}$ are used to generate the D^0 signal phase space distributions in each of 1000 pseudo-experiment using directly the angular model, while the coefficients $I_{5,\dots,9}$ are set to 0, as in the SM (supposing also not to observe *CP* asymmetry). This allows a consistent comparison between the generated coefficients and the re-fitted ones. In fact, in order to estimate possible biases on the fitted angular parameters, in each pseudo-experiment a quantity called *pull* is calculated as

$$\text{pull}_i = \frac{I_i^{\text{fit}} - I_i^{\text{gen}}}{\sigma_{I_i}},$$

  where σ_{I_i} is the uncertainty on I_i^{fit} as obtained by the fit. Ideally, if the fit does not introduce any bias and estimate correctly the uncertainties, the pull values have to be distributed as a gaussian around 0 with standard deviation equal to 1. The mean of the pull distribution is thus a measure of the bias. An example of angular fit is shown in Fig. 5.5 in case of an high statistics $D^0 \to \pi^+\pi^-\mu^+\mu^-$ simulated sample using the amplitude model.

- Simulation of SM null test: a single pseudo-experiment is performed in each $m(\mu^+\mu^-)$ region, using in this case the amplitude model to generate the D^0 phase space distributions. The values of the main angular coefficients for SM null test ($I_{5,\dots,9}$) are then determined and a correction for the biases evaluated at the previous step is applied. This allows to study the expected precision on the $I_{5,...,9}$ measurements and also to check whether the basic amplitude model, with SM contributions only, produce significant deviations from zero for these coefficients.

Bias studies

A total number of 1000 pseudo-experiments is performed in each di-muon mass region. In case of $D^0 \to K^+K^-\mu^+\mu^-$ decay, only the full integrated $m(\mu^+\mu^-)$ region is studied, since in η and the low mass region the statistic is too low to perform the angular fit. In order not to introduce any bias the background taken from $D^0 \to h^+h^-\pi^+\pi^-$ control sample is sampled in each pseudo-experiment with a bootstrap technique [299], which consist of a flat random sampling with replacement. Moreover, the number of generated signal and background candidates fluctuate in each pseudo-experiment according to a Poissonian distributions with the number of expected candidates as the Poissonian mean (corresponding to the yields obtained in Sect. 4.7.1.4).

Before performing the bias studies the pseudoexperiment implementation is tested with the signal component only and, afterwards, with a simulated combinatorial background with no correlations between the D^0 invariant mass and the phase space variables. In this case the means of the pull distributions are compatible with 0, while the standard deviations are compatible with 1.

An example of pull distributions for the coefficients $I_{2,...,9}$ is shown in Fig. 5.6, in case of a $m(\mu^+\mu^-)$ integrated fit of $D^0 \to \pi^+\pi^-\mu^+\mu^-$ decay, with the observed Run II nominal signal and background yields.

As shown in case of a $m(\mu^+\mu^-)$ integrated fit, biases are significantly different from zero for some coefficients, in particular the maximum value is observed in I_3 and I_5 that show biases of the order of $0.4\sigma_{\text{fit}}$. The biases for each coefficients in each di-muon mass region are shown in Fig. 5.7. Their values are less widespread with the respect to the $m(\mu^+\mu^-)$ integrated one, suggesting that the bias could be related to the total amount of background in the $m(D^0)$ mass spectrum. In order to check how the background can harm angular fit on the *sweighted* angular distributions, the biases are determined by varying the fraction of background while generating the signal with the nominal yield. The measured biases are shown in Fig. 5.8 in case of $m(\mu^+\mu^-)$ $D^0 \to \pi^+\pi^-\mu^+\mu^-$ integrated sample, where a background fraction equal to 1 corresponds to the one observed on Run II data. An increase of the bias values as a function of the background fraction is evident. Some coefficients like I_2, I_3, I_5 and I_9 are affected by an increasing bias as a function of the background fraction, while coefficients I_4 and I_6 biases show a weaker dependence. The coefficients I_7 and I_8 are instead not significantly affected by an increasing background presence. This general behaviour suggests that a possible optimisation of the selection strategy for the $D^0 \to h^+h^-\mu^+\mu^-$ decays could be to tighten PID cuts to increase the purity.

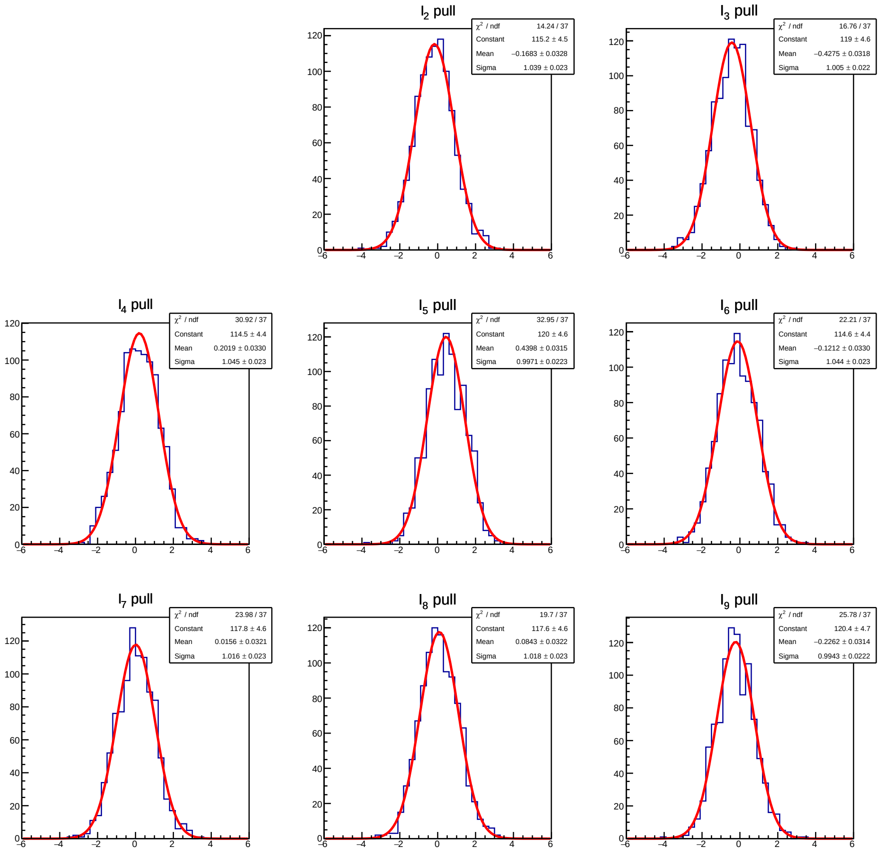

FIGURE 5.6. Pull distributions of the fitted angular coefficients for the $D^0 \to \pi^+\pi^-\mu^+\mu^-$ decay, integrated in $m(\mu^+\mu^-)$ and with the observed Run II nominal signal and background yields.

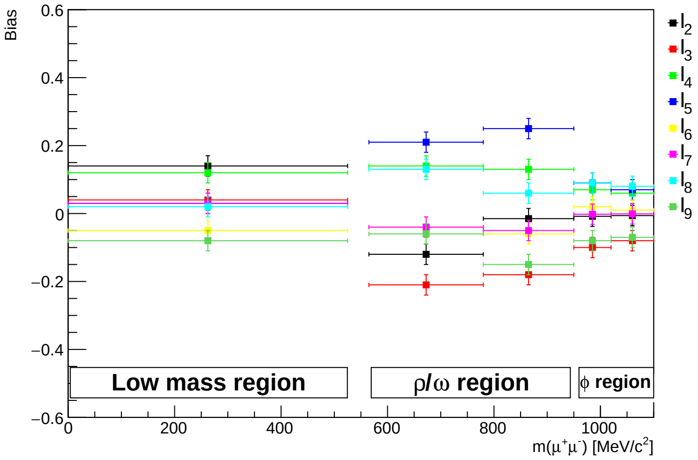

FIGURE 5.7. Bias of the fitted angular coefficients for the $D^0 \to \pi^+\pi^-\mu^+\mu^-$ decay, in each $m(\mu^+\mu^-)$ region, with the observed Run II nominal signal and background yields.

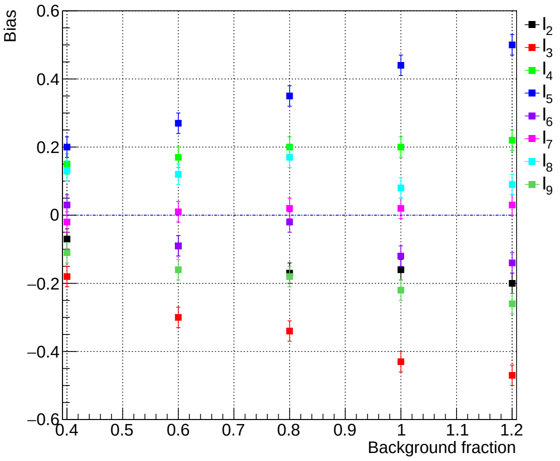

FIGURE 5.8. Bias of the fitted angular coefficients for the $D^0 \to \pi^+\pi^-\mu^+\mu^-$ decay, integrated in $m(\mu^+\mu^-)$ spectrum, as a function of the background fraction sampled in each pseudoexperiment. The nominal background fraction as observed in data is equal to 1.

SM null test simulation

As previously mentioned, a single pseudoexperiment is performed in each $m(\mu^+\mu^-)$ region using the amplitude model to generate the D^0 phase space distributions. Since the values of the fitted angular parameters ($I_{5,\ldots,9}$) has to be 0 in the SM (assumption that has been checked also by fitting a single pseudoexperiment with high signal only statistics) this study allows to check whether the fit on the amplitude model, with SM contributions only, can affect the SM null tests.

The raw values are also corrected in each $m(\mu^+\mu^-)$ region with the biases studied previously. When performing the bias correction an implicit assumption is done, i.e. that the bias on a given coefficient I_i can be corrected for each value of I_i, despite the bias having be determined for a generated I_i^{gen} equal to 0. In fact in principle the bias can be different if the real values of the coefficients are not equal to 0, so several studies are currently taking place to check the validity of this assumption. The corrected and uncorrected coefficients $I_{5,\ldots,9}$ as a function of $m(\mu^+\mu^-)$ are shown in Fig. 5.10 in the case of $D^0 \to \pi^+\pi^-\mu^+\mu^-$ sample. Most of the coefficients show raw values which are compatible with 0 within one σ, being σ the statistical uncertainty obtained by the fit, except the I_5 point in the low $m(\mu^+\mu^-)$ region and the I_9 point of the last $m(\mu^+\mu^-)$ (corresponding to the left side of ϕ). A similar behaviour is observed for the corrected coefficients. The same study is performed on the $D^0 \to K^+K^-\mu^+\mu^-$, where the fit is done by integrating the $m(\mu^+\mu^-)$ spectrum due to the low statistics in the low mass region.

It is important to remark that the bias determination and the simulation of the SM null test are independent, in the sense that the biases have been determined by generating angular distributions with fixed $I_{5,\ldots,9}$ values and without using the ones obtained from the fit on the

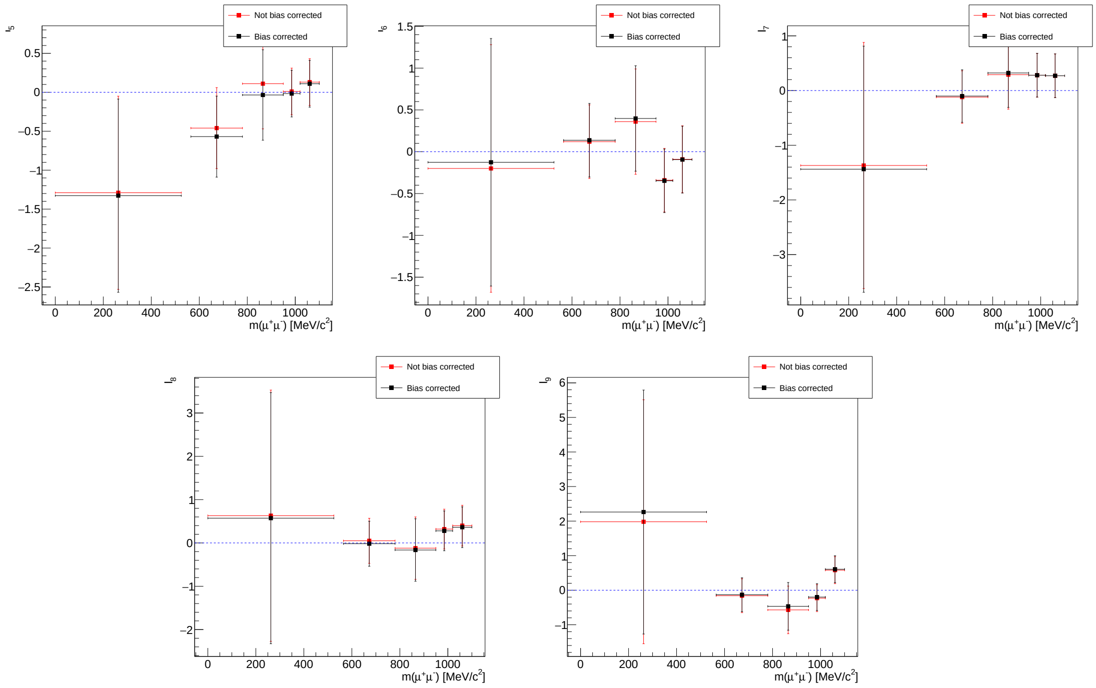

FIGURE 5.9. Fitted coefficients $I_{5,\ldots,9}$ with and without the bias correction, as a function of $m(\mu^+\mu^-)$ for the $D^0 \to \pi^+\pi^-\mu^+\mu^-$ sample.

amplitude model.

5.5 Summary and future prospects

In this chapter the validation of the angular fit procedure to be performed on the rare decays $D^0 \to h^+h^-\mu^+\mu^-$ has been discussed. The low statistics has various consequences: the first is that it is possible to neglect physical effects of higher orders in the dynamics that can contribute to $I_{5,6,7}$, like for example intermediate pseudoscalar resonances decaying directly in two muons, or the non-vanishing lepton masses, making the measurement of the coefficients $I_{5,6,7}$ an excellent opportunity to perform SM null tests. The presence of backgrounds in the D^0 invariant mass spectrum makes the angular fit with low statistics not particularly affected by bias, even though the biases increase as a function of the background fraction for most of the important coefficients. These biases do not exceed $0.5\,\sigma$ and therefore it has been proposed to carry out an a-posteriori bias correction on the fitted coefficients. The development of a basic amplitude model with the main SM contributions allows to test the $I_{5,\ldots,9}$ measurement, where it is observed that the parameters are compatible with the null value within one σ. Other studies are in progress to check whether it is possible to carry out the bias correction even if the coefficient values is not zero, since the biases themselves may vary as a function of the parameters. A further possibility is not to perform any correction on the raw coefficients and considering the biases as

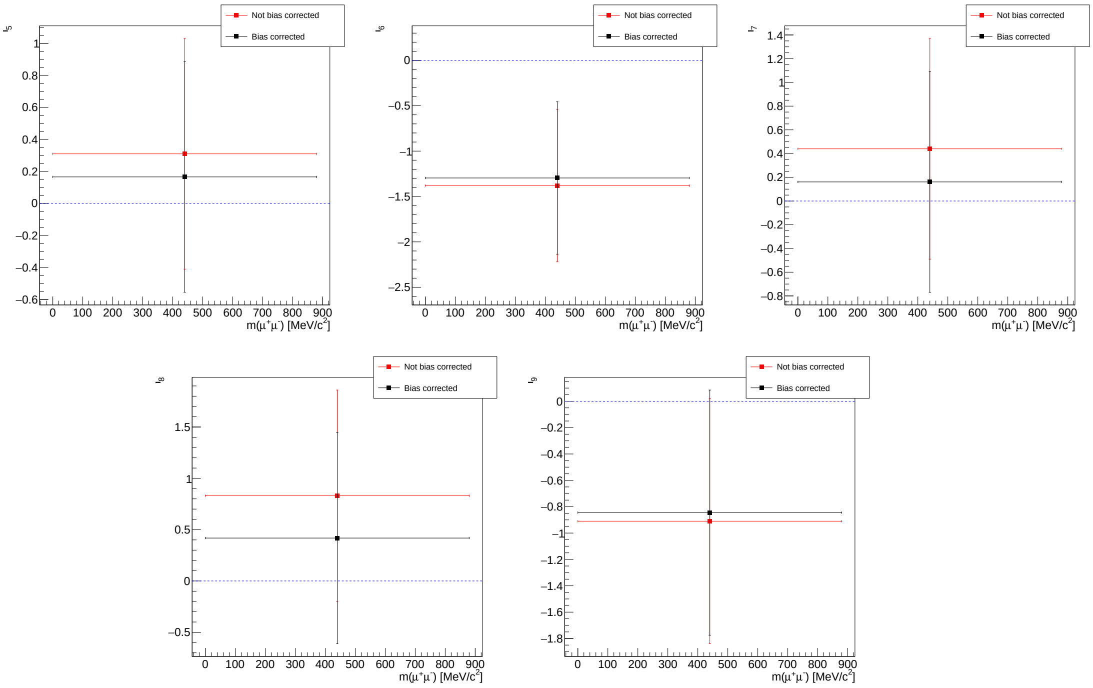

FIGURE 5.10. Fitted coefficients $I_{5,\ldots,9}$ with and without the bias correction, as a function of $m(\mu^+\mu^-)$ for the $D^0 \to \pi^+\pi^-\mu^+\mu^-$ sample.

systematic uncertainties. Apart from the bias values it should be emphasized that the fits always converge, also in $m(\mu^+\mu^-)$ regions with low statistics, and that the uncertainties are correctly estimated having the distributions of the gaussian pulls a standard deviation compatible with 1. We can therefore conclude that with the current observed statistics, using Run II dataset, an angular fit on $D^0 \to h^+h^-\mu^+\mu^-$ decays can be performed with biases under control, in particular performing the analysis as a function of $m(\mu^+\mu^-)$ in the five main populated regions, while for $D^0 \to K^+K^-\mu^+\mu^-$ decay an angular fit integrating in $m(\mu^+\mu^-)$ is possible, due to the too low statistics in the low $m(\mu^+\mu^-)$ region.

CONCLUDING REMARKS

This thesis shows the study of rare decays $D^0 \to \pi^+\pi^-\mu^+\mu^-$ and $D^0 \to K^+K^-\mu^+\mu^-$ at LHCb experiment. These decays offer a unique opportunity to probe new physics in up-type quark sector, exploiting also the rich set of angular observables due to the five dimensional phase space. A complete and optimised selection on Run II dataset has been described, corresponding to an integrated luminosity of $4.9\,\text{fb}^{-1}$, allowing an improvement on the expected asymmetry precision by a factor of 2 and 1.5 for $D^0 \to \pi^+\pi^-\mu^+\mu^-$ and $D^0 \to K^+K^-\mu^+\mu^-$ respectively, with respect to the current known measurements. A slightly further improvement in the asymmetry precision is thus expected with the inclusion of the Run I dataset, corresponding to an overall dataset with an integrated luminosity of approximately $8\,\text{fb}^{-1}$.

The possibility to perform a first-ever complete angular analysis in these decays is successfully studied. In particular a basic amplitude model has been developed and used to generate simulated pseudo-experiments to validate the angular fit. The current statistics for the $D^0 \to \pi^+\pi^-\mu^+\mu^-$ decay allows to perform a full angular analysis and measure five angular observables related to SM null test, in different regions of the di-muon invariant mass spectrum, with a precision that goes from 20% in the low mass region to 3.1% in the region dominated by the $\phi \to \mu^+\mu^-$ decay. The lower statistics of $D^0 \to K^+K^-\mu^+\mu^-$ allows to perform the angular fit integrating the full di-muon mass spectrum. The angular fit shows bias values not compatible with zero, but not exceeding $0.5\,\sigma$, where σ is the uncertainty on the single fitted angular parameter. Therefore they can be kept under control, either with an a-posteriori correction or by introducing a systematic uncertainty, being the measurements dominated by statistical uncertainties. Moreover, since it has been demonstrated that most of the biases are related to the doubly misidentified background pollution, a different selection strategy is currently being carried out in order to further suppress this source of background. A further complication that has been studied, that is also an interesting spectroscopical aspect, is the possible contribution of the cascade topology due to decay $D^0 \to a_1(1260)^\pm\pi^\mp$, which at the present time is not included in the theoretical calculations of $D^0 \to \pi^+\pi^-\mu^+\mu^-$ differential decay rate [168], and which we have shown not to affect SM null tests within the current experimental precision. Since the exact fraction of $a_1(1260)$ mediated decays is unknown and it is the first time an angular analysis is performed on this decays, discussions with theorists are ongoing to better understand potential issues.

In the amplitude and angular model implementation an important role has been played using the Hydra framework, a state-of-art collection of libraries for parallel computing, in order to speed-up the generation of high statistics phase space distributions and the angular fit. Without such an implementation the computation time becomes too large to perform essential studies for the fit feasibility and validation.

Concerning the LHCb upgrade operations, the tests on the muon readout electronics and on the nSYNC chip, discussed in Chap. 3, have been successfully performed, with excellent results in terms of performance and radiation hardness. The radiation tests have shown no failure behaviour, no single event latchup and a negligible current increase after an integrated dose corresponding to 10 times the one expected for 10 years of LHCb upgrade operations. The irradiation test of the nSYNC chip allowed also to assure the radiation hardness of the UMC 130 nm technology, measuring the SEU cross section per bit, $(0.53 \pm 0.04)\cdot 10^{-13}$ cm^2, an important achievement since it is the first result for SEU cross section of this technology. The number of expected single-errors during the LHCb upgrade operations has been obtained and it has negligible effects for the normal data taking conditions.

Appendix A

Angular conventions and coefficients I_i

In this chapter the angular convention for parametrise the $D^0 \to h^+h^-\mu^+\mu^-$ angular distributions is discussed. These conventions are referred to LHCb convention, since they are common to other LHCb analyses [300].

Variable $\cos\theta_{\mu^+}$

The variable $\cos\theta_{\mu^+}$ is defined as the cosine of the helicity angle for the dimuon system, where the helicity angle θ_{μ^+} is defined as the angle between the momentum of the positive muon in the rest frame of the dimuon system with respect to the dimuon flight direction as seen from the rest frame of the D^0. An equivalent definition to not mix two reference frames is: the angle between the momentum of the positive muon and the inverse of the momentum of the D^0 all defined in the dimuon system. For the $\overline{D}^0$ the negative muon is considered. Quantitatively,

$$\cos\theta_{\mu^+} = \frac{\vec{p}^{\,\{\mu\mu\}}_{\mu^+} \cdot \vec{p}^{\,\{D\}}_{\mu\mu}}{|\vec{p}^{\,\{\mu\mu\}}_{\mu^+}||\vec{p}^{\,\{D\}}_{\mu\mu}|} \tag{A.1}$$

where $\vec{p}^{\,\{X\}}_{i}$ indicates the momentum of the particle i in the rest frame of particle X. The angle definition is also shown in Fig. A.1.

Variable $\cos\theta_{h^+}$

The variable $\cos\theta_{h^+}$ is defined as the cosine of the helicity angle for the dihadron system, where the helicity angle θ_{h^+} is defined as the angle between the momentum of the positive hadron in the rest frame of the digadron system with respect to the dihadron flight direction as seen from the rest frame of the D^0. An equivalent definition to not mix two reference frames is: the angle

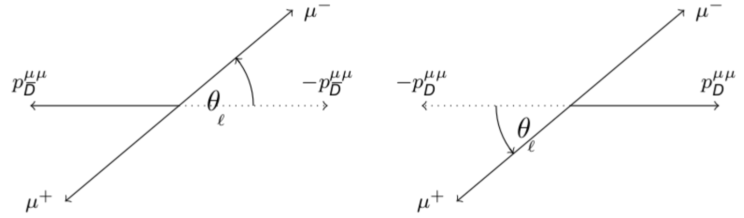

FIGURE A.1. Schematic representation of the variable $\cos\theta_\mu$ for $\overline{D}^0$ (left) and D^0 (right). Modified from [300].

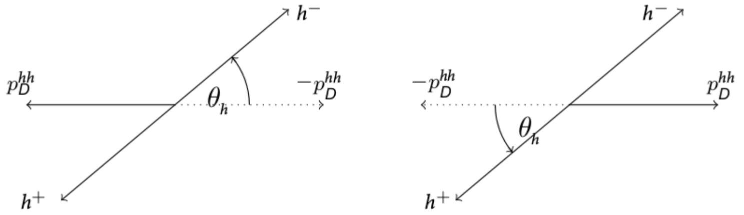

FIGURE A.2. Schematic representation of the variable $\cos\theta_h$ for $\overline{D}^0$ (left) and D^0 (right). Modified from [300].

between the momentum of the positive hadron and the inverse of the momentum of the D^0 all defined in the dihadron system. For the $\overline{D}^0$ the negative hadron is considered. Quantitatively,

$$\cos\theta_{h^+} = \frac{\vec{p}_{h^+}^{\{hh\}} \cdot \vec{p}_{hh}^{\{D\}}}{|\vec{p}_{h^+}^{\{hh\}}||\vec{p}_{hh}^{\{D\}}|} \tag{A.2}$$

The angle definition is also shown in Fig. A.2.

Variable ϕ

The variable ϕ is the angle between the two decay planes of the dimuon and dihadron system in the D^0 rest frame. The normal direction to the planes are defined as

$$\vec{n}_{\mu^+\mu^-}^{\{D\}} = \vec{p}_{\mu^+}^{\{D\}} \times \vec{p}_{\mu^+}^{\{D\}}, \tag{A.3}$$

$$\vec{n}_{h^+h^-}^{\{D\}} = \vec{p}_{h^+}^{\{D\}} \times \vec{p}_{h^+}^{\{D\}}. \tag{A.4}$$

(A.5)

The angle between the two normals shows an ambiguity. To solve it both the $\cos\phi$ and $\sin\phi$ have to be calculated. The angle ϕ is finally defined as

$$\cos\phi = \vec{n}_{\mu^+\mu^-}^{\{D\}} \cdot \vec{n}_{h^+h^-}^{\{D\}}, \tag{A.6}$$

$$\sin\phi = (\vec{n}_{\mu^+\mu^-}^{\{D\}} \times \vec{n}_{h^+h^-}^{\{D\}}) \cdot \frac{\vec{p}_{h^+h^-}^{\{D\}}}{|\vec{p}_{h^+h^-}^{\{D\}}|}. \tag{A.7}$$

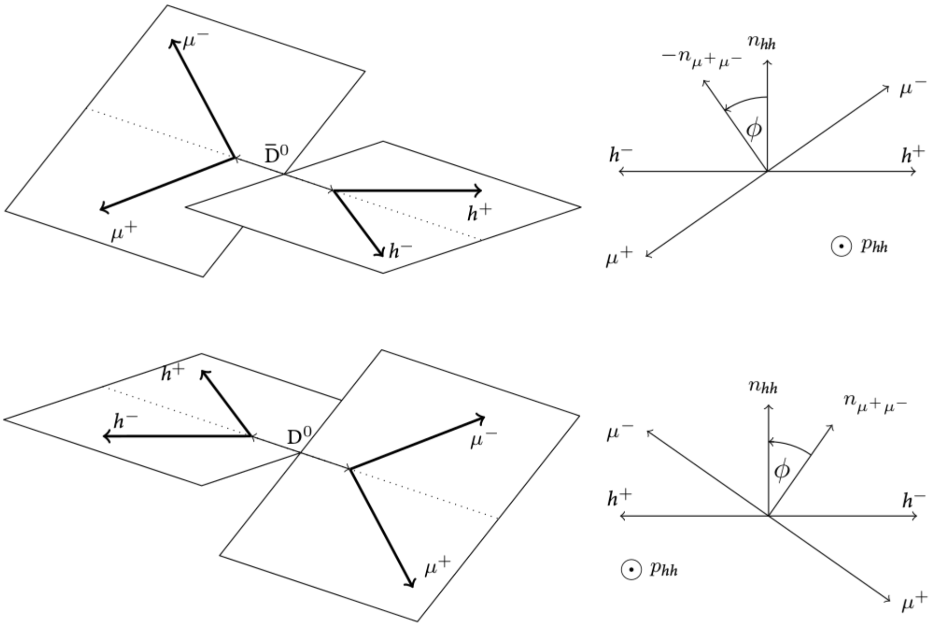

FIGURE A.3. Schematic representation of the angle ϕ for $\overline{D}^0$ (left) and D^0 (right). Modified from [300].

An analogous definition holds for $\bar{D}^0$.

It is important to note that this convention is the same as the one used for $D^0 \to h^+h^-\mu^+\mu^-$ theoretical predictions, despite the apparently slightly different definitions [168]. However the convention is different, only from the angle ϕ with respect to the one used for the amplitude model, described in Appendix D, where a different symbol (χ) is used. The relation is $\chi = \phi + \pi$. The angle definition is also shown in Fig. A.3.

Angular coefficients I_i

The I_i coefficients as function of $\sin\theta_h$ and of generalised tranversivity amplitudes, $H^{L/R}_{0,\|,\perp}$, are reported in the following [168],

$$I_1 = \frac{1}{16}\left[|H_0^L|^2 + (L \to R) + \frac{3}{2}\sin^2\theta_h(|H_\perp^L|^2 + |H_\parallel^L| + (L \to R))\right], \tag{A.8}$$

$$I_2 = -\frac{1}{16}\left[|H_0^L|^2 + (L \to R) + -\frac{1}{2}\sin^2\theta_h(|H_\perp^L|^2 + |H_\parallel^L| + (L \to R))\right], \tag{A.9}$$

$$I_3 = \frac{1}{16}\left[|H_\perp^L| - |H_\parallel^L|^2 + (L \to R)\right]\sin^2\theta_h, \tag{A.10}$$

$$I_4 = -\frac{1}{8}\left[\Re(H_0^L H_\parallel^{L*}) + (L \to R)\right]\sin\theta_h, \tag{A.11}$$

$$I_5 = -\frac{1}{4}\left[\Re(H_0^L H_\perp^{L*}) - (L \to R)\right]\sin\theta_h, \tag{A.12}$$

$$I_6 = \frac{1}{4}\left[\Re(H_\parallel^L H_\perp^{L*}) - (L \to R)\right]\sin^2\theta_h, \tag{A.13}$$

$$I_7 = -\frac{1}{4}\left[\Im(H_0^L H_\parallel^{L*}) - (L \to R)\right]\sin\theta_h, \tag{A.14}$$

$$I_8 = -\frac{1}{8}\left[\Im(H_0^L H_\perp^{L*}) + (L \to R)\right]\sin\theta_h, \tag{A.15}$$

$$I_9 = \frac{1}{8}\left[\Im(H_\perp^L H_\parallel^{L*}) + (L \to R)\right]\sin^2\theta_h, \tag{A.16}$$

where L, R indicates the handedness of the lepton current and the term $(L \to R)$ indicates to replicate the previously written terms with the right-handed ones.

Appendix B

Trigger Configurations for Run II

In the following all the TCKs used in the analysis for Run II data are reported, together with the main threshold variations for the used L0 and Hlt1 lines.

		Track(Muon)MVA	**L0**		**TrackMuon**			**TwoTrackMVA**		
	TCK (hex)	b	$p_T^{L0}(\mu)$	$E_T^{L0}(h)$	IPχ^2	GhostProb	PT	thr.	GhostProb	PT
2016 MD data	0x11291603	1.1 (-)	23	135	10	-	910	0.95	-	500
	0x11291604	1.1 (-)	27	149	10	-	910	0.95	-	500
	0x11291605	1.1 (-)	31	155	10	-	910	0.95	-	500
	0x11371609	2.3 (1.1)	27	155	35	0.2	1100	0.97	0.2	600
	0x1137160E	2.3 (1.1)	27	155	35	0.2	1100	0.97	0.2	600
	0x11381609	1.1 (1.1)	31	155	35	0.2	1100	0.95	0.2	600
	0x1138160E	1.1 (1.1)	31	155	35	0.2	1100	0.95	0.2	600
	0x1138160F	1.1 (1.1)	37	157	35	0.2	1100	0.95	0.2	600
2016 MU data	0x11321609	1.1 (-)	27	155	10	-	910	0.95	-	500
	0x11341609	1.1 (-)	27	155	10	9999	910	0.95	0.2	500
	0x11351609	2.3 (1.1)	27	155	35	0.2	1100	0.97	0.2	600
	0x11361609	2.3 (1.1)	27	155	35	0.2	1100	0.97	0.2	600
	0x11381611	1.1 (1.1)	31	163	35	0.2	1100	0.95	0.2	600
	0x11381612	1.1 (1.1)	33	163	35	0.2	1100	0.95	0.2	600
2016 sim.	0x5138160F	1.1 (1.1)	37	157	35	0.2	1100	0.95	0.2	600

Table B.1. TCKs and thresholds for the main L0 and Hlt1 lines in 2016.

		TrackMVA	**L0**		**TrackMuon**			**TwoTrackMVA**		
	TCK (hex)	b	$p_T^{L0}(\mu)$	$E_T^{L0}(h)$	IPχ^2	GhostPr	PT	thr.	GhostPr	PT
2015 MD data	0x10600A2	1.1	39	106	10	-	910	0.95	-	500
	0x10600A3	1.1	57	151	10	-	910	0.95	-	500
	0x10600A6	1.1	57	151	10	-	910	0.95	-	500
	0x10600A7	1.1	49	130	10	-	910	0.95	-	500
	0x10700A1	1.1	45	105	10	-	910	0.95	-	500
	0x10800A2	1.1	31	96	10	-	910	0.95	-	500
2015 MU data	0x10800A2	1.1	57	151	10	-	910	0.95	-	500
	0x11400A8	1.1	57	151	10	-	910	0.95	-	500
2015 sim.	0x411400A2	1.1	57	151	10	-	910	0.95	-	500

Table B.2. TCKs and thresholds for the main L0 and Hlt1 lines in 2015.

		Track(Muon)MVA	**L0**		**TrackMuon**			**TwoTrackMVA**		
	TCK (hex)	b	$p_T^{L0}(\mu)$	$E_T^{L0}(h)$	IPχ^2	GhostProb	PT	thr.	GhostProb	PT
2017 MU data	0x114E1702	1.1 (1.1)	15	125	35	0.2	1100	0.95	0.2	600
	0x114E1703	1.1 (1.1)	23	135	35	0.2	1100	0.95	0.2	600
	0x11501703	1.1 (1.1)	23	135	35	0.2	1100	0.95	0.2	600
	0x11501704	1.1 (1.1)	27	149	35	0.2	1100	0.95	0.2	600
	0x11501705	1.1 (1.1)	31	155	35	0.2	1100	0.95	0.2	600
	0x11501706	1.1 (1.1)	39	163	35	0.2	1100	0.95	0.2	600
	0x11561707	1.1 (1.1)	35	156	35	0.2	1100	0.95	0.2	600
	0x11601707	1.1 (1.1)	35	156	35	0.2	1100	0.95	0.2	600
	0x11601708	1.1 (1.1)	23	135	35	0.2	1100	0.95	0.2	600
	0x11611709	1.1 (1.1)	29	145	35	0.2	1100	0.95	0.2	600
2017 MD data	0x11541707	1.1 (1.1)	27	155	35	0.2	1100	0.95	0.2	600
	0x115417A7	1.1 (1.1)	35	156	35	0.2	1100	0.95	0.2	600
	0x11561707	1.1 (1.1)	35	156	35	0.2	1100	0.95	0.2	600
	0x11611707	1.1 (1.1)	35	156	35	0.2	1100	0.95	0.2	600
	0x11611708	1.1 (1.1)	23	135	35	0.2	1100	0.95	0.2	600
	0x11611709	1.1 (1.1)	29	145	35	0.2	1100	0.95	0.2	600
2017 sim.	0x51611709	1.1 (1.1)	29	145	35	0.2	1100	0.95	0.2	600

Table B.3. TCKs and thresholds for the main L0 and Hlt1 lines in 2017.

		Track(Muon)MVA	**L0**		**TrackMuon**			**TwoTrackMVA**		
	TCK (hex)	b	$p_T^{L0}(\mu)$	$E_T^{L0}(h)$	IPχ^2	GhostProb	PT	thr.	GhostProb	PT
2018 MU data	0x11671801	1.1 (1.1)	19	159	35	0.2	1100	0.95	0.2	600
	0x11711801	1.1 (1.1)	19	159	35	0.2	1100	0.95	0.2	600
	0x11731801	1.1 (1.1)	19	159	35	0.2	1100	0.95	0.2	600
	0x11741801	1.1 (1.1)	19	159	35	0.2	1100	0.95	0.2	600
	0x11771801	1.1 (1.1)	19	159	35	0.2	1100	0.95	0.2	600
	0x117718A1	1.1 (1.1)	19	159	35	0.2	1100	0.95	0.2	600
	0x117A18A2	1.1 (1.1)	19	159	35	0.2	1100	0.95	0.2	600
	0x117A18A4	1.1 (1.1)	19	159	35	0.2	1100	0.95	0.2	600
2018 MD data	0x11741801	1.1 (1.1)	19	159	35	0.2	1100	0.95	0.2	600
	0x11751801	1.1 (1.1)	19	159	35	0.2	1100	0.95	0.2	600
	0x11771801	1.1 (1.1)	19	159	35	0.2	1100	0.95	0.2	600
	0x117A18A2	1.1 (1.1)	19	159	35	0.2	1100	0.95	0.2	600
	0x117A18A4	1.1 (1.1)	19	159	35	0.2	1100	0.95	0.2	600
2018 sim.	-	1.1 (1.1)	19	159	35	0.2	1100	0.95	0.2	600

Table B.4. TCKs and thresholds for the main L0 and Hlt1 lines in 2018.

Appendix C

Maximum Likelihood methods

In this chapter the Maximum Likelihood (ML) methods are described, focusing in particular on extended ML fit, the use of parameter constraints and discussing some aspects of uncertainty calculation in case of a weighted dataset.

Maximum Likelihood fit

The ML method is one of the most widely used methods in high-energy physics for parameter estimation from the observation of experimental data. Consider a set of N measurements of a variable x, indicated as $\vec{x} = (x_1, ..., x_N)$, whose measurements are performed in a statistically independent way, and each of which follows a probability density function $f(x; \vec{\theta})$, where $\vec{\theta} = (\theta_1, ..., \theta_m)$ represents a set of m parameters to be estimated. The joint probability density function for the observed values $\vec{x}$ is given by the likelihood function, already encountered in the description of the identification variables, defined as the product of the f functions, evaluated in each point:

$$\mathscr{L}(\vec{\theta}) = \prod_i^N f(x_i; \vec{\theta}). \tag{C.1}$$

The best estimators of the parameters $\vec{\theta}$ are indicated as $\hat{\vec{\theta}}$ and those for which the function $\mathscr{L}(\vec{\theta})$ has its global maximum. Working with the negative logarithm of the likelihood function

$$-\ln \mathscr{L}(\vec{\theta}) = \sum_i^N \ln f(x_i; \vec{\theta}), \tag{C.2}$$

is more convenient since only sums appear in the expression and the best estimators are obtained minimizing the expression. The estimators found with the ML method, in the asymptotic limit

$N \to \infty$, are consistent and without bias (i.e. they converge to the exact values $\vec{\theta}$). In this limit, they also reach the minimum variance limit, for which the estimators are more efficient. It can be demonstrated that for a large number of events in the data sample and for any pdf $f(\vec{x}, \vec{\theta})$ the likelihood will approach a multivariate gaussian distribution for the parameters:

$$\mathscr{L} \propto e^{-\frac{1}{2}(\vec{\theta}-\hat{\vec{\theta}})^{\mathrm{T}}\mathcal{H}(\vec{\theta}-\hat{\vec{\theta}})}, \tag{C.3}$$

where $\mathcal{H}$ is a $m \times m$ matrix related to the width of the gaussian and thus to the uncertainties on the parameters. In fact the covariance matrix $\mathcal{V}(\hat{\vec{\theta}})$ can be estimated as

$$\hat{\mathcal{V}}_{jk}(\hat{\vec{\theta}}) = \left[- \left. \frac{\partial^2 \ln \mathscr{L}}{\partial\theta_j \partial\theta_k} \right|_{\vec{\theta}=\hat{\vec{\theta}}} \right]^{-1} = \mathcal{H}^{-1}, \tag{C.4}$$

and the errors on the parameters are then obtained as $\hat{\sigma}(\theta_i) = \sqrt{\hat{\mathcal{V}}_{ii}(\hat{\vec{\theta}})}$.
The ML method can be *unbinned*, when each event enters separately within the $\mathscr{L}$ expression, or *binned*, when the events are grouped in bins of the x observable, and using then the number of events in each bin within the likelihood.

Weighted ML fit

The dataset $\vec{x}$ on which one wants to make a ML fit can be weighted, with weights $\vec{w}$. This is for example the case of the efficiency corrected dataset used in the analysis described in Chap. 4. There are various ways in the literature to define consistently a weighted ML procedure, the most common in high energy physics is to build the following likelihood:

$$\mathscr{L}(\vec{\theta}) = \prod_i^N [f(x_i; \vec{\theta})]^{w_i}. \tag{C.5}$$

Intuitively, as the contribution of each event enters as a multiplicative factor, the individual contributions are raised to the value of the weight of the corresponding event. However, the method to estimate the parameter errors in Eq. (C.4) is no longer correct, since the correct scaling of the parameter errors must be $\sum_i w_i^2 / \sum_i w_i$. There are typically two ways to calculate the correct errors: the first one, implemented in ROOT within the RooFit package, is to calculate the covariance matrix as $\hat{\mathcal{V}}_{jk} = \mathcal{H}^{-1}\mathcal{F}\mathcal{H}^{-1}$ where

$$\mathcal{H} = \left[- \left. \frac{\partial^2 \sum_i w_i \ln f(x_i; \vec{\theta})}{\partial\theta_j \partial\theta_k} \right|_{\vec{\theta}=\hat{\vec{\theta}}} \right], \tag{C.6}$$

$$\mathcal{F} = \left[- \left. \frac{\partial^2 \sum_i w_i^2 \ln f(x_i; \vec{\theta})}{\partial\theta_j \partial\theta_k} \right|_{\vec{\theta}=\hat{\vec{\theta}}} \right]. \tag{C.7}$$

Thus $\mathcal{H}$ is equivalent to the previous case, but with w_i inside the likelihood definition, while $\mathcal{F}$ is defined in the same way but contains w_i^2. Another useful method that avoids the recalculation of the matrices is to scale $\ln \mathscr{L}$ by a factor α defined as

$$\alpha = \frac{\sum_i^N w_i}{\sum_i^N w_i^2}, \tag{C.8}$$

before the ML fit procedure. In this way the errors are properly computed with the Eq. (C.4), because the correct scaling is applied directly on the likelihood and not a posteriori in the covariance matrix.

Extended ML fit

The function $f(\vec{x}, \vec{\theta})$ is normalized to 1 in the whole observation domain D. This implies that the joint probability density describes only the form of the distribution, while the number N of events is determined by the observed value only. However, the observed value of the number of events is not, in general, a good estimator of the expected value of events, so it is preferred to relax the normalization condition, defining a new function $F(\vec{x} : \vec{\theta})$ normalised as

$$\int_D F(\vec{x} : \vec{\theta}) d\vec{x} = \mathscr{N}(\vec{\theta}). \tag{C.9}$$

In this case the function F describes also the expected number of events $\mathscr{N}$. Repeating the experiment in the same conditions, the observed number N of events fluctuates according to a Poisson distribution around the expected value $\mathscr{N}$. The Poissonian term can be incorporated as a multiplicative term in the likelihood function, that will be named *extended*, and becomes

$$\mathscr{L}(\vec{\theta}; \mathscr{N}) = e^{-\mathscr{N}} \frac{\mathscr{N}^N}{N!} \prod_i^N f(x_i; \vec{\theta}) = \frac{e^{-\mathscr{N}}}{N!} \prod_i^N F(x_i; \vec{\theta}). \tag{C.10}$$

In this way the value $\mathscr{N}$ can be estimated as another fit parameter.

ML fit with constraints

Often an external knowledge of some parameters θ_i, based on other experimental or preliminary studies, for example an estimation like $\theta_j = \mu_j \pm \sigma_j$, can be added to the ML fit as a constraint. The likelihood will be multiplied by the probability function of the parameter θ as

$$\mathscr{L}(\vec{\theta}) = \prod_i^N f(x_i; \vec{\theta}) \mathcal{C}(\theta_j) \tag{C.11}$$

where the $\mathcal{C}(\theta_j)$ is the probability density function for the parameter θ_j, usually a gaussian with μ_j and σ_j. This procedure is useful because a constraint on a parameter leads to a reduction of its final uncertainty with respect to the case in which it is free to float in the fit procedure. This method also can be applied to constants for which an uncertainty is known, in order to propagate it to the other fit parameters in a consistent and systematic way using the ML fit.

APPENDIX D

DEVELOPMENT OF THE AMPLITUDE MODEL

The D^0 decay is modelised using the isobar model and the helicity formalism. The procedure is similar to that used in [301] and [302]. There are two possible topologies:

1. $D^0 \to R_1 R_2$ with $R_1 \to h^+h^-$ and $R_2 \to \mu^+\mu^-$, with $h = \pi, K$;
2. $D^0 \to R_1' h_1$ with $R_1' \to R_2 h_2$ and $R_2 \to \mu^+\mu^-$.

First topology

In the helicity formalism, a coordinate system in which the mother is at rest is needed to describe each two-body decay. In order to define the D^0 rest reference a boost from the laboratory frame is performed: the z axis is then fixed by the direction of the boost $\vec{p}_{D^0}$, while the choice of the x and y axes is arbitrary, due to the rotational invariance of the D^0 angular distribution.

For this reason, there is the freedom to rotate the xyz frame around the z axis in order that the angle $\phi_{R_1} = 0$. For the subsequent decays a Lorentz transformation has to be performed towards the frames in which the new decaying particle is at rest. Consider for now the conventions as shown Fig. D.1 (these conventions are only preliminary) in order to be more general in the mathematical description: a proper rotation of the reference frames in order to simplify the calculations will be done later.

For each decay there is an amplitude contribution in the helicity formalism:

- $D^0 \to R_1 R_2$ decay:

$$\mathcal{H}^{D^0} = \sqrt{\frac{2S_{D^0}+1}{4\pi}}\, D^{0\,*}_{M_{D^0},\,M'_{D^0}}(0,\theta_{R_1},0)\, A^{D^0}_{\lambda_{R_1},\lambda_{R_2}} = \sqrt{\frac{1}{4\pi}}\, A^{D^0}_{\lambda_{R_1},\lambda_{R_1}}, \tag{D.1}$$

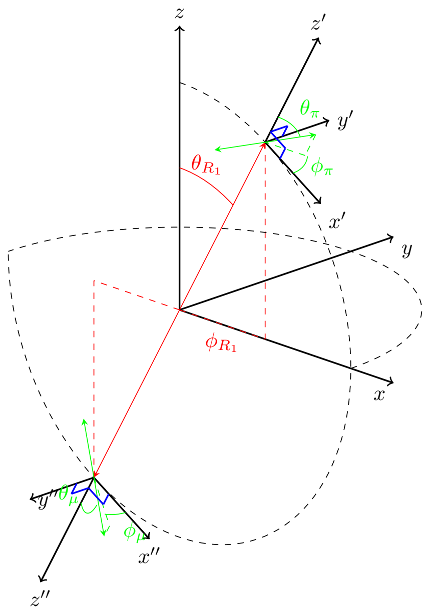

FIGURE D.1. Preliminary reference frame conventions for the first decay topology.

where $M'_{D^0} = \lambda_{R_1} - \lambda_{R_2}$, since it is calculated in the rotated z axis (z'), and for the conservation of angular momentum $|\lambda_{R_1} - \lambda_{R_2}| \leq 0$. Then $\lambda_{R_1} = \lambda_{R_2}$ with $|\lambda_{R_{1,2}}| \leq min[J_{R_1}, J_{R_2}]$. The rotational invariance is evident from the fact that the Wigner function is equal to 1.

- $R_1 \to h^+h^-$ decay:

$$\begin{aligned} \mathcal{H}^{R_1} &= \sqrt{\frac{2S_{R_1}+1}{4\pi}}\, D^{S_{R_1}\,*}_{M_{R_1},\,M'_{R_1}}(\phi_{h^+},\theta_{h^+},0)\, A^{R_1}_{\lambda_{h^+},\lambda_{h^-}}\, \mathcal{R}(m_{hh}) = \\ &= \sqrt{\frac{2S_{R_1}+1}{4\pi}}\, D^{S_{R_1}\,*}_{\lambda_{R_1},0}(\phi_{h^+},\theta_{h^+},0)\, A^{R_1}_{0,0}\, \mathcal{R}(m_{hh}) = \\ &= \sqrt{\frac{2S_{R_1}+1}{4\pi}}\, e^{+i\,\lambda_{R_1}\,\phi_{h^+}}\, d^{S_{R_1}\,*}_{\lambda_{R_1},0}(\theta_{h^+})\, A^{R_1}_{0,0}\, \mathcal{R}(m_{hh}), \end{aligned} \tag{D.2}$$

where $M_{R_1} = \lambda_{R_1}$ since it is calculated in an axis (z') parallel to $\vec{p}_{R_1}$, while $M'_{R_1} = 0$ since it is the difference of the helicites of the two hadrons. $\mathcal{R}(m_{hh})$ is instead the dynamical factor containing the lineshape of the distribution on m_{hh} spectrum.

- $R_2 \to \mu^+\mu^-$ decay:

$$\begin{aligned}
\mathcal{H}^{R_2} &= \sqrt{\frac{2S_{R_2}+1}{4\pi}}\, D^{S_{R_2}*}_{M_{R_2},\, M'_{R_2}}(\phi_{\mu^+}, \theta_{\mu^+}, 0)\, A^{R_2}_{\lambda_{\mu^+},\lambda_{\mu^-}}\, \mathcal{R}(m_{\mu\mu}) = \\
&= \sqrt{\frac{2S_{R_2}+1}{4\pi}}\, D^{S_{R_2}*}_{\lambda_{R_1},\lambda_{\mu^+}-\lambda_{\mu^-}}(\phi_{\mu^+}, \theta_{\mu^+}, 0)\, A^{R_2}_{\lambda_{\mu^+},\lambda_{\mu^-}}\; \mathcal{R}(m_{\mu\mu}) = \\
&= \sqrt{\frac{2S_{R_2}+1}{4\pi}}\; e^{+i\,\lambda_{R_1}\,\phi_{\mu^+}}\; d^{S_{R_2}*}_{\lambda_{R_1},\lambda_{\mu^+}-\lambda_{\mu^-}}(\theta_{\mu^+})\, A^{R_2}_{\lambda_{\mu^+},\lambda_{\mu^-}}\; \mathcal{R}(m_{\mu\mu}),
\end{aligned} \tag{D.3}$$

  where the fact that $M_{R_2} = \lambda_{R_1}$ has been used, and $\lambda_{R_1} = \lambda_{R_2}$ from the angular momentum conservation on the D^0 decay, while M'_{R_2} is the difference of the helicities of the two muons, since it is evaluated on an axis along $\vec{p}_{\mu^+}$ in the R_2 rest frame.

Building model for the first topology

With these conventions the x' and x'' axes are the same and the angle between the decay planes (of the di-hadron and di-muon system) is:

$$\chi = \phi_{\mu^+} + \phi_{\pi^+}. \tag{D.4}$$

Indeed the multiplication of the R_1 and R_2 contributions gives exactly:

$$e^{+i\,\lambda_{R_1}\,\phi_{h^+}} e^{+i\,\lambda_{R_1}\,\phi_{\mu^+}} = e^{+i\,\lambda_{R_1}\,\chi}. \tag{D.5}$$

Since the physical angle is that between the planes, χ, a rotation of the two frames together ($x'y'z'$ and $x''y''z''$) can always be done such that $\phi_{\mu^+} \to 0$ and $\phi_{h^+} \to \chi$. In this convention the two x axes (x' and x'') are still the same but lye on the same plane defined by $\vec{p}_{\mu^+}$ and $\vec{p}_{R_2}$ in D^0 rest frame.
Therefore the final convention is shown in the Fig. D.2.

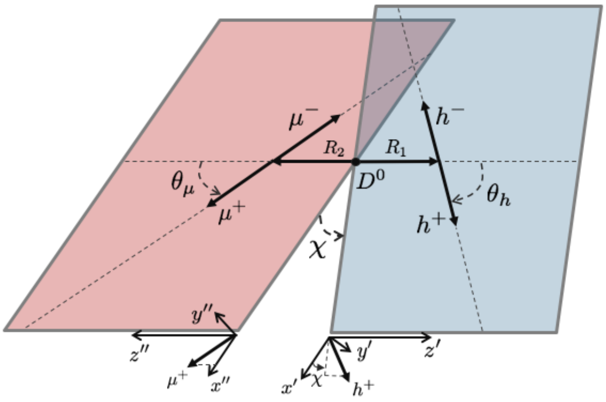

FIGURE D.2. Final reference frame conventions for the first decay topology.

It is important to remark some features:

- x' and x'' axes are the same and lye on the $\mu^+\mu^-$ plane, z' and z'' are opposite and, as consequence, y' and y'' are opposite too;
- boosting along $\vec{p}_{R_2}$ does not change the azimuthal angle χ;
- the χ angle is computed as the angle formed by the $\vec{p}_{h^+}$ projection on the $y''-x''$ plane. This is analogous to the following computation:

$$\cos\chi = \frac{(\vec{p}_{\mu^-}\times\vec{p}_{\mu^+})\cdot(\vec{p}_{h^+}\times\vec{p}_{h^-})}{|\vec{p}_{\mu^-}\times\vec{p}_{\mu^+}|\cdot|\vec{p}_{h^+}\times\vec{p}_{h^-}|}, \tag{D.6}$$

$$\sin\chi = \frac{(\vec{p}_{\mu^+}+\vec{p}_{\mu^-})\cdot[(\vec{p}_{\mu^-}\times\vec{p}_{\mu^+})\times(\vec{p}_{h^+}\times\vec{p}_{h^-})]}{|\vec{p}_{\mu^+}+\vec{p}_{\mu^-}|\cdot|\vec{p}_{\mu^-}\times\vec{p}_{\mu^+}|\cdot|\vec{p}_{h^+}\times\vec{p}_{h^-}|}; \tag{D.7}$$

- the axis in which the muon helicity will be computed can be defined rotating the R_2 rest frame ($x''y''z''$) by the helicity angle θ_μ around y'', such that $z'''=\vec{p}_{\mu^+}$. In this frame the $\vec{p}_{R_1}$ is still lying in the plane $x'''z'''$. This will be important for the alignment of the second topology frames, in order to proper align the helicity states.

The final amplitude is:

$$\begin{aligned}\mathcal{H}^{D^0\to R_1R_2}_{\lambda_{\mu^+},\lambda_{\mu^-}} &= \mathcal{N}\sum_{\lambda_{R_1}} A^{D^0}_{\lambda_{R_1},\lambda_{R_1}}\, A^{R_1}_{0,0}\, A^{R_2}_{\lambda_{\mu^+},\lambda_{\mu^-}}\cdot \\ & e^{+i\lambda_{R_1}\chi}\, d^{S_{R_1}*}_{\lambda_{R_1},0}(\theta_{h^+})\, d^{S_{R_2}*}_{\lambda_{R_1},\lambda_{\mu^+}-\lambda_{\mu^-}}(\theta_{\mu^+})\, B'_{L_{D^0}}(p,p_0,d)\cdot(p/p_0)^{L_{D^0}}\,\mathcal{R}^{R_2}(m_{\mu\mu})\,\mathcal{R}^{R_1}(m_{hh}).\end{aligned} \tag{D.8}$$

where $B'_{L_{D^0}}(p,p_0,d)$ is the Blatt-Weisskopf barrier factor, p is the momentum of one resonance in the D^0 rest frame considering the measured resonance mass, p_0 is the momentum of one resonance in the D^0 rest frame considering the nominal resonance mass (at the pole), d is the decay vertex radius and L_{D^0} is the orbital angular momentum of the D^0 daughters. We have also performed the coherent sum on λ_{R_1} since they are intermediate states and not measurable.

Reducing free complex coefficients

Since the complex number $A^{R_1}_{0,0}$ does not depend on any helicity, the two complex numbers can be factorise:

$$A^{R_1}_{0,0}\cdot A^{R_2}_{\lambda_{\mu^+},\lambda_{\mu^-}} = A^{R_1,R_2}_{\lambda_{\mu^+},\lambda_{\mu^-}}, \tag{D.9}$$

and also the coherent sum on λ_R can be factorised out:

$$\begin{aligned}\mathcal{H}^{D^0\to R_1R_2}_{\lambda_{\mu^+},\lambda_{\mu^-}} &= \mathcal{N}\, A^{R_1,R_2}_{\lambda_{\mu^+},\lambda_{\mu^-}}\, B'_{L_{D^0}}(p/p_0)^{L_{D^0}}\,\mathcal{R}^{R_2}(m_{\mu\mu})\,\mathcal{R}^{R_1}(m_{hh})\cdot \\ &\cdot\left(\sum_{\lambda_{R_1}} A^{D^0}_{\lambda_{R_1},\lambda_{R_1}}\, e^{+i\lambda_{R_1}\chi}\, d^{S_{R_1}*}_{\lambda_{R_1},0}(\theta_{h^+})\, d^{S_{R_2}*}_{\lambda_{R_1},\lambda_{\mu^+}-\lambda_{\mu^-}}(\theta_{\mu^+})\right).\end{aligned} \tag{D.10}$$

There is still a multiplication of free complex numbers, in particular of $A^{R_1,R_2}_{\lambda_{\mu^+},\lambda_{\mu^-}}$ and $A^{D^0}_{\lambda_{R_1},\lambda_{R_1}}$ inside the coherent sum. Thus a further reduction of the numbers of free complex coefficients can be performed, because the overall phase and magnitude of $A^{R_1,R_2}_{\lambda_{\mu^+},\lambda_{\mu^-}}$ can be reabsorbed in the $A^{D^0}_{\lambda_{R_1},\lambda_{R_1}}$ coefficients. So for each contribution the following fixing is performed, considering also the relation of conservation of parity:

$$A^{R_1,R_2}_{\lambda_{\mu^+},\lambda_{\mu^-}} = (1,0), \tag{D.11}$$

$$A^{R_1,R_2}_{-\lambda_{\mu^+},-\lambda_{\mu^-}} = (-\mathcal{P}(R_2)(-1)^{1-s_{R_2}},0) \tag{D.12}$$

where $\mathcal{P}(R_2)$ is the parity of R_2 and the conservation of parity relation has been used:

$$A^{R}_{-\lambda_{\mu^+},-\lambda_{\mu^-}} = \mathcal{P}(R_2)\mathcal{P}(\mu^+)\mathcal{P}(\mu^-)(-1)^{s_{\mu^+}+s_{\mu^-}-s_{R_2}}A^{R}_{\lambda_{\mu^+},\lambda_{\mu^-}}. \tag{D.13}$$

From the point of view of the implementation of the formula, the amplitude fit parameters can be merged to the angular distribution, while all the dynamics factors (lineshape and barrier factors) can be implemented separately.

Resonance contributions

There are several resonances that can contribute to the first topology of quasi-two-body decay, listed in Sect. 5.1.1.

As consequence we can divide the possible decay in the following categories, defining the resonances spin as S, P, D, meaning $J_{res} = 0, 1, 2$ respectively, and defining the first resonance as $R_1 \to h^+h^-$. In the following, for each categories, the possible helicities and orbital angular momentum values are discussed. They are obtained using both angular momentum and parity conservation.

- $D^0 \to SS$: remembering that $\lambda_{R_1} = \lambda_{R_2}$, with $|\lambda_{R_{1,2}}| \leq min[J_{R_1}, J_{R_2}]$, as shown before, in this case we obtain $\lambda_{R_1} = \lambda_{R_2} = 0$ and $\lambda_{\mu^+} = \lambda_{\mu^-} = \pm 1/2$. The minimum orbital angular momenta are $L_{D^0} = 0$, $L_{R_1} = 0$, $L_{R_2} = 0$.
- $D^0 \to PS$: in this case it follows that $\lambda_{R_1} = \lambda_{R_2} = 0$ and $\lambda_{\mu^+} = \lambda_{\mu^-}$. The minimum orbital angular momenta are $L_{D^0} = 1$, $L_{R_1} = 1$, $L_{R_2} = 0$.
- $D^0 \to SP$: in this case it follows that $\lambda_{R_1} = \lambda_{R_2} = 0$ and $\lambda_{\mu^+} = -\lambda_{\mu^-}$. The minimum orbital angular momenta are $L_{D^0} = 1$, $L_{R_1} = 0$, $L_{R_2} = 0$. The latter is possible because the aligned spin of the muons (opposite helicities) conserve the spin 1 of the resonance.
- $D^0 \to PP$: in this case it follows that $\lambda_{R_1} = \lambda_{R_2} = +1, 0, -1$ and $\lambda_{\mu^+} = -\lambda_{\mu^-}$. The minimum orbital angular momenta are $L_{D^0} = 0, 1, ...$, $L_{R_1} = 1$, $L_{R_2} = 0$.
- $D^0 \to DS$: in this case it follows that $\lambda_{R_1} = \lambda_{R_2} = 0$ and $\lambda_{\mu^+} = \lambda_{\mu^-}$. The minimum orbital angular momenta are $L_{D^0} = 2$, $L_{R_1} = 2$, $L_{R_2} = 0$.

- $D^0 \to DP$: in this case it follows that $\lambda_{R_1} = \lambda_{R_2} = +1, 0, -1$ and $\lambda_{\mu^+} = -\lambda_{\mu^-}$. The minimum orbital angular momenta are $L_{D^0} = 1, 2, ...$, $L_{R_1} = 2$, $L_{R_2} = 0$.

Second topology

Having built already the first topology, the reference frames for the second topology can be now defined already with a final convention, i.e. having already performed some convenient rotations with respect to a full general configuration. In order to be consistent with the previous topology, also in this case the x'' has been chosen to be the one from which the angle χ in the one between the decay planes, lying in the $\mu^+\mu^-$ plane as in the previous case. Let's consider the conventions as shown in Fig. D.3.

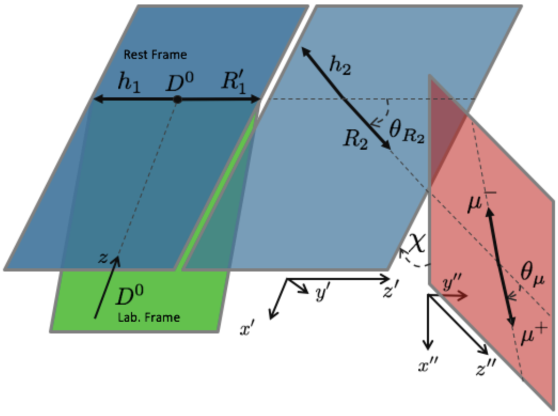

FIGURE D.3. Final reference frame conventions for the second decay topology.

In the laboratory frame, the D^0 momentum define the z axis of the first reference frame, along which a boost towards the D^0 rest frame is performed. The plane containing the z axis, the $\vec{p}_{R_1'}$ and $\vec{p}_{h_1}$ is the green one in Fig. D.3. It is important to note that, due to the rotational invariance of the D^0 angular distribution, a rotation of the xyz frame around the z axis can be performed so that the azimuthal angle $\phi_{R_1'} = 0$, i.e. $\vec{p}_{R_1}$ lyes in the zx plane, with a non null polar angle. In the D^0 rest frame, $\vec{p}_{R_1'}$ defines the z' axis of the second reference frame. Without loss of generality, a rotation around z' can be done in order to align the x' axis so that $\phi_{R_2} = 0$. Boosting along $\vec{p}_{R_1'}$ does not change the azimuthal angle, i.e. the R_1' daughters momenta remain in the same plane. It is worth noting that $\vec{p}_{R_2}$, $\vec{p}_{h_2}$ and $\vec{p}_{h1}$ lye on the same plane, both in D^0 rest frame and in R_1' rest frame. From the R_1' rest frame the Lorentz transformation to the R_2 rest frame can be done. While the z'' axis is fixed by $\vec{p}_{R_2}$, there is still the freedom to define the x'' axis. The more convenient choice is to define it such that $\phi_{\mu^+} = 0$, which is the same definition done in the first topology configuration. The angle between planes can be then evaluated in the R_2 rest frame from the x'' axis towards the D^0, or h_1, momentum projection.

For each decay there is an amplitude contribution in the helicity formalism:

- $D^0 \to R'_1 h_1$ decay:

$$\mathcal{H}^{D^0} = \sqrt{\frac{1}{4\pi}}\, D^{0\,*}_{M_{D^0},\,M'_{D^0}}(0,\theta_{R'_1},\gamma)\, A^{D^0}_{\lambda_{R'_1},\lambda_{h_1}} = \sqrt{\frac{1}{4\pi}}\, A^{D^0}_{\lambda_{R'_1},\lambda_{h_1}}, \tag{D.14}$$

where $M'_{D^0} = \lambda_{R'_1} - \lambda_{h_1} = \lambda_{R'_1}$, since it is calculated in the z' axis, and $\lambda_{h_1} = 0$ since it is a pion or a kaon. For the conservation of angular momentum $|\lambda_{R'_1}| \leq 0$. Then $\lambda_{R_1} = \lambda_{h_1} = 0$. The angle γ in the Wigner function is used to rotate the $x'y'z'$ frame and put $\phi_{R_2} = 0$. It is written only for completeness since the Wigner function is equal to 1, due to the rotational invariance.

- $R'_1 \to R_2\, h_2$ decay:

$$\begin{aligned}\mathcal{H}^{R'_1} &= \sqrt{\frac{2S_{R'_1}+1}{4\pi}}\, D^{S_{R'_1}\,*}_{M_{R'_1},\,M'_{R'_1}}(0,\theta_{R_2},\chi)\, A^{R'_1}_{\lambda_{R_2},\lambda_{h_2}}\, \mathcal{R}(m_{R_2\,h_2}) = \\ &= \sqrt{\frac{2S_{R'_1}+1}{4\pi}}\, D^{S_{R'_1}\,*}_{0,\lambda_{R_2}}(0,\theta_{R_2},\chi)\, A^{R'_1}_{\lambda_{R_2},0}\, \mathcal{R}(m_{R_2\,h_2}) = \\ &= \sqrt{\frac{2S_{R'_1}+1}{4\pi}}\, e^{+i\,\lambda_{R_2}\,\chi}\, d^{S_{R'_1}\,*}_{0,\lambda_{R_2}}(\theta_{R_2})\, A^{R'_1}_{\lambda_{R_2},0}\, \mathcal{R}(m_{R_2\,h_2}),\end{aligned} \tag{D.15}$$

where $M_{R'_1} = \lambda_{R'_1}$, but $\lambda_{R'_1} = 0$ from the previous decay for the angular momentum conservation, and $M'_{R_1} = \lambda_{R_2} - \lambda_{h_2} = \lambda_{R_2}$ since h_2 is a pion or a kaon. $\mathcal{R}(m_{R_2\,h_2})$ is the dynamical factor of the distribution on $m_{R_2\,h_2}$ spectrum. Since the only decay in this topology is $D^0 \to a^{\pm}(1260)\pi^{\mp}$ where $a^{\pm}(1260) \to \rho(\mu^+\mu^-)\pi^{\pm}$, we know that the spin $S_{R'_1}$ and S_{R_2} are always equal to 1.
Here an important remark is necessary. The χ angle occurs here in the Wigner function, in the third argument, in order to rotate properly the $x''y''z''$ reference frame and align the x'' axis along the $\vec{p}_{\mu^+}$ transverse projection. If the third argument of the Wigner function is set equal to zero at this step, which is a legitimate choice for the rotational alignment, the x'' axis would lye in the $x'z'$ plane and the exponential containing the angle χ will appear not in this formula but in the one of the next decay, $R_2 \to \mu^+\mu^-$. The exponential will be exactly the same, because the opposite sign resulting from the inversion of the angle direction cancels out with the sign introduced by the Wigner function, since χ will be in the first argument and not in the third one as in this case. The description is then equivalent.

- $R_2 \to \mu^+\mu^-$ decay:

$$\begin{aligned}\mathcal{H}^{R_2} &= \sqrt{\frac{2S_{R_2}+1}{4\pi}}\, D^{S_{R_2}*}_{M_{R_2},\,M'_{R_2}}(0,\theta_{\mu^+},0)\, A^{R_2}_{\lambda_{\mu^+},\lambda_{\mu^-}}\, \mathcal{R}(m_{\mu\mu}) = \\ &= \sqrt{\frac{2S_{R_2}+1}{4\pi}}\, D^{S_{R_2}*}_{\lambda_{R_2},\lambda_{\mu^+}-\lambda_{\mu^-}}(0,\theta_{\mu^+},0)\, A^{R_2}_{\lambda_{\mu^+},\lambda_{\mu^-}}\, \mathcal{R}(m_{\mu\mu}) = \\ &= \sqrt{\frac{2S_{R_2}+1}{4\pi}}\, d^{S_{R_2}*}_{\lambda_{R_2},\lambda_{\mu^+}-\lambda_{\mu^-}}(\theta_{\mu^+})\, A^{R_2}_{\lambda_{\mu^+},\lambda_{\mu^-}}\, \mathcal{R}(m_{\mu\mu}),\end{aligned} \tag{D.16}$$

where $M_{R_2} = \lambda_{R_2}$, and M'_{R_2} is the difference of the helicities of the two muons, since it is evaluated on an axis along $\vec{p}_{\mu^+}$ in the R_2 rest frame.

Building model for the second topology

Setting S_{R_2} and $S_{R'_1}$ equal to 1, the complete second topology model is built, similarly to the first one:

$$\begin{aligned}\mathcal{H}^{D^0\to R'_1 h_2}_{\lambda_{\mu^+},\lambda_{\mu^-}} &= \mathcal{N}'\, A^{R_2}_{\lambda_{\mu^+},\lambda_{\mu^-}}\;\, B'_{L_{D^0}}(p/p_0)^{L_{D^0}}\; \mathcal{R}^{R'_1}(m_{R'_1\,h_2})\; \mathcal{R}^{R_2}(m_{\mu\mu})\cdot \\ &\cdot\left(\sum_{\lambda_{R_2}} A^{R'_1}_{\lambda_{R_2},0}\, e^{+i\,\lambda_{R_2}\,\chi}\, d^1_{0,\lambda_{R_2}}(\theta_{R_2})\; d^1_{\lambda_{R_2},\lambda_{\mu^+}-\lambda_{\mu^-}}(\theta_{\mu^+})\right).\end{aligned} \tag{D.17}$$

The overall phase and magnitude of $A^{R_2}_{\lambda_{\mu^+},\lambda_{\mu^-}}$ can be reabsorbed for each contribution in the $A^{R'_1}_{\lambda_{R_2},0}$ coefficients, which are inside the coherent sum. So for each contribution the following fixing is performed, considering also the relation of conservation of parity:

$$A^{R_2}_{\lambda_{\mu^+},\lambda_{\mu^-}} = (1,0), \tag{D.18}$$

$$A^{R_2}_{-\lambda_{\mu^+},-\lambda_{\mu^-}} = (-\mathcal{P}(R_2)(-1)^{1-S_{R_2}},0), \tag{D.19}$$

but since $\mathcal{P}(R_2) = \mathcal{P}(\rho^0) = -1$ and $S_{R_2} = 1$ it follows that

$$A^{R_2}_{-\lambda_{\mu^+},-\lambda_{\mu^-}} = (1,0). \tag{D.20}$$

From the point of view of the implementation of the formula, the amplitude fit parameters can be merged to the angular distribution, while all the dymanics factors can be implemented separately.

Complete model - frames alignment

Is is important to remark that:

- the x'' axis is the one from which we compute the angle χ between the decay planes, and it lyes on the $\mu^+\mu^-$ plane, in particular along the μ^+ momentum transverse projection. This description is the same as in the first topology;
- the axis in which the muon helicity will be computed can be defined rotating the R_2 rest frame ($x''y''z''$) by the helicity angle θ_μ around y'', so that $z''' = \vec{p}_{\mu^+}$, in the same way done for the first topology. In this frame the $\vec{p}_{h_2}$ is lying in the plane $x'''z'''$.

The spin quantization axes between the first and second topology can be different, so there can be a mismatch of the helicity states between the two cases. In order to add the contributions together a proper alignment has to be performed to get consistent and comparable helicity

states. The helicity of the intermediate resonances, such as R_1, R_2 and R'_1, are not observable and a coherent sum over all the possibile helicity values has been done ($\lambda_{R_2} = +1, 0, -1$). In this case a difference between the spin quantization axes has no consequences after the coherent sum. The muons are instead final state particles and before adding the contributions coherently a rotation of the $|\lambda_\mu^{\{2\}}\rangle$ states towards $|\lambda_\mu^{\{1\}}\rangle$ ones must be done.
The z''' axis is the same in both cases because it is directed along $\vec{p}_{\mu^+} - \vec{p}_{\mu^-}$ direction. The x''' axis is instead different: there is an azimuthal angle α_μ between the two definitions, as shown in Fig. D.4

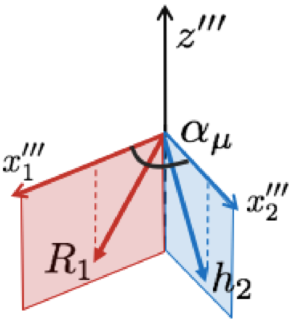

FIGURE D.4. R_2 rest frame with z''' aligned along $\vec{p}_{\mu^+}$, and the different x''' representations for the two topologies.

In order to calculate the α_μ it is important to note that in the first topology $\vec{p}_{R_1}$ lyes in the $x'''_1 z'''$ plane, while in the second topology the $\vec{p}_{h_2}$ lyes in the $x'''_2 z'''$ plane, so:

$$\cos(\alpha_\mu) = \frac{\vec{a}_{R_1} \cdot \vec{a}_{h_2}}{|\vec{a}_{R_1}||\vec{a}_{h_2}|}, \tag{D.21}$$

$$\sin(\alpha_\mu) = \frac{(\vec{p}_{\mu^+} \times \vec{a}_{R_1}) \cdot \vec{a}_{h_2}}{|\vec{p}_{\mu^+}||\vec{a}_{R_1}||\vec{a}_{h_2}|} \tag{D.22}$$

The same derivation is described in [302] (Eqs. (20)-(22)) in which there are analogous terms to the ones discussed here. The rotation is then:

$$|\lambda_\mu^{\{2\}}\rangle \to e^{i\Delta\lambda_\mu \alpha_\mu} |\lambda_\mu^{\{2\}}\rangle, \tag{D.23}$$

where $\Delta\lambda_\mu = \lambda_{\mu^+} - \lambda_{\mu^-}$.

The complete final model is:

$$\mathcal{S} = \sum_{\lambda_{\mu^+}, \lambda_{\mu^-} = \pm 1/2} \left| \sum_j \left[\sum_{\lambda_R} \mathcal{H}^{D^0 \to R_1 R_2}_{\lambda_{\mu^+}, \lambda_{\mu^-}} \right]_j + \sum_k \left[\sum_{\lambda_{R_2}} e^{i\Delta\lambda_\mu \alpha_\mu} \mathcal{H}^{D^0 \to R'_1 h_2}_{\lambda_{\mu^+}, \lambda_{\mu^-}} \right]_k \right|^2, \tag{D.24}$$

where the sums in j and k refer to possible different resonances that contribute to the first and second topology respectively, while the sum in λ_μ is incoherent since the muons helicities are measurable and identify states that do not interfere.

List of Tables

1.1 List of SM elementary particles with their mass, spin, interactions (W stands for weak, S for strong and EM for electromagnetic), year and place of first direct observation. 3
1.2 Branching fractions of $D^0 \to \pi^+\pi^-\mu^+\mu^-$ (top) and $D^0 \to K^+K^-\mu^+\mu^-$ (bottom) decays in different intervals of di-muon mass [190]. The uncertainties are respectively statistical, systematic and due to the limited knowledge of the normalization branching fraction. . . . 29

2.1 Muon stations in which hits are required for a positive `IsMuon` decision, as a function of the momentum. 60

3.1 Values for average TID, hadrons and 1 MeV neutrons equivalent fluence for the different interesting regions in all the four stations. 95
3.2 Summary of the fluence and dose values integrated during the proton irradiation test. . . 102
3.3 Final cross section results, averaged between the two tests, for all the nSYNC functional blocks. The estimation of the expected events per day and in 10 years of upgrade operation are shown. The normalised cross sections per bit are also showed. 109

4.1 List of simulated samples used in the analysis and the corresponding statistics at generator level. 125
4.2 L0Muon_PT requirements applied offline on data. 128
4.3 Trigger fiducial cuts applied on 2016 data sample. 129
4.4 Stripping selection requirements. 131
4.5 Mass ranges for $m(D^0)$ and ΔM on data. 133
4.6 Definition of the di-muon mass binning scheme used in the analysis. 134
4.7 Effective sample size for $D^0 \to K^+K^-\mu^+\mu^-$ and $D^0 \to \pi^+\pi^-\mu^+\mu^-$ after the reweighting procedure. 145
4.8 Effective weighted yields as result of the ML fit on the D^0 mass spectrum for fully selected Run II $D^0 \to \pi^+\pi^-\mu^+\mu^-$ and $D^0 \to K^+K^-\mu^+\mu^-$. 151
4.9 Raw yields not efficiency corrected as result of the ML fit on the D^0 mass spectrum for fully selected Run II $D^0 \to \pi^+\pi^-\mu^+\mu^-$ and $D^0 \to K^+K^-\mu^+\mu^-$. 152
4.10 Raw expected precision on asymmetry measurements in each di-muon mass bin for the fully selected Run II candidates of $D^0 \to \pi^+\pi^-\mu^+\mu^-$ and $D^0 \to K^+K^-\mu^+\mu^-$. 153

5.1 List of possible decay topologies for the $D^0 \to \pi^+\pi^-\mu^+\mu^-$ decay. 157
5.2 Resonances that can contribute to $D^0 \to \pi^+\pi^-\mu^+\mu^-$ and $D^0 \to K^+K-\mu^+\mu^-$. 158
5.3 List of amplitude contributions simulated in the amplitude model. 158

B.1 TCKs and thresholds for the main L0 and Hlt1 lines in 2016. 179
B.2 TCKs and thresholds for the main L0 and Hlt1 lines in 2015. 180
B.3 TCKs and thresholds for the main L0 and Hlt1 lines in 2017. 180
B.4 TCKs and thresholds for the main L0 and Hlt1 lines in 2018. 180

Table **Page**

List of Figures

1.1 Feynman diagrams of $K^0 \to W^+W^-$ contributing to the $K^0 \to \mu^+\mu^-$ decay, from [49]. . . 8

1.2 Examples of Feynman diagrams describing a SD contribution (left) and a LD contribution (right), mediated by two π^0 mesons, to the $D^0 - \overline{D}^0$ mixing. Diagrams taken from [114]. . 13

1.3 Example of Feynman diagrams for current-current operators, in particular $\mathcal{O}_1$ (left) and one possible diagram with QCD correction $\mathcal{O}_2$ (right). 21

1.4 Example of Feynman diagrams for QCD penguin operators (right) and electroweak penguin operators (left), for which $\mathcal{O}^{QED}_{3,...,6}$ are a particular case. 22

1.5 Example of Feynman diagrams for the semileptonic penguin (left) and box (right) operators. 23

1.6 Example of two Feynman diagrams showing a SD penguin contribution to the $D^0 \to \pi^+\pi^-\mu^+\mu^-$ decay (left), and a diagram representing a LD contribution via the ρ^0 meson decaying in two muons (right). 28

1.7 Differential branching fraction (modified from [168]) of $D^0 \to \pi^+\pi^-\mu^+\mu^-$ (left) and $D^0 \to K^+K^-\mu^+\mu^-$ (right) as a function of q^2, considering different models to highlight the theoretical uncertainties on the strong phases. The Cappiello et al. model refers to the theoretical model used in [165]. 28

1.8 Scheme showing the angles chosen to parametrise the $D^0 \to h^+h^-\mu^+\mu^-$ phase space. . . . 30

1.9 The observable $\langle I_6 \rangle$ as a function of q^2 for some NP models which have primed $C'_{9,10}$ Wilson coefficients, or same of order of magnitude between SM C_9 and C_{10}. A relative strong phase of π between ρ^0 and ω mesons is assumed. 32

2.1 The CERN accelerator complex [209]. 36

2.2 Simulation of polar angles distribution of the produced $b\bar{b}$ pairs at $\sqrt{s} = 14$ TeV. The LHCb acceptance is highlighted in red. 37

2.3 Scheme of the vertical section of the LHCb detector. 38

2.4 Drawing of the LHCb magnet (left) and the magnetic field along the z axis (right). 39

2.5 Scheme of the VELO layout, with R sensors in blue and Φ sensors in red. A representation of the two conditions of VELO fully closed and fully open is also shown (bottom). 41

2.6 Left: view of the TT detector with the readout electronics in blue and the other readout sectors. Right: View of the TT module with three readout sections. 42

2.7 Left: scheme of the tracking system, with the OT (light blue), the beam pipe (brown) and the ST (violet). Right: section of a straw-tube in an OT module. 43

2.8 Schematic side view of the RICH-1 (left) and RICH-2 (right) detectors. 44

2.9 Left: Cherenkov angle versus particle momentum [221]. Right: a typical LHCb event in RICH-1 with Cherenkov rings interpolation. 44

2.10 Schematic representation of the separation between photons, electrons and hadrons within the calorimeter system. 46

2.11 Illustrations of the ECAL cell (left) and HCAL cell (right) structures. 46

2.12 Side (left) and front (right) view of the LHCb Muon System. The R1-R4 projective scaling is also represented. 47

2.13 Left: schematic representation of a section of a four gap MWPC. Right: schematic drawing of the triple-GEM detectors, with the GEM foils, gas gaps and their corresponding dimensions. 48

2.14 Left: front view of one top quadrant of stations M2-M3 showing the x and y logical strips per region, and the corresponding sectors. Right: example of mixed readout adopted in R1-R2 regions of M2-M3, in particular the case M2R1 is shown here. The logical pad (in black) is obtained by the coincidence between crossing vertical wire pads and cathode pads. 49

2.15 Scheme of the readout and control electronics chain of the LHCb Muon System. 51

2.16 The LHCb trigger schemes for Run I (left) and Run II (right). 54

2.17 The LHCb trigger schemes for Run I (left) and Run II (right). 58

2.18 Trigger scheme for Run III in the LHCb experiment. 63

2.19 Expected trigger yields for different decays of B mesons, as a function of the instantaneous luminosity. 63

2.20 Schematic representation of the GBT chipset, with the optical link, the GBTx chip, the GBT-SCA and the GBT-FPGA. 64

2.21 The 120 bits of the GBT frame and the internal division as foreseen by the GBT protocol. 64

2.22 Schematic complete view of the readout architecture. In the yellow box on the left the data path is represented, from the FE to the storage, through the TELL40 boards. The FE electronics receives both the fast and slow commands from the SOL40 board, which is indeed interfaced to the SODIN and the ECS. The communication between the boards is implemented with the GBT chipset, while communication between boards and host PCs is done by PCIe buses. 65

2.23 Side view of the upgraded LHCb experiment. 67

2.24 Schematic drawing of the extra shielding foreseen behind HCAL and around the beam pipe. 68

2.25 Schematic view of the muon readout architecture. In the yellow box on the left the data path is represented, from the CARDIAC boards, to the TELL40 boards, through the nODE boards. The nODE receives both the fast and slow commands from the SOL40 board, while the CARIDIAC boards are pulsed or configured through the nPDM and nSB, which communicate theirselves with the SOL40 boards, from which fast and slow commands can be received. 69
2.26 Schematic view of the nSYNC architecture and its interface with the GBT chipset. 71
2.27 The 112 bits of the nSYNC frame and its inclusion in the GBT frame in wide-bus mode, i.e. using the FEC bits space as a payload extension. 72
2.28 Schematic structure of the nODE boards with all the components. 72

3.1 Top view of the nSYNC test PCB. 76
3.2 DCO calibration curve showing the calibrated DCO code values as a function of TDC resolution. The different colours represent the 48 channels. 77
3.3 DCO calibration curve showing the calibrated DCO code values as a function of channel number. The different colours represent the 25 possible resolutions, from 8 to 32. 78
3.4 Left: the 48 channels average counts per bin is shown, after sending 10 synchronous input signals every 10 ps to each channel, scanning the 25 ns time interval. The wrong clock cycle association is affecting the first and last bin. Right: example of the eye diagram of a single channel, acquired sending a Pseudo Random Binary Sequence on the output lines is shown. 79
3.5 Schematic representation of the MiniDAQ_1 setup, with the AMC40 and AMC_TP boards. The PC is connected through the local Gigabit Ethernet (GbE) to the COM express module, which is able to instruct properly the FE interface of the FPGA, reading and writing its memory. Another 10 GbE connects the PC and the Tx/Rx minipods in order to access directly the data at TELL40 stage. 81
3.6 Schematic view of the nSYNC chain test. The nSYNC test board is connected to the I^{2}C bus of the GBT-SCA chip, present on the VLDB board (through the I^{2}C level shifter).The master GBTx of the VLDB is connected through the optical fibre to the AMC40 optical interface. 82
3.7 Picture of the first nODE prototypes, with the main components highlighted. 83
3.8 Picture of the first connection between the nODE prototype and the MiniDAQ system, similarly to Fig. 3.5 in which the role of FE is done by the nODE board. 84
3.9 WinCC main panel of the software developed to test the nODE and nSYNC functionalities within the MiniDAQ control system. For each nSYNC the main configuration registers can be accessed, with a special space for low level I^{2}C communication. The main commands like calibration, reset and TFC emulation can be easily sent, while another space is dedicated to the monitoring (TDC calibrated DCO values, histograms content, error counters, etc.). . . 86
3.10 Picture of atomic displacement on Si crystal by an energetic PKA. The PKA has a typical range of 100 nm at 50 keV. Figure taken from [276]. 89

3.11 Scheme of the charge build-up mechanism under radiation, in which the effect of tunneling near the Si interface is visible. Figure taken from [276]. 90

3.12 Scheme of e-h creation due to a ion passing through the device. The corresponding current pulse with the fast and slow components is shown on the right. Figure taken and modified from [276]. 92

3.13 Left: a schematic view of the LHCb detector and the approximative positions of the nODE racks near M2, where the radiation levels are more important. Right: Output of the FLUKA simulations for TID, measured in Gy/collision, with the interesting regions highlighted in dark red. 94

3.14 Output of the FLUKA simulations for hadrons fluence, measured in hadrons per collision per cm^2, in the interesting regions near each station. 94

3.15 Left: Schematic view of the LNS complex, with the beam line for the CATANA test room highlighted in red. Right: Lateral beam profile without collimator. 96

3.16 Probability per unit of flux to deposit an energy equal or larger than E_{dep} in the sensitive volume, as a function of E_{dep}, for a typical LHC environment (CMS tracker) and using a 60 MeV proton beam. Plot taken from [278]. 97

3.17 Scheme of the experimental setup connections. 98

3.18 Scheme of the 5 states FSM of the DAQ software. After the power ON, the FSM goes into the IDLE state in which the main hardware components are not yet initialised. If they initialise correctly the status becomes READY to launch the run. 99

3.19 Scheme of the sequential procedure of the acquisition loop. The TDC calibration and the download of the histograms can be disabled or activated periodically when needed. The final logic for error handling is used in the FSM logic to decide if staying in the running status. 100

3.20 Picture of the main front panel of the DAQ software. 100

3.21 Left: picture of the final experimental setup within the CATANA room, in particular the nSYNC test board and the oscilloscope are shown. Right: The main control PC, the two power supplies and the various connections are shown. 101

3.22 Picture of the nSYNC test board in front of the beam collimator. The I^{2}C bus, the power connections and the probes for the PLL and LVDS drivers are highlighted. 101

3.23 Displacement damage as a function of energy for neutrons, protons, pions and electrons. The Y axis was rescaled to represent the relative damage with respect to 1 MeV neutrons. 102

3.24 Current consumption on the I/O ring (left) and the chip core (right) for the first chip tested, covering the whole irradiation test. The increasing trend is not visible at this scale, except in the last run. The intermediate step is due to a different frame pattern on the LVDS output, which causes a natural greater current consumption. 103

3.25 Current consumption on the I/O ring for the first chip tested during the first run (left) and the last run (right). In the last run, after the irradiation stops, some fluctuations of the current are present due to changes in the internal functionalities, related to the communication with the chip. After that, a decreasing current trend of the annealing is clearly observed. 104

3.26 Left: PLL jitter as measured by the oscilloscope before, during and after the irradiation test. A slight increase in the jitter of ~ 2 ps is clearly evident. Right: output LVDS jitter measured by the oscilloscope before, during and after the irradiation test. Maximum fluctuations of order of ~ 4 ps are present but no particular trend was observed. 104

3.27 Left: DCO control word as a function of chosen resolution for the channel n.0 of the first nSYNC tested. Right: DCO control word as a function of the channel number at the nominal resolution for the first nSYNC tested. Each curve is obtained for different TID. The curve corresponding to a TID of 0 Gy is slightly at lower DCO values with respect to the other curves, however this trend is within the dithering correction and it is considered negligible. 105

3.28 DCO control word as a function of chosen resolution, for the channel n.31 of the first nSYNC tested. Each curve is obtained for different TID. The curve corresponding to a TID of 0 Gy is slightly at lower DCO values with respect to the other curves, however this trend is within the dithering correction and it is considered negligible for the TDC functionality. . 106

3.29 Number of SEU in the TDC not-protected registers (left) and the not-protected histogram registers (right). The plot and cross sections shown refer to the first chip tested. 107

3.30 Number of bit-flips as a function of all the bins (3 bytes wide) for all the 48 histograms, for the first chip tested for a proton fluence of $1.09 \cdot 10^{12}$. The bins are ordered in a sequential way, starting from channel 0. No holes or blocks of channels more vulnerable than others are observed. 107

3.31 Number of detected SEU in the EDAC protected registers (left) and the TMR protected configuration registers (right). The plot and cross sections shown refer to the first chip tested. 108

3.32 Left: the safety shielded enclosure with the X-Ray tube and the moving system inside. Right: picture of the X-Ray tube and the moving system. 110

3.33 Picture of the nSYNC package and the exposed die after the decapsulation. 111

3.34 Measured X-Ray spectrum, with the three peaks used to perform the energy calibration. . 112

3.35 Comparison between the measured X-Ray spectrum (blue), the one corrected for the detector efficiency only (red) and the one with also the air absorption correction (green). 113

3.36 Comparison between the simulated Al-filtered X-Ray spectrum (blue) and the measured one (red), for 104 μm thick Al filter (left) and 208 μm thick (right). In the latter case the spectrum is highlu hardened, being the low energy peaks reduced by an order of magnitude. 113

3.37 Left: average dose rate, in Gy/s, in the Si-PIN detector as a function of the X-Ray tube current, for different Al filter thicknesses. Right: average dose rate, in Gy/s, as a function of the distance from the tube, for different Al filter thicknesses. 115

3.38 Maximum local estimated dose rate, in Gy/s, as a function of the depth in silicon, in μm, for different Al filters. A 100 μ thick Al filter is able to reduce the local dose rate at the surface by an order of magnitude, and in the bulk (at 150 μm) by a factor ~ 2. 116

3.39 Left: picture of the nSYNC test board mounted in front of the X-Ray tube at a distance of 25 mm. Right: picture of the nSYNC test board with the radiochromic film above the chip package, used for alignment purpose. The dark X-Ray spot on the film is visible. 117

3.40 Current for the I/O ring (left) and the chip core (right), for the test on the first chip. One equivalent LHCb upgrade is highlighted in orange. The nSYNC was at 25 mm far from the X-Ray source and a 100 μm thick Al filter was used. 117

3.41 Current for the I/O ring (left) and the chip core (right), for the test on the second chip. One equivalent LHCb upgrade is highlated in orange. The nSYNC was at 25 mm far from the source and a 100 μm thick Al filter was used. 118

3.42 Current increment in the I/O nSYNC, in percentage, with respect to the dose rate. The first two points refer to the protons irradiation test, the last one refers to the X-Ray test, in which a wider range was observed (2-4%). A 10% of dose rate uncertainty was taken into account. 119

4.1 Scatter plot of the $\log(\chi^2_{\text{IP}}(\mu_1))$ with respect to $p_{\text{T}}(\mu_1)$ before the `TrackMuonMVA` fiducial cut (left) and after the fiducial cut (right), for the 2016 $D^0 \to \pi^+\pi^-\mu^+\mu^-$ data sample after the stripping selection and with only `TrackMuonMVA_TOS` on μ_1 required. 129

4.2 Distribution of $p_{\text{T}}(\mu_1)$ before the `TrackMuon` fiducial cut (left) and after the fiducial cut (right), for the 2016 $D^0 \to \pi^+\pi^-\mu^+\mu^-$ data sample after the stripping selection and with only `TrackMuon_TOS` on μ_1 required. 130

4.3 Normalised χ^2_{IP} distributions for 2017 $D^0 \to \pi^+\pi^-\mu^+\mu^-$ candidates, from MC sample (blue) and data right sideband (red) defined by $m(D^0) > 1890\,\text{MeV}/c^2$, after the trigger, preselection and ΔM cut. 132

4.4 Raw asymmetry $A = (N_{\pi^+} - N_{\pi^-})/(N_{\pi^+} + N_{\pi^-})$ for $D^0 \to \pi^+\pi^-\mu^+\mu^-$ candidates in Run II *MagDown* MC sample, as a function of the soft pion p_x and p_z, before the fiducial cuts (left) and after the fiducial cuts (right). 135

4.5 Raw asymmetry for $D^0 \to \pi^+\pi^-\mu^+\mu^-$ candidates in Run II *MagDown* MC sample, as a function of the soft pion p_x and p_z with the condition $|p_y/p_z| < 0.02$, before the fiducial cuts (left) and after the fiducial cuts (right). 136

4.6 Distribution of ΔM (top) and D^0 invariant mass (bottom) for $D^0 \to \pi^+\pi^-\mu^+\mu^-$ (left) and $D^0 \to K^+K^-\mu^+\mu^-$ candidates (right) after the trigger, preselection and soft pion fiducial cuts requirements, except for the ΔM cut. 137

4.7 Left: ROC curve of the BDT classifier trained on even data samples for $D^0 \to \pi^+\pi^-\mu^+\mu^-$. Right: BDT distributions for the signal (blue) and background samples (red) and comparison between the ones for the training samples (points) and test samples (bars). 139

4.8 Left: ROC curve of the BDT classifier trained on even data samples for $D^0 \to K^+K^-\mu^+\mu^-$. Right: BDT distributions for the signal (blue) and background samples (red) and comparison between the ones for the training samples (points) and test samples (bars). 139

4.9 Distributions of the BDT input variables for signal (blue) and combinatorial background (red) for the $D^0 \to \pi^+\pi^-\mu^+\mu^-$ sample. 140

4.10 Scan of the uncertainty on the raw asymmetry on a randomly tagged sample in the two dimensional space of minimum BDT and ProbNNmu requirements for $D^0 \to \pi^+\pi^-\mu^+\mu^-$ (left) and $D^0 \to K^+K^-\mu^+\mu^-$ Run II data. 141

4.11 Output distributions of the BDT reweighter for $D^0 \to \pi^+\pi^-\mu^+\mu^-$ sample (left) and $D^0 \to K^+K^-\mu^+\mu^-$ (right) for simulated events at generator level (red) and fully selected (blue). The bottom panels show the ratio between the number of events of the two samples in each BDT bin, thus it is the inverse of the efficiency. 142

4.12 Efficiency variation as a function of the phase space variables for $D^0 \to K^+K^-\mu^+\mu^-$ candidates. 143

4.13 Efficiency variation as a function of the phase space variables for $D^0 \to \pi^+\pi^-\mu^+\mu^-$ candidates.143

4.14 Phase-space distributions of simulated $D^0 \to \pi^+\pi^-\mu^+\mu^-$ candidates at generator level (red) and fully selected and efficiency corrected (blue). The bottom panels show the ratio between the two distributions. 144

4.15 Phase-space distributions of simulated $D^0 \to K^+K^-\mu^+\mu^-$ candidates at generator level (red) and fully selected and efficiency corrected (blue). The bottom panels show the ratio between the two distributions. 145

4.16 Fit to the D^0 mass distribution of simulated $D^0 \to \pi^+\pi^-\mu^+\mu^-$ (left) and $D^0 \to K^+K^-\mu^+\mu^-$ (right) candidates after the full selection. 147

4.17 Fit to the D^0 mass distribution of data samples of hadronic $D^0 \to \pi^+\pi^-\pi^+\pi^-$ (left) and $D^0 \to K^+K^-\pi^+\pi^-$ (right) decays after the selection, where two oppositely charged pions have muon mass assigned and one of those has also muon PID requirements on `ProbNN`μ. . 148

4.18 Fit to the D^0 mass distribution of data samples of $D^0 \to \pi^+\pi^-\mu^+\mu^-$ (left) and $D^0 \to K^+K^-\mu^+\mu^-$ (right) decays in ΔM sideband. 149

4.19 D^0 mass distributions and fit overlaid, for fully selected Run II $D^0 \to \pi^+\pi^-\mu^+\mu^-$ and $D^0 \to K^+K^-\mu^+\mu^-$ integrated in $m(\mu\mu)$. 150

4.20 D^0 mass distributions and fit overlaid, for fully selected Run II $D^0 \to \pi^+\pi^-\mu^+\mu^-$ in $m(\mu^+\mu^-)$ bins. The fits on the full ρ/ω and ϕ bins are reported. 150

4.21 D^0 mass distributions and fit overlaid, for fully selected Run II $D^0 \to K^+K^-\mu^+\mu^-$ in $m(\mu^+\mu^-)$ bins. 151

5.1 Distributions of $m(\mu^+\mu^-)$ vs. $m(\pi^+\pi^-)$ (left) and the relative projections (two plots on the right) after the sPlot background subtraction for the fully selected Run II $D^0 \to \pi^+\pi^-\mu^+\mu^-$.164

5.2 Distributions of $m(\mu^+\mu^-)$ vs. $m(K^+K^-)$ (left) and the relative projections (two plots on the right) after the sPlot background subtraction for the fully selected Run II $D^0 \to K^+K^-\mu^+\mu^-$.164

5.3 Distributions of $m(\pi^+\pi^-)$, $m(\mu^+\mu^-)$, $\cos\theta_\mu$ and ϕ (from left to right respectively) of the simulated $D^0 \to \pi^+\pi^-\mu^+\mu^-$ amplitude model. 164

5.4 Distributions of $m(K^+K^-)$, $m(\mu^+\mu^-)$, $\cos\theta_\mu$ and ϕ (from left to right respectively) of the simulated $D^0 \to K^+K^-\mu^+\mu^-$ amplitude model. 165

5.5 Example of angular fit, integrated $m(\mu^+\mu^-)$, on ϕ and $\cos\theta_{\mu^+}$ observables in case of an high statistics $D^0 \to \pi^+\pi^-\mu^+\mu^-$ simulated sample using the amplitude model. 167

5.6 Pull distributions of the fitted angular coefficients for the $D^0 \to \pi^+\pi^-\mu^+\mu^-$ decay, integrated in $m(\mu^+\mu^-)$ and with the observed Run II nominal signal and background yields. 169

5.7 Bias of the fitted angular coefficients for the $D^0 \to \pi^+\pi^-\mu^+\mu^-$ decay, in each $m(\mu^+\mu^-)$ region, with the observed Run II nominal signal and background yields. 169

5.8 Bias of the fitted angular coefficients for the $D^0 \to \pi^+\pi^-\mu^+\mu^-$ decay, integrated in $m(\mu^+\mu^-)$ spectrum, as a function of the background fraction sampled in each pseudoexperiment. The nominal background fraction as observed in data is equal to 1. 170

5.9 Fitted coefficients $I_{5,\ldots,9}$ with and without the bias correction, as a function of $m(\mu^+\mu^-)$ for the $D^0 \to \pi^+\pi^-\mu^+\mu^-$ sample. 171

5.10 Fitted coefficients $I_{5,\ldots,9}$ with and without the bias correction, as a function of $m(\mu^+\mu^-)$ for the $D^0 \to \pi^+\pi^-\mu^+\mu^-$ sample. 172

A.1 Schematic representation of the variable $\cos\theta_\mu$ for $\overline{D}^0$ (left) and D^0 (right). Modified from [300]. 176

A.2 Schematic representation of the variable $\cos\theta_h$ for $\overline{D}^0$ (left) and D^0 (right). Modified from [300]. 176

A.3 Schematic representation of the angle ϕ for $\overline{D}^0$ (left) and D^0 (right). Modified from [300]. 177

D.1 Preliminary reference frame conventions for the first decay topology. 186

D.2 Final reference frame conventions for the first decay topology. 187

D.3 Final reference frame conventions for the second decay topology. 191

D.4 R_2 rest frame with z''' aligned along $\vec{p}_{\mu^+}$, and the different x''' representations for the two topologies. 194

Figure **Page**

[

	QCD	quantum chromodynamics
	SM	Standard Model
	NP	New Physics
	CP	Charge-Parity
	VEV	vacuum expectation value
	CKM	Cabibbo-Kobayashi-Maskawa
	FCNC	flavour changing neutral current
	WWA	Weisskopf-Wigner approximation
	GIM	Glashow, Iliopoulos, Maiani
	LD	long distance
	SD	short distance
	OPE	Operator Product Expansion
	LLA	leading-logarithms approximation
	NLL	next-to-leading-logarithms
	NNLO	next-to-next-to-leading-order
	VDM	Vector Meson Dominance
	BSM	beyond Standard Model
	LHCb	Large Hadron Collider beauty
	LHC	Large Hadron Collider
	CERN	European Organization for Nuclear Research
Acronyms]Acronyms	PS	Proton Synchroton
	SPS	Super Proton Synchroton
	VELO	Vertex Locator
	RICH	Ring Imaging CHerenkov detector
	TT	Tracker Turicensis
	ST	Silicon Tracker
	IT	Inner Tracker
	OT	Outer Tracker
	ECAL	electromagnetic calorimeter
	HCAL	hadronic calorimeter
	MIP	Minimum Ionizing particle
	MWPC	Multi-Wire Proportional Chamber
	GEM	Gas Electron Multiplier
	FEB	Front-End Board
	CARDIAC	Carioca-Dialog card
	ASD	amplifier-shaper-discrimination
	IB	Intermediate Board
	TDC	Time to digital converter
	ODE	Off Detector Electronics
	nODE	new Off Detector Electronics
	TFC	Timing and Fast Control

TTCrx	Timing, Trigger and Control Receiver
FIFO	First In First Out
DAQ	Data Acquisition
SB	Service Board
nSB	new Service Board
PDM	Pulse Distribution Module
nPDM	new Pulse Distribution Module
ELMBs	Embedded Local Monitoring Board
I^{2}C	Inter Integrated Circuit
TCK	Trigger Configuration Key
HLT	High Level Trigger
TIS	Trigger Independent of Signal
TOS	Trigger On Signal
DLL	delta-log-likelihood
FPGA	Field Programmable Gate Array
COTS	Commercial Off-the-Shelf
JTAG	Joint Test Action Group
SPI	Serial Peripheral Interface
ECS	Experiment Control System
SciFi	Scintillating Fiber tracker
UT	Upstream Tracker
GIF	Gamma Irradiation Facility
DCO	Digitally Controlled Oscillator
FSM	Finite State Machine
BXID	bunch-crossing identification number
LVDS	Low-voltage differential signaling
PLL	Phase-locked loop
PRBS	Pseudo Random Binary Sequence
COM	computer-on-module
DIM	Distributed Information Management
RPC	Remote Procedure Call
VLDB	Versatile Link Demo Board
BER	bit error ratio
NIEL	non-ionising energy loss
TID	Total Ionising Dose
SEU	Single Event Upset
SEL	Single Event Latch-up
TMR	Triple Modular Redundancy
EDAC	Error Detection And Correction
SEM	Secondary Emission Monitor
GPIB	General Purpose Interface Bus
ZIF	Zero Insertion Force
PV	primary vertex
SV	secondary vertex
CF	Cabibbo-favoured

SCS	singly Cabibbo-suppressed
DCS	doubly Cabibbo-suppressed
MC	Monte Carlo
PDF	probability density function
MVA	multivariate analysis
BDT	boosted decision tree
KDE	kernel density estimate
IP	impact parameter
DIRA	direction angle
DLL	delta-log-likelihood
PID	particle identification

REFERENCES

[1] LHCb, R. Aaij *et al.*, *Angular analysis of the $B^0 \to K^{*0}\mu^+\mu^-$ decay using 3 fb^{-1} of integrated luminosity*, JHEP **02** (2016) 104, `arXiv:1512.04442`. ↪ cited on page iv

[2] Belle, S. Wehle *et al.*, *Lepton-Flavor-Dependent Angular Analysis of $B \to K^*\ell^+\ell^-$*, Phys. Rev. Lett. **118** (2017), no. 11 111801, `arXiv:1612.05014`. ↪ cited on page iv

[3] ATLAS, M. Aaboud *et al.*, *Angular analysis of $B_d^0 \to K^*\mu^+\mu^-$ decays in pp collisions at $\sqrt{s} = 8$ TeV with the ATLAS detector*, JHEP **10** (2018) 047, `arXiv:1805.04000`. ↪ cited on page iv

[4] S. L. Glashow, *Partial-symmetries of weak interactions*, Nuclear Physics **22** (1961), no. 4 579 . ↪ cited on page 2

[5] S. Weinberg, *A Model of Leptons*, Phys. Rev. Lett. **19** (1967) 1264. ↪ [see prev. ref.]

[6] A. Salam, *Weak and Electromagnetic Interactions*, Conf. Proc. **C680519** (1968) 367. ↪ [see prev. ref.]

[7] G. Altarelli, *The Standard model of particle physics*, `arXiv:hep-ph/0510281`. ↪ [see prev. ref.]

[8] M. E. Peskin and D. V. Schroeder, *An Introduction to Quantum Field Theory*, Addison-Wesley, Reading, USA, 1995. ↪ cited on page 2

[9] E. P. Wigner, *On Unitary Representations of the Inhomogeneous Lorentz Group*, Annals Math. **40** (1939) 149, [Reprint: Nucl. Phys. Proc. Suppl.6,9(1989)]. ↪ cited on page 2

[10] P. W. Higgs, *Broken Symmetries and the Masses of Gauge Bosons*, Phys. Rev. Lett. **13** (1964) 508. ↪ cited on pages 2, 4

[11] F. Englert and R. Brout, *Broken Symmetry and the Mass of Gauge Vector Mesons*, Phys. Rev. Lett. **13** (1964) 321. ↪ [see prev. ref.]

[12] G. S. Guralnik, C. R. Hagen, and T. W. B. Kibble, *Global Conservation Laws and Massless Particles*, Phys. Rev. Lett. **13** (1964) 585. ↪ cited on pages 2, 4

[13] Particle Data Group, M. Tanabashi *et al.*, *Review of Particle Physics*, Phys. Rev. D **98** (2018) 030001. ↪ cited on pages 2, 7, 10, 122, 157, 162

[14] G. A. et al, *Observation of a new particle in the search for the Standard Model Higgs boson with the ATLAS detector at the LHC*, Physics Letters B **716** (2012), no. 1 1 . ↪ cited on page 3

[15] A. H. Compton, *A Quantum Theory of the Scattering of X-rays by Light Elements*, Phys. Rev. **21** (1923) 483. ↪ cited on page 3

[16] UA1 collaboration, G. Arnison and others, *Experimental observation of isolated large transverse energy electrons with associated missing energy at $\sqrt{s}$=540 GeV*, Phys. Lett. **B 122** (1983), no. 1, 103. ↪ cited on page 3

[17] UA1 collaboration, G. Arnison *et al.*, *Experimental observation of lepton pairs of invariant mass around 95 GeV/c^2 at the CERN SPS collider*, Physics Letters **B 126** (1983), no. 5, 398. ↪ cited on page 3

[18] Pluto, C. Berger *et al.*, *Observation of a Narrow Resonance Formed in e^+ e^- annihilation at 9.46*

GeV, Phys. Lett. **76B** (1978) 243. ↪ cited on page 3

[19] J. J. Thomson, *Cathode Rays*, Philosophical Magazine **44** (1897) 293. ↪ cited on page 3

[20] J. C. Street and E. C. Stevenson, *New Evidence for the Existence of a Particle of Mass Intermediate Between the Proton and Electron*, Phys. Rev. **52** (1937) 1003. ↪ cited on page 3

[21] M. L. Perl *et al.*, *Evidence for Anomalous Lepton Production in* $e^+ - e^-$ *annihilation*, Phys. Rev. Lett. **35** (1975) 1489. ↪ cited on page 3

[22] C. L. Cowan *et al.*, *Detection of the free neutrino: A Confirmation*, Science **124** (1956) 103. ↪ cited on page 3

[23] G. Danby *et al.*, *Observation of High-Energy Neutrino Reactions and the Existence of Two Kinds of Neutrinos*, Phys. Rev. Lett. **9** (1962) 36. ↪ cited on page 3

[24] K. Kodama *et al.*, *Observation of tau neutrino interactions*, Physics Letters B **504** (2001), no. 3 218 . ↪ cited on page 3

[25] E. D. Bloom *et al.*, *High-Energy Inelastic* $e - p$ *Scattering at* 6° *and* 10°, Phys. Rev. Lett. **23** (1969) 930. ↪ cited on page 3

[26] M. Breidenbach *et al.*, *Observed Behavior of Highly Inelastic Electron-Proton Scattering*, Phys. Rev. Lett. **23** (1969) 935. ↪ cited on page 3

[27] J. J. Aubert *et al.*, *Experimental Observation of a Heavy Particle* J, Phys. Rev. Lett. **33** (1974) 1404. ↪ cited on pages 3, 7, 17

[28] J.-E. Augustin *et al.*, *Discovery of a Narrow Resonance in* e^+e^- *Annihilation*, Phys. Rev. Lett. **33** (1974) 1406. ↪ cited on pages 3, 7, 17

[29] S. W. Herb *et al.*, *Observation of a Dimuon Resonance at 9.5 GeV in 400-GeV Proton-Nucleus Collisions*, Phys. Rev. Lett. **39** (1977) 252. ↪ cited on page 3

[30] D0 Collaboration, S. Abachi *et al.*, *Search for High Mass Top Quark Production in* $p\overline{p}$ *Collisions at* $\sqrt{s} = 1.8$ *TeV*, Phys. Rev. Lett. **74** (1995) 2422. ↪ cited on page 3

[31] CDF Collaboration, F. Abe *et al.*, *Observation of Top Quark Production in* $\overline{p}p$ *Collisions with the Collider Detector at Fermilab*, Phys. Rev. Lett. **74** (1995) 2626. ↪ cited on page 3

[32] M. Kobayashi and T. Maskawa, *CP-Violation in the Renormalizable Theory of Weak Interaction*, Progress of Theoretical Physics **49** (1973) 652, `arXiv:http://oup.prod.sis.lan/ptp/article-pdf/49/2/652/5257692/49-2-652.pdf`. ↪ cited on page 5

[33] N. Cabibbo, *Unitary Symmetry and Leptonic Decays*, Phys. Rev. Lett. **10** (1963) 531. ↪ cited on page 5

[34] M. Gell-Mann, *A Schematic Model of Baryons and Mesons*, Phys. Lett. **8** (1964) 214. ↪ cited on page 6

[35] G. Zweig, *An SU(3) model for strong interaction symmetry and its breaking. Version 2*, pp. 22–101. 1964. ↪ cited on page 6

[36] H. Foeth *et al.*, *Search for* $K_L \to \mu^+\mu^-$ *and* $K_L \to e^+e^-$ *decays*, Phys. Lett. **30B** (1969) 282. ↪ cited on page 6

[37] M. Bott-Bodenhausen *et al.*, *Search for decay of neutral kaons into charged lepton pairs*, Physics Letters B **24** (1967), no. 4 194 . ↪ cited on page 6

[38] N. Cabibbo, *Unitary Symmetry and Leptonic Decays*, Phys. Rev. Lett. **10** (1963) 531, [,648(1963)]. ↪ cited on page 6

[39] M. Kobayashi and T. Maskawa, *CP Violation in the Renormalizable Theory of Weak Interaction*, Prog. Theor. Phys. **49** (1973) 652. ↪ cited on page 6

[40] J. H. Christenson, J. W. Cronin, V. L. Fitch, and R. Turlay, *Evidence for the 2π Decay of the K_2^0 Meson*, Phys. Rev. Lett. **13** (1964) 138. ↪ cited on pages 6, 16

[41] L. Wolfenstein, *Parametrization of the Kobayashi-Maskawa Matrix*, Phys. Rev. Lett. **51** (1983) 1945. ↪ cited on page 7

[42] S. Descotes-Genon and P. Koppenburg, *The CKM Parameters*, Ann. Rev. Nucl. Part. Sci. **67** (2017) 97, `arXiv:1702.08834`. ↪ cited on page 7

[43] J. Charles *et al.*, *CP violation and the CKM matrix: assessing the impact of the asymmetric B factories*, The European Physical Journal C - Particles and Fields **41** (2005) 1. ↪ [see prev. ref.]

[44] G. Eigen, G. Dubois-Felsmann, D. G. Hitlin, and F. C. Porter, *Global CKM Fits with the Scan Method*, Phys. Rev. **D89** (2014), no. 3 033004, `arXiv:1301.5867`. ↪ [see prev. ref.]

[45] A. Hocker, H. Lacker, S. Laplace, and F. Le Diberder, *A New approach to a global fit of the CKM matrix*, Eur. Phys. J. **C21** (2001) 225, `arXiv:hep-ph/0104062`. ↪ [see prev. ref.]

[46] M. Ciuchini *et al.*, *2000 CKM triangle analysis: A Critical review with updated experimental inputs and theoretical parameters*, JHEP **07** (2001) 013, `arXiv:hep-ph/0012308`. ↪ cited on page 7

[47] S. L. Glashow, J. Iliopoulos, and L. Maiani, *Weak Interactions with Lepton-Hadron Symmetry*, Phys. Rev. D **2** (1970) 1285. ↪ cited on page 7

[48] L. Maiani, *The GIM Mechanism: origin, predictions and recent uses*, in *Proceedings, 48th Rencontres de Moriond on Electroweak Interactions and Unified Theories: La Thuile, Italy, March 2-9, 2013*, pp. 3–16, 2013. `arXiv:1303.6154`. ↪ cited on page 8

[49] E. Leader and E. Predazzi, *An Introduction to gauge theories and modern particle physics. Vol. 1: Electroweak interactions, the new particles and the parton model*, vol. 3, Cambridge University Press, 2011. ↪ cited on pages 8, 197

[50] E. Aprile, *The Xenon1T Dark Matter Search Experiment*, in *Sources and Detection of Dark Matter and Dark Energy in the Universe* (D. Cline, ed.), (Dordrecht), pp. 93–96, Springer Netherlands, 2013. ↪ cited on page 9

[51] E. Aprile *et al.*, *Physics reach of the XENON1T dark matter experiment*, Journal of Cosmology and Astroparticle Physics **2016** (2016) 027. ↪ cited on page 9

[52] C. E. Aalseth *et al.*, *DarkSide-20k: A 20 tonne two-phase LAr TPC for direct dark matter detection at LNGS*, The European Physical Journal Plus **133** (2018) 131. ↪ cited on page 9

[53] P. Agnes *et al.*, *First results from the DarkSide-50 dark matter experiment at Laboratori Nazionali del Gran Sasso*, Physics Letters B **743** (2015) 456 . ↪ cited on page 9

[54] ATLAS, A. Airapetian *et al.*, *ATLAS: Detector and physics performance technical design report. Volume 2*, . ↪ cited on page 9

[55] CMS, S. Chatrchyan *et al.*, *The CMS Experiment at the CERN LHC*, JINST **3** (2008) S08004. ↪ cited on page 9

[56] O. S. Bruning *et al.*, *LHC Design Report*, . ↪ cited on page 9

[57] M. Klasen, M. Pohl, and G. Sigl, *Indirect and direct search for dark matter*, Progress in Particle and Nuclear Physics **85** (2015) 1 . ↪ cited on page 9

[58] N. Prantzos *et al.*, *The 511 keV emission from positron annihilation in the Galaxy*, Rev. Mod. Phys. **83** (2011) 1001. ↪ cited on page 9

[59] G. Isidori and F. Teubert, *Status of indirect searches for New Physics with heavy flavour decays after the initial LHC run*, Eur. Phys. J. Plus **129** (2014), no. 3 40, `arXiv:1402.2844`. ↪ cited on page 9

[60] F. Mahmoudi, *Indirect search for New Physics: complementarity to direct searches*, in *25th*

Rencontres de Blois on Particle Physics and Cosmology Blois, France, May 26-31, 2013, 2013. `arXiv:1310.2556`. ↪ cited on page 9

[61] V. C. Rubin, N. Thonnard, and W. K. Ford, Jr. *Rotational properties of 21 SC galaxies with a large range of luminosities and radii, from NGC 4605 /R = 4kpc/ to UGC 2885 /R = 122 kpc/*, Astrophys. J. **238** (1980) 471. ↪ cited on page 9

[62] K. G. Begeman, A. H. Broeils, and R. H. Sanders, *Extended rotation curves of spiral galaxies: dark haloes and modified dynamics*, Monthly Notices of the Royal Astronomical Society **249** (1991) 523, `arXiv:http://oup.prod.sis.lan/mnras/article-pdf/249/3/523/18160929/mnras249-0523.pdf`. ↪ cited on page 9

[63] M. Bartelmann and P. Schneider, *Weak gravitational lensing*, Physics Reports **340** (2001), no. 4 291 . ↪ cited on page 9

[64] G. Bertone, D. Hooper, and J. Silk, *Particle dark matter: Evidence, candidates and constraints*, Phys. Rept. **405** (2005) 279, `arXiv:hep-ph/0404175`. ↪ cited on page 9

[65] S. Scopel, *Particle dark matter candidates*, J. Phys. Conf. Ser. **120** (2008) 042003, `arXiv:0711.2870`. ↪ [see prev. ref.]

[66] L. Bergstrom, *Dark Matter Candidates*, New J. Phys. **11** (2009) 105006, `arXiv:0903.4849`. ↪ [see prev. ref.]

[67] L. Roszkowski, E. M. Sessolo, and S. Trojanowski, *WIMP dark matter candidates and searches-current status and future prospects*, Rept. Prog. Phys. **81** (2018), no. 6 066201, `arXiv:1707.06277`. ↪ [see prev. ref.]

[68] J. S. Sidhu, R. J. Scherrer, and G. Starkman, *Death by Dark Matter*, `arXiv:1907.06674`. ↪ cited on page 9

[69] F. S. N. Lobo, *The Dark side of gravity: Modified theories of gravity*, `arXiv:0807.1640`. ↪ cited on page 9

[70] S. Capozziello and M. Francaviglia, *Extended Theories of Gravity and their Cosmological and Astrophysical Applications*, Gen. Rel. Grav. **40** (2008) 357, `arXiv:0706.1146`. ↪ [see prev. ref.]

[71] J. A. R. Cembranos, *Modified gravity and dark matter*, J. Phys. Conf. Ser. **718** (2016), no. 3 032004, `arXiv:1512.08752`. ↪ cited on page 9

[72] G. 't Hooft, *Naturalness, chiral symmetry, and spontaneous chiral symmetry breaking*, NATO Sci. Ser. B **59** (1980) 135. ↪ cited on page 10

[73] Y. Hamada, H. Kawai, and K.-y. Oda, *Bare Higgs mass and potential at ultraviolet cutoff*, in *Proceedings, 1st Toyama International Workshop on Higgs as a Probe of New Physics 2013 (HPNP2013): Toyama, Japan, February 13-16, 2013*, 2013. `arXiv:1305.7055`. ↪ cited on page 10

[74] M. Holthausen, K. S. Lim, and M. Lindner, *Planck scale Boundary Conditions and the Higgs Mass*, JHEP **02** (2012) 037, `arXiv:1112.2415`. ↪ [see prev. ref.]

[75] F. Bezrukov, M. Yu. Kalmykov, B. A. Kniehl, and M. Shaposhnikov, *Higgs Boson Mass and New Physics*, JHEP **10** (2012) 140, `arXiv:1205.2893`, [,275(2012)]. ↪ [see prev. ref.]

[76] I. Masina, *Higgs boson and top quark masses as tests of electroweak vacuum stability*, Phys. Rev. **D87** (2013), no. 5 053001, `arXiv:1209.0393`. ↪ [see prev. ref.]

[77] G. Degrassi *et al.*, *Higgs mass and vacuum stability in the Standard Model at NNLO*, JHEP **08** (2012) 098, `arXiv:1205.6497`. ↪ cited on page 10

[78] S. P. Martin, *A Supersymmetry primer*, `arXiv:hep-ph/9709356arXiv:hep-ph/9709356`, [Adv. Ser. Direct. High Energy Phys.18,1(1998)]. ↪ cited on pages 10, 25

[79] H. Baer, V. Barger, P. Huang, and X. Tata, *Natural Supersymmetry: LHC, dark matter and ILC searches*, JHEP **05** (2012) 109, `arXiv:1203.5539`. ↪ cited on pages 10, 25

[80] M. Schmaltz and D. Tucker-Smith, *Little Higgs review*, Ann. Rev. Nucl. Part. Sci. **55** (2005) 229, `arXiv:hep-ph/0502182`. ↪ cited on pages 10, 26

[81] L. Randall and R. Sundrum, *A Large mass hierarchy from a small extra dimension*, Phys. Rev. Lett. **83** (1999) 3370, `arXiv:hep-ph/9905221`. ↪ cited on pages 10, 26

[82] L. Randall and R. Sundrum, *An Alternative to compactification*, Phys. Rev. Lett. **83** (1999) 4690, `arXiv:hep-th/9906064`. ↪ cited on pages 10, 26

[83] I. Doršner *et al.*, *Physics of leptoquarks in precision experiments and at particle colliders*, Phys. Rept. **641** (2016) 1, `arXiv:1603.04993`. ↪ cited on pages 10, 26

[84] W. Buchmuller, R. Ruckl, and D. Wyler, *Leptoquarks in Lepton - Quark Collisions*, Phys. Lett. **B191** (1987) 442, [Erratum: Phys. Lett.B448,320(1999)]. ↪ cited on pages 10, 26

[85] T. Blake *et al.*, *Round table: Flavour anomalies in $b \to sl^+l^-$ processes*, EPJ Web Conf. **137** (2017) 01001. ↪ cited on page 10

[86] Z.-z. Xing, *Quark Mass Hierarchy and Flavor Mixing Puzzles*, Int. J. Mod. Phys. **A29** (2014) 1430067, `arXiv:1411.2713`. ↪ cited on page 10

[87] F. Feruglio, *Pieces of the Flavour Puzzle*, Eur. Phys. J. **C75** (2015), no. 8 373, `arXiv:1503.04071`. ↪ cited on page 10

[88] Super-Kamiokande Collaboration, Y. Fukuda, T. Hayakawa *et al.*, *Evidence for Oscillation of Atmospheric Neutrinos*, Phys. Rev. Lett. **81** (1998) 1562. ↪ cited on page 10

[89] SNO Collaboration, Q. R. Ahmad *et al.*, *Measurement of the Rate of $\nu_e + d \to p + p + e^-$ Interactions Produced by ^8B Solar Neutrinos at the Sudbury Neutrino Observatory*, Phys. Rev. Lett. **87** (2001) 071301. ↪ cited on page 10

[90] A. Kusenko, *Sterile neutrinos: The Dark side of the light fermions*, Phys. Rept. **481** (2009) 1, `arXiv:0906.2968`. ↪ cited on page 10

[91] C. Giunti and C. W. Kim, *Fundamentals of Neutrino Physics and Astrophysics*, 2007. ↪ cited on page 10

[92] R. N. Mohapatra and G. Senjanović, *Neutrino Mass and Spontaneous Parity Nonconservation*, Phys. Rev. Lett. **44** (1980) 912. ↪ cited on page 10

[93] P. Minkowski, *$\mu \to e\gamma$ at a Rate of One Out of 10^9 Muon Decays?*, Phys. Lett. **67B** (1977) 421. ↪ cited on page 10

[94] G. Steigman, *Observational tests of antimatter cosmologies*, Ann. Rev. Astron. Astrophys. **14** (1976) 339. ↪ cited on page 10

[95] M. Dine and A. Kusenko, *The Origin of the matter - antimatter asymmetry*, Rev. Mod. Phys. **76** (2003) 1, `arXiv:hep-ph/0303065`. ↪ cited on pages 10, 11

[96] A. D. Sakharov, *Violation of CP Invariance, C asymmetry, and baryon asymmetry of the universe*, Pisma Zh. Eksp. Teor. Fiz. **5** (1967) 32, [Usp. Fiz. Nauk161,no.5,61(1991)]. ↪ cited on page 10

[97] G. R. Farrar and M. E. Shaposhnikov, *Baryon asymmetry of the universe in the standard electroweak theory*, Phys. Rev. **D50** (1994) 774, `arXiv:hep-ph/9305275`. ↪ cited on page 11

[98] P. Huet and E. Sather, *Electroweak baryogenesis and standard model CP violation*, Phys. Rev. **D51** (1995) 379, `arXiv:hep-ph/9404302`. ↪ [see prev. ref.]

[99] M. B. Gavela, M. Lozano, J. Orloff, and O. Pene, *Standard model CP violation and baryon asymmetry. Part 1: Zero temperature*, Nucl. Phys. **B430** (1994) 345, `arXiv:hep-ph/9406288`.

↪ cited on page 11

[100] J. A. Harvey and M. S. Turner, *Cosmological baryon and lepton number in the presence of electroweak fermion-number violation*, Phys. Rev. D **42** (1990) 3344. ↪ cited on page 11

[101] V. A. Kuzmin, V. A. Rubakov, and M. E. Shaposhnikov, *On anomalous electroweak baryon-number non-conservation in the early universe*, Physics Letters B **155** (1985), no. 1 36 . ↪ [see prev. ref.]

[102] F. R. Klinkhamer and N. S. Manton, *A saddle-point solution in the Weinberg-Salam theory*, Phys. Rev. D **30** (1984) 2212. ↪ cited on page 11

[103] D. Baumann, P. J. Steinhardt, and N. Turok, *Primordial Black Hole Baryogenesis*, `arXiv:hep-th/0703250`. ↪ cited on page 11

[104] S. W. Hawking, *Black hole explosions*, Nature **248** (1974) 30. ↪ [see prev. ref.]

[105] B. J. Carr, *Some cosmological consequences of primordial black-hole evaporations*, Astrophys. J. **206** (1976) 8. ↪ cited on page 11

[106] C. Caprini and D. G. Figueroa, *Cosmological Backgrounds of Gravitational Waves*, Class. Quant. Grav. **35** (2018), no. 16 163001, `arXiv:1801.04268`. ↪ cited on page 11

[107] V. Weisskopf and E. P. Wigner, *Calculation of the natural brightness of spectral lines on the basis of Dirac's theory*, Z. Phys. **63** (1930) 54. ↪ cited on page 11

[108] V. Weisskopf and E. Wigner, *Over the natural line width in the radiation of the harmonius oscillator*, Z. Phys. **65** (1930) 18. ↪ cited on page 11

[109] S. Bianco, F. L. Fabbri, D. Benson, and I. Bigi, *A Cicerone for the physics of charm*, Riv. Nuovo Cim. **26N7** (2003) 1, `arXiv:hep-ex/0309021`. ↪ cited on pages 11, 17

[110] T. Ohl, G. Ricciardi, and E. H. Simmons, *D-$\bar{D}$ mixing in heavy quark effective field theory: The Sequel*, Nucl. Phys. **B403** (1993) 605, `arXiv:hep-ph/9301212`. ↪ cited on page 13

[111] I. I. Y. Bigi and N. G. Uraltsev, *D^0-$\bar{D}^0$ oscillations as a probe of quark hadron duality*, Nucl. Phys. **B592** (2001) 92, `arXiv:hep-ph/0005089`. ↪ [see prev. ref.]

[112] A. F. Falk *et al.*, *The D^0-$\bar{D}^0$ mass difference from a dispersion relation*, Phys. Rev. **D69** (2004) 114021, `arXiv:hep-ph/0402204`. ↪ [see prev. ref.]

[113] A. F. Falk, Y. Grossman, Z. Ligeti, and A. A. Petrov, *SU(3) breaking and D^0-$\bar{D}^0$ mixing*, Phys. Rev. **D65** (2002) 054034, `arXiv:hep-ph/0110317`. ↪ cited on page 13

[114] A. Di Canto, *Measurement of CP–Violating Asymmetries in $D^0 \to \pi^+\pi^-$ and $D^0 \to K^+K^-$ Decays at CDF*, PhD thesis, Pisa U., 2012-04, doi: 10.2172/1248346. ↪ cited on pages 13, 197

[115] M. S. Sozzi, *Discrete symmetries and CP violation: From experiment to theory*, 2008. ↪ cited on page 13

[116] G. C. Branco, L. Lavoura, and J. P. Silva, *CP Violation*, Int. Ser. Monogr. Phys. **103** (1999) 1. ↪ cited on pages 13, 15, 19

[117] BaBar, B. Aubert *et al.*, *Observation of CP violation in the B^0 meson system*, Phys. Rev. Lett. **87** (2001) 091801, `arXiv:hep-ex/0107013`. ↪ cited on page 16

[118] Belle, K. Abe *et al.*, *Observation of large CP violation in the neutral B meson system*, Phys. Rev. Lett. **87** (2001) 091802, `arXiv:hep-ex/0107061`. ↪ cited on page 16

[119] BABAR Collaboration, B. Aubert *et al.*, *Direct CP Violating Asymmetry in $B^0 \to K^+\pi^-$ Decays*, Phys. Rev. Lett. **93** (2004) 131801. ↪ cited on page 16

[120] Belle, Y. Chao *et al.*, *Evidence for direct CP violation in $B^0 \to K^+pi^-$ decays*, Phys. Rev. Lett. **93** (2004) 191802, `arXiv:hep-ex/0408100`. ↪ [see prev. ref.]

[121] Belle, A. Poluektov *et al.*, *Evidence for direct CP violation in the decay $B^\pm \to D^{(*)}K^\pm$*

, $D \to K_s^0\pi^+\pi^-$ and measurement of the CKM phase ϕ_3, Phys. Rev. **D81** (2010) 112002, `arXiv:1003.3360`. ↪ [see prev. ref.]

[122] BaBar, P. del Amo Sanchez *et al.*, *Measurement of CP observables in $B^{+-} - > D_{CP}K^{+-}$ decays and constraints on the CKM angle γ*, Phys. Rev. **D82** (2010) 072004, `arXiv:1007.0504`. ↪ [see prev. ref.]

[123] LHCb, R. Aaij *et al.*, *Observation of CP violation in $B^\pm \to DK^\pm$ decays*, Phys. Lett. **B712** (2012) 203, `arXiv:1203.3662`, [Erratum: Phys. Lett.B713,351(2012)]. ↪ [see prev. ref.]

[124] LHCb, R. Aaij *et al.*, *First observation of CP violation in the decays of B_s^0 mesons*, Phys. Rev. Lett. **110** (2013), no. 22 221601, `arXiv:1304.6173`. ↪ cited on page 16

[125] LHCb, R. Aaij *et al.*, *Observation of CP Violation in Charm Decays*, Phys. Rev. Lett. **122** (2019), no. 21 211803, `arXiv:1903.08726`. ↪ cited on page 17

[126] S. Müller, U. Nierste, and S. Schacht, *Sum Rules of Charm CP Asymmetries beyond the $SU(3)_F$ Limit*, Phys. Rev. Lett. **115** (2015), no. 25 251802, `arXiv:1506.04121`. ↪ cited on page 17

[127] D. Pirtskhalava and P. Uttayarat, *CP Violation and Flavor SU(3) Breaking in D-meson Decays*, Phys. Lett. **B712** (2012) 81, `arXiv:1112.5451`. ↪ cited on page 17

[128] J. Prentki and J. Steinberger, eds., *W.K.H.Panofsky in Proceedings, 14th International Conference on High-Energy Physics (ICHEP 68)*, (Geneva), CERN, CERN, 1968. ↪ cited on page 17

[129] NA1 Collaboration, S. R. Amendolia *et al.*, *λ_c photoproduction and lifetime measurement*, Z. Phys. C **36** (1987) 513. ↪ cited on page 17

[130] CDF, W. Ashmanskas *et al.*, *Silicon vertex tracker: A Fast precise tracking trigger for CDF*, Nucl. Instrum. Meth. **A447** (2000) 218. ↪ cited on page 17

[131] M. Suzuki, *Fragmentation of Hadrons from Heavy Quark Partons*, Phys. Lett. **71B** (1977) 139. ↪ cited on page 17

[132] J. D. Bjorken, *Properties of Hadron Distributions in Reactions Containing Very Heavy Quarks*, Phys. Rev. **D17** (1978) 171. ↪ [see prev. ref.]

[133] A. Chodos *et al.*, *A New Extended Model of Hadrons*, Phys. Rev. **D9** (1974) 3471. ↪ [see prev. ref.]

[134] A. H. Hoang, *Heavy quarkonium dynamics*, `arXiv:hep-ph/0204299arXiv:hep-ph/0204299`. ↪ [see prev. ref.]

[135] G. 't Hooft, *A Two-Dimensional Model for Mesons*, Nucl. Phys. **B75** (1974) 461. ↪ [see prev. ref.]

[136] L. Lellouch, *Phenomenology from lattice QCD*, Nucl. Phys. Proc. Suppl. **117** (2003) 127, `arXiv:hep-ph/0211359`, [,127(2002)]. ↪ [see prev. ref.]

[137] S. M. Ryan, *Heavy quark physics from lattice QCD*, Nucl. Phys. Proc. Suppl. **106** (2002) 86, `arXiv:hep-lat/0111010`. ↪ [see prev. ref.]

[138] HPQCD, UKQCD, MILC, Fermilab Lattice, C. T. H. Davies *et al.*, *High precision lattice QCD confronts experiment*, Phys. Rev. Lett. **92** (2004) 022001, `arXiv:hep-lat/0304004`. ↪ [see prev. ref.]

[139] M. A. Shifman, A. I. Vainshtein, and V. I. Zakharov, *QCD and Resonance Physics. Theoretical Foundations*, Nucl. Phys. **B147** (1979) 385. ↪ [see prev. ref.]

[140] M. A. Shifman, A. I. Vainshtein, and V. I. Zakharov, *QCD and Resonance Physics: Applications*, Nucl. Phys. **B147** (1979) 448. ↪ [see prev. ref.]

[141] I. I. Y. Bigi *et al.*, *The Pole mass of the heavy quark. Perturbation theory and beyond*, Phys. Rev. **D50** (1994) 2234, `arXiv:hep-ph/9402360`. ↪ [see prev. ref.]

[142] M. Beneke and V. M. Braun, *Heavy quark effective theory beyond perturbation theory: Renormalons, the pole mass and the residual mass term*, Nucl. Phys. **B426** (1994) 301, `arXiv:hep-ph/9402364`.

↪ cited on page 17

[143] I. I. Bigi and A. I. Sanda, *CP violation*, , [Camb. Monogr. Part. Phys. Nucl. Phys. Cosmol.9,1(2009)]. ↪ cited on page 17

[144] S. de Boer, *Probing the standard model with rare charm decays. PhD Thesis*, PhD thesis, Technische Universität Dortmund, 2017-08. ↪ cited on pages 17, 20, 24

[145] A. Paul, I. I. Bigi, and S. Recksiegel, *On $D \to X_u l^+ l^-$ within the Standard Model and Frameworks like the Littlest Higgs Model with T Parity*, Phys. Rev. **D83** (2011) 114006, `arXiv:1101.6053`. ↪ cited on pages 17, 23, 26

[146] T. Mannel, *Effective Field Theories in Flavor Physics*, Springer Tracts Mod. Phys. **203** (2004) 1. ↪ cited on pages 18, 20

[147] M. Neubert, *Effective field theory and heavy quark physics*, in *Physics in $D \geq 4$. Proceedings, Theoretical Advanced Study Institute in elementary particle physics, TASI 2004, Boulder, USA, June 6-July 2, 2004*, pp. 149–194, 2005. `arXiv:hep-ph/0512222`. ↪ cited on page 18

[148] K. G. Wilson, *The renormalization group and critical phenomena*, Rev. Mod. Phys. **55** (1983) 583. ↪ cited on page 18

[149] K. G. Wilson, *Non-Lagrangian Models of Current Algebra*, Phys. Rev. **179** (1969) 1499. ↪ cited on page 18

[150] T. Appelquist and J. Carazzone, *Infrared singularities and massive fields*, Phys. Rev. D **11** (1975) 2856. ↪ cited on page 18

[151] J. F. Donoghue, E. Golowich, and B. R. Holstein, *Dynamics of the standard model*, Camb. Monogr. Part. Phys. Nucl. Phys. Cosmol. **2** (1992) 1, [Camb. Monogr. Part. Phys. Nucl. Phys. Cosmol.35(2014)]. ↪ cited on page 18

[152] T. Muta, *Foundations of quantum chromodynamics. Second edition*, World Sci. Lect. Notes Phys. **57** (1998) 1. ↪ cited on page 18

[153] M. Neubert, in *Theory of Exclusive Hadronic B Decays*, D. Blaschke, M. A. Ivanov, and T. Mannel, eds., pp. 3–41, Springer Berlin Heidelberg, Berlin, Heidelberg, 2004. ↪ cited on pages 18, 19

[154] T. Feldmann, B. Müller, and D. Seidel, *$D \to \rho \ell^+ \ell^-$ decays in the QCD factorization approach*, JHEP **08** (2017) 105, `arXiv:1705.05891`. ↪ cited on page 19

[155] G. Buchalla, A. J. Buras, and M. E. Lautenbacher, *Weak decays beyond leading logarithms*, Rev. Mod. Phys. **68** (1996) 1125, `arXiv:hep-ph/9512380`. ↪ cited on page 19

[156] G. Buchalla, *Heavy quark theory*, in *Heavy flavor physics: Theory and experimental results in heavy quark physics and CP violation. Proceedings, 55th Scottish Universities Summer School in Physics, SUSSP 2001, St. Andrews, UK, August 7-23, 2001*, pp. 57–104, 2002. `arXiv:hep-ph/0202092`. ↪ cited on page 20

[157] G. Burdman, E. Golowich, J. L. Hewett, and S. Pakvasa, *Rare charm decays in the standard model and beyond*, Phys. Rev. **D66** (2002) 014009, `arXiv:hep-ph/0112235`. ↪ cited on pages 21, 23, 25, 26, 157, 162

[158] S. Fajfer, P. Singer, and J. Zupan, *The radiative leptonic decays $D^0 \to e^+e^-\gamma, \mu^+\mu^-\gamma$ in the standard model and beyond*, The European Physical Journal C - Particles and Fields **27** (2003) 201. ↪ [see prev. ref.]

[159] K. G. Chetyrkin, M. Misiak, and M. Munz, *Weak radiative B meson decay beyond leading logarithms*, Phys. Lett. **B400** (1997) 206, `arXiv:hep-ph/9612313`, [Erratum: Phys. Lett.B425,414(1998)]. ↪ [see prev. ref.]

[160] C. Bobeth, M. Misiak, and J. Urban, *Photonic penguins at two loops and m_t dependence of $BR[B \to X_s l^+ l^-]$*, Nucl. Phys. **B574** (2000) 291, `arXiv:hep-ph/9910220`. ↪ [see prev. ref.]

[161] P. Gambino, M. Gorbahn, and U. Haisch, *Anomalous dimension matrix for radiative and rare semileptonic B decays up to three loops*, Nucl. Phys. **B673** (2003) 238, `arXiv:hep-ph/0306079`. ↪ [see prev. ref.]

[162] S. de Boer, B. Müller, and D. Seidel, *Higher-order Wilson coefficients for $c \to u$ transitions in the standard model*, JHEP **08** (2016) 091, `arXiv:1606.05521`. ↪ cited on page 21

[163] F. Halzen and A. D. Martin, *Quarks and Leptons: an introductory course in Modern Particle Physics*, 1984. ↪ cited on page 22

[164] M. Benayoun, H. B. O'Connell, and A. G. Williams, *Vector meson dominance and the ρ meson*, Phys. Rev. **D59** (1999) 074020, `arXiv:hep-ph/9807537`. ↪ cited on page 23

[165] L. Cappiello, O. Cata, and G. D'Ambrosio, *Standard Model prediction and new physics tests for $D^0 \to h^+ h^- \ell^+ \ell^- (h = \pi, K : \ell = e, \mu)$*, JHEP **04** (2013) 135, `arXiv:1209.4235`. ↪ cited on pages 23, 26, 27, 28, 197

[166] S. Fajfer, S. Prelovsek, and P. Singer, *Rare charm meson decays $D \to P \ell^+ \ell^-$ and $c \to u \ell^+ \ell^-$ in SM and MSSM*, Phys. Rev. **D64** (2001) 114009, `arXiv:hep-ph/0106333`. ↪ cited on pages 23, 26

[167] G. Burdman and I. Shipsey, *D^0 - $\bar{D}^0$ mixing and rare charm decays*, Ann. Rev. Nucl. Part. Sci. **53** (2003) 431, `arXiv:hep-ph/0310076`. ↪ cited on page 23

[168] S. De Boer and G. Hiller, *Null tests from angular distributions in $D \to P_1 P_2 l^+ l^-$, $l = e, \mu$ decays on and off peak*, Phys. Rev. **D98** (2018), no. 3 035041, `arXiv:1805.08516`. ↪ cited on pages 24, 27, 28, 30, 31, 32, 157, 165, 173, 177, 197

[169] S. de Boer and G. Hiller, *Flavor and new physics opportunities with rare charm decays into leptons*, Phys. Rev. **D93** (2016), no. 7 074001, `arXiv:1510.00311`. ↪ cited on pages 24, 25, 26, 33

[170] E. Golowich, J. Hewett, S. Pakvasa, and A. A. Petrov, *Relating D^0–$\overline{D}^0$ mixing and $D^0 \to l^+ l^-$ with new physics*, Phys. Rev. D **79** (2009) 114030. ↪ [see prev. ref.]

[171] A. Paul, I. I. Bigi, and S. Recksiegel, *$D^0 \to \gamma\gamma$ and $D^0 \to \mu^+ \mu^-$ rates on an unlikely impact of the littlest Higgs model with T parity*, Phys. Rev. D **82** (2010) 094006. ↪ [see prev. ref.]

[172] R.-M. Wang *et al.*, *Decays $D^+_{(s)} \to \pi(K)^+ \ell^+ \ell^-$ and $D^0 \to \ell^+ \ell^-$ in the MSSM with and without R-parity*, Int. J. Mod. Phys. **A30** (2015), no. 12 1550063, `arXiv:1409.0181`. ↪ cited on page 26

[173] S. Fajfer and N. Košnik, *Prospects of discovering new physics in rare charm decays*, Eur. Phys. J. **C75** (2015), no. 12 567, `arXiv:1510.00965`. ↪ cited on pages 25, 26

[174] A. Khodjamirian, T. Mannel, and A. A. Petrov, *Direct probes of flavor-changing neutral currents in e^+ e^--collisions*, JHEP **11** (2015) 142, `arXiv:1509.07123`. ↪ cited on page 25

[175] E. Solodov, *CMD-3, SND experiments at VEPP2000*, 54th Rencontres de Moriond, QCD and High Energy Interactions (2019). ↪ cited on page 25

[176] B. Khazin, *Physics and detectors for VEPP-2000*, Nucl. Phys. Proc. Suppl. **181-182** (2008) 376. ↪ cited on page 25

[177] S. De Boer, *Charm decays*, PoS **BEAUTY2018** (2018) 022, `arXiv:1807.05845`. ↪ cited on page 25

[178] S. Fajfer, N. Košnik, and S. c. v. Prelovšek, *Updated constraints on new physics in rare charm decays*, Phys. Rev. D **76** (2007) 074010. ↪ cited on page 26

[179] S. Fajfer and S. Prelovsek, *Effects of littlest Higgs model in rare D meson decays*, Phys. Rev. **D73** (2006) 054026, `arXiv:hep-ph/0511048`. ↪ cited on page 26

[180] S. Fajfer and S. Prelovsek, *Search for new physics in rare D decays*, Conf. Proc. **C060726** (2006)

811, `arXiv:hep-ph/0610032`, [,811(2006)]. ↪ cited on page 26

[181] I. I. Bigi and A. Paul, *On CP Asymmetries in Two-, Three- and Four-Body D Decays*, JHEP **03** (2012) 021, `arXiv:1110.2862`. ↪ cited on page 26

[182] S. Fajfer and N. Kosnik, *Leptoquarks in FCNC charm decays*, Phys. Rev. **D79** (2009) 017502, `arXiv:0810.4858`. ↪ cited on page 26

[183] S. Sahoo and R. Mohanta, *New physics effects in charm meson decays involving* $c \to u l^+ l^- (l_i^\mp l_j^\pm)$ *transitions*, Eur. Phys. J. **C77** (2017), no. 5 344, `arXiv:1705.02251`. ↪ cited on page 26

[184] X.-D. Guo *et al.*, *Looking for New Physics via Semi-leptonic and Leptonic rare decays of* D *and* D_s, Chin. Phys. **C41** (2017), no. 9 093107, `arXiv:1703.08799`. ↪ cited on page 26

[185] C. Delaunay, J. F. Kamenik, G. Perez, and L. Randall, *Charming CP Violation and Dipole Operators from RS Flavor Anarchy*, JHEP **01** (2013) 027, `arXiv:1207.0474`. ↪ cited on page 26

[186] A. Paul, A. De La Puente, and I. I. Bigi, *Manifestations of warped extra dimension in rare charm decays and asymmetries*, Phys. Rev. **D90** (2014), no. 1 014035, `arXiv:1212.4849`. ↪ cited on page 26

[187] E791, E. M. Aitala *et al.*, *Search for rare and forbidden charm meson decays* $D^0 \to V\ell^+\ell^-$ *and* $hh\ell\ell$, Phys. Rev. Lett. **86** (2001) 3969, `arXiv:hep-ex/0011077`. ↪ cited on page 27

[188] LHCb, R. Aaij *et al.*, *Search for the decay* $D_0 \to \pi^+\pi^-\mu^+\mu^-$, Phys. Lett. **B728** (2014) 234, `arXiv:1310.2535`. ↪ cited on pages 27, 123

[189] LHCb, R. Aaij *et al.*, *First observation of the decay* $D^0 \to K^-\pi^+\mu^+\mu^-$ *in the* ρ^0-ω *region of the dimuon mass spectrum*, Phys. Lett. **B757** (2016) 558, `arXiv:1510.08367`. ↪ cited on page 27

[190] LHCb, R. Aaij *et al.*, *Observation of* D^0 *meson decays to* $\pi^+\pi^-\mu^+\mu^-$ *and* $K^+K^-\mu^+\mu^-$ *final states*, Phys. Rev. Lett. **119** (2017), no. 18 181805, `arXiv:1707.08377`. ↪ cited on pages 27, 29, 124, 157, 195

[191] E. Byckling and K. Kajantie, *Particle Kinematics*, University of Jyvaskyla, Jyvaskyla, Finland, 1971. ↪ cited on page 29

[192] N. Cabibbo and A. Maksymowicz, *Angular Correlations in Ke-4 Decays and Determination of Low-Energy pi-pi Phase Shifts*, Phys. Rev. **137** (1965) B438, [Erratum: Phys. Rev.168,1926(1968)]. ↪ cited on page 29

[193] F. Kruger, L. M. Sehgal, N. Sinha, and R. Sinha, *Angular distribution and CP asymmetries in the decays* $\bar{B} \to K^-\pi^+e^-e^+$ *and* $\bar{B} \to \pi^-\pi^+e^-e^+$, Phys. Rev. **D61** (2000) 114028, `arXiv:hep-ph/9907386`, [Erratum: Phys. Rev.D63,019901(2001)]. ↪ cited on page 30

[194] D. Das, G. Hiller, M. Jung, and A. Shires, *The* $\overline{B} \to \overline{K}\pi\ell\ell$ *and* $\overline{B}_s \to \overline{K}K\ell\ell$ *distributions at low hadronic recoil*, JHEP **09** (2014) 109, `arXiv:1406.6681`. ↪ cited on page 31

[195] C. Bobeth, G. Hiller, and G. Piranishvili, *CP Asymmetries in bar B* $\to \bar{K}^*(\to \bar{K}\pi)\bar{\ell}\ell$ *and Untagged* $\bar{B}_s$, $B_s \to \phi(\to K^+K^-)\bar{\ell}\ell$ *Decays at NLO*, JHEP **07** (2008) 106, `arXiv:0805.2525`. ↪ cited on page 31

[196] C. Bobeth, G. Hiller, and D. van Dyk, *General analysis of* $\bar{B} \to \bar{K}^{(*)}\ell^+\ell^-$ *decays at low recoil*, Phys. Rev. **D87** (2013), no. 3 034016, `arXiv:1212.2321`, [Phys. Rev.D87,034016(2013)]. ↪ cited on page 31

[197] KTeV, E. Abouzaid *et al.*, *A Measurement of the K0 charge radius and a CP violating asymmetry together with a search for CP violating e1 direct photon emission in the rare decay* $K(L) \to \pi^+\pi^-e^+e^-$, Phys. Rev. Lett. **96** (2006) 101801, `arXiv:hep-ex/0508010`. ↪ cited on page 33

[198] C. Lazzeroni, *New NA48 results on CP violation*, Eur. Phys. J. **C33** (2004) S330. ↪ [see prev. ref.]

[199] LHCb, R. Aaij *et al.*, *Measurement of the polarization amplitudes and triple product asymmetries in the* $B_s^0 \to \phi\phi$ *decay*, Phys. Lett. **B713** (2012) 369, `arXiv:1204.2813`. ↪ [see prev. ref.]

[200] LHCb, R. Aaij *et al.*, *Search for CP violation using triple product asymmetries in $\Lambda_b^0 \to pK^-\pi^+\pi^-$, $\Lambda_b^0 \to pK^-K^+K^-$ and $\Xi_b^0 \to pK^-K^-\pi^+$ decays*, JHEP **08** (2018) 039, `arXiv:1805.03941`. ↪ [see prev. ref.]

[201] FOCUS, J. M. Link *et al.*, *Search for T violation in charm meson decays*, Phys. Lett. **B622** (2005) 239, `arXiv:hep-ex/0506012`. ↪ [see prev. ref.]

[202] BaBar, P. del Amo Sanchez *et al.*, *Search for CP violation using T-odd correlations in $D^0 \to K^+K^-\pi^+\pi^-$ decays*, Phys. Rev. **D81** (2010) 111103, `arXiv:1003.3397`. ↪ [see prev. ref.]

[203] BaBar, J. P. Lees *et al.*, *Search for CP violation using T-odd correlations in $D^+ \to K^+K_S^0\pi^+\pi^-$ and $D_s^+ \to K^+K_S^0\pi^+\pi^-$ decays*, Phys. Rev. **D84** (2011) 031103, `arXiv:1105.4410`. ↪ [see prev. ref.]

[204] LHCb, R. Aaij *et al.*, *Search for CP violation using T-odd correlations in $D^0 \to K^+K^-\pi^+\pi^-$ decays*, JHEP **10** (2014) 005, `arXiv:1408.1299`. ↪ cited on page 33

[205] S. Fajfer and N. Košnik, *Resonance catalyzed CP asymmetries in $D \to P\ell^+\ell^-$*, Phys. Rev. **D87** (2013), no. 5 054026, `arXiv:1208.0759`. ↪ cited on page 33

[206] LHCb, R. Aaij *et al.*, *Measurement of Angular and CP Asymmetries in $D^0 \to \pi^+\pi^-\mu^+\mu^-$ and $D^0 \to K^+K^-\mu^+\mu^-$ decays*, Phys. Rev. Lett. **121** (2018), no. 9 091801, `arXiv:1806.10793`. ↪ cited on pages 34, 135, 153

[207] A. A. Alves *et al.*, *The LHCb detector at the LHC*, Journal of Instrumentation **3** (2008) S08005. ↪ cited on pages 35, 37

[208] L. Evans and P. Bryant, *LHC machine*, Journal of Instrumentation **3** (2008) S08001. ↪ cited on page 35

[209] C. De Melis, *The CERN accelerator complex. Complexe des accélérateurs du CERN*, OPEN-PHO-ACCEL-2016-001 (2016), General Photo. ↪ cited on pages 36, 197

[210] LHCb, R. Aaij *et al.*, *Measurement of the b-quark production cross-section in 7 and 13 TeV pp collisions*, Phys. Rev. Lett. **118** (2017), no. 5 052002, `arXiv:1612.05140`, [Erratum: Phys. Rev. Lett.119,no.16,169901(2017)]. ↪ cited on page 37

[211] LHCb, R. Aaij *et al.*, *Measurements of prompt charm production cross-sections in pp collisions at $\sqrt{s} = 13$ TeV*, JHEP **03** (2016) 159, `arXiv:1510.01707`, [Erratum: JHEP05,074(2017)]. ↪ cited on page 37

[212] LHCb Collaboration, R. Antunes-Nobrega *et al.*, *LHCb reoptimized detector design and performance: Technical Design Report*, Technical Design Report LHCb, CERN, Geneva, 2003. ↪ cited on page 37

[213] H. Burkhardt and P. Grafström, *Absolute Luminosity from Machine Parameters*, Tech. Rep. LHC-PROJECT-Report-1019. CERN-LHC-PROJECT-Report-1019, 2007. ↪ cited on page 37

[214] F. Follin and D. Jacquet, *Implementation and experience with luminosity levelling with offset beam*, in *Proceedings, ICFA Mini-Workshop on Beam-Beam Effects in Hadron Colliders (BB2013): CERN, Geneva, Switzerland, March 18-22 2013*, pp. 183–187, 2014. `arXiv:1410.3667`. [,183(2014)], doi: 10.5170/CERN-2014-004.183. ↪ cited on page 38

[215] LHCb Collaboration, S. Amato *et al.*, *LHCb magnet: Technical Design Report*, Technical Design Report LHCb, CERN, Geneva, 2000. ↪ cited on page 38

[216] LHCb Collaboration, P. R. Barbosa-Marinho *et al.*, *LHCb VELO (VErtex LOcator): Technical Design Report*, Technical Design Report LHCb, CERN, Geneva, 2001. ↪ cited on page 39

[217] R. Aaij *et al.*, *Performance of the LHCb Vertex Locator*, JINST **9** (2014) P09007, `arXiv:1405.7808`. ↪ cited on page 40

[218] LHCb Collaboration, P. R. Barbosa-Marinho *et al.*, *LHCb inner tracker: Technical Design Report*, Technical Design Report LHCb, CERN, Geneva, 2002. revised version number 1 submitted on 2002-11-13 14:14:34. ↪ cited on page 41

[219] LHCb Collaboration, P. R. Barbosa-Marinho *et al.*, *LHCb outer tracker: Technical Design Report*, Technical Design Report LHCb, CERN, Geneva, 2001. ↪ cited on page 42

[220] LHCb Collaboration, S. Amato *et al.*, *LHCb RICH: Technical Design Report*, Technical Design Report LHCb, CERN, Geneva, 2000. ↪ cited on page 43

[221] LHCb RICH Group, M. Adinolfi *et al.*, *Performance of the LHCb RICH detector at the LHC*, Eur. Phys. J. **C73** (2013) 2431, `arXiv:1211.6759`. ↪ cited on pages 44, 198

[222] LHCb Collaboration, S. Amato *et al.*, *LHCb calorimeters: Technical Design Report*, Technical Design Report LHCb, CERN, Geneva, 2000. ↪ cited on page 44

[223] LHCb Collaboration, P. R. Barbosa-Marinho *et al.*, *LHCb muon system: Technical Design Report*, Technical Design Report LHCb, CERN, Geneva, 2001. ↪ cited on page 46

[224] LHCb Collaboration, *LHCb muon system: addendum to the Technical Design Report*, Technical Design Report LHCb, CERN, Geneva, 2003. ↪ [see prev. ref.]

[225] LHCb Collaboration, *LHCb muon system: second addendum to the Technical Design Report*, Technical Design Report LHCb, CERN, Geneva, 2005. Submitted on 9 Apr 2005. ↪ cited on page 46

[226] F. Sauli, *Principles of operation of multiwire proportional and drift chambers*, (Geneva), p. 92 p, CERN, CERN, 1977. CERN, Geneva, 1975 - 1976, doi: 10.5170/CERN-1977-009. ↪ cited on page 48

[227] W. Bonivento *et al.*, *A triple GEM detector with pad readout for high rate charged particle triggering*, Nucl. Instrum. Methods Phys. Res. , A **488** (2002), no. 1-2 493. ↪ cited on page 48

[228] F. Sauli, *Gem: A new concept for electron amplification in gas detectors*, Nuclear Instruments and Methods in Physics Research Section A: Accelerators, Spectrometers, Detectors and Associated Equipment **386** (1997), no. 2 531 . ↪ cited on page 48

[229] LHCb Collaboration, *Nu, Mu and Pile-Up. The LHCb definitions of what we see and what we don't see.*, `https://twiki.cern.ch/twiki/bin/view/LHCb/NuMuPileUp`. ↪ cited on page 51

[230] LHCb, F. Dordei, *LHCb detector and trigger performance in Run II*, EPJ Web Conf. **164** (2017) 01016. 10 p. ↪ cited on page 51

[231] LHCb Collaboration, R. Antunes-Nobrega *et al.*, *LHCb trigger system: Technical Design Report*, Technical Design Report LHCb, CERN, Geneva, 2003. revised version number 1 submitted on 2003-09-24 12:12:22. ↪ cited on page 51

[232] R. Aaij *et al.*, *The LHCb Trigger and its Performance in 2011*, JINST **8** (2013) P04022, `arXiv:1211.3055`. ↪ cited on page 51

[233] LHCb Collaboration, *LHCb Tracking Strategies*, `https://twiki.cern.ch/twiki/bin/view/LHCb/LHCbTrackingStrategies`. ↪ cited on pages 53, 57

[234] R. Frühwirth, *Application of kalman filtering to track and vertex fitting*, Nuclear Instruments and Methods in Physics Research Section A: Accelerators, Spectrometers, Detectors and Associated Equipment **262** (1987), no. 2 444 . ↪ cited on pages 53, 58

[235] T. Likhomanenko *et al.*, *LHCb Topological Trigger Reoptimization*, J. Phys. Conf. Ser. **664** (2015), no. 8 082025, `arXiv:1510.00572`. ↪ cited on pages 53, 127

[236] M. Frank *et al.*, *Deferred High Level Trigger in LHCb: A Boost to CPU Resource Utilization*, J. Phys. Conf. Ser. **513** (2014) 012006. ↪ cited on page 54

[237] G. Dujany and B. Storaci, *Real-time alignment and calibration of the LHCb Detector in Run II*, J.

Phys. Conf. Ser. **664** (2015), no. 8 082010. ↪ cited on page 54

[238] M. Clemencic *et al.*, *Recent developments in the LHCb software framework Gaudi*, J. Phys. Conf. Ser. **219** (2010) 042006. ↪ cited on page 54

[239] LHCb Collaboration, *The Brunel project*, `http://cern.ch/lhcbdoc/brunel/`. ↪ cited on page 55

[240] LHCb Collaboration, *The DaVinci project*, `http://cern.ch/lhcbdoc/davinci/`. ↪ cited on page 55

[241] R. Brun and F. Rademakers, *ROOT: An object oriented data analysis framework*, Nucl. Instrum. Meth. **A389** (1997) 81. ↪ cited on page 55

[242] LHCb Collaboration, *The Moore project*, `http://cern.ch/lhcbdoc/moore/`. ↪ cited on page 55

[243] LHCb Collaboration, *The Gauss project*, `http://cern.ch/lhcbdoc/gauss`. ↪ cited on page 55

[244] T. Sjöstrand *et al.*, *An Introduction to PYTHIA 8.2*, Comput. Phys. Commun. **191** (2015) 159, `arXiv:1410.3012`. ↪ cited on page 55

[245] A. Ryd *et al.*, *EvtGen: A Monte Carlo Generator for B-Physics*, . ↪ cited on page 55

[246] GEANT4, S. Agostinelli *et al.*, *GEANT4: A Simulation toolkit*, Nucl. Instrum. Meth. **A506** (2003) 250. ↪ cited on page 55

[247] LHCb Collaboration, *The Boole project*, `http://cern.ch/lhcbdoc/boole/`. ↪ cited on page 55

[248] LHCb Collaboration, *The LHCb Stripping*, `https://twiki.cern.ch/twiki/bin/view/LHCb/LHCbStripping`. ↪ cited on page 55

[249] S. Tolk, J. Albrecht, F. Dettori, and A. Pellegrino, *Data driven trigger efficiency determination at LHCb*, Tech. Rep. LHCb-PUB-2014-039. CERN-LHCb-PUB-2014-039, CERN, Geneva, May, 2014. ↪ cited on page 56

[250] F. Archilli *et al.*, *Performance of the Muon Identification at LHCb*, JINST **8** (2013) P10020, `arXiv:1306.0249`. ↪ cited on page 59

[251] LHCb, R. Aaij *et al.*, *LHCb Detector Performance*, Int. J. Mod. Phys. **A30** (2015), no. 07 1530022, `arXiv:1412.6352`. ↪ cited on page 60

[252] LHCb, R. Aaij *et al.*, *Implications of LHCb measurements and future prospects*, Eur. Phys. J. **C73** (2013), no. 4 2373, `arXiv:1208.3355`. ↪ cited on pages 61, 62

[253] *Letter of Intent for the LHCb Upgrade*, Tech. Rep. CERN-LHCC-2011-001. LHCC-I-018, CERN, Geneva, Mar, 2011. ↪ cited on page 61

[254] LHCb collaboration, I. Bediaga *et al.*, *Framework TDR for the LHCb Upgrade: Technical Design Report*, Tech. Rep. CERN-LHCC-2012-007. LHCb-TDR-12, Apr, 2012. ↪ cited on page 61

[255] N. Tuning, *Lessons learned from LHCb about making precise flavour measurements*, . ↪ cited on page 61

[256] *LHCb Trigger and Online Upgrade Technical Design Report*, Tech. Rep. CERN-LHCC-2014-016. LHCB-TDR-016, May, 2014. ↪ cited on page 62

[257] F. Alessio *et al.*, *Clock and timing distribution in the LHCb upgraded detector and readout system*, JINST **10** (2014) C02033. 10 p, CERN-Poster-2014-461. ↪ cited on page 64

[258] F. Alessio and R. Jacobsson, *A New Readout Control System for the LHCb Upgrade at CERN*, Tech. Rep. LHCb-PROC-2012-024. CERN-LHCb-PROC-2012-024, CERN, Geneva, Jun, 2012. ↪ cited on page 64

[259] J. Barbosa, F. Alessio, and C. Gaspar, *The new version of the LHCb SOL40-SCA core to drive front-end GBT-SCAs for the LHCb upgrade*, PoS **TWEPP-17** (2018) 078. ↪ cited on page 62

[260] P. Moreira *et al.*, *The GBT Project*, in *Proceedings, Topical Workshop on Electronics for Particle*

Physics (TWEPP09), CERN, CERN, 2009. doi: 10.5170/CERN-2009-006.342. ↪ cited on page 64

[261] CMS, L. Amaral *et al.*, *The versatile link, a common project for super-LHC*, JINST **4** (2009) P12003. ↪ cited on page 64

[262] A. Caratelli *et al.*, *The GBT-SCA, a radiation tolerant ASIC for detector control and monitoring applications in HEP experiments*, JINST **10** (2015), no. 03 C03034. ↪ cited on page 64

[263] M. Bellato *et al.*, *A PCIe gen3 based readout for the LHCb upgrade*, Journal of Physics: Conference Series **513** (2014) 012023. ↪ cited on page 65

[264] J. P. Cachemiche *et al.*, *The PCIe-based readout system for the LHCb experiment*, JINST **11** (2016), no. 02 P02013. 12 p. ↪ [see prev. ref.]

[265] J. Mitra *et al.*, *GBT link testing and performance measurement on PCIe40 and AMC40 custom design FPGA boards*, JINST **11** (2016), no. 03 C03039. 12 p. ↪ cited on page 65

[266] L. Collaboration, *LHCb VELO Upgrade Technical Design Report*, Tech. Rep. CERN-LHCC-2013-021. LHCB-TDR-013, Nov, 2013. ↪ cited on page 66

[267] L. Collaboration, *LHCb Tracker Upgrade Technical Design Report*, Tech. Rep. CERN-LHCC-2014-001. LHCB-TDR-015, Feb, 2014. ↪ cited on page 66

[268] L. Collaboration, *LHCb PID Upgrade Technical Design Report*, Tech. Rep. CERN-LHCC-2013-022. LHCB-TDR-014, Nov, 2013. ↪ cited on pages 66, 71

[269] D. Brundu, *A new readout electronics for the LHCb Muon Detector Upgrade*, Jun, 2018. ↪ cited on pages 69, 71

[270] S. Cadeddu *et al.*, *The nSYNC ASIC for the new readout electronics of the LHCb Muon Detector Upgrade.*, Nucl. Instrum. Meth. **936** (2018) 378. ↪ cited on page 69

[271] S. Cadeddu, V. De Leo, C. Deplano, and A. Lai, *The SYNC chip in the electronics architecture of the LHCb muon detector*, IEEE Trans. Nucl. Sci. **57** (2010) 2790. ↪ cited on page 69

[272] Chance Elliott and Vipin Vijayakumar and Wesley Zink and Richard Hansen, *National Instruments LabVIEW: A Programming Environment for Laboratory Automation and Measurement*, JALA: Journal of the Association for Laboratory Automation **12** (2007), no. 1 17, `arXiv:https://doi.org/10.1016/j.jala.2006.07.012`. ↪ cited on page 80

[273] G. Vouters *et al.*, *LHCb upgrade MiniDAQ Handbook*, Tech. Rep. LHCb-INT-2014-010. CERN-LHCb-INT-2014-010, CERN, Geneva, Apr, 2014. ↪ cited on page 80

[274] C. Gaspar, M. Dönszelmann, and P. Charpentier, *DIM, a portable, light weight package for information publishing, data transfer and inter-process communication*, Comput. Phys. Commun. **140** (2001) 102. ↪ cited on page 80

[275] R. Martin Lesma *et al.*, *The Versatile Link Demo Board (VLDB)*, JINST **12** (2017), no. 02 C02020. 12 p. ↪ cited on page 81

[276] Holmes-Siedle, A. and Adams, L. , *Handbook of radiation effects*, Oxford science publications, Oxford University Press, 1993. ↪ cited on pages 89, 90, 92, 199, 200

[277] A. Ferrari, P. R. Sala, A. Fasso, and J. Ranft, *FLUKA: A multi-particle transport code (Program version 2005)*, . ↪ cited on page 93

[278] F. Faccio, *Radiation effects in devices Radiation effects in devices and technologies, Presented at School "Rivelatori ed Elettronica per Fisica delle Alte Energie, Astrofisica, Applicazioni Spaziali e Fisica Medica", INFN Laboratori Nazionali di Legnaro (Padova), 20-24 Aprile 2009*, 2009. ↪ cited on pages 97, 200

[279] M Huhtinen and F Faccio, *Computational method to estimate Single Event Upset rates in an accel-*

erator environment, Nuclear Instruments and Methods in Physics Research Section A: Accelerators, Spectrometers, Detectors and Associated Equipment **450** (2000), no. 1 155 . ↪ cited on page 97

[280] M. J. Boschini, P. G. Rancoita and M. Tacconi, *SR-NIEL Calculator: Screened Relativistic (SR) Treatment for Calculating the Displacement Damage and Nuclear Stopping Powers for Electrons, Protons, Light- and Heavy- Ions in Materials*, 2014. ↪ cited on page 102

[281] D. Brundu *et al.*, *An X-Ray facility to perform irradiation tests and TID studies on electronics and detectors*, Tech. Rep. LHCb-PUB-2018-007. CERN-LHCb-PUB-2018-007, CERN, Geneva, Mar, 2018. ↪ cited on pages 109, 115

[282] Hubbell, J. H. and Seltzer, S. M. , *Tables of X-Ray Mass Attenuation Coefficients and Mass Energy-Absorption Coefficients (version 1.4). National Institute of Standards and Technology, Gaithersburg, MD.*, 2004. ↪ cited on pages 111, 112

[283] M. A. Clemens, *Energy deposition mechanisms for proton- and neutron-induced single event upsets in modern electronic devices*, PhD thesis, Nashville, Tennessee, 2012-05. ↪ cited on page 119

[284] M. Lisovyi, A. Verbytskyi, and O. Zenaiev, *Combined analysis of charm-quark fragmentation-fraction measurements*, Eur. Phys. J. **C76** (2016), no. 7 397, `arXiv:1509.01061`. ↪ cited on page 122

[285] F. Dettori, *Measurement of strange hadron production ratios and perspectives for the search of $D^0 \to \mu^+\mu^-$ decay at LHCb*, PhD thesis, Cagliari U., 2011. ↪ cited on page 122

[286] Fitzpatrick, Conor and Williams, J Michael and Meloni, Simone and Boettcher, Thomas Julian and Whitehead, Mark Peter and Dziurda, Agnieszka and Vesterinen, Mika Anton, *Upgrade trigger: Bandwidth strategy proposal*, Tech. Rep. LHCb-PUB-2017-006. CERN-LHCb-PUB-2017-006, CERN, Geneva, Feb, 2017. ↪ cited on page 127

[287] LHCb Collaboration, *Decay Tree Fitter*, `https://twiki.cern.ch/twiki/bin/view/LHCb/DecayTreeFitter`. ↪ cited on page 132

[288] W. D. Hulsbergen, *Decay chain fitting with a Kalman filter*, Nucl. Instrum. Meth. **A552** (2005) 566, `arXiv:physics/0503191`. ↪ cited on page 132

[289] LHCb, R. Aaij *et al.*, *Measurement of CP asymmetry in $D^0 \to K^-K^+$ decays*, Phys. Lett. **B767** (2017) 177, `arXiv:1610.09476`. ↪ cited on page 135

[290] A. Hocker *et al.*, *TMVA - Toolkit for Multivariate Data Analysis*, `arXiv:physics/0703039`. ↪ cited on page 136

[291] B. Viaud, *On the potential of multivariate techniques for the determination of multidimensional efficiencies*, The European Physical Journal Plus **131** (2016) 191. ↪ cited on page 141

[292] L. Anderlini *et al.*, *The PIDCalib package*, Tech. Rep. LHCb-PUB-2016-021. CERN-LHCb-PUB-2016-021, CERN, Geneva, Jul, 2016. ↪ cited on page 153

[293] A. A. Alves Junior, *Multithreadcorner/hydra*, 2018. doi: 10.5281/zenodo.1206261. ↪ cited on page 155

[294] Belle Collaboration, Garmash, A. et al. , *Dalitz analysis of the three-body charmless decays $B^+ \to K^+\pi^+\pi^-$ and $B^+ \to K^+K^+K^-$*, Phys. Rev. D **71** (2005) 092003. ↪ cited on page 156

[295] P. d'Argent *et al.*, *Amplitude Analyses of $D^0 \to \pi^+\pi^-\pi^+\pi^-$ and $D^0 \to K^+K^-\pi^+\pi^-$ Decays*, JHEP **05** (2017) 143, `arXiv:1703.08505`. ↪ cited on page 162

[296] H. B. O'Connell, B. C. Pearce, A. W. Thomas, and A. G. Williams, *$\rho - \omega$ mixing, vector meson dominance and the pion form-factor*, Prog. Part. Nucl. Phys. **39** (1997) 201, `arXiv:hep-ph/9501251`. ↪ cited on page 162

[297] Chung, S. U. and Brose, J. and Hackmann, R. and Klempt, E. and Spanier, S. and Strassburger, C. , *Partial wave analysis in K-matrix formalism*, Annalen der Physik **507** (1995),

no. 5 404, `arXiv:https://onlinelibrary.wiley.com/doi/pdf/10.1002/andp.19955070504`. ↪ cited on page 162

[298] G. J. Gounaris and J. J. Sakurai, *Finite width corrections to the vector meson dominance prediction for rho —> e+ e-*, Phys. Rev. Lett. **21** (1968) 244. ↪ cited on page 162

[299] I. Narsky and F. C. Porter, *Statistical analysis techniques in particle physics*, Wiley-VCH, Weinheim, Germany, 2014. ↪ cited on page 168

[300] C. Langenbruch, *Angular conventions for the decays* $B^0 \to K^*\mu^+\mu^-$ *and* $B_s^0 \to \phi\mu^+\mu^-$, Tech. Rep. LHCb-INT-2012-021. CERN-LHCb-INT-2012-021, CERN, Geneva, Aug, 2012. ↪ cited on pages 175, 176, 177, 204

[301] LHCb, R. Aaij *et al.*, *Observation of* $J/\psi p$ *Resonances Consistent with Pentaquark States in* $\Lambda_b^0 \to J/\psi K^- p$ *Decays*, Phys. Rev. Lett. **115** (2015) 072001, `arXiv:1507.03414`. ↪ cited on page 185

[302] Belle, K. Chilikin *et al.*, *Experimental constraints on the spin and parity of the* $Z(4430)^+$, Phys. Rev. **D88** (2013), no. 7 074026, `arXiv:1306.4894`. ↪ cited on pages 185, 194

ACKNOWLEDGEMENTS

In these three years of PhD I had the opportunity and the pleasure to know and to work with several people, as well as being supported by colleagues, friends and family. Therefore a sincere thanks is due to all of them. First of all I would like to thank my parents, who have always been present, even when I was physically distant, and who have always encouraged me to follow my passions, and not to give up in the face of apparent difficulties. A special thanks to Piera, who has been always by my side in these three years of PhD, with whom I have shared everything, from joys and satisfactions to efforts and obstacles.

I wish to thank my supervisor Alessandro Cardini, for giving me the opportunity to work within the LHCb experiment, for the interesting discussions and brainstorming of physics, detectors and electronics, and for continuously renewing in me an interdisciplinary curiosity, that we have in common. I also wish to thank all those who have had the task of co-supervision during these three years. Thanks to Andrea Contu, for the physics he taught me and for guiding me in a complicated analysis, for the interesting ideas and suggestions during the writing of the thesis. Thanks to Angelo di Canto and Dominik Mitzel for the interesting discussions and advice, for teaching me the pragmatism and concreteness in an analysis work. A special thanks to Augusto, for guiding me in the analysis work, for teaching me a lot of physics and a working style focused on studying and deepening, but also for his support and the time spent together, for all the political discussions and philosophical chats, always accompanied by a good cigar and a good amaro. Thanks to Sandro and Luigi, with whom I worked in the testing phase of the nSYNC chip; it was a pleasure to discuss and work with them, I really feel part of a great close-knit team.

I would also like to thank the Frascati electronics group and the CERN readout group, in particular Paolo Ciambrone and Federico Alessio, who I respect for their competence and expertise; it has been a privilege to collaborate with them and their groups. Thanks to LHCb muon group, and in particular to Wander and Oleg, for the help during my months of muon piquet and for the stimulating work, which always reminds me how important and non-trivial is to make the detector work properly. Thanks to Francesco and Marianna, who followed me during the master's thesis and always available for interesting discussions, their initial help was fundamental in tracing this path. An extended thanks to the LHCb collaboration and to the LHCb group of Cagliari for welcoming me as a colleague in a stimulating environment. I would like to thank the Università di Cagliari and the Instituto Nazionale di Fisica Nucleare (INFN), in particular the section of Cagliari, for the financial and technical-administrative support that made this work possible. I thank the Cagliari PhD school, in particular the coordinators Paolo Ruggerone, Umberto D'Alesio and Alessandro De Falco, for their coordination work and for the support they have given us.

I thank my old friends, with the hope of taking back the lost time: Michele, Marco, Matteo, Daniele, Albertixeddu, Laura, Giulia, Federica. I would like to thank all my friends, colleagues in Cagliari and at CERN, and my PhD colleagues of the XXXII cycle: Matteo, Emmanuele, Mauro, Andrea, Gianluca, Danilo, Silvia, Gaia, Isabella, Michela, Kirtana, Luca, Saverio, Carlo, Angelo, Elisa, Paola, Andrea, Giovanna for the happy and carefree moments spent together.